UNIVERSITAT POLITÈCNICA DE CATALUNYA BARCELONATECH

Polymers and peptide-polymer conjugates as bioactive platforms and carriers for the encapsulation of biomolecules

presented by

Silvana Maione

UNIVERSITAT POLITÈCNICA DE CATALUNYA
BARCELONATECH
Escola Tècnica Superior d'Enginyeria Industrial de Barcelona

Polymers and Peptide-Polymer Conjugates as Bioactive Platforms and Carriers for the Encapsulation of Biomolecules

Presented by

Silvana Maione

Supervisor:

Prof. Carlos Alemán

Thesis submitted to obtain the degree Doctor of Philosophy in *Polymers and Biopolymers* at Universitat Politècnica de Catalunya

Barcelona, September 2017

Departament d'Enginyeria Química

Grup d'Innovació en Materials i Enginyeria Molecular

A mio marito,

che mi hai accompagnato giorno dopo giorno in questa avventura.

Abstract

In the last decade, conductive polymers have received great interest in both scientific and technological levels due to the electroactive properties exhibited by these materials. For this reason, the main aim of this Doctoral Thesis is to study the applications of some conducting polymers, mainly derived from polythiophene, in the field of biomedicine and biotechnology.

According to the objectives proposed in this Document, different studies focused on the preparation and characterization of graft copolymers have been carried out using macromonomers formed by oligo-thiophenes to which PEG chains of well-defined molecular weight have been incorporated as substituents. After this, the behavior of these new polymers has been investigated in terms of cytotoxicity and biocompatibility using cell adhesion and cell proliferation assays.

Then, the synthesis and characterization of conducting polymer-peptide hybrids have been developed. Initially, the methodology used for the preparation of these materials has been optimized using model systems in which the peptide has been replaced by an amino acid, which has been engineered by chemical similarity. After evaluate different synthetic approaches, hybrids constructed by combining the same conducting polymer and the RG*D peptide have been prepared, where RG*D is a sequence analogous to the RGD (Arg-Gly-Asp) in which the central Gly residue is replaced by the above mentioned engineered amino acids. The biocompatibility and the bioactivity of all these compounds have been examined.

The last part of this thesis is oriented towards the encapsulation of small biomolecules in polymeric nanostructures that can be used as transport systems and controlled release systems when incorporated into the organism. The encapsulation of simple amino acids has been examined firstly, this research evolving towards the immobilization of linear and cyclic hydrophobic peptides. In all cases encapsulation was carried out by electrospraying or electrospinning.

Results obtained in this Thesis have been reported in the following publications:

- "Polythiophene-*g*-poly(ethylene glycol) Graft Copolymers from Electroactive Scaffolds".

A.-D. Bendrea, G. Fabregat, J. Torras, S. Maione, L. Cianga, L. J. del Valle, I. Cianga & C. Alemán. *J. Mater. Chem. B* **2013**, *1*, 4135-4145.

- "Effect of the Graft Ratio on the Properties of Polythiophene-*g*-poly(ethylene glycol)".

S. Maione, G. Fabregat, L. J. del Valle, A.-D. Bendrea, L. Cianga, I. Cianga, F. Estrany & C. Alemán. *J. Polym. Sci., Part B: Polym. Phys.* **2015**, *53*, 239-252.

- "Electro-Biocompatibility of Conjugates Designed by Chemical Similarity".

S. Maione, G. Fabregat, L. J. del Valle, G. Ballano, C. Cativiela & C. Alemán. *J. Pept. Sci.* **2014**, *20*, 537-546.

- "Electroactive Polymer-Peptide Conjugates for Adhesive Biointerfaces".

S. Maione, A. M. Gil, G. Fabregat, L. J. del Valle, J. Triguero, A. Laurent, D. Jacquemin, F. Estrany, A. I. Jiménez, D. Zanuy, C. Cativiela & C. Alemán. *Biomater. Sci.* **2015**, *3*, 1395-1405.

- Electrospray Loading and Release of Hydrophobic Gramicidin in Polyester Microparticles".

S. Maione, L. J. del Valle, M. M. Pérez-Madrigal, C. Cativiela, J. Puiggalí & C. Alemán. *RSC Adv.* **2016**, *6*, 69634-69640.

- "Biodegradable Nanofibrous Scaffolds as Smart Delivery Vehicles for Amino Acids".

S. Maione, M. M. Pérez-Madrigal, L. J. Del Valle, A. Díaz, L. Franco, C. Cativiela, J. Puiggalí & C. Alemán. *J. Appl. Polym. Sci.* **2017**, *134*, 44883 (1-14).

Aknowledgements

Ahora que ha llegado el momento de redactor los agradecimientos, me doy cuenta que este es el final de un largo trayecto. Ha sido una experiencia muy importante para mí, que me ha ayudado a superar muchos límites y a aprender muchas cosas nuevas.

En primer lugar me gustaría darle las gracias a mi tutor, Carlos Alemán, que me dio la posibilidad de entrar a formar parte de la grande familia del grupo IMEM. Gracias a su constante apoyo, su buen criterio y sus consejos he podido llevar a cabo este proyecto, que me entusiasmó desde su comienzo.

Agradezco también la colaboración de todos los profesores y de los investigadores del departamento de Ingenieria Química de la UPC que me han guiado cuando estaba perdida o estancada con algún maquinario o algún tipo de ensayo.

A las "Chemical's girls", doctorandas y doctoras, que he conocido en este camino me gustaría decirles que les considero mucho más que simples amigas. Angelica, Ana, Georgina, Mar, Neudys, Elena, Yolanda, Cinthia, Ana Pg os habéis converitdo en mi familia aquí en Barcelona. Gracias por estar siempre presentes aunque ya no nos vemos todos los días. Os deseo a todas una vida llena de amor y de felicidad.

Un pensiero especial va a mis amigos de Ecuador, Pablo y Cristina, que han compartido conmigo muchos momentos unicos. Gracias por haberme regalado vuestra amistad, es la cosa más valiosa que me puedo llevar de esta experiencia.

En esta occasión me gustaría saludar a todos mis compañeros de APS. Sois una gran familia y estoy orgullosa de formar parte de ella.

Ahora me toca cambiar de idioma para que los italianos no se sientan excluidos ☺

A mia mamma e a mio padre, mi piacerebbe dirvi ancora una volta grazie per tutto l'amore e il supporto che mi date quotidianamente. Anche se siamo lontani fisicamente, vi sento vicini con il cuore e questo mi da la forza di continuare a lottare tutti i giorni per raggiungere i mei sogni che so, appartengono anche a voi. Spero un giorno di riuscire a provare le stesse sensazione che provete con noi figlie "ribelli" ma tranquille.

Un abbraccio forte alla mia sorellina super dottoressa Felicetta, quanto mi piacerebbe poter condividere ancora di piú con te. A volte messaggi e telefonate non sono abbastanza, peró basta rivederci per tornare bambine insieme. Grazie per la gioia que mi trasmetti e perché mi fai ricordare che sono le piccole cose quelle che piú contano nella vita. Ti voglio bene.

E continuando con la famiglia, mi piacerebbe salutare tutti i Cifariello che ho conosciuto in questi anni. Spero possiamo vivere sempre piú momenti felici insieme.

E per utlimo vorrei dedicare due righe a Nunzio che dopo essere stato il mio primo fidanzato durante dieci anni, giusto l'anno scorso é diventato mio marito... Come tu ben sai, non ci siamo mai persi in tutti questi anni perché tra di noi c'é qualcosa che ci unisce e anche se non saprei spiegare bene cos'é, so che non finirá mai. La mia vita senza te non avrebbe senso per questo ti prometto che continueró ad amarti fino al mio ultimo respiro. Grazie perché mi fai sempre sentire come una principessa ed effettivamente con te mi sembra di vivere un sogno. Ti amo vita mia!

Mi piacerebbe concludere dicendo grazie a tutte quelle persone che ho incontrato nella mia vita, ogniuno di loro sicuramente mi ha aiutato ad essere quella che sono adesso.

Y para concluir me gustaría dar las gracias a todos aquellos que he conocido a lo largo de mi vida, cadauno de ellos me ha ayudado a ser la que soy hoy.

Table of contents

LIST OF ABBREVIATIONS

Abbreviation	Meaning
POLYMERS	
PAc	Polyacetylene
PANI	Polyaniline
PCL	Polycaprolactone
PE44	poly(tetramethylene succinate)
PEDOT	Poly(3,4-ethylenedioxythiophene)
PEG	Poly(ethylene glycol)
PET	Polyethylene terephthalate
PGA	Poly(glycolic acid)
PHAs	Polyhydroxyalkanoates
PLA	Poly(lactic acid)
PLCL	Poly(lactide-*co*-caprolactone)
PLGA	Poly(lactide-*co*-glycol acid)
PMMA	Poly(methylmethacrylate)
PPy	Polypyrrole
PS	Polystyrene
PSU	Polysulfones
PTh (PTh$_3$)	Polythiophene (Poly(α-terthiophene))
PTh-g-PEG$_n$	PEG chains grafted to PTh backbone (*n*: molecular weight of PEG chains,)
PUs	Polyurethanes
PVA	Poly(vinyl alcohol)
S-PEEK	Sulfonate poly(ether ether ketone)
CHEMICAL COMPOUND	
Bu$_4$NPF$_6$	Tetra butyl ammonium hexafluorophosphate
DCM	Dichloromethane mixture
DMSO	Dimethyl sulfoxide
EDOT	3,4-ethylenedioxythiophene
EDTA	Ethylenediaminetetraacetic acid
GA	Gramicidin
GA-L	Linear gramicidin
GA-S	Gramicidin soviet
GM	Gentamicin
GO	Graphene oxide

ITO	Indium-tin oxide
MTT	3-(4,5-dimethylthiazol-2-yl)-2,5-diphenyltetrazolium bromide
PBS	Phosphate buffered saline
PBS-EtOH	PBS supplemented with 70 *v/v*-% of ethanol
PE44-GA	PE44 microspheres loaded with GA-L
RGDS	Arg-Gly-Asp-Cys
TFA	Trifluroacetic acid
Th_3	α-Terthiophene
U-PE44	Unloaded PE44 microspheres
GENERAL ABBREVIATIONS	
AA	Amino acid
AFM	Atomic force microscopy
AISI	American iron and steel institute
AMBER	Assisted model building with energy refinement
ANOVA	Analysis of variance
ASH	Average step height
ATCC	American type culture collection
ATR	Attenuated total reflection
BCRP	Breast cancer resistance protein
BET	Brunauer–Emmett–Teller
CA	Chronoamperometry
CD	Circular dichroism
CP	Conducting polymer
CV	Cyclic voltammetry
DL	Doping level
DLS	Dynamic light scattering
DMEM	Dulbecco's modified Eagle medium
DTGA	Differential thermal gravimetric analysis
DSC	Differential scanning calorimetry
DSSC	Dye-sensitized solar cell
E. coli	*Escherichia coli*
ECM	Extra cellular matrix
EDX	Energy-dispersive X-ray spectroscopy
EOS	Equation-of-State method
FBS	Fetal bovine serum
GAFF	Generalized AMBER force-field
LB	Luria-Bertani
LE	Loading efficiency

LEA	Loss of electroactivity [%]
MD	Molecular dynamics
MDCK	Madin Darby canine kidney
nHA	Hydroxyapatite nanoparticles
OWK	Owen-Wend-Kaelble model
PCM	Polarizable Continuum Model
RCC	Renal cell carcinoma
RCS	Refrigeration cooling system
RESP	Restrained electrostatic potential
RMS	Root mean square
S. aureus	*Staphylococcus aureus*
SEM	Scanning electron microscopy
TCPS	Tissue culture polystyrene
TGA	Thermogravimetric analyses
VD	Vertical distance
VSI	Vertical scanning interferometry
WAXD	Wide-Angle X-ray Diffraction
XPS	X-ray photoelectron spectroscopy

LIST OF SYMBOLS

$\Delta\,\theta$	Difference between the initial and the final contact angle measurements
θ	Contact angle [º]
χ_c	Degree of crystallinity
$\Delta\,Q$	Difference between the voltammetric charges (in C) of the first and the last oxidation-reduction cycles
d	Average particle diameter
$d_{e\text{-}e}$	End-to-end distance (Å)
D_{av}	Average diameter
D_{eff}	Effective particle diameter
F	Faraday constant
j_{max}	Maximum value of anodic current density
$L_{(hkl)}$	Average crystallite size in the orthogonal direction to the plane (*hkl*)
M_w	Weight average molecular weight
n_{av}	Number of electrons per monomer
n_{ox}	Number of electrons consumed to incorporate a monomer into the polymer and to oxidize the resulting chain
Q_{pol}	Polymerization charge consumed in the polymerization process (in mC/cm^2)
R_{max}	Maximum height of the topographic peaks
R_q	Root mean square roughness
ε_g	Band gap energy, also named π-π^* lowest transition energy [eV]
λ_{max}	Maximum wavelength [nm]
λ^{onset}	Onset wavelength [nm]

LIST OF FIGURES

Chapter 1. INTRODUCTION

Chapter 3. POLYTHIOPHENE-G-POLY(ETHYLENE GLYCOL) GRAPH COPOLYMERS AS HYBRID BIOPLATFORMS FOR TISSUE ENGINEERING

LIST OF TABLES

Chapter 5. BIODEGRADABLE NANOFIBROUS SCAFFOLDS AS SMART DELIVERY VEHICLES FOR AMINO ACIDS

Chapter 6. LOADING AND RELEASE OF HYDROPHOBIC GRAMICIDIN IN MICRO- AND NANOSTRUCTURED POLYESTER

CHAPTER 1

Introduction

1.1 POLYMERS FOR BIOMEDICAL APPLICATIONS

Biomaterials can be broadly classified into: metals, ceramics, natural or synthetic polymers and composites. Synthetic polymers, which represent the largest and versatile class of biomaterials, are extensively applied in multitude of biomedical applications. This versatility should be attributed to their chemical variability, relative ease of preparation, and high adaptability, since their physical and chemical properties can be tailored to the specific needs of their applications.

Technological advancements over the last two decades, particularly in the field of biomaterials, have revolutionized the biomaterials-based health care industry. These technological developments have enhanced the longevity and quality of life due to the production of efficient and sophisticated medical devices. Overall, these advancements have been driven by several factors, including: significant changes in the life style pattern, increasing medical needs of the growing and aging world population, social pressure to reduce health care costs and increasing awareness among the public regarding the advantages of using modern biomaterials in medical devices [1].

Biomaterials are the platform necessary for the proper development and progress of emerging fields such as tissue engineering, nanotechnology, and the delivery of bioactive agents for treating, repairing, and restoring function of tissues.

In addition to the above mentioned advantages, another crucial factor for the success of polymer-based biomaterials is their cost, which is relatively low with respect to inorganic biomaterials. The latter has acted as a powerful catalyst facilitating rapid advances in the convergence of concepts, ideas and research tools at the interfaces between very different disciplines (i.e. chemistry, materials science, biomedical engineering, surface science, biophysics and biology). These symbiotic relationships have driven the maturation of polymeric biomaterials based technologies from scientific breakthroughs to the commercial applications at a very rapid pace over the past few years.

1.1.1 Polymers scaffolds for biomedical applications

Traditionally, polymers have been used across different disciplines in a variety of applications, as for example medical, personal care, and food applications.

This Thesis is focused on polymers used in biomedicine, specifically those designed as scaffolds for tissue engineering and regenerative medicine. In the last 10 years lots of energies have been spent in the field of tissue engineering with the object of regenerate tissues and organs in the human body. Consequently, advances have been developed in multitude of disciplines, including cell biology, biomaterials science, imaging and surface chemistry [2]. The general strategies adopted by tissue engineering are classified in three groups:

- implantation of isolated cells or cell substitutes into the organism,
- delivery of tissue-inducing substances (such as growth factors),
- placing of cells on/within different matrices.

The design and fabrication of scaffolds is among the major areas of biomaterials research since scaffolds play a unique role in tissue regeneration and repair. Others important aspects are: how to incorporate cells for transplantation or biomolecules to attract cells and, also, how to introduce growing factors and/or small molecules/peptides that promote cell survival and tissue regeneration. Part of the work developed in this Thesis is related with the interaction between polymeric scaffolds and cells or biomolecules.

Scaffolds are typically defined as *three-dimension porous solid biomaterials* designed to perform at least some of the following functions:

- promote cell-biomaterial interactions, cell adhesion, and extracellular matrix deposition;
- permit sufficient transport of gases, nutrients, and regulatory factors to allow cell survival, proliferation, and differentiation;

- biodegrade at controllable rate that approximates the rate of tissue regeneration under the culture conditions of interest;
- cause minimal degree of inflammation or toxicity in vivo [3].

1.1.2 Natural polymers and synthetic polymers for scaffolds

Natural polymers, like proteins (e.g. silk, collagen, gelatine, fibrinogen, elastin, keratin, actin, and myosin), polysaccharides (e.g. cellulose, amylose, dextran, chitin, and glycosaminoglycans), and polynucleotides (e.g. DNA and RNA) are important biodegradable biomaterials used often in clinical applications due to their ability to interact with cells.

However, synthetic polymers, which are often cheaper than biologic scaffolds, are widely used in the biomedical field since their properties can be tailored for specific applications. Furthermore, they can be uniformly produced at large-scale and have a long shelf time. Nowadays, synthetic polymers represent the largest group of biodegradable polymers and, indeed, many of these commercially available materials show properties (e.g. tensile strength, elastic modulus, and degradation rate) comparable to those of biological tissues. Examples of these polymers are: poly(lactic acid) (PLA), poly(glycolic acid) (PGA) and their copolymers poly(lactide-co-glycol acid) (PLGA). Principles for synthesizing a biologically active scaffold, including the critical importance of the degradation rate, were described in detail in 1980 [4].

The choice of the polymer to create scaffolds, which is dictated by its final application, requires thoughtful consideration of the polymer's physical and chemical properties: molecular weight, solubility, shape and structure, hydrophilicity/hydrophobicity, lubricity, surface energy, water absorption degradation, erosion mechanism, etc... Moreover polymeric scaffolds are drawing a great attention due to their unique properties, such as high surface-to-volume ratio, high porosity with very small pore size, biodegradation, and mechanical properties. All these characteristics, which are significant for tissue engineering and organ substitution, have been used to grow skin and cartilage [5], bone and cartilage [6], liver [7],

heart valves and arteries [8], bladder [9], pancreas [10], nerves [11], corneas [12], and various other soft tissues [13].

Poly(ethylene glycol) (PEG) is one of the most widely explored polymers, used either alone or as surface modifier, for its properties of low cell adhesion and protein adsorption [14]. It is proposed that ordered water surrounding each PEG chain provides a hydration shell that limits protein adsorption and thus recognition by immune cells such as macrophages. Interestingly, the limited protein and cell adhesion to PEG has also been pursued to limit tissue adhesion after surgery [15,16]. Thus, a key advantage of polymers such as PEG is their capacity to tune adhesive properties through attachment of specific proteins or peptides. Figure 1.1.1 shows the linear and typical cross-linked chemical structures of PEG.

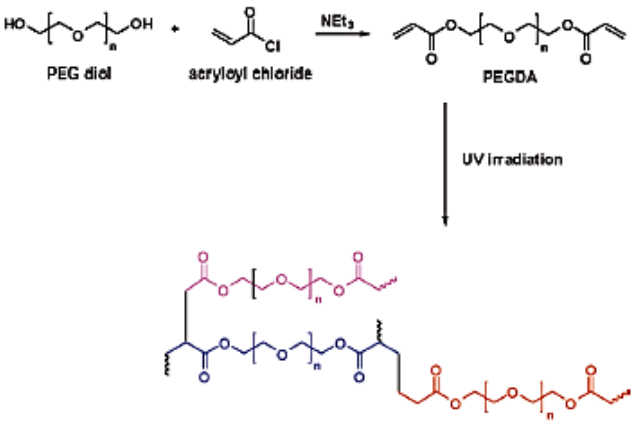

Figure 1.1.1 Scheme showing the preparation and chemical structure of cross-linked PEG.

1.1.3 Scaffolds design

The decreasing availability of organs for transplantation and the growing need for suitable replacements have motivated the apparition of tissue engineering. Since 1980, researchers have developed many novel techniques to shape polymers into complex architectures that exhibit the desired properties for specific tissue-engineering applications. These

fabrication techniques have resulted in reproducible scaffolds for the regeneration of specific tissues. Scaffolding is essential in this endeavour to act as a three-dimensional template for tissue ingrowths or, in other words, the polymeric scaffold is designed to mimic the extracellular matrix required for cell adhesion and proliferation [17].

Both the scaffold design and the polymer choice largely depend on the final application. Typical scaffold designs have included meshes, fibres, sponges and foams, and so forth. These designs are chosen because they promote uniform cell distribution, diffusion of nutrients and/or the growth of organized cell communities [18]. Depending on the intended use, these structures are also conducive to cell proliferation, migration, and/or differentiation. The three-dimensionality of the scaffold is a key factor in tissue engineering, where a 3D cell construct is meant to integrate into a 3D tissue. Figure 1.1.2 summarizes some of these design features required in a 3D scaffold.

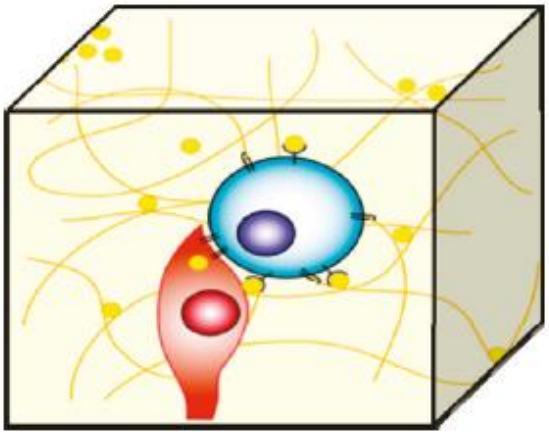

Figure 1.1.2 The tissue engineered scaffold is a three-dimensional structure that provides cells with the appropriate microenvironment of chemical, topographical, and mechanical cues, including cell-cell and cell-matrix interactions.

1.2 BIODEGRADABLE POLYMERS AS ENCAPSULATING MATERIALS

Although there are numerous studies related with the immobilization of small peptides (even with only five residues), the number of studies related to the encapsulation of individual amino acids (AAs) is very low. However, the release of AAs is extremely important for various industries, such as those related to the manufacture of feed for livestock and fish farms. For example, it is known that diets for farmed fish contain AAs in crystalline state, 80% of which is lost during the first minute in which the particles are suspended in water.

Within this context Lopez-Alvarado *et al.* [19] encapsulated AAs in alginates, proteins and lipids, which were used these compounds to prepare food for fish's larvae. In the first two cases, 90% and 60% (w/w), respectively, of AAs were released in the first two minutes of contact with water. The best results were obtained with lipid capsules, which managed to retain about 98% w/w of AA after two minutes. Liposomes have also been used to retain AAs with best results (i.e. 50% w/w release in 90 minutes).

Part of the work realized in this Thesis was devoted to the encapsulation of biomolecules in small polymeric nanostructures, which can be used as conveyor systems and as controlled release systems when they enter the organism.

Regarding with this, the encapsulation of amino acids is extremely relevant due to the important role of these compounds in living organisms, for example in the metabolism and the protection of the cardiovascular system. At this point, it should be remarked that the essential and semi-essential amino acids are incorporated through the diet.

This thesis will explain how to design a polymer-amino acid system that is biocompatible, biodegradable, extrudable and able to provide a more controlled release than currently used systems.

1.2.1 Electrospinning of bioactive polymers

This electrofluidodynamic process offers the option to form high-performance bioactive systems based on polymer yarns of nanofibers or coatings of nanobeads with high surface-to-volume ratios. Figure 1.2.1 is an illustration of the electrofluidodynamic process, with an explanation of the basic mechanism, describing the main parameters.

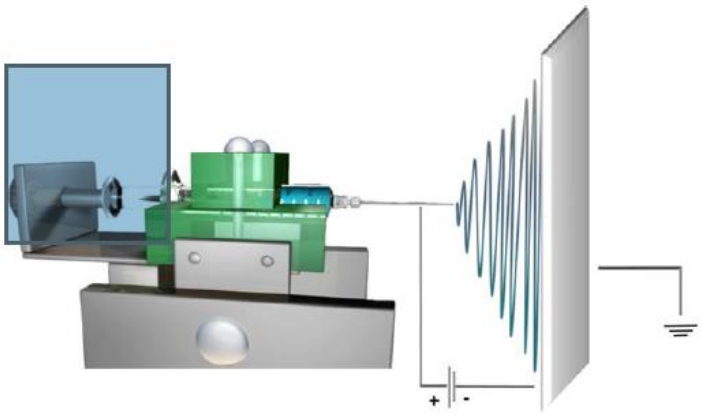

Figure 1.2.1 Typical setup of the electrofluidodynamic process that consists of a syringe, filled with the polymer solution, pumped at a relatively low constant rate (generally at 0.1-1 mL/h) and coupled to a stainless steel needle used as a conducting capillary, a high-voltage power supply (in the range of 5 to 30 kV), two electrodes, and a grounded metallic collector. When the applied electric field is high enough to overcome the polymer-solution drop surface tension, the solvent is evaporated and one or more electrically charged polymer jets are spun on the collector to form a non-woven mat.

This process generally results in the formation of a “white” colored mat using a wide range of polymers, including biopolymers [20]. For the nomenclature, when a mat of continuous fibers is obtained, the process is called “electrospinning”. Among other fiber-like structures, this mainly includes tubular and flat nanofibers (image in Figure 1.2.2a) as well as ultrathin fibers of above 1 mm with ribbon-like profiles and rough surfaces (image in Figure 1.2.2b).

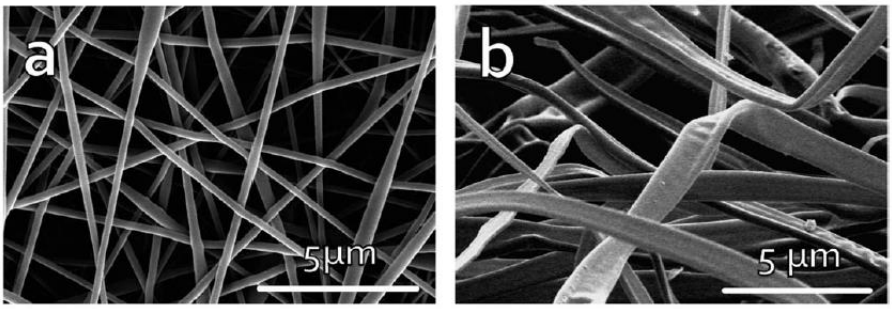

Figure 1.2.2 Selected morphologies of electrospun fibers of: (a) Thin and tubular nanofibers of poly(vinyl alcohol) (PVA) obtained from aqueous solutions; (b) Coarse and ribbon-like fibers of zein, a protein found in corn, obtained from acidified solutions. *Images reproduced from S. Torres-Gines, R. Pérez-Masiá, J. M. Lagaron; Polymer Engineering & Science, vol. 56, pp. 500–527, 2016.*

When round-like structures are attained, as observed either for coarse capsules (Figure 1.2.3a) or nanobeads (Figure 1.2.3b), the process is denoted as "electrospraying". However, the term electrospinning is also extensively used to cover both processes.

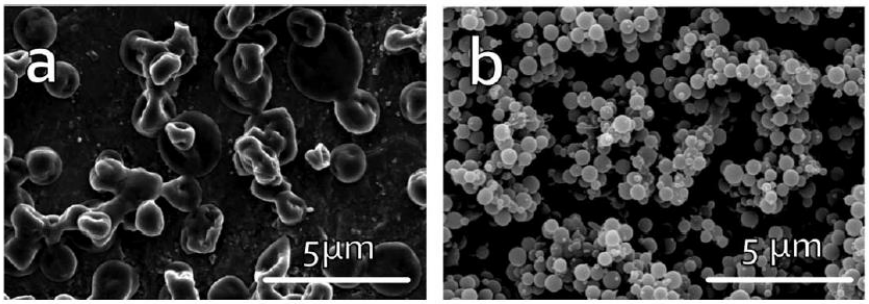

Figure 1.2.3 Selected morphologies of electrospun beads of: (a) Coarse and heterogeneous capsules of zein obtained from diluted ethanol solutions; (b) Round-like nanobeads of dextran obtained from aqueous solutions. *Images reproduced from S. Torres-Gines, R. Pérez-Masiá, J. M. Lagaron; Polymer Engineering & Science, vol. 56, pp. 500–527, 2016.*

The formation of structures via electrospinning and electrospraying basically requires specific viscoelastic properties, electric conductivities and surface energies from the materials to be processed. In this sense, only polymers with appropriate molecular weights would meet these requirements[21], even though it is also possible to process low molecular

weight polymers by incorporating gums and surfactant additives [22,23], and/or blending them with other easily electrospinnable polymers [24-26].

For the generation of structures through electrospinning and/or electrospraying, the polymer must firstly change to liquid state, either as a molten polymer or as a polymer solution. However, polymer solutions are generally preferred because the resultant structures are usually thinner than those obtained from molten (plasticized) polymers.

1.2.2 Elecrospinning of naturally and synthetic polymers

Some polymers have inherent specific bioactive properties, mainly biopolymers. In materials classification, biopolymers include both bio-based polymers and biodegradable polymers.

Bio-based polymers can be further differentiated by naturally occurring polymers and synthetic polymers produced by means of monomers obtained from biological sources.

Naturally occurring polymers are biomacromolecules (i.e. molecules of large molecular weights produced in nature by living organisms. They are of great interest for food technology and packaging industry because they can be considered non-toxic, edible, biocompatible and biodegradable, renewable, and sustainable. These properties also make these natural materials of enormous interest in other fields such as biomedicine, pharmaceutics, cosmetics, and other related areas. The most widespread biopolymers are polysaccharides and proteins.

A wide range of them can be electrospun with specific fiber arrangements, structural integrity, and fully bioactivity. Table 1.2.1 gathers some of the most widespread examples of electrospun biopolymers with their projected bioactive applications.

Polymer(s)	Functionality and Application	References
Alginates	Wound dressing promoting healing that can be removed with less pain than conventional biomedical products	[27, 28]
Cellulose and derivatives	Ion-exchange medium for protein separations, enzyme immobilization, and drug delivery capacity	[29,30]
Chitosan and derivatives	Human keratinocytes with fibroblast support and antimicrobial coatings for food and food packaging applications	[21, 31-33]
Collagen, gelatin, elastin and fibrinogen	Complete muscle, bone and skin reconstruction for tissue interfaces and wound dressings	[34-36]
Silk fibroin	Cell adhesion and proliferation devices and advanced materials with improved frictional surface for functional textiles and clothing design	[37-39]
Zein	Biomaterials with water resistance properties, offering enhanced thermal resistance, and certain biological valuable coatings for food and food packaging applications	[40-42]

Table 1.2.1 Summary of electrospun systems from naturally occurring polymers for the development of bioactive materials.

On the other hand, most biopolymers, and also a limited number of synthetic polymers, are biodegradable (i.e. they degrade under biological conditions into products that are eventually reused in nature under certain conditions). For tissue engineering applications, the main advantage of biodegradable polymers is that they can be resorbed. If the *in vivo* degradation takes place at a well-defined rate to non-toxic and readily excreted degradation products, these biomaterials can find applications as non-removable implants and as drug vehicles.

Biodegradable electrospun fibers of synthetic polymers find uses in biomedicine similar to those previously described for naturally occurring polymers due to the elimination of a second surgery to remove the biomedical device. However, the main difference with respect to the previously presented biomaterials is that synthetic polymers provide controlled repetitive chemical structures, facilitating specific cellular responses. For this reason, the morphology of electrospun synthetic polymers facilitates cell adhesion.

Typical examples of biodegradable synthetic polymers for electrospinning are aliphatic polyesters. Table 1.2.2 summarizes the bioactive applications of the commented electrospun fibers obtained from synthetic polymers.

Polymer(s)	Functionality and application	References
PLA Poly(latic acid)	Biomaterials for nerve and smooth muscle regeneration, neural stem and endothelial cell proliferation	[34,43-45]
PCL Polycaprolacone	Artificial organs with enhanced growth of fibroblasts, mesenchymal stem, mammary carcinoma and murine embryonic stem cell.	[46-50]
PGA Poly(glycol acid)	Replica of the physiologic human tissues with enhanced mechanical properties and superior thermal resistance.	[34, 51, 52]
PLGA Poly(lacic-co-glycol acid)	Skin regeneration and enhanced cell support.	[53-55]
PLCL Poly(lactide-co-caprolactone)	Support for smooth muscle and endothelial cells.	[56-58]
PHAs Polyhydroxyalkanoates	Support for human osteoblasts, mouse fibroblasts, tissue response and chondrocytes.	[59,60]
PVA Poly(vinyl alcohol)	Biofilters and biomembranes.	[61,62]

PUs Polyurethanes	Tissue engineering devices and smart textiles with high barrier to liquid and exogenous microorganisms.	[63-65]
PS Polystyrene	Devices for determination of chemicals in plasma, biocompatible materials, sorbents for solid-phase extraction of organic pollutants in water and for oil spill cleanup and abortions.	[66-68]
NYLON-6	Selective water filters, cell attachment promoting devices, reinforcing fillers for dental composites, biomembranes for dye removal and adsorbent materials for SME.	[69,70]
PET Polyethylene terephtalate	Biocompatible materials with endothelial cells and membranes in apples juice clarification.	[71-73]
PMMA Poly(methyl methacrylate)	Superhydrophobic units for active packaging.	[74]
PSU Polysulfones	Treatment sewage for environmental engineering.	[75]
S-PEEK Sulfonate poly(ether ether ketone)	Filtration devices for multi-sectorial applications.	[76]

Table 1.2.2 Summary of electrospun systems from synthetic polymers for the development of bioactive materials.

1.2.3 Functionalization of electrospun nanostructures

As a second route, electrospun surfaces can be further functionalized to display specific bioactive characteristics. This approach becomes crucial for synthetic polymers, as this represents a straight-forward strategy to functionalize any type of polymer. This option consists on the incorporation of one or more bioactive fillers and substances into the polymer solution for electrospinning. The bioactive component is then

incorporated to the polymer's matrix as droplets of liquid or solid particles. Later, depending on the substance nature and the desired application, this bioactive component would remain at the surface or inside the electrospun fibers.

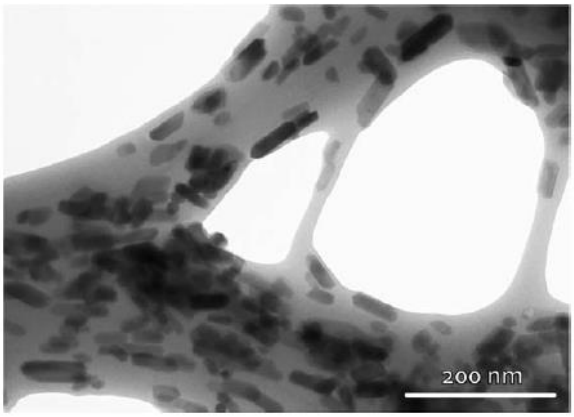

Figure 1.2.4 Electrospun PLA-collagen hybrid fibers containing hydroxyapatite nanoparticles (nHA). Single crystals can be observed inside the electrospun fibers, showing a rod-like morphology with lengths and widths between 40 and 130 nm and between 20 and 50 nm, respectively. *Images reproduced from S. Torres-Gines, R. Pérez-Masiá, J. M. Lagaron; Polymer Engineering & Science, vol. 56, pp. 500–527, 2016.*

In many cases loaded bioactive compounds can be released from the polymeric fibers, large matrices tending to release encapsulated compounds more slowly and over longer time periods. However, in addition of the fiber size, the miscibility and the distribution of the substances in the polymer matrices are also critical parameters affecting noticeably to the release profiles. For this reason, a continuous research interest has been paid to the use of biopolymers and synthetic matrices as drug delivery vehicles.

1.3 CONDUCTING POLYMERS AS BIOACTIVE PLATFORMS

Although at present time there are over 25 conducting polymers (CPs) [77] (excluding their corresponding derivatives) with potential technological applications, the first CP, polyacetylene (PAc), was obtained in 1974 by Heeger, MacDiarmid and Shirakawa [78]. Table 1.3.1 lists the more relevant conduting polymers. This kind of materials merges the benefits of metals and conventional polymers, exhibiting ability to conduct charge, great electrical and optical properties with flexibility in processing and ease of synthesis.

The early work on CPs was triggered by the observation that the conductivity of PAc increased 10^9 times upon oxidation with iodine vapor [79,80]. The underlying phenomenon, which was named ‘‘doping’’ by analogy with the doping of the semiconductors, is essential to gain the conductivity in organic polymers.

As PAc is unstable in air, the search for better CPs started after the discovery of these materials. Among different options, polyheterocycles have emerged as a family of CPs with both good stability and high conductance [81]. This family contains the three most important CPs: polypyrrole (PPy), polyaniline (PANI), and polythiophene (PTh) [82-84].

Conducting polymers	**Abbreviations**
Polypyrrole	PPy
Polyaniline	PANI
Poly(3,4-ethylenedioxythiophene)	PEDOT
Polythiophene	PTh
Polythiophene-vinylene	PTh-V
Poly (2,5-thienylenevinylene)	PTV
Poly (3-alkylthiophene)	PAT
Poly(p-phenylene)	PPP
Poly-p-phenylene-sulphide	PPS

Poly(p-phenylenevinylen)	PPV
Poly (p-phenilene-terephthalamide)	PPTA
Polyacetylene	PAc
Poly(isothianaphthene)	PITN
Poly (α-naphtylamine)	PNA
Polyazulene	PAZ
Polyfuran	Pfu
Polysoprene	PIP
Poybutadiene	PBD
Poly(3-octylthiophnene-3-methylthiopene)	POTMT
Pony (p-phenylene terephthalmide)	PPTA

Table 1.3.1 A list of CPs and their abbreviations.

Among PTh derivatives (Figure 1.3.1), poly(3,4-ethyl-enedioxythiophene) (PEDOT) deserves special attention. PEDOT is formed by the polymerization of a bicyclic monomer, 3,4-ethylenedioxythiophene [80]. Compared to PTh, PEDOT has a dioxyethylene group across the 3- and 4-positions of the heterocyclic ring (Figure 1.3.2) that greatly improves its properties with respect to PTh (i.e. by lowering its band gap, reduction and oxidation potential). The structural characteristics of PEDOT are also responsible of its high electrical conductivity and stability (chemical, environmental and thermal) [85,86].

Currently, PEDOT is used in biosensing and bioengineering applications [87], e.g. in neural electrodes [88], nerve grafts and heart muscle patches [85]. A particularly interesting example is the neural electrode that was interfaced with the surrounding brain tissue through the in situ polymerization of PEDOT. The synthesized PEDOT filaments extended far enough from the electrode to reach the neurons forming sensitive contacts with their plasma membrane [89].

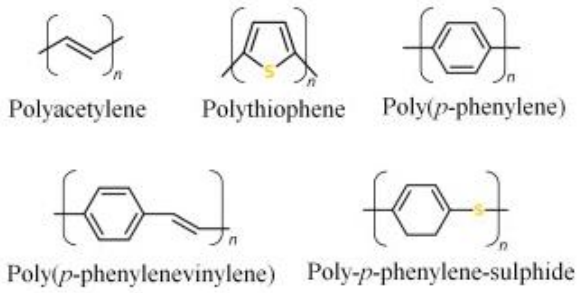

Figure 1.3.1 Chemical structure of PTh and some other representative CPs.

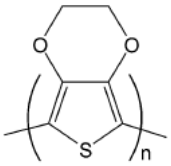

Figure 1.3.2 PEDOT's chemical structure.

The conducting ability results from the combination of a number of factors. As is schematically displayed in Figure 1.3.3, CPs present a conjugated backbone that it is formed by a series of alternating single and double bonds. Single and double bonds involve a chemically strong and localized σ-bond, while double bonds also contain a less strongly localized π-bond [90]. The *p*-orbitals in the series of π-bonds overlap each other, allowing the electrons to be more easily delocalized and move freely between the atoms [91].

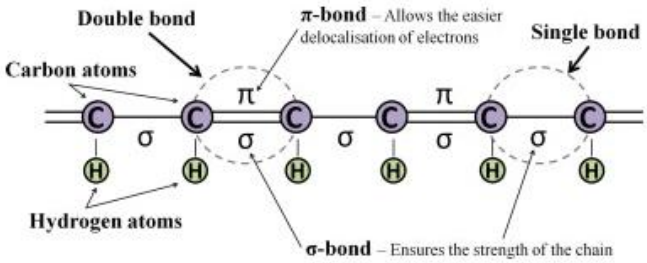

Figure 1.3.3 Scheme of the conjugated backbone in CPs: a chain containing alternating single and double bonds.

The final key to the conductivity of these polymers is the dopant. The polymer is synthesized in its oxidized form and only in the presence of the dopant molecules, which are negative charged species in most cases, the backbone is stabilized and the charge neutralized [92]. The dopant introduces also a charge carrier into the system by removing or adding electrons from/to the polymer chain and re-localizing them as polarons or bipolarons [93,94]. As an electrical potential is applied, the dopants start to move in or out of the polymer (depending on the polarity), disrupting the stable backbone and allowing charge to be passed through a polymer [90,93].

1.3.1 Synthesis and processing

The doping process occurs during synthesis and can be carried out chemically or electrochemically [80,90]. During chemical synthesis the monomer solution is mixed with an oxidizing agent (e.g. ferric chloride and ammonium persulfate) [95,96]. This process creates a powder or a thick film of polymer, allowing its bulk production. By this method all types of CPs can be created, including those that cannot be synthesized with the electrochemical method. On the other hand the conductivity of the polymers when synthesized using the chemical method is always lower than that of their electrochemically synthesized counterparts [97].

Electrochemical polymerization (Figure 1.3.4) occurs by applying an electrical current through electrodes placed inside a solution containing the monomer, the solvent and the doping agent [98-100]. This method allows the deposition of a polymer film with a well-controlled thickness and morphology. The electrical current causes the monomer to oxidize and deposit onto the working electrode, forming insoluble polymer chains. The properties of the synthesized films depend on the experimental conditions used during the polymerization process: deposition charge, time, temperature, solvent, doping agent and electrode system [101-104].

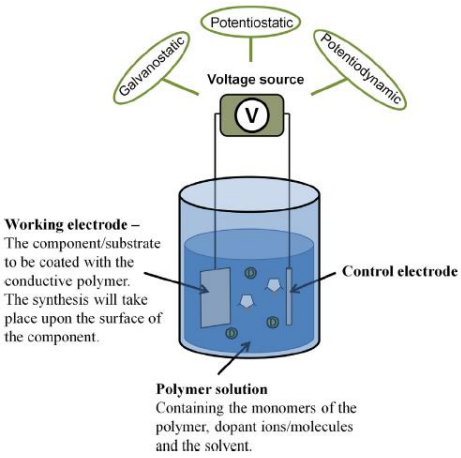

Figure 1.3.4 Scheme of the electrochemical synthesis set-up.

Electrochemical synthesis can be carried out using three techniques: the galvanostatic, the potentiostatic and potentiodynamic methods.

In potentiostatic polymerization, the potential of the electrodes is controlled, while the current varies [105]. This protects the integrity of the component to be coated, making this method ideal for the manufacture of biosensors. The electrical current can vary depending on a number of factors (e.g. the electrode material and the plating conditions), thus a coulometer is necessary to control the amount of polymer that is deposited [80,105]. All the copolymers synthetized in this Thesis have been prepared by potentiostatic polymerization.

In galvanostatic polymerization, the electrical current is controlled instead of the potential. This means that the rate at which the polymer is deposited is steady and can be controlled accurately.

During the potentiodynamic deposition, the polymerizing potential is swept between a low and high potential limit in cycles. This causes the polymer to be deposited in layers, with each layer becoming electrically active before the preparation of the next one. Potentiodynamic electrosynthesis has been observed to produce a different surface morphology to the potentiostatic and galvanostatic methods. For example, in a study comparing PEDOT synthesized using the three methods, it was found that the potentiostatic and galvanostatic routes produced a porous,

globular surface, while the potentiodynamic method generated a rod-like, fibrous morphology [106-108].

1.3.2 Properties and application of CPs

It is important to underline that many types of CPs (e.g. PPy, PANI and PTh) have shown to support the growth of a large variety of cell types. Additionally, the biocompatibility of CPs, if insufficient, can easily be improved through bonding biocompatible molecules, segments and side chains onto the polymer.

The biocompatibility is theorized to be dependent not only on the protocols used during their preparation but also on the post-synthesis treatment, as it was shown that rinsing, extraction and ageing all have a significant effect on biocompatibility. As mentioned above, the dopants and the synthesis conditions might also have affected the behavior of cells in a negative way, as they change the surface topography of the polymer, which can result in altered cell behavior. PEDOT has shown good biocompatibility, amongst others, with epithelial [87], neural [109] and neuroblastoma cells [110], L929 [111] and NIH_3T_3 fibroblasts [87].

CPs can also be used in many disciplines of science, including the medical, pharmaceutical and agricultural fields where is required the controlled delivery of chemical compounds [112]. The molecules loaded in such polymers through doping can be controllably expelled through the application of a reducing (negative) electrical potential [113]. The fact that these kinds of polymers are porous and have delocalized charge carriers helps in the diffusion of the loaded molecules [114,115].

1.4 References

1. S.A. Guelche, J.O. Hollinger; "An Introduction to Biomaterials"; *CRC Press*, 2006.
2. M.S. Shoichet; *Macrom.*, vol. 43, pp. 581–591, 2010.
3. R. Langer, D.A. Tirrell; *Nature*, vol. 428, pp. 487–492, 2004.
4. I.V. Yannas, J. F. Burke; *J. Biom. Mat. Res.*, vol. 14, pp. 65–81, 1980.
5. W.H. Eaglstein, V. Falanga; *Adv. Wound Care*, vol. 11, supplement 4, pp. 1–8, 1998.
6. B.D. Boyan, C. H. Lohmann, J. Romero, Z. Schwartz; *Clinics in Plastic Surgery*, vol. 26, pp. 629–645, 1999.
7. J. Mayer, E. Karamuk, T. Akaike, E. Wintermantel; *J. Controlled Release*, vol. 64, pp. 81–90, 2000.
8. J.E. Mayer, T. Shin'oka, D. Shum-Tim; *Current Opinion in Cardiology*, vol. 12, pp. 528–532, 1997.
9. F. Oberpenning, J. Meng, J.J. Yoo, A. Atala; *Nature Biotec.*, vol. 17, pp. 149–155, 1999.
10. E. Tziampazis, A. Sambanis; *Biotechnology Progress*, vol. 11, pp. 115–126, 1995.
11. J. Mohammad, J. Shenaq, E. Rabinovsky, S. Shenaq; *Plastic and Reconstr. Surgery*, vol. 105, pp. 660–666, 2000.
12. L. Germain, F.A. Auger, E. Grandbois, R. Guignard, M. Giasson, H. Boisjoly, S.L. Guérin; *Pathobio.*, vol. 67, pp. 140–147, 1999.
13. C.A. Diedwardo, P. Petrosko, T.O. Acarturk, P.A. Dimilia, W.A. Laframboise, P.C. Johnson; *Clinics in Plastic Surgery*, vol. 26, pp. 647–656, 1999.
14. E.W. Merrill, E.W. Salzman, S. Wan, N. Mahmud, L. Kushner, J. N. Lindon, J. Curme; *Trans. Am. Soc. Artif. Intern. Organs*, vol. 28, pp. 482–7, 1982.
15. C.P. Pathak, N.P. Desai, J.A. Hubbell, J.L. Hill, A.S. Sawhney; *US Patent 5 410 016-A*, 1995.
16. A.S. Sawhney, P.K. Jarrett, A.J. Coury, R.S. Rudowsky, M.D. Powell, L.Z. Avila, D.J. Enscore, S.D. Goodrich, W.C. Nason, F. Yao, D. Weaver, S.P. Barman, M.D. Lyman; *US Patent 6 177 095*, 2001.
17. L.E. Freed, G. Vunjak-Novakovic, R.J. Biron, D.B. Eagles, D.C. Lesnoy, S.K. Barlow, R. Langer; *Biotech.*, vol. 12, pp. 689–693, 1994.

18. L.E. Freed, G. Vunjak-Novakovic; *Adv. Drug Deliv. Rev.*, vol. 33, pp. 15–30, 1998.
19. J. López-Alvarado, C.J. Langdon, S.I. Teshima, A. Kanazawa; *Aquacult.*, vol. 122, pp. 335–346, 1994.
20. S. Torres-Giner, A. Fernandez, E. Gimenez, M.J. Ocio, J.M. Lagaron; "Novel Electrospun Functionalized Nanofibers based on Biopolymers", Proceedings of COST868 First Annual Workshop on Biotechnical Functionalization of Renewable Polymeric Materials, Graz, Austria, 2007.
21. S. Torres-Giner, M.J. Ocio, J.M. Lagaron; *Eng. Life Sci.*, vol. 8, pp. 303-314, 2008.
22. R. Pérez-Masiá, J.M. Lagaron, A. López-Rubio; *Food Biopr. Tech.*, vol. 7, pp. 3236-3245, 2014.
23. R. Pérez-Masiá, J.M. Lagaron, A. Lopez-Rubio; *Carbohydr. Polym.*, vol. 101, pp. 249-255, 2014.
24. S. Torres-Giner, M.J. Ocio, J.M. Lagaron; *Carbohydr. Polym.*, vol. 77, pp. 261-266, 2009.
25. S. Torres-Giner, A. Martínez-Abad, J.V. Gimeno-Alcañiz, M.J. Ocio, J.M. Lagaron; *Adv. Eng. Mater.*, vol. 14, pp. B112-122, 2012.
26. M. Bognitzki, T. Fresem, M. Steinhart, A. Greiner, J.H. Wendorff, A. Schaper, M. Hellwig; *Polym. Eng. Sci.*, vol. 41, pp. 982-989, 2001.
27. H. Nie, A. He, J. Zheng, S. Xu, J. Li, C.C. Han; *Biomacrom.*, vol. 9, pp. 1362-1365, 2008.
28. T. Suksamran, P. Opanasopit, T. Rojanarata, T. Ngawhirunpat, U. Ruktanonchai, P. Supaphol; *J. Microencap.*, vol. 26, pp. 563-570, 2009.
29. L. Zhang, T.J. Menkhaus, H. Fong; *J. Membr. Sci.*, vol. 319, pp. 176-184, 2008.
30. D.G. Yu, J.H. Yu, L. Chen, G.R. Williams, X. Wang; *Carbohydr. Polym.*, vol. 90, pp. 1016-1023, 2012.
31. H.K. Noh, S.W. Lee, J.M. Kim, J.E. Oh, K.H. Kim, C.P. Chung, S.C. Choi, W.H. Park, B.M. Min; *Biomater.*, vol. 27, pp. 3934-3944, 2006.
32. J.M. Dang, K.W. Leong; *Adv. Mater.*, vol. 19, pp. 2775-2779, 2007.
33. A. Neamnark, N. Sanchavanakit, P. Pavasant, R. Rujiravanit, P. Supaphol; *Eur. Polym. J.*, vol. 44, pp. 2060-2086, 2008.

34. T.A. Telemeco, C. Ayres, G.L. Bowling, G.E. Wnek, E.D. Bolland, N. Cohen, C.M. Baumgarten, J. Mathews, D.G. Simpson; *Acta Biomater.*, vol. 1, pp. 377-385, 2005.
35. M. Li, M.J. Mondrinos, M.R. Gandhi, F.K. Koas Weiss, P.I. Lelkes; *Biomater.*, vol. 26, pp. 5999-6008, 2005.
36. D. Gugutkov, J. Gustavsson, M.P. Ginebra, G. Altankov; *Biomater. Sci.*, vol. 1, pp. 1065-1073,2013.
37. A. Alessandrino, B. Marelli, C. Arosio, S. Fare, M.C. Tanzi, G. Freddi; *Eng. Life Sci.*, vol. 8, pp. 219-225, 2008.
38. J. Zhou, C. Cao, X. Max; *Int. J. Biol. Macromol.*, vol. 45, pp. 504-510, 2009.
39. M. Akada, M. Kotaki, M. Sato, S. Sukigara; *Text. Res. J.*, vol. 53, pp. 245-248, 2007.
40. C. Yao, X. Li, T. Song; *J. Appl. Polym. Sci.*, vol. 103, pp. 380-385, 2007.
41. M.A. Busolo, S. Torres-Giner, J. M. Lagaron; "Enhancing the Gas Barrier Properties of Polylactic Acid by Means of Electrospun Ultrathin Zein Fibers," Proceedings of Annual Technical Conference - ANTEC, Chicago, USA, vol. 5, pp. 2763-2768, 2009.
42. S. Torres-Gines, A. Martinez-Abad, J.M. Lagaron; *J. App. Polym. Sci.*, vol. 131, pp. 9270-9276, 2014.
43. F. Yang, C.Y. Xu, M. Kotaki, S.H. Wang, S. Ramakrishna; *J. Biomater. Sci., Polym. Ed.*, vol. 15, pp. 1483-1497, 2004.
44. F. Yang, R. Murugan, S. Wang, S. Ramakrishna; *Biomater.*, vol. 26, pp. 2603-2610, 2005.
45. Z. Alvareza, O. Castaño, A.A. Castells, M.A. Mateos-Timoneda, J.A. Planell, E. Engel, S. Alcantara; *Biomater.*, vol. 35, pp. 4769-4781, 2014.
46. N. Bolgen, Y.Z. Menceloglu, K. Acatay, I. Vargel, E. Piskin; *J. Biomater. Sci., Polym. Ed.*, vol. 16, pp. 1537-1555, 2005.
47. M.I. Van Lieshout, C.M. Vaz, M.C.M. Rutten, G.W.M. Peters, F.P.T. Baaijens; J. Biomater. Sci., Polym. Ed., vol. 17, pp. 77-89, 2006.
48. L.C. Ionescu, G.C. Lee, K.L. Huang, R.L. Mauck; *Acta Biomater.*, vol. 8, pp. 3687-3694, 2012.

49. M. Rampichova, J. Chvojka, M. Buzgo, E. Prosecka, P. Mikes, L. Vyslouzilova, D. Tvrdık, P. Kochova, T. Gregor, D. Lukas, E. Amler; *Cell Prolif.*, vol. 46, pp. 23-37, 2013.
50. Y.A. Elnakady, M.F. Al Rez, H. Fouad, S. Abuelreich, A.S. A.M. Albarrag, A. Mahmood, O.Y. Alothman, T. Elsarnagawy, S.G. Ansari; *Sci. Adv. Mat.*, vol. 7, pp. 407, 2015.
51. E.D. Boland, G.E. Wnek, D.G. Simpson, K.J. Pawlowski, G.L. Bowlin; *J. Macromol. Sci. Part A*, Pure App. Chem., vol. 38, pp. 1231-1243, 2001.
52. H. Hosseinkhani, M. Hosseinkhani, S. Hattori, R. Matsuoka, N. Kawaguchi; *J. Biomed. Mater. Res., Par A.*, vol. 94, pp. 1-8, 2010.
53. X. Xin, M. Hussain, J.J. Mao; *Biomater.*, vol. 28, pp. 316-325, 2007.
54. S.G. Kumbar, S.P. Nukavarapu, R. James, L.S. Nair, C.T. Laurencin; *Biomater.*, vol. 29, pp. 4100-4107, 2008.
55. R. James, S.G. Kumbar, C.T. Laurencin, G. Balian, A.B. Chhabra; *Biomed. Mater.*, vol. 6, s. 025011, 2011.
56. X. Mo, Z. Chen, H.J. Weber; *Front. Mater. Sci. China*, vol. 1, pp. 20-23, 2007.
57. A.R. Chandrasekaran, J. Venugopal, S. Sundarrajan, S. Ramakrishna; *Biomed. Mater.*, vol. 6, s. 015001, 2011.
58. K.K. Sankaran, K.S. Vasanthan, U.M. Krishnan, S. Sethuraman; *J. Tissue Eng. Regen. Med.*, vol. 8, pp. 640-651, 2014.
59. O.H. Kwon, I.S. Lee, Y.G. Ko, W. Meng, K.H. Jung, I.K. Kang, Y. Ito; *Biomed. Mater.*, vol. 2, pp. 52-58, 2007.
60. T. Ho-Wang, M. Wang; *Polym. Eng. Sci.*, vol. 51, pp. 1325-1338, 2011.
61. X.H. Qin, S.Y. Wang; *J. App. Polym. Sci.*, vol. 109, pp. 951-956, 2008.
62. X.H. Qin; *Chem. Fibres Int.*, vol. 58, pp. 127-129, 2008.
63. S. Lee, S.K. Obendorf; *Text. Res. J.*, vol. 77, pp. 696-702, 2007.
64. E. Borg, A. Frenot, P. Walkenstrom, K. Gisselfalt, C. Gretzer, P. Gatenholm; *J. App. Polym. Sci.*, vol. 108, pp. 491-512, 2008.
65. P.C. Caracciolo, V. Thomas, Y.K. Vohra, F. Buffa, G.A. Abraham; *J. Mater. Sci.: Mater. Med.*, vol. 20, pp. 2129-2137, 2009.
66. B. Maddaha, S.S. Javadia, A. Mirzaeia, M. Rahimi- Nasrabadia; *J. Liquid Chrom. Rel. Tech.*, vol. 38, pp. 208, 2015.

67. J. Lin, Y. Shang, B. Ding, J. Yang, J. Yu, S.S. Al-Deyab; *Marine Pol. Bul.*, vol. 64, pp. 347-352, 2012.
68. J. Wu, N. Wang, L. Wang, H. Dong, Y. Zhao, L. Jiang; *Appl. Mater. Sci.*, vol. 6, pp. 3207-3212, 2006.
69. A. Huber, A. Pickett, K.M. Shakesheff; *Eur. Cells Mater.*, vol. 14, pp. 56-63, 2007.
70. D. Aussawasathien, C. Teerawattananon, A. Vongachariya; *J. Membr. Sci.*, vol. 315, pp. 11-19, 2008.
71. Z. Ma, M. Kotaki, T. Yong, W. He, S. Ramakrishna; *Biomater.*, vol. 26, pp. 2527-2536, 2005.
72. H. Savoji, A. Hadjizadeh, M. Maire, A. Ajji, M.R. Wertheimer, S. Lerouge; *Macromol. Biosci.*, vol. 14, pp. 1084-1095, 2014.
73. B. Veleirinho, J.A. Lopes-da-Silva; *Process. Biochem.*, vol. 44, pp. 353-356, 2009.
74. M. Ma, M. Gupta, Z. Li, L. Zhai, K.K. Gleason, R.E. Cohen, M.F. Rubner, G.C. Rutledge; *Adv. Mater.*, vol. 19, pp. 255-259, 2007.
75. Z. Xu, Q. Gu, H. Hu, F. Li; *Environ. Technol.*, vol. 29, pp. 13-21, 2008.
76. K.P. Rajesh, T.S. Natarajan; *J. Nanosci. Nanotechnol.*, vol. 9, pp. 540, 2009.
77. D.D. Ateh, H.A Navsaria, P. Vadgama; *J. Roy. Soc. Int.*, vol. 3, pp. 741–752, 2006.
78. The Nobel Prize in Chemistry 2000 was awarded jointly to Alan J. Heeger, Alan G. MacDiarmid and Hideki Shirakawa for the discovery and development of conductive polymers.
79. H. Shirakawa, E.J. Louis, A.G. MacDiarmid, C.K. Chiang, A.J. Heeger; *J. Chem. Soc., Chem. Commun.*, vol. 16, pp 578–580, 1977.
80. D.D. Zhou, X.T. Cui, A. Hines, R.J. Greenberg; *Implant. neural prostheses*, vol. 2, pp. 217–52, 2010.
81. N.K. Guimard, N. Gomez, C.E. Schmidt; *Prog. Polym. Sci.*, vol. 37, pp. 876-921, 2007.
82. M.T. Cortés, J.C. Moreno; *e-Polymers*, vol. 4, pp. 1-42, 2003.
83. D.H. Kim, M. Abidian, D.C. Martin; *J. Biomed. Mater. Res.*, vol. 71A, pp. 577-585, 2004.
84. N.K.E. Guimard, J.L. Sessler, C.E. Schmidt; *Macromol.*, vol. 42, pp. 502-511, 2009.

85. A. Peramo, M.G. Urbanchek, S.A. Spanninga, L.K. Povlich, P. Cederna, D.C. Martin; *Tissue Eng., Part A*, vol. 14, pp. 423-432, 2008.
86. C.A. Thomas, K. Zong, P. Schottland, J.R. Reynolds; *Adv. Material.*, vol. 12, pp. 225-225, 2000.
87. L. Ghasemi-Mobarakeh, M.P. Prabhakaran, M. Morshed, M.H. Nasr-Esfahani, H. Baharvand, S. Kiani, S.S. Al-Deyab, S. Ramakrishna; *J. Tissue Eng., Regen. Med.*, vol. 5, pp. 17-35, 2011.
88. M. Asplund, E. Thaning, J. Lundberg, A.C. Sandberg-Nordqvist, B. Kostyszyn, O. Inganäs, H. von Holst; *Biomed. Mater.*, vol. 4, pp. 1-12, 2009.
89. S.M. Richardson-Burns, J.L. Hendricks, D.C. Martin; *J. Neural. Eng.*, vol. 4, pp. L6-13, 2007.
90. R. Ravichandran, S. Sundarrajan, J.R. Venugopal, S. Mukherjee, S. Ramakrishna; *J. R. Soc. Interface*, vol. 7, pp. S559-579, 2010.
91. J.Y. Wong, R. Langer, D.E. Ingber; *Proc. Natl. Acad. Sci. USA*, vol. 91, pp. 3201-3204, 1994.
92. G. Wallace, G. Spinks; *Soft Matter*, vol. 3, pp. 665-671, 2007.
93. X. Liu, K.J. Gilmore, S.E. Moulton, G.G. Wallace; *J. Neural Eng.*, vol. 6, pp. 1-10, 2009.
94. J.L. Bredas, G.B. Streer; *Acc. Chem. Res.*, vol. 18, pp. 309-315, 1985.
95. Y. Tan, K. Ghandi; *Synth. Met.*, vol. 175, pp. 183-191, 2013.
96. S.P. Armes; *Synth. Met.*, vol. 20, pp. 365-371, 1987.
97. P.A. Calvo, J. Rodriguez, H. Grande, D. Mecerreyes, J.A. Pomposo; *Synth. Met.*, vol. 126, pp. 111-116, 2002.
98. N.C.T. Martins, T. Moura e Silva, M.F. Montemora; J.C.S. Fernandes, M.G.S., *Electrochim. Acta*, vol. 53, pp. 475-4763, 2008.
99. P. Herrasti, L. Díaz, P. Ocón, A. Ibáñez, E. Fatas; *Electrochim. Acta*, vol. 49, pp. 3693-3699, 2004.
100. S. Choi, S. Park; *J. Electrochem. Soc.*, vol. 149, pp. E26-34, 2002.
101. C.M. Li, C.Q. Sun, W. Chen, L. Pan; *Surf. Coat Technol.*, vol. 198, pp. 474-477, 2005.
102. D.A. Kaplin, S. Qutubuddin; *Polymer*, vol. 36, pp. 1275-1286, 1995.
103. S.J. Sutton, A.S. Vaughan; *Polymer*, vol. 36, pp. 1849-1857, 1995.

104. A. Kaynak; Material Res. Bull., vol. 32, pp. 271-285, 1997.
105. G.G. Wallace, M. Smyth, H. Zhao; *Trends Analyt. Chem.*, vol. 18, pp. 245-251, 1999.
106. S. Patra, K. Barai, N. Munichandraiah; *Synth. Met.*, vol. 158, pp. 430-435, 2008.
107. S.K. Mondal, K.R. Prasad, N. Munichandraiah; *Synth. Met.*, vol. 148, pp. 275-286, 2005.
108. T.C. Girija, M.V. Sangaranarayanan; *Synth. Met.*, vol. 159, pp. 244-250, 2006.
109. D.H. Kim, S.M. Richardson-Burns, J.L. Hendricks, C. Sequera, D.C. Martin; *Adv. Funct. Mater.*, vol. 17, pp. 79-86, 2007.
110. M.H. Bolin, K. Svennersten, X. Wang, I.S. Chronakis, A. Richter-Dahlfors, E.W.H. Jager, M. Berggren; *Sens. Actuator B*, vol. 142, pp. 451-456, 2009.
111. V. Karagkiozaki, P.G. Karagiannidis, M. Gioti, P. Kavatzikidou, D. Georgiou, E. Georgaraki, S. Logothetidis; *Biochim. Biophys. Acta*, vol. 1830, pp. 4294-4304, 2013.
112. A. Guiseppi-Elie; *Biomater.*, vol. 31, pp. 2701-2716, 2010.
113. C.J Small, C.O. Too, G.G. Wallace; *Polym. Gels Netw.*, vol. 5, pp. 251-265, 1997.
114. R. Wadhwa, C.F. Lagenaur, X.T. Cui; *J. Control Release*, vol. 110, pp. 531-541, 2006.
115. Y. Li, K.G. Neoh, E.T. Kang; *J. Biomed. Mater. Res.*, vol. 73A, pp. 171-81, 2005.

CHAPTER 2

Objectives

2.1 Outline of the Thesis: specific objectives

The results of this Thesis have been organized in four different Chapters, depending on not only the chemical structure of the examined material but also on the explored biomedical application.

Chapter 3, entitled "*Polythiophene-g-poly(ethylene glycol) graph copolymers as hybrid bioplatforms for tissue engineering*" is focused on the application as supportive cellular matrices of hybrid materials made of well-defined PEG chains grafted to the conjugated PTh backbone. This research arises as a consequence of a first study [1] in which thiophene-based oligomers consisting of a pentathiophene sequence in which the central ring bears a PEG side chain were prepared by chemical synthesis and subsequently polymerized by potentiostatic methods. In that work, the effects of the polymerization potential, the length of the PEG branches and the dopant agent on the structure and properties of such graft copolymers were carefully examined [1]. The specific objectives of Chapter 3, which is focused on the both the optimization and applications, of PTh-*g*-PEG copolymers are:

1) To evaluate the electronic, electrochromic and superficial properties, internal organization at the molecular level of PTh-*g*-PEG copolymers considering PEG chains and unsubstituted thiophene (Th) blocks of different length.
2) To investigate the biocompatibility of PTh-*g*-PEG copolymers as a function of the length of the PEG fragment and PEG/Th ratio.
3) To study the behavior as bioactive platform for cellular adhesion and proliferation of PTh-*g*-PEG copolymers.
4) To compare the properties of PTh-*g*-PEG with those obtained for poly(α-terthiophene) (PTh_3), a polymer made exclusively of Th units.

The tittle of Chapter 4 is "*Poly(3,4-ethylenedioxythiophene)-peptide conjugates based on chemical similarity*". In previous studies, Dr. G. Fabregat [2,3] proved the importance of the chemical similarity concept in

the preparation of electroactive CP-peptide conjugates without undesirable linkers, which usually are in detriment of electrochemical and electrical properties. More specifically, Fabregat *et al.*[2,3] proposed the chemical modification of the peptide by replacing one of its coded amino acids by an exotic amino acid, which was specially designed to achieve a direct coupling with the CP. The success of this strategy was demonstrated designing and preparing by organic synthesis new glycine (Gly) and Alanine (Ala) derivatives, which were subsequently conjugated to PEDOT chains using an electrochemical polymerization approach. Although such PEDOT-amino acid conjugates displayed many advantages by preserving the properties of the CP and the individual patent amino acids, the concept of chemical similarity was not completely extended to PEDOT-peptide conjugates.

In this Thesis, we have addressed the study of PEDOT-peptide conjugates in two different parts, which are relatively independent. The first one is devoted to present a new polymerization strategy for the preparation PEDOT-peptide conjugates. For this purpose, we have followed the approach of Fabregat *et al.* [2,3] comparing different synthetic strategies using simple Gly and Ala derivatives rather than a complete peptide. After this, in the second part of the Chapter, the strategy developed in the first part has been applied to prepare a new PEDOT-peptide conjugate inspired in the Arg-Gly-Asp (RGD) adhesive sequence, in which the central residue has been replaced by an exotic amino acid designed by chemical similarity. The specific objectives of Chapter 4 are:

1) To incorporate a variation in the synthetic approach developed by Fabregat *et al.* [2,3] that is expected to improve the properties of the conjugates.
2) To examine the influence of the synthetic strategy in the electrochemical, electronic, morphological and topographical properties, the wettability, and the behavior as the bioactive platform of a given conjugate designed by chemical similarity.

3) To analyze the bioelectrocompatibility (*i.e.* influence of living cells on the electrochemical properties) of the PEDOT-based conjugates designed by chemical similarity, that was never studied before.
4) Design by chemical similarity, synthesize and characterize a PEDOT-peptide conjugate inspired in the RGD adhesive sequence.
5) Investigate the performance of the new PEDOT-peptide conjugate as soft bioelectroactive support for cell attachment, comparing its behavior with that of PEDOT alone.

In Chapter 5, which is entitled "*Biodegradable Nanofibrous Scaffolds as Smart Delivery Vehicles for Amino Acids*", we approach a very difficult task: the encapsulation individual AAs in a carrier matrix for their controlled release. Difficulties are mainly related with the small size of AAs, which favors their immediate and uncontrolled release from the matrix through simple diffusive processes, and their chemical diversity (*i.e.* from a chemical point of view, AAs are typically classified in hydrophobic, polar and charged AAs). From a practical point of view, the correct encapsulation and controlled release of AAs is very relevant in the livestock and fisheries sectors: a safe and nutritionally improved animal and fish feed supply ensures healthy animals and people. Thus, the general objective of Chapter 5 is to study the loading of AAs into biodegradable non-toxic polymeric nanofibers (NFs) using the electrospinning technique. Appropriated incorporation of fibre-based formulations to cattle feed is expected to be an attractive way to supply AAs, thus improving their bioavailability through controlled delivery. The specific objectives of Chapter 5 are:

1) Load non-polar, polar and charged AAs into polymeric biodegradable NFs using electrospinning.
2) Examine the influence of the loaded AAs on the properties of the polymeric carrier, paying especial attention to the effects of the chemical nature of the AA in the variation of the properties.

3) Investigate the release and degradation assays in different environments to ascertain the advantages and limitations of this AA-loading approach.

Chapter 6, entitled "*Loading and release of hydrophobic gramicidin in micro- and nanostructured polyester*", has been devoted to the encapsulation and release of highly insoluble peptides in structured polymer matrices. Thus, the insolubility of biomolecules is known to represent a major limitation for their processing and, therefore, encapsulation. Among insoluble biomolecules with therapeutic applications, gramicidin (GA) deserves special mention because of its versatility (i.e. it is active as bactericide, antibiotic, and potential therapeutic agent for different carcinomas). Accordingly, the objectives of this Chapter have been focused on the loading of linear gramicidin (GA-L) and two derivatives of gramicidin soviet (GA-S), as representative and potentially interesting insoluble peptides, into particles and fibers of poly(tetramethylene succinate) (PE44), a biodegradable and biocompatible aliphatic polyester.

Chapter 6 is divided in two different parts. In the first part, we successfully examine the loading of GA-L into microspheres of PE44 using the electrospraying technique. Unfortunately, the encapsulation of GA-S derivatives into PE44 microparticles was not achieved, which has been attributed to the extremely high molecular rigidity of these biomolecules. Therefore, in the second part of the Chapter we investigate the encapsulation of GA-L and the two GA-S derivatives into PE44 fibers using the electrospinning technique. The specific objectives of Chapter 6 can be summarized as follows:

1) Optimize the processing conditions to obtain GA-loaded PE44 microspheres with well-defined morphology.
2) Characterize the main properties of the GA-loaded PE44 structures, comparing them those of unloaded PE44.
3) Check the influence of the PE44 processing conditions (i.e. by electrospraying and electrospinning) in the bioactivity of the peptide.

4) Examine the GA release from the loaded structures in different environments.
5) Compare the antibiotic potency and the biocompatibility of the different GA-loaded PE44 systems.

2.2 References

1. A.D. Bendrea, G. Fabregat, L. Cianga, F. Estrany, L.J. del Valle, I. Cianga, C. Alemán; *Polym. Chem.*, vol. *4*, pp. 2709-2723, 2013.
2. G. Fabregat, G. Ballano, E. Armelin, L.J. del Valle, C. Cativiela, C. Alemán; *Polym. Chem.*, vol. 4, pp. 1412-14124, 2013.
3. G. Fabregat, G. Ballano, J. Casanovas, A. Laurent, E. Armelin, L.J. del Valle, C. Cativiela, D. Jacquemin, C. Alemán; *RSC Adv.*, vol. 3, pp. 21069-21083, 2013.

CHAPTER 3

Polythiophene-*g*-poly(ethylene glycol) graph copolymers as hybrid bioplatforms for tissue engineering

3.1 POLYTHIOPHENE-*g*-POLY(ETHYLENE GLYCOL) GRAPH COPOLYMERS FOR ELECTROACTIVE SCAFFOLDS*

3.1.1 Introduction

The discovery of a new class of organic polymers with conducting properties in the late 1970s opened up a new era in the field of polymer science [1]. In the last few decades CPs have attracted considerable interest because of their interesting electrical, electrochemical, optical and magnetic properties [2]. Among them, polyheterocycles such as PPy, PTh, PANI and some of their derivatives have received particular attention because they exhibit good stabilities, good conductivities and ease of synthesis [2–4]. PTh derivatives have been settled among the most promising CPs for technological applications, poly(3-hexylthiophene) and, especially, PEDOT being the most popular. PEDOT (Figure 3.1.1), which exhibits low band gap (1.6–1.7 eV), high conductivity (up to 550 S cm^{-1}) and good environmental stability [5–7], has been employed to fabricate electrochromic devices [8], fuel cells [9], field emitters [10] and dye-sensitized solar cells (DSSCs) [11].

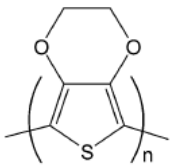

Figure 3.1.1 Chemical structure of PEDOT.

Most CPs present a number of important advantages for biomedical applications, including biocompatibility, ability to entrap and controllably release biological molecules (i.e. reversible doping), ability to transfer charge from a biochemical reaction, and the potential to easily alter the electrical, chemical, physical, and other properties of the CPs to better suit

*Results discussed in section 3.1 were published in J. Mater. Chem. B, 2013, 1, 4135-4145.

the nature of the specific application. These unique characteristics are useful in many biomedical applications, such as biosensors, tissue-engineering scaffolds, neural probes, drug-delivery devices, and bio-actuators. Biomedical applications of CPs have been recently reviewed [12,13]. In spite of this, there is always a desire to further optimize a material for a specific application.

The two common properties desired for all biomedical applications are biocompatibility and redox stability (i.e. electroactivity and electrochemical stability), but beyond these needs, CP modifications tend to be specific for the application. For example, it is important to improve the ability of CPs to act as a bioactive platform for cellular proliferation. This can be achieved physically (i.e. physical adsorption of molecules that enhance proliferation of a variety of cell types) or chemically (i.e. functionalizing the CPs with the desired molecules through chemical bonds). Functionalization of CPs with different molecules has allowed biomedical engineers to modify CPs with biological sensing elements, and to turn on and off different signaling pathways to create CPs that enhance cellular adhesion and proliferation and improve their biocompatibility [14–17].

Among polymer-polymer hybrid materials, graph copolymers made of components with very different properties are receiving increasing attention [18-23]. Graft copolymers amplify the characteristic properties of their individual components, exhibiting unusual features because of their confined structure, compact organization and notable chain end effects. Within this context, copolymers formed by an all conjugated PTh backbone and other polymeric grafted chains have been prepared to improve the very limited processability and solubility of unsubstituted PTh (e.g. poly(methyl acrylate) [24,25] and polystyrene [26,27]), to fabricate donor-π-acceptor molecular species (e.g. poly(styrene-graft-C_{60}) [28]) or to prepare hydrophilic conducting surfaces (e.g. poly(ethylene glycol) monomethacrylate [29]).

In a very recent study, we reported the synthesis and characterization of hybrid materials made of well-defined PEG chains grafted to the conducting PTh backbone, which were denoted PTh-*g*-PEG_n (where *n* refers to the molecular weight of PEG chains) [30]. PEG is a biocompatible hydrophilic polymer with many practical applications in biology, biotechnology and biomedicine [31,32], that is frequently used for the fabrication of polymer-biomolecule [33,34], polymer-polymer [35] and polymer-inorganic [36,37] hybrid materials. The fabrication of PTh-*g*-PEG_n (Figure 3.1.2) was achieved through a two-steps process, which consisted of the chemical synthesis of macromonomers (i.e. pentathiophene substituted with PEG chains of M_w=1000 or 2000) and the anodic polymerization of such macromonomers [30].

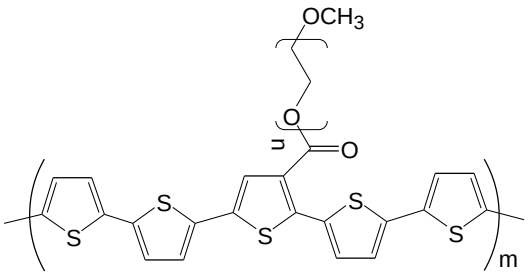

PTh-*g*-PEG_{1000}: *n*= 22

PTh-*g*-PEG_{2000}: *n*= 44

Figure 3.1.2 Chemical structure of PTh-*g*-PEG_n.

The chemical structure, composition, morphology and electrochemical properties of the resulting materials, PTh-*g*-PEG_{1000} and PTh-*g*-PEG_{2000}, were investigated using FTIR, X-ray photoelectron spectroscopy (XPS), scanning electron microscopy (SEM), atomic force microscopy (AFM) and cyclic voltammetry (CV). Furthermore, the ability of these hybrids to adsorb both extracellular and plasma proteins was investigated, their affinity towards globular proteins being higher than towards fibrillar proteins [30].

This work is mainly focused in the electronic, electrochromic and superficial properties, internal organization at the molecular level and behavior as cellular matrix of PTh-*g*-PEG_{1000} and PTh-*g*-PEG_{2000}. More specifically, the electronic and electrochromic properties of the hybrids

have been investigated using UV-vis spectroscopy. After this the surface wettability of the graft copolymers have been examined and compared with that of PEDOT, a polar PTh derivate that was proved to enhance cellular adhesion and proliferation [38,39], by measuring the contact angle. Next, the relative organization of the PTh backbone and the PEG side chains in graft copolymers have been examined using atomistic Molecular Dynamics (MD) simulations. For this purpose, an assembly formed by two copolymer molecules deposited in an surface has been simulated considering both desolvated (i.e. gas-phase) and aqueous solution environments. Finally, the biocompatibility and behavior of the two hybrids as biological platforms have been examined using cellular adhesion and proliferation assays.

3.1.2 Methods

Synthesis

The macromonomers used for the anodic polymerization of PTh-*g*-PEG_{1000} and PTh-*g*-PEG_{2000} consisted on a pentathiophene bearing a PEG chain of M_w=1000 and M_w=2000, respectively, at the central thiophene ring. These macromonomers, hereafter denoted Th_5-PEG_{1000} and Th_5-PEG_{2000} (Figure 3.1.3), were prepared by chemical synthesis using the route described in reference 30.

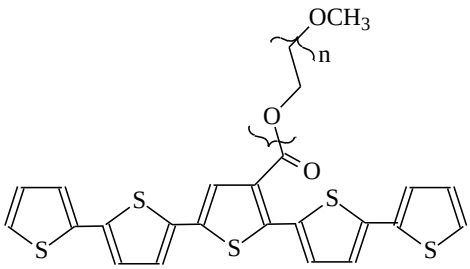

Th_5-PEG_{1000}: *n*= 22
Th_5-PEG_{2000}: *n*= 44

Figure 3.1.3 Chemical structure of Th_5-PEG_{1000} and Th_5-PEG_{2000}.

On the other hand, PTh-*g*-PEGn graft copolymers were prepared by chronoamperometry (CA) under a constant potential using an Autolab PGSTAT302N equipped with the ECD module (Ecochimie, The Netherlands). All polymerizations were carried out in a standard three-electrode cell under nitrogen atmosphere (99.995% in purity) at room temperature. The anodic compartment was filled with 15 mL of a $1 \cdot 10^{-3}$ M Th_5-PEGn solution in a mixture of acetonitrile:dichloromethane (DCM) (50:50 v/v) containing 0.1 M of a supporting electrolyte, while the cathodic compartment was filled with 10 mL of the same electrolyte solution. Steel AISI 316 and indium-tin oxide (ITO) sheets of 1.0×0.5 and 0.5×0.5 cm^2, respectively, were employed as working electrodes. The counter electrode was a platinum sheet of 1.0×0.50 cm^2 while the reference electrode was an Ag|AgCl electrode containing a KCl saturated aqueous solution (E^o = 0.222 V at 25ºC), which was connected to the working compartment through a salt bridge containing the electrolyte solution. Graft copolymers were prepared considering the following experimental conditions:

- PTh-*g*-PEG_{1000} and PTh-*g*-PEG_{2000}: $LiClO_4$ as supporting electrolyte and constant potential of 0.70 and 0,75 V, respectively.
- PTh-*g*-PEG_{2000}: Tetra butyl ammonium hexafluorophosphate (Bu_4NPF_6) as supporting electrolyte and a potential of 0.80 V.

UV-vis spectroscopy

UV-vis absorption spectra of macromonomers in solution were registered using a Specord 200 spectrophotometer. Spectra of macromonomers and PTh-*g*-PEGn films were obtained using a UV-vis-NIR Shimadzu 3600 spectrophotometer equipped with a tungsten halogen visible source, a deuterium arc UV source, a photomultiplier tube UV-vis detector, and an InGaAs photodiode and cooled PbS photocell NIR detectors. Spectra were recorded in the absorbance mode using the integrating sphere accessory (model ISR-3100), the wavelength range being 185-3300 nm. The interior of the integrating sphere was coated with highly diffuse $BaSO_4$ reflectance standard. Uncoated ITO glass was used

as reference. Hybrid material films were deposited on ITO-glass electrodes for measurements. Single-scan spectra were recorded at a scan speed of 60 nm/min. Measurements, data collection and data evaluation were controlled by the computer software UVProbe version 2.31.

Wettability

Contact angle measurements were performed using the sessile drop method, at room temperature and controlled humidity. Images of 1 μL distilled water drops were recorded after stabilization (30 s) using a CAM-200 equipment from KSV-Finland. Contact angle values were obtained as the average of five independent measures for each sample.

Optical profilometry

The thickness of the films was determined using a WYKO 9300NT optical profiler (Veeco, Plainview, NY). Different scratches were intentionally provoked on PTh-*g*-PEG_{1000} and PTh-*g*-PEG_{2000} films and measured to allow statistical analysis of data. Imaging of the films was conducted using the following optimized settings: vertical scanning interferometry (VSI) mode, full resolution, 5-mm back scan and 10-mm primary scan, 10× and 50× Michelson LR objective lens (fields of view of 2.0×) for image sizes of 237×315 μm^2 and 64×48 μm^2, respectively.

Atomic force microscopy

Topographic AFM images were obtained with a Molecular Imaging PicoSPM using a NanoScope IV controller under ambient conditions. The tapping mode AFM was operated at constant deflection. The row scanning frequency was set to 1 Hz and the physical tip-sample motion speed was 10 $\mu m \cdot s^{-1}$. The root-mean-square (RMS) roughness was determined using the statistical application of the Nanoscope software, which calculates the average considering all the values recorded in the topographic image with exception of the maximum and the minimum. AFM measurements were

performed on various parts of the films, which produced reproducible images similar to those displayed in this work. The scan window sizes used in this work were 5×5 μm^2.

Molecular dynamics simulations

Graft copolymers were simulated using an assembly of two molecules, each one containing a backbone with 20 thiophene rings and four grafted PEG chains with 22 repeating units (Figure 3.1.2). Accordingly, the molecular weight of the PEG chain in these model graft copolymers corresponds to that of PTh-*g*-PEG_{1000}. The two molecules were attached to the center of a square surface (L= 133.98 Å) formed by 900 spherical particles (i.e. 30×30 particles with a distance of 4.62 Å between neighboring particles) through a bond between the α-carbon of the first backbone thiophene ring and one spherical particle of the surface. The distance between the spherical particles used to attach the molecules was 26.1 Å. MD simulations were performed on two model systems, which can be described as follows:

- The two molecules tethered to the surface in the gas-phase. This solvent-free model corresponds to the situation encountered in AFM experiments. MD simulations of this model system involved 2462 explicit particles.
- The two molecules attached to the surface in aqueous solution. For this purpose, a spherical water cap with a radius of 70 Å and centered in the middle of tethered molecules was constructed and, subsequently, filled with 92513 explicit water molecules. This solvated model represents the situation found in cell attachment assays. The model involved a total of 280001 explicit particles.

The potential energy of the simulated systems was computed using the AMBER force field [40]. All the bonding and van der Waals parameters, with exception of the S–C–C–S torsion, were taken from the Generalized AMBER force-field (GAFF) [41]. The parameters for the S–C–C–S torsion were extracted from a recent study in which force-field parameters

compatible with AMBER were developed by computing the potential of mean forces for the inter-ring rotation of different 2,2'-bithiophene derivatives [42]. Atomic charges were adjusted using the Restrained ElectroStatic Potential (RESP) strategy [43]. The van der Waals parameters of the spherical particles used to construct the surface [R= 2.35 Å and ε= 0.90 kcal/mol] were extrapolated from previous studies devoted to investigate the structure of organic systems tethered to rigid surfaces [44,45]. Water molecules were represented using the TIP3P model [46].

MD simulations were performed using the AMBER 12.0 program [47]. Simulations in aqueous solution were performed by applying an atom-pair distance cut-off at 12 Å to compute van der Waals and electrostatic interactions, whereas gas-phase simulations were performed without cut-off. Bond lengths involving hydrogen atoms were constrained using the SHAKE algorithm with a numerical integration step of 2 fs [48]. The positions of the spherical particles at the surface were restrained applying a force constant of 40 kcal/mol·Å^2.

Before starting the MD run series, 5×10^3 steps of energy minimization were performed to relax conformational and structural tensions. After this, the systems in the gas-phase and in solution were progressively heated from 0 to 298 K along 45 ps of MD and, subsequently, equilibrated at the latter temperature for 15 ps. The last snapshot of the equilibration was used as the starting point for the production series. Coordinates were saved every 10 ps for further analysis for simulation lengths of 5 ns.

Cellular adhesion and proliferation

Vero cells (African green monkey kidney epithelial cell line) were cultured in Dulbecco's modified Eagle medium (DMEM) supplemented with 10% fetal bovine serum, 1% penicillin/streptomycin and 2 mM L-glutamine at 37ºC in a humidified atmosphere of 5% CO_2 in air. The cultured medium was changed every two days and, for sub-culture, cell monolayers were rinsed with phosphate buffered saline (PBS) and detached by incubation with 0.25% trysin/EDTA for 5 min at 37ºC. Cell

concentration was determined by counting at the Neubauer camera using 4% trypan blue as dye vital. The detached cells with viability ≥ 95% were used for cultures following the conditions for the adhesion and proliferation assays.

PTh-*g*-PEG_{1000} and PTh-*g*-PEG_{2000} films deposited onto steel AISI 316 sheets of 1 cm^2 were placed in plates of 24 wells and sterilized using UV irradiation for 15 min in a laminar flux cabinet. Samples were incubated with 1 mL of culture medium during 30 min under culture conditions to equilibrate the material. Finally, the medium was aspired and the material was evaluated for cell adhesion and proliferation by exposing cells to direct contact with the material surface. An aliquot of 50 mL containing 5×104 cells (adhesion assays) or 2×104 cells (proliferation assays) was deposited on the substrate of each well. The plate was incubated under culture conditions for 60 min to promote the cell attachment to the film surface. Finally, 1 mL of the culture medium was added to each well. Controls of adhesion and proliferation were simultaneously performed by culturing cells on the surface of the tissue culture polystyrene (TCPS) plates and uncoated steel. Cell adhesion and proliferation were evaluated after 24 hours and 7 days of culture, respectively, using the MTT [3-(4,5-dimethylthiazol-2-yl)-2,5-diphenyltetrazolium bromide] assay, which determines the cell viability. The viability results were normalized to TCPS control as relative percentages.

Results were derived from the average of four replicates (n= 4) for each independent experiment. ANOVA and Turkey tests were performed to determine the statistical significance, which was considered at a confidence level of 95% ($p < 0.05$).

The cells onto PTh-*g*-PEG_{1000} and PTh-*g*-PEG_{2000} films were examined by epifluorescence microscopy (BA410 Model, Motic Spain S.L.). For this purpose, Vero cells were fixed and permeabilized with cold acetic acid:methanol (1:3) for 3 min and subsequently replaced with fresh fixative for further 3 min. After drain the fixative, air-dry material was immersed in 2 mL of stain (0.1 μg/mL bisbenzimide Hoechst 33258 in PBS) and incubated for 5 min at room temperature in the dark to stain

nuclei. Then, stain was removed and films were mounted in a nonfluorescent medium. The bisbenzimide fluorescence and intrinsic fluorescence of films were observed with standard fluorescence filters sets: MF31000 filter (Exciter D350/50x and Emitter D460/50m) and a MF31001 filter (Exciter D480/30x and Emitter D535/40m), respectively.

Scanning electron microscopy

SEM studies were performed using a Focussed Ion Beam Zeiss Neon 40 scanning electron microscope operating at 5 kV, equipped with an EDX spectroscopy system. Samples were mounted on a double-side adhesive carbon disc and sputtercoated with a thin layer of carbon to prevent sample charging problems. Before the carbon coating for examination, samples covered with cells were fixed in a 2.5% glutaraldehyde PBS solution overnight at 4˚C. Then, they were dehydrated by washing in an alcohol battery (30˚, 50˚, 70˚, 90˚, 95˚ and 100˚) at 4˚ C for 30 minutes per wash. Finally, samples were air-dried, and sputter-coated with carbon before SEM observation.

Electrochemical characterization

The electrochemical behavior of PTh-*g*-PEG_{1000} and PTh-*g*-PEG_{2000} was studied by CV considering two different environments: films directly obtained from electropolymerization (i.e. as prepared samples) and films covered will cells. For this purpose, a sterilized phosphate buffer saline solution (PBS; pH= 7.2) was used as electrolyte in the three-electrode cell. Steel sheets of 1 cm^2 area were used as counter and working electrodes, an Ag|AgCl electrode being used as the reference electrode. Cyclic voltammograms were registered at a scan rate of 50 $mV \cdot s^{-1}$ in the potential range from -0.30 to +0.90 V. All CV assays were performed with an Autolab PGSTAT302N equipped with the ECD module (Ecochimie, The Netherlands).

The electroactivity refers to the charge storage ability and was determined by measuring the cathodic and anodic areas in the first control voltammogram (i.e. the electroactivity increases with the similarity between such areas). The electrochemical stability (electrostability) was evaluated by determining the loss of electroactivity with the number of consecutive oxidation-reduction cycles (LEA, in %):

$$LEA = \frac{\Delta Q}{Q_I} \cdot 100 \qquad \text{(Eqn. 3.1.1)}$$

where ΔQ is the difference between the voltammetric charges (in C) of the first and the last oxidation-reduction cycle, and QI is the voltammetric charge corresponding to the first cycle. In this work all LEA values are referred to a total of 10 consecutive oxidation-reduction cycles.

3.1.3 Results and Discussion

Electronic properties

Diluted DCM solutions of Th_5-PEG_{1000} and Th_5-PEG_{2000} macromonomers (i.e. 0.09 and 0.18% w/w, respectively) show an absorbance peak in the UV-vis range at λ_{max}= 402 and 376 nm respectively (Figure 3.1.4a), which corresponds to the π-π* transition of the rings. The UV-vis spectra of Th_5-PEG_{1000} and Th_5-PEG_{2000} films, which were prepared by drop casting on an ITO plate 20 μL of a 1 mM macromonomer solution in acetonitrile/DCM (50/50), are included in Figure 3.1.4a. As it can be seen, the π-π* transition of Th_5-PEG_{1000} (λ_{max}= 377 nm) and Th_5-PEG_{2000} (λ_{max}= 385 nm) shows blue and red shift, respectively, with respect to the spectra recorded for dilute solutions. Thus, the conjugation of the penthathiophene fragment in films, which relies upon overlap of the π-orbitals of the coplanar Th rings, is lower and higher than in diluted solution for Th_5-PEG_{1000} and Th_5-PEG_{2000}, respectively. This feature evidences that grafted PEG chains play a predominant role in the electronic

properties of macromonomers, their importance being expected to decrease upon polymerization.

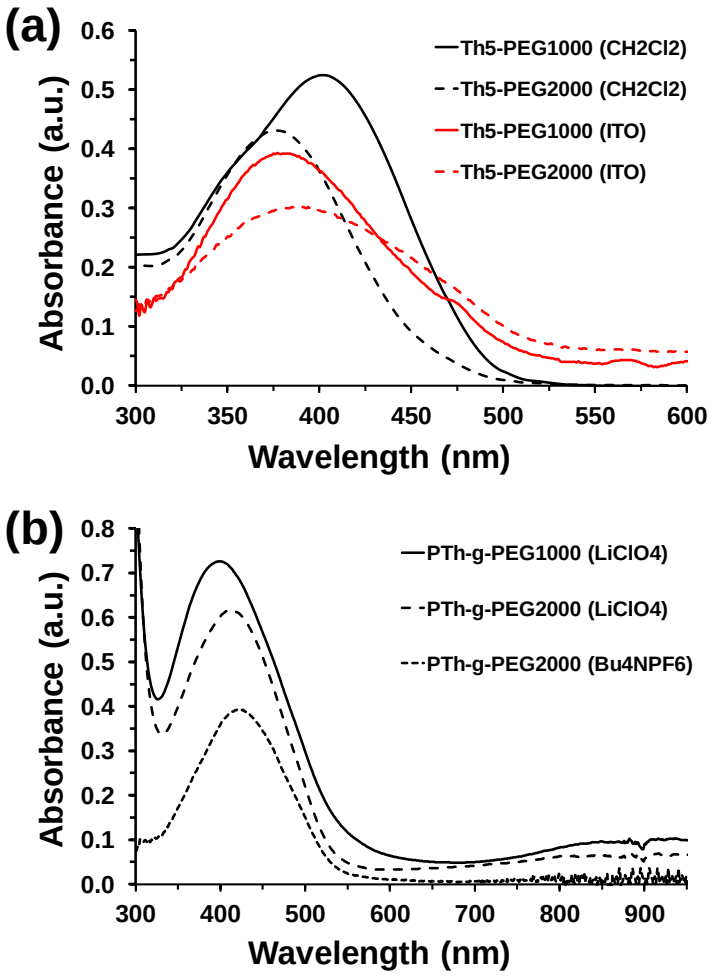

Figure 3.1.4 UV-vis spectra of: (a) Th_5-PEG_{1000} and Th_5-PEG_{2000} macromonomers in diluted DCM solution and deposited as a film onto ITO substrate; and (b) PTh-*g*-PEG_{1000} prepared using $LiClO_4$ as supporting electrolyte and PTh-*g*-PEG_{2000} obtained in presence of $LiClO_4$ and Bu_4NPF_6.

Figure 3.1.4b compares the UV-vis spectra of PTh-*g*-PEG_{1000} prepared using $LiClO_4$ as supporting electrolyte with those of PTh-*g*-PEG_{2000} obtained in presence of $LiClO_4$ and Bu_4NPF_6. The shape three spectra are rather similar and show a broad band with λmax at 400 (PTh-*g*-PEG_{1000}

with $LiClO_4$), 413 (PTh-*g*-PEG_{2000} with $LiClO_4$) and 423 nm (PTh-*g*-PEG_{2000} with Bu_4NPF_6), which corresponds to the π-π* transition.

The red shift with respect to the macromonomers originates from the increment of the conjugation length produced in the backbone upon polymerization. However, the width of the band reflects the coexistence of long and short effective conjugation lengths. Moreover, both PTh-*g*-PEG_{1000} and PTh-*g*-PEG_{2000} are less conjugated than poly[3-(3,6-dioxaheptyl)thiophene], an early reported PTh derivative containing small oligo(oxyethylene) substituents [i.e. R= $–(CH_2CH_2O)_2–CH_3$], which showed λ_{max}= 435 and 445 nm when produced by chemical and electrochemical polymerization, respectively [49]. Indeed, all these systems show less conjugation than unsubstituted PTh chemically [50] and electrochemically [51] produced (i.e. λ_{max}= 495 and 447 nm, respectively).

In a π-conjugated system, the band gap (ε_g) is defined as the difference between the lowest energy in the conduction band and the highest energy in the valence band. According to the zero order approximation, this is equal to the lowest excitation energy, which can be obtained from the onset value (λ^{onset}) at the lower energy edge of the absorption spectrum (i.e. $\varepsilon_g = 1240/\lambda^{onset}$). Specifically, the optical ε_g derived from the UV-vis spectra of PTh-*g*-PEG_{1000} (λ^{onset}= 552 nm) and PTh-*g*-PEG_{2000} (λ^{onset}= 542 nm) prepared using ClO_4^- as dopant is 2.25 and 2.29 eV, respectively, while that obtained for PTh-*g*-PEG_{2000} doped with PF_6^- (λ^{onset}= 547 nm) is 2.27 eV. According to these values, the energy gap associated to the lowest π-π* transition of PTh-*g*-PEG_n graft copolymers is slightly larger than those conventional PTh derivatives substituted at the 3-position [e.g. poly(thiophene-3-methyl acetate), 1.98-2.17 eV [52], poly(3-chlorothiophene), 2.14 eV [53], and poly(3-bromothiophene), 1.93-1.97eV [54]. This feature corroborates that the conjugation length at the backbone is lower for these graft copolymers than for derivatives with conventional substituents. Moreover, all these values are higher than the ε_g determined for PEDOT using electrochemical (1.98 eV) [55] or spectroscopic (1.6–1.7 eV) [5] methods (see Table 3.1.1), which is

consistent with the excellent electrochemical and electrical behavior of this PTh derivative.

	PTh-*g*-PEG$_{1000}$	**PTh-*g*-PEG$_{2000}$**	**PEDOT**
ε_g (eV)	2.25[a]	2.29[a]	1.6-1.7[a,b]; 1.98[c]
Contact angle (˚)	87	76	82
Roughness (nm)	11 ± 2	12 ± 2	111 ± 19
Adhesion of Vero cells (%/cm^2)	98.7 ± 4.7[d]	101.3 ±4.7[d]	117.3 ± 3.7[d,e]
Proliferation of Vero cells (%/cm^2)	149.2 ± 9.7[d]	166.3 ± 17.3[d]	100.0 ± 3.7[d,e]
Electroactivity (%)	162[f]	329[f]	131[e,f]

[a] Band gap determined by UV-vis spectroscopy. [b] Taken from ref. 5. [c] Band gap determined electrochemically in ref. 55. [d] The relative viability of Vero cells was established in relation to the TCPS control (i.e. viability of TCPS=100%). [e] Data taken from ref. 16. [f] Enhancement of the electroactivity in films covered with cells with respect to the uncovered ones.

Table 3.1.1 Comparison of the properties determined for PTh-*g*-PEG$_{1000}$, PTh-*g*-PEG$_{2000}$ and PEDOT.

Another interesting feature is that the oxidation band observed at ~900 nm for both PTh-*g*-PEG$_{1000}$ and PTh-*g*-PEG$_{2000}$ when prepared in presence of $LiClO_4$ is not detected when the supporting electrolyte is Bu_4NPF_6. This band, which can be attributed to the formation of polarons and bipolarons in PTh chains [52], evidences the influence of the dopant agent. Thus, the two graft copolymers form complexes with the ClO_4^- dopant anions while the vanishing of the band confirms the lack of complexes with PF_6^-.

Figure 3.1.5 shows the effects of additional oxidation in the electronic properties of PTh-*g*-PEG$_{1000}$ and PTh-*g*-PEG$_{2000}$ doped with ClO_4^-.

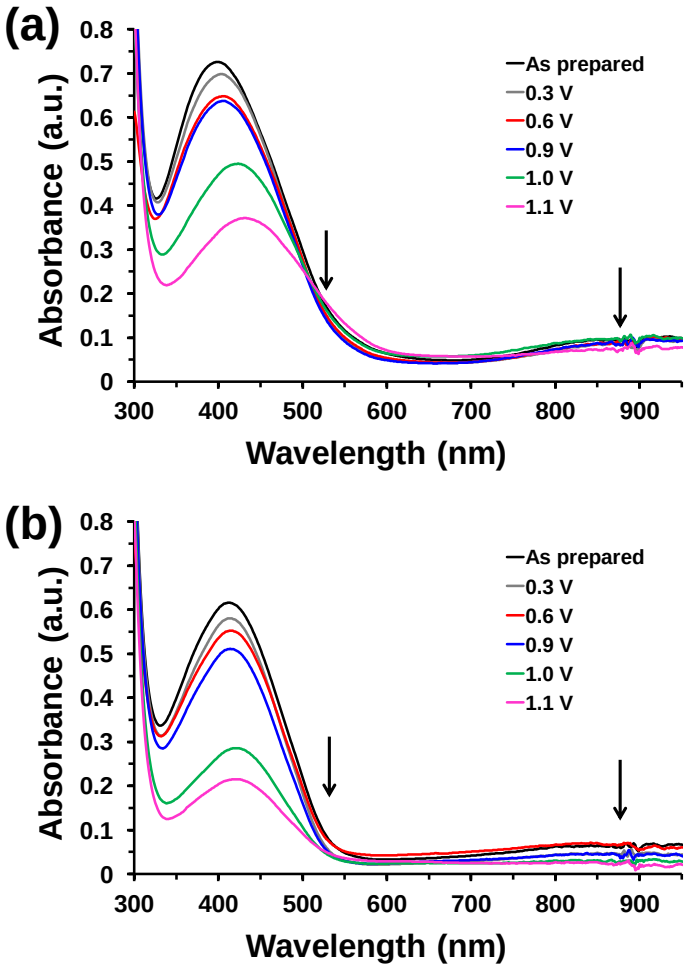

Figure 3.1.5 UV-vis spectra of (a) PTh-*g*-PEG$_{1000}$ and (b) PTh-*g*-PEG$_{2000}$ doped with ClO_4^- using as prepared samples and after re-oxidation with potentials of 0.3, 0.6, 0.9, 1.0 and 1.1 V.

For this purpose, after introduce the graft copolymer films in acetonitrile solutions with 0.1 M $LiClO_4$, a constant potential was applied during 10 s. UV-vis spectra were recorded after re-oxidation with potentials of 0.3, 0.6,

0.9, 1.0 and 1.1 V. As it can be seen, this oxidation process is accompanied by the reduction and the red shift of the absorbance band associated to the π-π* transition. Thus, the λ_{max} of as prepared PTh-*g*-PEG_{1000} and PTh-*g*-PEG_{2000} films increases from 400 and 413 nm, respectively, to 431 and 422 nm after apply a constant potential of 1.1 V during 10 s. Both the red shift and the decrease of the absorbance provoked by further oxidation are consistent with a reduction of the ε_g, which is slightly more pronounced for PTh-*g*-PEG_{1000} than for PTh-*g*-PEG_{2000}. On the other hand, the second band, which is observed at ~900 nm in the as prepared samples, shifts into the NIR region after additional oxidation. According to previous studies, this variation, which is similar for the two graft copolymers, has been attributed to polaron→bipolaron transitions between band gap states [56].

Regarding to the electrochromic properties of graft copolymers, as prepared PTh-*g*-PEG_{1000} and PTh-*g*-PEG_{2000} films doped with ClO_4^- showed a brownish orange and intense yellow color, respectively, while the latter hybrid obtained using Bu_4NPF_6 as supporting electrolyte displayed an intermediate color. Re-oxidation with potentials lower than 1.0 V does not provoke any variation in the color while films change to green and bluish green when the applied potential is 1.0 and 1.1 V, respectively. This behavior is fully consistent with that observed for conventional PThs [57].

Surface wettability

The average values of the contact angle (θ) determined for PTh-*g*-PEG_{1000} and PTh-*g*-PEG_{2000} films doped with ClO4- are θ= 87º and 76º, respectively, indicating that, as expected, the enlargement of the PEG chains increases the hydrophilicity at the surface. Zhang et al. reported that the contact angle of unsubstituted PTh obtained by electropolymerization is higher than 100˚ [58]. Thus, ultrathin films are compact and smooth while the surface becomes more irregular and porous as the thickness increases, enhancing the roughness. However, the influence of the

molecular weight of grafted chains in both the thickness and roughness of PTh-*g*-PEG$_n$ have been found to be very small.

Specifically, the AFM 2D images displayed in Figure 3.1.6 evidence that the surface of two copolymers presents nanometric aggregates.

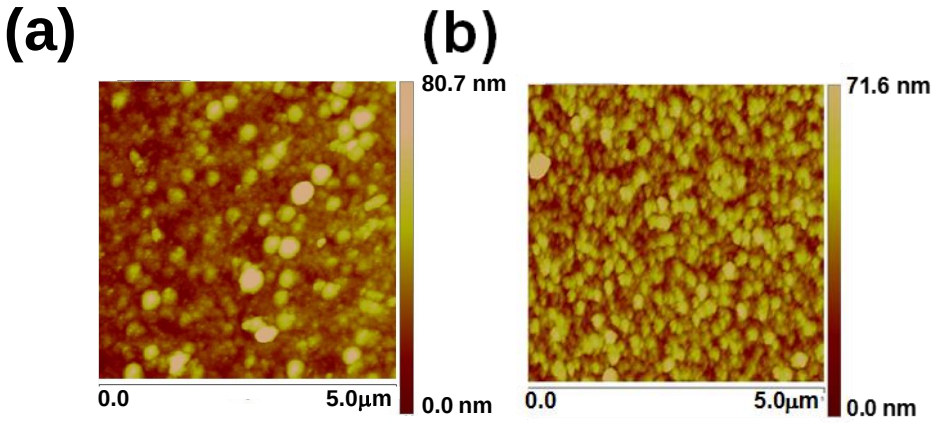

Figure 3.1.6 2D Height AFM images of (a) PTh-*g*-PEG$_{1000}$ and (b) PTh-*g*-PEG$_{2000}$ prepared using $LiClO_4$ as supporting electrolyte.

Although the frequency and size of such aggregates depend on the length of the PEG chains, the RMS roughness is very similar and noticeably low for the two materials: 11±2 and 12±2 nm for PTh-*g*-PEG$_{1000}$ and PTh-*g*-PEG$_{2000}$, respectively. Similarly, optical profilometry measurements indicate that the films of the two grafted copolymer are ultrathin, the thickness being ~230 and ~110 nm for PTh-*g*-PEG$_{1000}$ and PTh-*g*-PEG$_{2000}$, respectively. Accordingly, the observed $\Delta\theta$= -11º should be essentially attributed to the length of the PEG chains.

In order to compare the water-affinity of PEDOT, a polar PTh derivative that behave as a good cellular matrix [21,22], with that of PTh-*g*-PEG$_n$, ultrathin films of the former material were electrochemically prepared by CA under a constant potential of 1.40 V using acetonitrile as generation medium and $LiClO_4$ as supporting electrolyte. The thickness and roughness of the films obtained using a polymerization time of 10 s were ~240 nm and 111 ± 19 nm, respectively. The contact angle determined for PEDOT was θ= 82º (Table 3.1.1). Considering that the roughness of

PEDOT is one order of magnitude higher than those of graft copolymers, the contact angles determined for PTh-*g*-PEG_{1000} and PTh-*g*-PEG_{2000} suggest the behavior of these graft copolymers as supportive matrix for the cells growth should be excellent.

Microscopic organization of PTh backbone and PEG chains

MD simulations in the gas-phase and aqueous solution led to very different results, as is clearly evidenced by the atomistic structures displayed in Figure 3.1.7. Thus, inspection of snapshots selected at different time intervals indicates that, although the relative disposition of the PTh backbone and the PEG side groups is initially similar in the two environments, important differences appear after only 400 ps. More specifically, initially both PTh and PEG fragments are extended, even though the former are perpendicular to the rigid surface while the latter are parallel. This biphasic organization is preserved after 5 ns of MD in solution, the largest change being in this case the small conformational fluctuations underwent by the flexible PEG fragments. In contrast, in the gas-phase the graft PEG chains tend to wrap the PTh backbone and the whole system collapses onto the surface. This process starts after a few hundreds of picoseconds, being completely finished after 1 ns. Thus, the desolvated environment facilitates the formation of both short- and large-range interactions, giving place to the formation of a globular structure that also interacts with the surface.

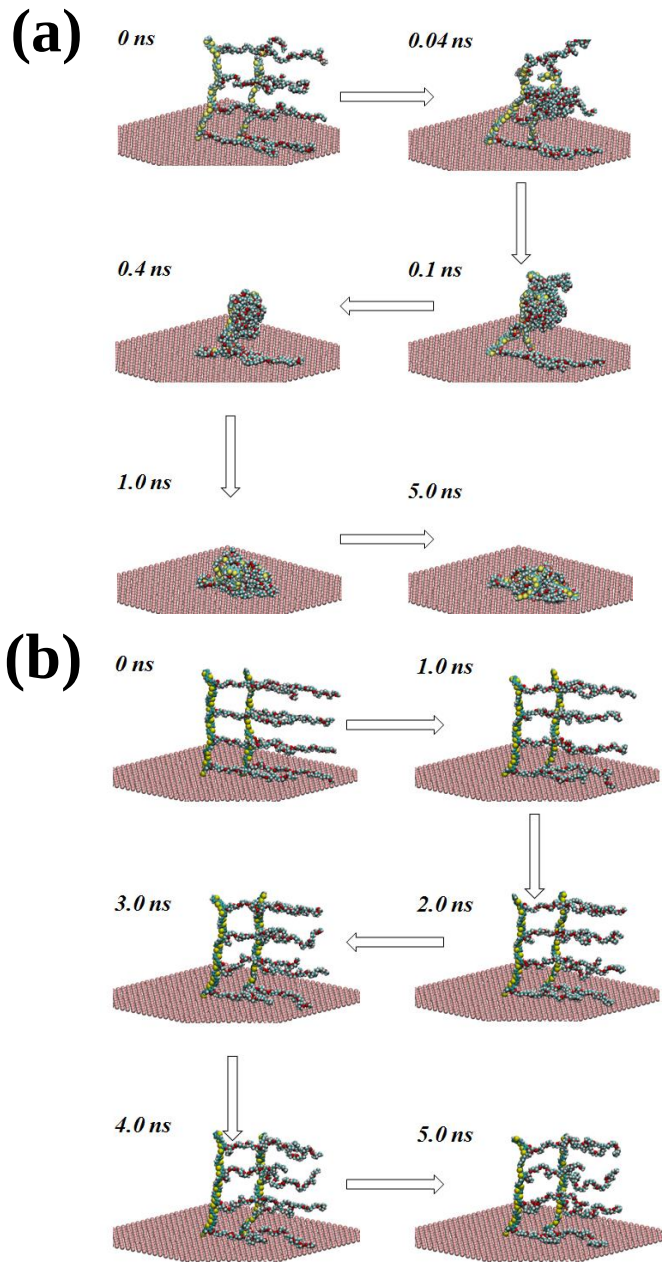

Figure 3.1.7 Selected snapshots from MD simulations (a) in the gas-phase and (b) in solution. Water molecules and hydrogen atoms have been omitted to clarify the representations.

In order to provide a more quantitative view of the conformational reorganization underwent by PTh-*g*-PEG$_{1000}$ chains in the gas-phase and solution, Figure 3.1.8 represents the temporal evolution of the end-to-end distance ($d_{e\text{-}e}$) for both the PTh and PEG segments.

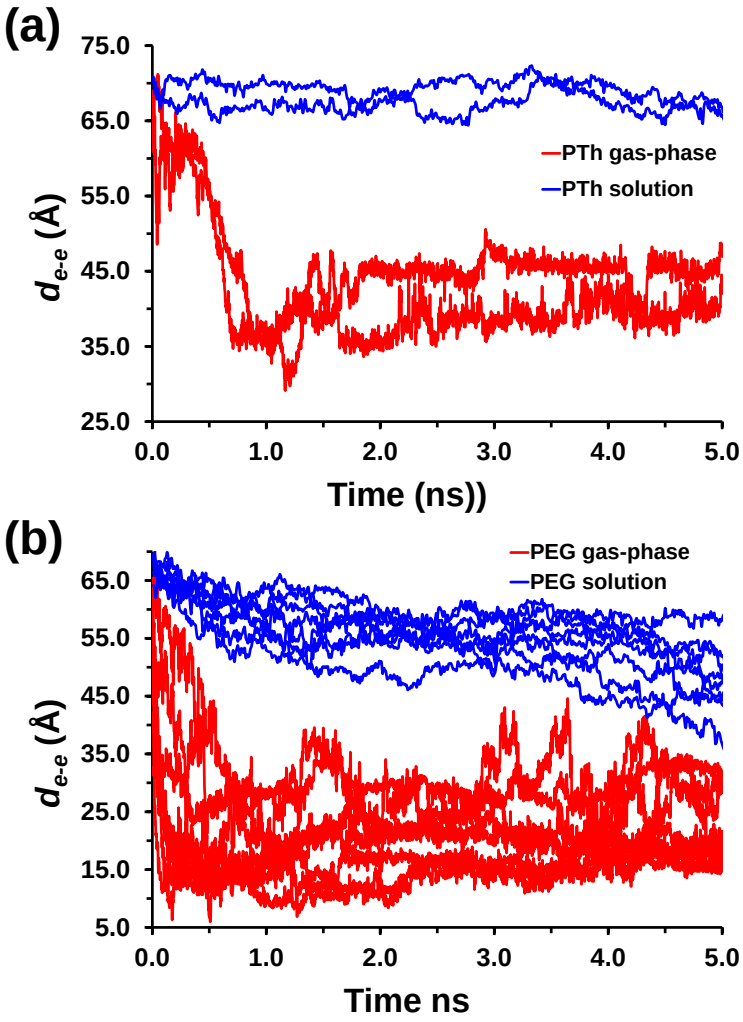

Figure 3.1.8 Temporal evolution of the end-to-end distance ($d_{e\text{-}e}$) determined from MD simulations of PTh-*g*-PEG$_{1000}$ in the gas-phase (red lines) and solution (blue lines) for: (a) backbone PTh segments (2 explicit molecules per simulation); and (b) side PEG segments (2 explicit molecules × 4 repeat units= 8 segments per simulation).

As it can be seen in Figure 3.1.8a, which displays the variation of the de-e for the PTh backbone of the two explicit molecules against the simulation time, the values obtained after thermal equilibration ($d_{e\text{-}e}$= 70.2 and 70.8 Å) remains practically constant during the whole trajectories (averages over the whole trajectory: 67.5±3.0 and 69.0±3.2 Å). In contrast, the $d_{e\text{-}e}$ drops in the gas-phase from 69.6 and 61.6 Å to ~35 Å after only 0.8 ns, which represents a drastic shrinkage of the backbone (~45-50%). After this, the PTh segment experiences a slight lengthening, which also takes 0.8 ns, allowing the system to alleviate the short-range repulsions generated by the fast initial contraction. Finally, the de-e values remain relatively constant at 38.8±4.2 and 44.4±3.5 Å during the last 3.4 ns of simulation.

The three-dimensional organization of the PTh-*g*-PEG_{1000} chains has been also examined by using the partial radial distribution functions. Figure 3.1.9a and 3.9b displays the partial distributions of the S···S ($g_{S\text{-}S}$) and O···O ($g_{O\text{-}O}$) pairs, respectively, in desolvated and aqueous environments, which have been calculated considering pairs of the same molecule (i.e. intramolecular pairs) and the sum of both intra- and intermolecular pairs (i.e. all pairs).

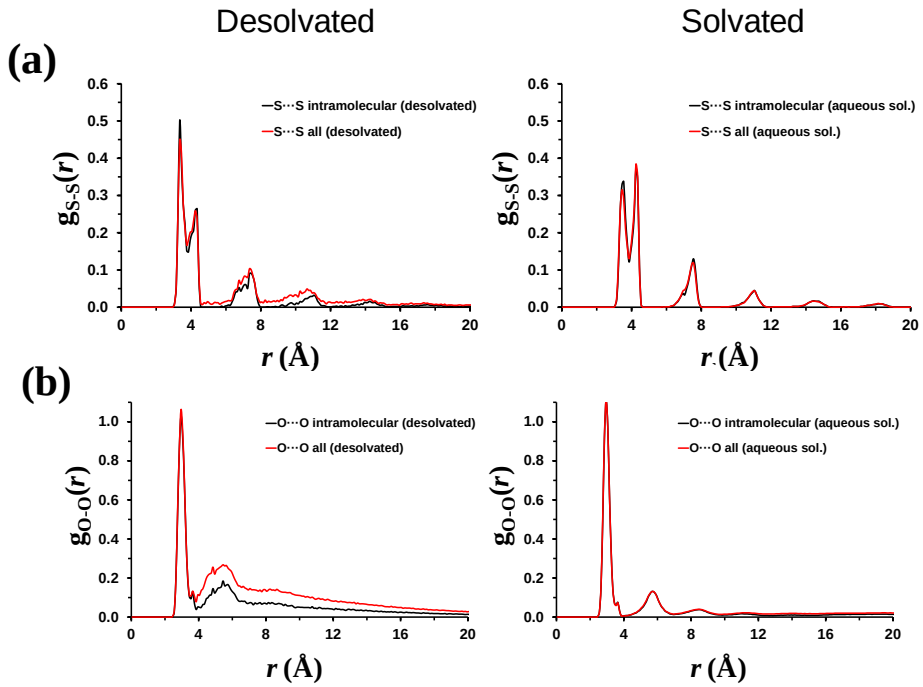

Figure 3.1.9 Partial radial distribution functions of (a) S···S and (b) O···O pairs from MD simulations of PTh-*g*-PEG_{1000} in the gas-phase (left) and solution (right). Two profiles are displayed in each case: intramolecular pairs (black) and all pairs (red).

As it can be seen, comparison intramolecular and all pairs $g_{S\text{-}S}(r)$ and $g_{O\text{-}O}(r)$ profiles indicates that the relatively ordered organization is, as expected, dominated by the intramolecular contribution. The $g_{S\text{-}S}(r)$ shows six well-defined peaks centered at 3.45, 4.25, 7.55, 10.85, 14.25 and 18.15 Å in aqueous solution while only four peaks centered at 3.35, 4.25, 7.05 and 10.55 Å are detected in the gas-phase, the latter two being relatively undefined. This feature clearly indicates that the PTh backbone is well organized in solution, adopting a structure that is practically perpendicular to the surface, as was displayed in Figure 3.1.7b. In contrast, such long-range order is loss in the desolvated system, the peaks at distances lower than 7.1 Å being due to the existence of short-range interactions. The $g_{O\text{-}O}(r)$ profiles show similar trends, even though the order in the PEG chains is considerably lower than that of PTh because of its intrinsic conformational flexibility, which is restricted in PTh due to the geometric restrictions of the thiophene ring. Thus, three well-defined peaks centered

at 2.85, 5.55 and 8.45 Å are displayed in solution while only two peaks at 2.95 and 5.45 Å are shown in the desolvated system, the last one broad and ill-defined.

Behavior as cellular matrix

The biocompatibility of PTh-*g*-PEG_{1000} and PTh-*g*-PEG_{2000} doped with ClO_4^- was determined by cell adhesion and proliferation assays. The Vero cell line was selected because of its adherent growth and epithelial-like characteristics. Quantitative results of cellular adhesion assays are displayed in Figure 3.1.10a, steel and TCPS (or culture plate) being used as control substrates. As it can be seen, the number of cells by area adhered to the surface is significantly higher for PTh-*g*-PEG_{1000} and, especially, PTh-*g*-PEG_{2000} than for TCPS and steel. Thus, the hybrids do not show cytotoxic effects within a short period of time (i.e. 24 h), acting as excellent supportive matrices. After seven days of culture, PTh-*g*-PEG_{2000} retains the same behavior while that of PTh-*g*-PEG_{1000} improves considerably, indicating that this material stimulates cellular proliferation more than PTh-*g*-PEG_{2000} and the controls. Thus, the results provided by cell proliferation assays, which are displayed in Figure 3.1.10b, reflect that the cell viability of the two hybrids is practically the same after seven days of culture and remarkably higher than that found for poly(3,4-ethylenedioxythiophene) [38,39].

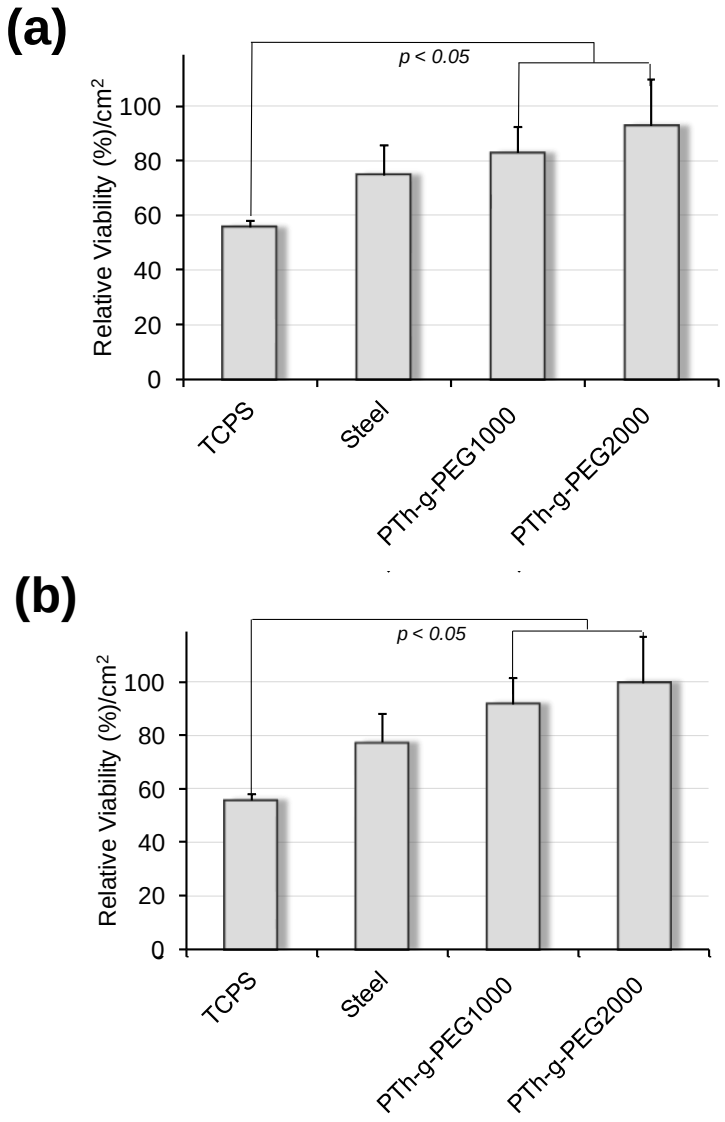

Figure 3.1.10 Cellular adhesion (a) and cellular proliferation (b) on PTh-*g*-PEG_{1000} and PTh-*g*-PEG_{2000} doped with ClO_4^-. The relative viability of Vero cells was established in relation to the TCPS control. Steel was also considered as a control substrate because the individual polymers and the blend were deposited on this material. $p < 0.05$ vs TCPS.

The ability of PTh-*g*-PEG_{1000} and PTh-*g*-PEG_{2000} to behave as cellular matrices is clearly shown in the fluorescence images displayed in Figure 3.1.11, which show not only the high density of adhered cells but also their homogeneous spreading onto the surface of the substrates.

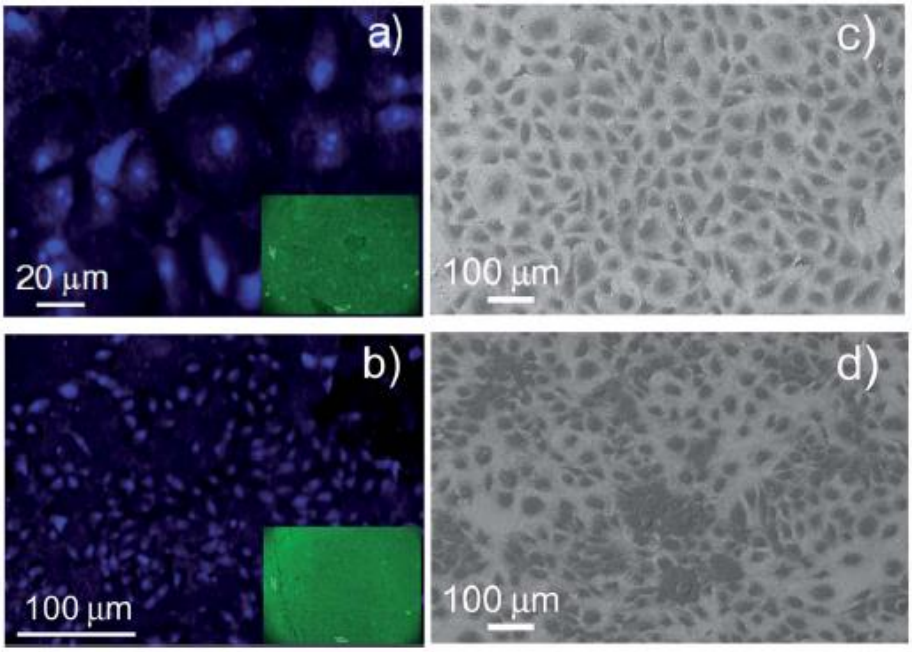

Figure 3.1.11 Fluorescence images of cell adhesion onto (a) PTh-*g*-PEG_{1000} and (b) PTh-*g*-PEG_{2000} surfaces. Cell adhesion was observed with nuclei stain using bisbenzimide. Insets show the intrinsic fluorescence of the hybrid matrix. SEM micrographs of cells adhered on the surface of (c) PTh-*g*-PEG_{1000} and (d) PTh-*g*-PEG_{2000}.

Table 3.1.1 compares the response of PEDOT towards Vero cells [16] with those of PTh-*g*-PEG_{1000} and PTh-*g*-PEG_{2000}. In all cases viability is relative to the TCPS control. As it can be seen, the number of adhered cells by unit of area is similar for the three compounds, even though from a quantitative point of view it is slightly higher for PEDOT. However, the cell viability in proliferation assays is remarkably higher for the two graft copolymers than for PEDOT. This feature evidences that grafted PEG chains improve significantly the cell response of PTh and result in an excellent bioactive platform for tissue engineering.

Electrochemical behavior of the cellular matrix

Control voltammograms in PBS of PTh-*g*-PEG_{1000} and PTh-*g*-PEG_{2000} as prepared (uncovered) and covered with Vero cells in PBS are displayed in Figure 3.1.12a. The electroactivity of the covered films is significantly higher (i.e. 162 and 329%, respectively) than that of the uncovered ones, this feature being particularly remarkable for PTh-*g*-PEG_{2000}. The remarkable activity of covered films, which is higher than for PEDOT (Table 3.1.1), should be attributed to the exchange of ions promoted by the adhered cells during oxidation-reduction process. Although the electrochemical behavior of the two hybrids is dominated by the PTh backbone, the role played by the latter effect is expected to be more important in the hybrid with smaller PEG chains, as is evidenced in Figure 3.1.12a. On the other hand, the current density at 0.90 V increases from 0.26 and 0.06 $mA \cdot cm^{-2}$ for uncovered PTh-*g*-PEG_{1000} and PTh-*g*-PEG_{2000}, respectively, to 0.74 and 0.39 $mA \cdot cm^{-2}$ for the systems coated with cells. This behavior also reflects the enhancement of the electrochemical properties provoked by the adhered cells.

Figure 3.1.12b compares the voltammograms recorded after 10 consecutive oxidation-reduction cycles in PBS for samples uncovered and coated with cells. As it can be seen, there is a significant reduction in the electroactivity with respect to the control voltammograms displayed in Figure 3.1.12a. The electrochemical stability of uncovered samples was slightly higher than that of samples coated with Vero cells. Thus, the LEA of uncovered and covered samples is ~65% and ~75%, respectively. This should be attributed to the fact that, in the first cycle, the electroactivity of the former samples in the first cycle is very low compared to that of the latter ones. Accordingly, it spite of such LEA values, the electroactivity of films coated with Vero cells is considerably higher than that of the uncoated films after 10 consecutive redox cycles (i.e. 79% and 228% for PBS of PTh-*g*-PEG_{1000} and PTh-*g*-PEG_{2000}, respectively).

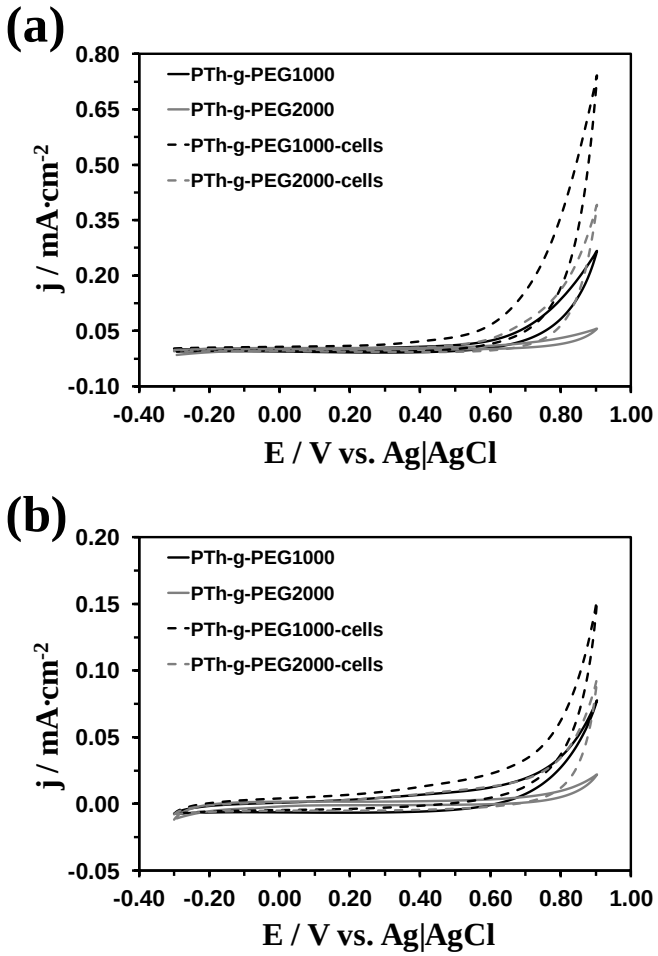

Figure 3.1.12 Cyclic voltammograms of PTh-*g*-PEG_{1000} (black) and PTh-*g*-PEG_{2000} (grey) films uncovered (solid line) and coated with Vero cells (dashed lines) in PBS. Voltammograms of both the as prepared samples (a) and after ten consecutive oxidation-reduction cycles (b) are displayed.

3.1.4 Conclusions

UV-vis spectroscopy analyses of macromonomers indicate that the electronic properties of the pentathiophene fragment are dominated by the size of the PEG chains. This effect is significantly reduced upon

polymerization, the π-conjugation of the PTh backbone playing a fundamental role in graft copolymers. The optical ε_g ranges from 2.25 to 2.29 eV, depending of the length of the PEG chain and the dopant agent. These values are ~0.3 eV larger than those typically found for 3-substituted PTh derivatives, indicating that PEG chains provokes a higher reduction in the conjugation length of the PTh backbone. Furthermore, the formation of polarons and bipolarons as well as the transition between such two states upon re-oxidation have been also detected by UV-vis spectroscopy.

The hydrophilicity of PTh-*g*-PEGn increases with n, the contact angle measured for PTh-*g*-PEG_{2000} being even higher than that of PEDOT. This behavior is fully consistent with the structure predicted by MD simulations in hydrated environments. More specifically, simulations indicate that PTh and PEG segments are perpendicular and parallel to the surface, respectively, both showing extended conformations are relatively ordered arrangements. Due to this biphasic organization polar PEG chains are completely accessible to the water molecules of the bulk. In a desolvated environment the copolymer chains collapse onto the surface, leading to an important reduction of the molecular order.

The behavior of the two hybrids as supportive matrix has been found to very good, especially that of PTh-*g*-PEG_{2000}. The two systems promote cells growth, their behavior as matrices for cellular proliferation being significantly higher than that reported for PEDOT due to the biocompatibility of the PEG fragments. Furthermore, the electrochemical activity and the maximum of current density are significantly higher for PTh-*g*-PEG_n films coated by cells than for uncoated samples. The overall of the results suggest that the graft copolymers studied in this work have many potential biotechnological applications, especially those in which electrochemical properties are used as elements for the communication with cells (e.g. biosensing and transmission components in orthopedic devices).

3.1.5 References

1. H. Shirakawa, E.J. Louis, A.G. MacDiarmid, C.K. Chiang, A.J. Heeger; *Chem. Soc. Chem. Commun.*, vol. 19, pp. 578-580, 1977.
2. T.A. Skoteheim, J.R. Reynolds, "Handbook of conducting polymers" 3rd edition; *CRC Press*, Boca Raton, FL 2007.
3. K. Kundu, D. Giri; *Am. Inst. Phys.*, vol. 105, pp. 11075-11080, 1996.
4. S.Y. Hong, D.S. Marnick; *Macromol.*, vol. 25, pp. 4652–4657, 1992.
5. L.B. Groenendaal, F. Jonas, D. Freitag, H. Pielartzik, J.R. Reynolds; *Adv. Mater.*, vol. 12, pp. 481-494, 2000.
6. S. Kirchmeyer, K. Reuter; *J. Mater. Chem.*, vol. 15, pp. 2077-2088, 2005.
7. L.A.A. Pettersson, T. Johansson, F. Karlsson, H. Arwin, O. Inganas; *Synth. Met.*, vol. 101, pp. 198-199, 1999.
8. A. Kumar, D.M. Welsh, M.C. Morvant, F. Piroux, K.A. Abboud, J.R. Reynolds; *Chem. Mater.*, vol. 10, pp. 896-902, 1998.
9. B. Winther-Jensen, O. Winther-Jensen, M. Forsyth, D.R. MacFarlane; *Sci.*, vol. 321, pp.671-674, 2008.
10. J. Joo, S.H. Park, D.S. Seo, S.J. Lee, H.S. Kim, K.W. Ryu, T.J. Lee, S.H. Seo. C.L. Lee; *Adv. Funct. Mater.*, vol. 15, pp. 1465-1470, 2005.
11. J.K. Koh, J. Kim, B. Kim, J.H. Kim, E. Kim; *Adv. Mater.*, vol. 23, pp. 1641-1646, 2011.
12. N.K. Guimard, N. Gomez, C.E. Schmidt; *Prog. Polym. Sci.*, 2007, prog. Polym. Sci., vol. 32, pp. 876-891, 2007.
13. D. Bendrea, L. Cianga, I. Cianga; *J. Biomat. Appl.*, vol. 26, pp. 3-84, 2011.
14. D.F. Li, H.J. Wang, J.X. Fu, W. Wang, X.S. Jia, J.Y. Wang; *J. Phys. Chem. B*, vol. 112, pp. 16290-16299, 2008.
15. S. Kamalesh, P. Tan, J. Wang, T. Lee, E.T. Kang, C.H. Wang; *J. Biomed. Mater. Res.*, vol. 52, pp. 467-478, 2000.
16. G. Fabregat, G. Ballano, E. Armelin, L. J. del Valle, C. Cativiela, C. Alemán; *Polym. Chem.*, vol. 4, pp. 1412-1424, 2013.
17. M.M. Pérez-Madrigal, E. Armelin, L.J. del Valle, F. Estrany, C. Alemán; *Polym. Chem.*, vol. 3, pp. 979-991, 2012.

18. N. Mohamed-Mahmoud, G. Olgun; *Prog. Polym. Sci.*, vol. 37, pp. 1597-1656, 2012.
19. C.J. Galvin, J. Genzer; *Prog. Polym. Sci.*, vol. 37, pp. 871-906, 2012.
20. V. Singh, P. Kumar, R. Sanghi; *Prog. Polym. Sci.*, vol. 37, pp. 340-364, 2012.
21. D. Neugebauer; *Polym.*, vol. 56, pp. 521-529, 2011.
22. C. Feng, Y.J. Li, D. Yang, J.H. Hu, X.H. Zhang, X.Y. Huang; *Chem. Soc. Rev.*, vol. 40, pp. 1282-1295, 2011.
23. D. Uhrig, J. Mays; *Polym. Chem.*, vol. 2, pp. 69-76, 2011.
24. P.J. Costanzo, K.K. Stokes; *Macromol.*, vol. 35, pp. 6804-6810, 2002.
25. A. Cirpan, S. Alkan, L. Toppare, Y. Hepuzer, Y. Yag; J. *Polym. Sci. Part A: Polym. Chem.*, vol. 40, pp. 4131-4140, 2002.
26. J. Shen, K. Ogino; *Chem. Lett.*, vol. 34, pp. 1616-1617, 2005.
27. J. Shen, K. Tsuchiya, K. Ogino; *J. Polym. Sci. Part A: Polym. Chem.*, vol. 46, pp. 1003-1013, 2008.
28. X. Chen, B. Gholamskhass, X. Han, G. Vamvouinis, S. Holdcroft; *Macromol. Rapid Commun.*, vol. 28, pp. 1792-1797, 2007.
29. F. Liu, Y. Chen, Y. Wei, L. Li, S. Shang; *J. Appl. Polym. Sci.*, vol. 123, pp. 2582-2587, 2012.
30. A.D. Bendrea, G. Fabregat, L. Cianga, F. Estrany, L.J. del Valle, I. Cianga, C. Alemán; *Polym. Chem.*, vol. 4, pp. 2709-2703, 2013.
31. S.P. Zhong, Y.P. Zhang, C.T. Lim; *Tissue Engin. Part B-Reviews*, vol. 18, pp. 77-87, 2012.
32. C. Mangold, F. Wurm, H. Frey; *Polym. Chem.*, vol. 3, pp. 1714-1721, 2012.
33. J. Peyre, V. Humblot, C. Methivier, J.M. Berjeaud, C.M. Pradier; *J. Phys. Chem. B*, vol. 47, pp. 13839-13847, 2012.
34. I. W. Hamley, M. J. Krysmann, V. Castelletto, L. Noirez; *Adv. Mater.*, vol. 20, pp. 4394-4397, 2008.
35. Y.Y. Xu, J.Y. Yuan, B. Fang, M. Drechsler, M. Mullner, S. Bolisetty, M. Ballauf, A.H.E. Muller; *Adv. Funct. Mater.*, vol. 20, pp. 4182-4189, 2010.
36. G. Sun, S.V. Graeter, L. Yu, S.F. Duan, J.P. Spatz, D. Ding; *Biomacromol.*, vol. 9, pp. 2569-2572, 2008.

37. K. Driesen, R. Van Deun, C. Gorller-Walrand, K. Binnemans; *Chem. Mater.*, vol. 16, pp, 1531-1535, 2004.
38. L.J. del Valle, D. Aradilla, R. Oliver, F. Sepulcre, A. Gamez, E. Armelin, C. Alemán, F. Estrany; *Eur. Polym. J.*, vol. 43, pp. 2342-2349, 2007.
39. L.J. del Valle, F. Estrany, E. Armelin, R. Oliver, C. Alemán; *Macromol. Biosci.*, vol. 8, pp. 1144-1151, 2008.
40. W.D. Cornell, P. Cieplak, C.L. Bayly, I.R. Gould, K.M. Merz, D.M. Ferguson, D.C. Spellmeyer, T. Fox, J.W. Caldwell, P.A. Kollman; *J. Am. Chem. Soc.*, vol. 117, pp. 5179–5197, 1995.
41. J. Wang, R.M. Wolf, J.W. Caldwell, D.A. Case; *J. Comput. Chem.*, vol. 15, pp. 1157-1174, 2004.
42. J. Preat, F. Rodríguez-Ropero, J. Torras, O. Bertran, D. Zanuy, C. Alemán; *J. Comput. Chem.*, vol. 31, pp. 1741-1751, 2010.
43. P. Cieplak, W. Cornell, C.I. Bayly, P.A. Kollman; *J. Comput. Chem.*, vol. 16, pp. 1357-1377, 1995.
44. D. Curcó, D. Zanuy, R. Nussinov, C. Alemán; *J. Comput. Chem.*, vol. 32, pp. 607-619, 2011.
45. D. Curcó, G. Revilla-López, C. Alemán, D. Zanuy; *J. Pept. Sci.*, vol. 17, pp. 132-138, 2011.
46. W.L. Jorgensen, J. Chandrasekhar, J.D. Madura, R.W. Impey, M.L. Klein; *J. Chem. Phys.*, vol. 79, pp. 926-935, 1983.
47. D.A. Case, T.A. Darden, T.E. Cheatham III, C.L. Simmerling, J. Wang, R.E. Duke, R. Luo, R.C. Walker, W. Zhang, K.M. Merz, B. Roberts, S. Hayik, A. Roitberg, G. Seabra, J. Swails, A.W. Goetz, I. Kolossváry, K.F. Wong, F. Paesani, J. Vanicek, R.M. Wolf, J. Liu, X. Wu, S.R. Brozell, T. Steinbrecher, H. Gohlke, Q. Cai, X. Ye, J. Wang, M.J. Hsieh, G. Cui, D.R. Roe, D.H. Mathews, M.G. Seetin, R. Salomon-Ferrer, C. Sagui, V. Babin, T. Luchko, S. Gusarov, A. Kovalenko, P.A. Kollman, *AMBER 12*, University of California: San Francisco, 2012.
48. J.P. Ryckaert, G. Ciccotti, H.J.C. Berendsen; *J. Comput. Phys.*, vol. 23, pp. 327-341, 1977.

49. L.H. Shi, F. Garnier, J. Roncali; *Macromol.*, vol. 25, pp. 6425-6429, 1992.
50. H.B. Yildiz, S. Kiralp, L. Toppare, Y. Yagci, K. Ito; *Macromol. Chem. Phys.*, vol. 100, pp. 124-127, 2006.
51. F. Alakhras, R. Holze; *Synth. Metals*, vol. 157, pp. 109-119, 2007.
52. A.L. Gomes, J. Casanovas, O. Bertran, J.S. de C. Campos, E. Armelin, C. Alemán; *J. Polym. Res.*, vol. 18, pp. 1509-1517, 2011.
53. Y. Pang, X. Li, G. Shi, L. Jin; *Thin Solid Films*, vol. 516, pp. 6512-6516, 2008.
54. J. Casanovas, D. Aradilla, J. Poater, M. Solà, F. Estrany, C. Alemán; *Phys. Chem. Chem. Phys.*, vol. 14, pp. 10050-10062, 2012.
55. D. Aradilla, F. Estrany, C. Alemán; *J. Appl. Polym. Sci.*, vol. 121, pp. 1982-1991, 2011.
56. G. Fabregat, C. Alemán, M.T. Casas, E. Armelin; *J. Phys. Chem. B*, vol. 116, pp. 5064-5070, 2012.
57. O. Inganäs; *Chem. Soc. Rev.*, vol. 39, pp. 2633-2642, 2010.
58. R.B. Pernites, R.R. Ponnapati, R.C. Advincula; *Adv. Mater.*, vol. 23, pp. 3207-3213, 2011.

3.2 EFFECT OF THE GRAFT RATIO ON THE PROPERTIES OF POLYTHIOPHENE-G-POLY(ETHYLENE GLYCOL)†

3.2.1 Introduction

Graft copolymers made of components with very different properties are receiving increasing attention [1-4]. These kinds of polymers are typically considered as hybrid materials able to amplify the properties of their individual components, exhibiting unusual characteristics because of their confined structure, compact organization and notable chain end effects.

Bottle-brush polymers, also called molecular brushes, are a special class of graft copolymers that usually contain a linear polymer backbone and densely grafted oligomeric side chains [5,6]. The unique self-assembly in solution or melt state and their potential application as nano-, bio-, and photonic-materials have drawn considerable attention [7,8]. Synthetically, such macromolecular architectures can be prepared by three major approaches: (i) -grafting onto, (ii) -grafting from and (iii) - grafting through, each approach having its intrinsic advantages and drawbacks [5]. The concept of brush polymers has been employed in the synthesis of conjugated polymers to increase solubility, as well as to demonstrate unique optical properties and morphology control [9,10].

Among bottle-brush copolymers, those formed by semiconducting conjugated PTh backbone and isolating polymers have been prepared in an attempt to combine different interesting properties in one material and to achieve multifunctional polymers. For example, the very limited solubility and processability of unsubstituted PTh has been improved by grafting polystyrene [11,12] poly(methyl acrylate) [13] or PEG [14] to the polyheterocyclic backbone. Grafting strategies have been also used to develop thermochromic polymers by anchoring thermoresponsive poly(N-isopropylacrylamide) and PEG on PTh backbone [15,16] as well as donor-

†*Results discussed in section 3.2 were published in J. Polym. Sci., Part B: Polym. Phys., 2015, 53, 239-252.*

π-acceptor molecular species by preparing PTh-*graft*-(styrene-*graft*-C_{60}) copolymers [17].

Most of the above-mentioned example of PTh bottle-brush copolymers were obtained by "grafting from" methods using chemical polymerization. Similar architectures were also reported by employing the same method but via electrochemical polymerization [18,19]. The "grafting through" approach for synthesis of molecular brushes offer the advantage of well-defined grafting density and side chain length, defect-free polymer structure, and even easy access to block copolymer synthesis [10,11]. Tacking in account these emphasized advantages, amphiphilic bottle-brush copolymers formed by anchoring PEG side chains to conjugated PTh backbone has been very recently prepared by using the "grafting through" approach via electrochemical or chemical polymerization [20,21]. Their suitability for various biotechnological and biomedical applications was demonstrated, as well. More specifically, macromonomers consisting of a pentathiophene sequence in which the central ring bears a PEG chain with M_w of 1000 or 2000 at the 3-position (Th_5-PEG_{1000} or Th_5-PEG_{2000}, respectively) were prepared by chemical synthesis and subsequently polymerized by potentiostatic methods, giving rise to PTh_5-*g*-PEG_{1000} or PTh_5-*g*-PEG_{2000}, respectively (Figure 3.2.1) [20].

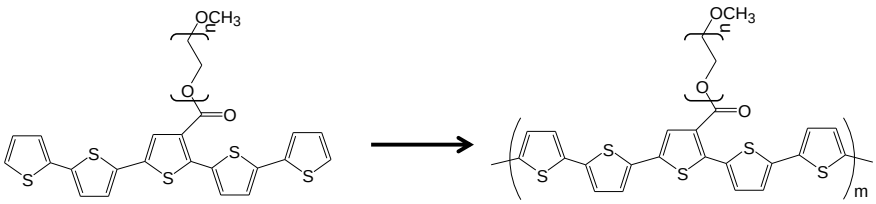

Th_5-PEG_{1000} (n= 22) PTh_5-*g*-PEG_{1000} (n= 22)

Th_5-PEG_{2000} (n= 42) PTh_5-*g*-PEG_{2000} (n= 42)

Figure 3.2.1 Macromonomers and grafted copolymers studied in Ref. 20.

The influence of the polymerization potential, the length of the PEG branches and the dopant agent on the structure and properties of these graft copolymers was carefully examined [20]. Results indicated that the two

PTh_5-*g*-PEG_n derivatives tend to undergo a high number of anodic oxidation processes, which give place to the formation of charged species. In order to take profit of the distribution of charged species on the surface, the performance of these materials as active surfaces for the selective adsorption of proteins was tested. As it was expected, the affinity of these materials, especially PTh_5-*g*-PEG_{2000}, towards globular proteins is higher than towards fibrillar proteins [20].

More recently, the ability of the PTh_5-*g*-PEG_n copolymers as cellular matrices was investigated [22], their behavior being significantly better than that reported for other biocompatible CPs, as for example PEDOT [23]. This result was fully consistent with the hydrophilicity observed for the graft copolymers [22], which increases with the molecular weight of the PEG chain, and with the biphasic molecular organization predicted by atomistic molecular dynamics simulations [22]. The behavior as bioactive matrices for cell viability was also proved by copolymers obtained by Suzuki polycondensation [21].

In this work we take advantage of a new macromonomer to investigate the effect of the PEG / Th ratio in the properties of graft copolymers made of PEG attached to PTh (PTh_n-*g*-PEG). More specifically, the synthesis and characterization of a macromonomer made of α-terthiophene (Th_3) bearing a PEG chain of M_W= 2000 at the 3-position of the central heterocycle (Th_3-PEG_{2000}, Figure 3.2.2), was recently reported by some of us [24].

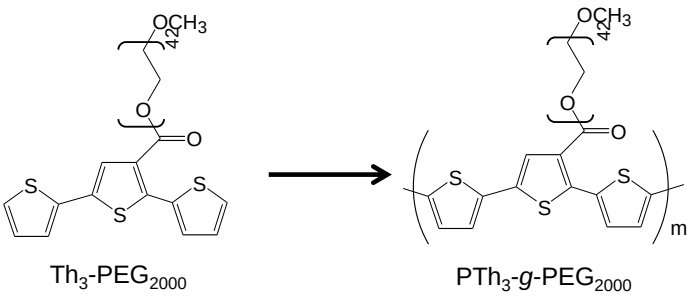

Figure 3.2.2 Macromonomer used in this work and grafted copolymer expected from its anodic polymerization.

Although our first aim was to increase the PEG / Th ratio of graft copolymers by preparing PTh_3-*g*-PEG_{2000} (Figure 3.2.2), anodic polymerization of Th_3-PEG_{2000} was completely unsuccessful even varying the experimental conditions (i.e. solvents, electrolyte, electrode, potential, etc) with respect to those used for PTh_5-g-PEG_{2000} [20,21]. This drawback was attributed to the steric effects provoked by the PEG chain at the reactive positions of the thiophene rings, which make difficult the polymerization process and preclude the formation of a homogeneous and stable film. In order to overcome this limitation, we have added Th_3 to the polymerization medium (Figure 3.2.3). The graft copolymer derived from the anodic copolymerization of Th_3-PEG_{2000} and Th_3, which has been denoted PTh_3*-*g*-PEG_{2000}, presents a PEG / Th ratio significantly lower than that of PTh_5-*g*-PEG_{2000}.

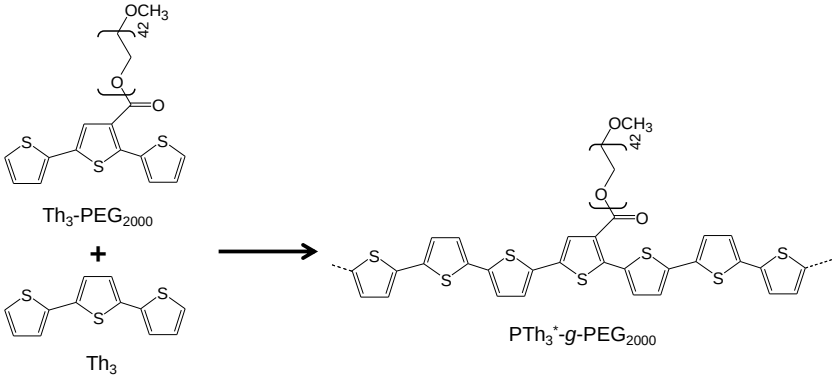

Figure 3.2.3 Chemical structure of PTh_3*-*g*-PEG_{2000}.

In this work we evaluate the properties of PTh_3*-*g*-PEG_{2000} comparing them not only with those obtained for PTh_5-*g*-PEG_{2000} but also with those of poly(α-terthiophene) (PTh_3). More specifically, surface (morphology, topography and wettability) and bulk properties (optical and electrochemical) of PTh_3*-*g*-PEG_{2000} and PTh_3 prepared under identical experimental conditions have been investigated. Furthermore, the cytotoxicity, biocompatibility and electrocompatibility of PTh_3*-*g*-PEG_{2000} have been examined to analyze the potential advantages of this copolymer with respect to PTh_5-*g*-PEG_{2000} in biomedical applications.

3.2.2 Methods

Materials

All used solvents were purified and dried by usual methods. PEG with M_w=2000 (Aldrich), 3-thiophene carboxylic acid (Aldrich), 2-thiophene boronic acid (Aldrich), N,N'-dicyclohexylcarbodiimide (Merk), 4-dimethylamino pyridine (Aldrich), $Pd(PPh_3)_4$ (Aldrich), anhydrous lithium perchlorate (Sigma-Aldrich) and 2,2':5',2"-Terthiophene (99%, Aldrich) were used as received.

For cell culture experiments, Cos-7 cells were purchased from ATCC (USA). Dulbecco's PBS without calcium chloride and magnesium chloride, DMEM (supplemented with 4500 mg of glucose/L, 110 mg of sodium pyruvate/L and 2 mM L-glutamine), penicillin-streptomycin, MTT (97.5%) and trypsin-EDTA solution (0.05% trypsin, 0.02% EDTA) were all purchased from Sigma-Aldrich (USA). Fetal bovine serum (FBS) and trypan blue stain (0.4%) were purchased from Gibco, UK. Dimethyl sulfoxide (99.0%) was purchased from Panreac Quimica S.A.U. (Spain) and sodium azide (NaN_3, ≥99.5%) from Sigma-Aldrich (USA).

For protein adsorption, collagen solution type I from calf skin (0.1% solution in 0.1 M acetic acid) was purchased from Sigma-Aldrich.

Synthesis and characterization of macromonomers

By using the synthetic strategy already reported [24], Th_3-PEG_{2000} macromonomer was synthesized using the chemical route presented in figure 3.2.4. The ^{1}H-NMR spectrum of Th_3-PEG_{2000} in acetone-d_6 was in excellent agreement with that already reported [24].

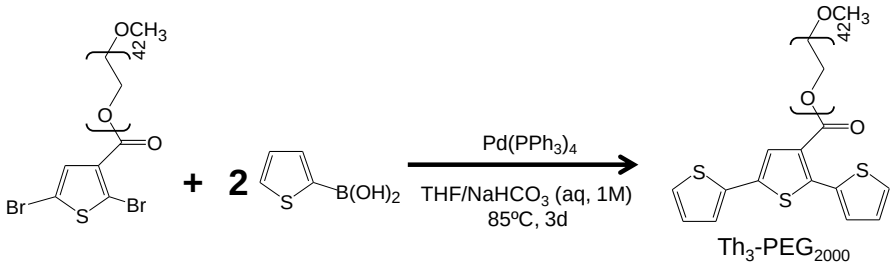

Figure 3.2.4 Chemical route for the synthesis of Th_3-PEG_{2000}.

Polymerization

All electrochemical assays, including polymerizations, were carried out in a standard three electrode cell of 50 mL under nitrogen atmosphere (99.995% in purity) at room temperature. The anodic compartment was filled with 10 mL of a 1mM acetonitrile solution of Th_3-PEG_{2000}:Th_3 mixture containing 0.1 M $LiClO_4$ as supporting electrolyte, while the cathodic compartment was filled with 10 mL of the same electrolyte solution. Steel AISI 316 sheets of 2 cm^2 area (surface roughness determined by AFM: 11.4 Å) were employed as working and counter electrodes. The reference electrode was an Ag|AgCl electrode containing a KCl saturated aqueous solution (E^0 = 0.222 V at 25ºC), which was connected to the working compartment through a salt bridge containing the electrolyte solution.

PTh_3*-*g*-PEG_{2000} films were prepared by CA using a constant potential of 1.0 V and considering two Th_3-PEG_{2000}:Th_3 weight ratios (75:25 and 50:50). After trials using different polymerization times (t = 300, 400 and 500 s), all PTh_3*-*g*-PEG_{2000} films for analyses were prepared using t = 400 s. PTh_3 films were prepared using the same experimental conditions but

considering a 1mM Th_3 acetonitrile solution with 0.1 M $LiClO_4$ as the generation medium.

Contact profilometry

The thickness of the films was determined using a Dektak 150 stylus profilometer (Veeco, Plainview, NY). Different scratches were intentionally provoked on the films and measured to allow statistical analysis of data. Imaging of the films was conducted using the following optimized settings: tip radius= 2.5 μm; stylus force= 1.5 mg; scan length= 1 μm; and speed= 1.5 nm/s. The thickness was measured using two different items:

- the vertical distance (VD), which corresponds to the difference between the height polymer and the height of the steel substrate without any average;
- the average step height (ASH), which measures the difference between the average height of the polymer and the average height of the steel substrate.

X-Ray photoelectron spectroscopy

XPS analyses were performed in a SPECS system equipped with a high-intensity twin-anode X-ray source XR50 of Mg/Al (1253 eV / 1487 eV) operating at 150 W, placed perpendicular to the analyzer axis, and using a Phoibos 150 MCD-9 XP detector. The X-ray spot size was 650 μm. The pass energy was set to 25 and 0.1 eV for the survey and the narrow scans, respectively. Charge compensation was achieved with a combination of electron and argon ion flood guns. The energy and emission current of the electrons were 4 eV and 0.35 mA, respectively. For the argon gun, the energy and the emission current were 0 eV and 0.1 mA, respectively. The spectra were recorded with a pass energy of 25 eV in 0.1 eV steps at a pressure below 6×10^{-9} mbar. These standard conditions of charge compensation resulted in a negative but perfectly uniform static charge.

The C 1s peak was used as an internal reference with a binding energy of 284.8 eV. The surface composition was determined using the manufacturer's sensitivity factors.

FTIR spectroscopy

FTIR spectra were recorded on a Nicolet 6700 spectrophotometer. For this purpose, films were scrapped off from the electrode and dried under vacuum. FTIR spectra were recorded using KBr discs at a 6 cm^{-1} resolution (60 scans).

Scanning electron microscopy

SEM studies were performed to investigate the effect of the applied synthetic approach on the surface morphology of the films. Dried samples were placed in a Focussed Ion Beam Zeiss Neon 40 scanning electron microscope operating at 5 kV, equipped with an EDX spectroscopy system.

Atomic force microscopy

Topographic images were obtained with an AFM Dimension 3100 microscope and an AFM MultimodeTM microscope using a NanoScope IV controller (Bruker) under ambient conditions in tapping mode. The RMS roughness (R_q), which is the average height deviation taken from the mean data plane, was determined using the statistical application of the NanoScope Analysis software (1.20, Veeco). AFM measurements were performed on various parts of the films, which produced reproducible images similar to those displayed in this work. The scan window size was 5×5 μm^2.

Wettability

Contact angle measurements were obtained using the sessile water drop method at room temperature and controlled humidity. Images of 5 µL distillated water drops on the nanomembrane surfaces were recorded after stabilization (10 s) with the equipment OCA 20 (DataPhysics Instruments GmbH, Filderstadt). The software SCA20 was used to analyze the images and acquire the contact angle value. Contact angle values were obtained as the average of 10 independent measures for each sample.

UV-vis spectroscopy

Spectra of PTh_3*-*g*-PEG_{2000} and PTh_3 films were obtained using a UV-vis-NIR Shimadzu 3600 spectrophotometer equipped with a tungsten halogen visible source, a deuterium arc UV source, a photomultiplier tube UV-vis detector, and an InGaAs photodiode and cooled PbS photocell NIR detectors. Spectra were recorded in the absorbance mode using the integrating sphere accessory (model ISR-3100), the wavelength range being 185-3300 nm. The interior of the integrating sphere was coated with highly diffuse $BaSO_4$ reflectance standard. Uncoated ITO glass was used as reference. Films were deposited on ITO-glass electrodes for measurements. Single-scan spectra were recorded at a scan speed of 60 nm/min. Measurements, data collection and data evaluation were controlled by the computer software UVProbe version 2.31.

Electrochemical properties

The electroactivity and electrostability were studied by CV using a 0.1 M PBS solution (pH= 7.4 adjusted with NaOH). The initial and final potentials were –0.40 V, and the reversal potential was 0.80 V. A scan rate of 50 mV/s was used in all cases. The electroactivity and electrostability were determined through direct measure of the anodic and cathodic areas in the control voltammograms using the GPES software.

Cytotoxicity, cellular adhesion and cellular proliferation

All cellular assays were performed using Cos-7 cells, which are fibroblast-like, from monkey kidney. These carcinogenic cells were selected due to their fast growth. Cells were cultured in DMEM high glucose supplemented with 10% FBS, penicillin (100 units/mL), and streptomycin (100 µg/mL). The cultures were maintained in a humidified incubator with an atmosphere of 5% CO_2 and 95% O_2 at 37ºC. Culture media were changed every two days. When the cells reached 80-90% confluence, they were detached using 1-2 mL of trypsin (0.25% trypsin/EDTA) for 5 min at 37 °C. Finally, cells were re-suspended in 5 mL of fresh medium, their concentration was determined by counting with a Neubauer camera using 0.4% trypan blue as a vital dye.

PTh_3*-*g*-PEG_{2000} (75:25 and 50:50 Th_3-PEG_{2000}:Th_3) and PTh_3 deposited onto steel AISI 316 sheets of 1 cm^2 were placed in plates of 24 wells and sterilized using UV irradiation for 15 min in a laminar flux cabinet. Controls for cytotoxicity were simultaneously performed by culturing cells on the surface of the TCPS plates and steel plates, whereas steel plates were the only control for adhesion and proliferation assays. For cytotoxicity and adhesion assays, an aliquot of 50 µL containing 5×10^4 cells was deposited on the nanomembrane of each well. Then, cell attachment to the nanomembrane surface was promoted by incubating under culture conditions for 30 min. Finally, 500 µL of the culture medium were added to each well. After 24 h, all cells in the well were quantified to evaluate the cytotoxicity of the materials, whereas cellular adhesion was determined by quantifying exclusively the cells attached to PTh_3*-*g*-PEG_{2000}, PTh_3 or the control. For proliferation assays, the 50 µL aliquots deposited on each well contained 2×10^4 cells. Quantification of viable cells onto the evaluated materials was performed after 72 hours of culture.

Cell adhesion and viability were evaluated by the colorimetric MTT assay, which determines the cell viability [25]. This assay measures the ability of the mitochondrial dehydrogenase enzyme of viable cells to cleave the tetrazolium rings of the MTT and form formazan crystals, which are impermeable to cell membranes and, therefore, are accumulated in

healthy cells. This process is detected by a color change: the characteristic pale yellow of MTT transforms into the dark-blue of formazan crystals. Specifically, 50 mL of MTT solution (5 mg/mL in PBS) were added to each well. After 3 h of incubation, samples were washed twice with PBS and stored in clean wells. In order to dissolve formazan crystals, 1 mL of DMSO/methanol/water (70/20/10 % v/v) was added. Finally, the absorbance at 540 mm was measured using a UV-vis spectrophotomether (UV-3600, Shimadzu). The resulting viability results were normalized to TCP control as relative percentages. Results were derived from the average of four replicates (n= 4) for each independent experiment.

The toxicity of the Th_3 monomer was determined using Cos-7 cells. From a stock 100×10^{-3} M monomer solution in acetonitrile concentrations ranging from 0.2×10^{-3} to 20×10^{-3} M in culture medium were prepared by dilution. Experiments were carried out at 96-wells plates. An aliquot of 50 mL of 2×10^5 cells/mL was seeded at each well and 50 mL of monomer solution was added to reach a final volume of 100 mL in each well with monomer concentrations ranging from 0.1 to 10×10^{-3} M. Controls were run at the same plate without monomer (zero concentration) and with acetonitrile as solvent control. The cells were maintained in culture for 24 h. After this, the MMT assay was used to determine the cell viability.

Adsorption of collagen

We have used a 0.1% (1 mg/mL) solution of calf skin collagen in 0.1 M acetic acid (Sigma-Aldrich). A thin protein layer coating was deposited onto the surface of PTh_3*-*g*-PEG_{2000} and PTh_3 films to facilitate the attachment of anchorage-dependent cells. For this purpose, films were placed into a culture plate of 24 wells, and sterilized by exposure to UV light during 15 min. The collagen solution (1 mg/mL) was diluted 10-fold with sterile water to obtain a working concentration of 0.01%. Then, films were superficially coated with 10 µg/cm^2. In order to facilitate the binding of the collagen to the films, materials were incubated overnight at 37 °C. The excess of fluid was removed from the coated surface, and allows it to

dry overnight at room temperature in the laminar flux cabinet. Finally, the coated films were rinsed with PBS before seeding cells onto the matrix for evaluated the cytoxicity and cellular adhesion.

Statistical analyses

The statistical analysis was performed by one-way ANOVA followed by Tukey's test. The analyses were performed with a confidence level of 95% ($p<0.05$)

3.2.3 Results and discussion

Preparation of PTh_3^*-*g*-PEG_{2000}

Independently of the polymerization time, as prepared PTh_3*-g-PEG_{2000} and PTh_3 films doped with ClO_4^- showed brownish orange and dark blue color, respectively, which represent a significant difference with respect to the intense yellow color of PTh_5-*g*-PEG_{2000} prepared with the same dopant [22]. All these materials were completely insoluble, as is usual in polymers prepared by anodic polymerization. The thickness of PTh_3^*-*g*-PEG_{2000} and PTh_3 films was determined by profilometry, results considering the VD and ASH procedures being fully consistent (Table 3.2.1).

Samples	PTh_3	PTh_3*-*g*-PEG_{2000} (75:25)	PTh_3*-*g*-PEG_{2000} (50:50)
As prepared	924±67/ 933±31	902±161/ 883±172	829±76/ 818±43
After 10 redox cycles	863±71 / -	731±79 / -	706±58 / -
Δ[a]	7.1%	18.9%	14.8%

[a] Porosity was quantified through the parameter Δ calculated as the variation of the thickness before applying any redox cycles and after 10 consecutive redox cycles relative to the thickness of the as prepared samples.

Table 3.2.1 Average thickness (in nm) determined by contact profilometry using the VD / ASH procedure and porosity (in %) for PTh_3 and PTh_3*-*g*-PEG_{2000} prepared using different Th_3-PEG_{2000}:Th_3 ratios in the generation medium.

The thickness of all films was around 0.9±0.1 μm, independently of the content of Th_3-PEG_{2000} units. This value is noticeably higher than that reached for PTh_5-*g*-PEG_{2000} using a polymerization time of 1500 s and a potential of 0.75 V (i.e. 109±5 nm) [23], which is fully consistent with the poor polymerizability of Th_3-PEG_{2000} macromonomers.

Sample	C1s	O1	Cl2p	S2p
PTh_3*-*g*-PEG_{2000} (75:25)	67.82	14.66	4.08	13.44
PTh_3*-*g*-PEG_{2000} (50:50)	72.44	9.12	2.43	16.01
PTh_3	66.70	12.49	3.87	16.94

Table 3.2.2 Atomic percent composition (C_{1s}, O_{1s}, Cl_{2p} and S_{2p}) obtained by XPS for 75:25 and 50:50 PTh_3*-*g*-PEG_{2000} graft copolymers and PTh_3 (Eqn. 3.2.4).

Table 3.2.2 compares the atomic percent compositions obtained for PTh_3*-*g*-PEG_{2000} and PTh_3 using XPS (Figure 3.2.5). The C/S ratio obtained for PTh_3 (3.9) is in good agreement with the expected value (4.0). However, the C/S ratio of the two PTh_3*-*g*-PEG_{2000} copolymers (5.0 and

4.5 for 75:25 and 50:50, respectively) is considerably closer to that expected for PTh_3 than to that of PTh_3-*g*-PEG_{2000} (32.7), corroborating the difficulties associated to the polymerization of Th_3-PEG_{2000} macromonomers. These values confirm that the content of Th_3 units is higher for the 50:50 copolymer than for the 75:25 one. On the other hand, the Cl/S ratio of PTh_3-*g*-PEG_{2000} (0.30 and 0.15 for 75:25 and 50:50, respectively) and PTh_3 (0.23) reflect that the doping level is relatively low in all cases, especially for the systems with a higher content of Th_3 units.

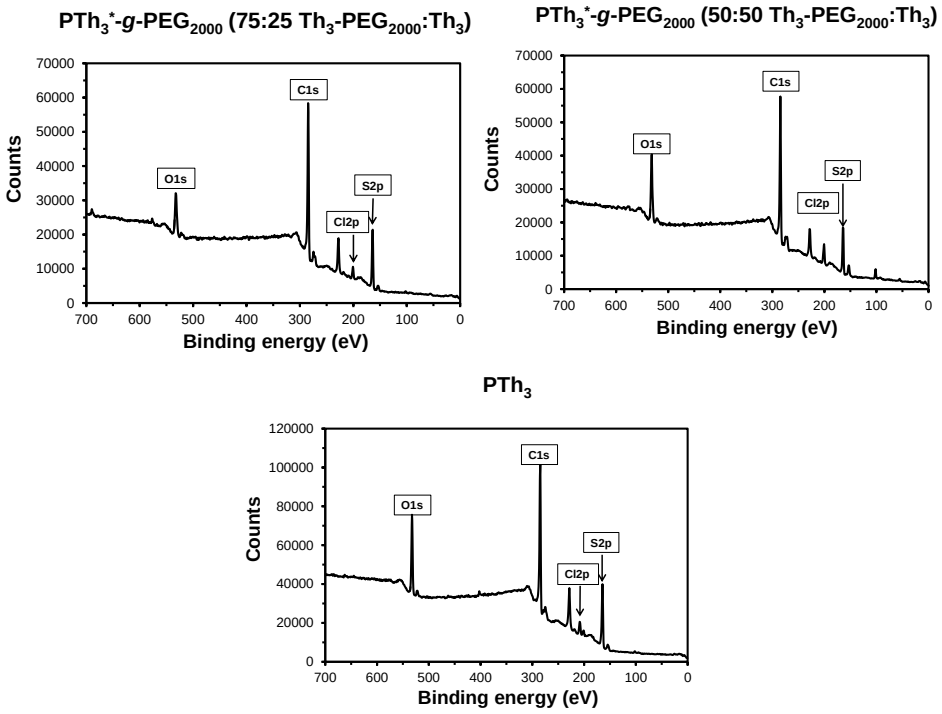

Figure 3.2.5 XPS spectra of PTh_3*-*g*-PEG_{2000} graft copolymers prepared using 75:25 and 50:50 Th_3-PEG_{2000}:Th_3 ratios and of PTh_3.

The FTIR spectra of PTh_3*-*g*-PEG_{2000} and PTh_3 are displayed in figure 3.2.6. The C^{α}–H out of plane ring deformation absorption in the spectrum of PTh_3 is detected at 735 cm^{-1} as a shoulder only, proving that the polymerization of Th_3 mainly involves linkages at the α–α' positions (i.e. PTh_3 chains tend to grow linearly). This is consistent with the absorption shoulder detected at 3070 cm^{-1} for PTh_3, which also evidences a low

fraction of hydrogen atoms at the C^{α}-position of the Th ring. These shoulder are not observed for the PTh_3*-*g*-PEG_{2000} copolymers. The peak at 791 cm^{-1} corresponds to the C^{β}–H out of plane bending modes. The absorption intensity at 1630 cm^{-1} has been attributed to the C=C stretching vibration of the Th ring, reflecting the conjugation behavior of the polyaromatic backbone. On the other hand, the band at 1120 cm^{-1} corresponds to the ClO_4^- dopant agent.

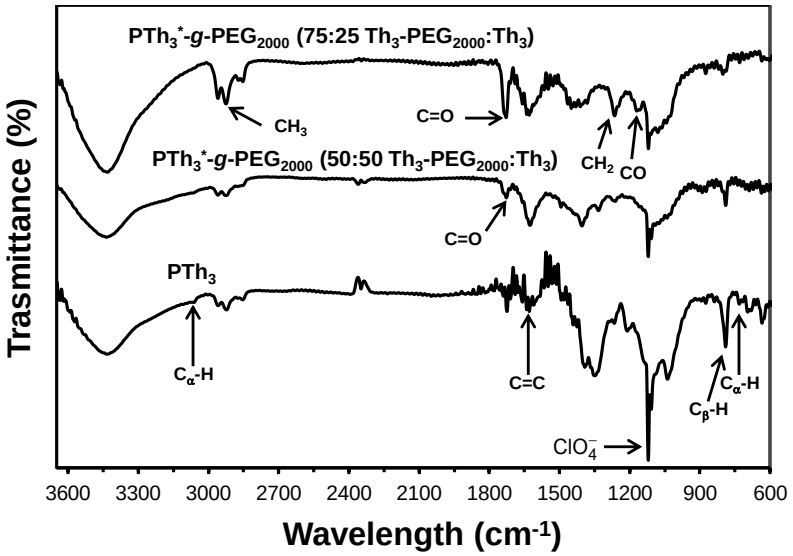

Figure 3.2.6 FTIR spectra of PTh_3 and of PTh_3*-*g*-PEG_{2000} graft copolymers prepared using 75:25 and 50:50 Th_3-PEG_{2000}:Th_3 ratios.

The absorptions originating from the PEG component, which are similar to those reported for PTh_5-*g*-PEG_{2000} [20], appear at 2925 cm^{-1} (antisymmetric CH_3), 1402 and 1327 cm^{-1} (CH_2 wagging), 1265 cm^{-1} (CH_2 twisting) and 1160 cm^{-1} (υ_{CO}). The peak associated to the C=O group of the ester linkage between the conjugated PTh chain and the PEG chain has been identified at 1728 cm^{-1}. This peak is more intense for the 75:25 copolymer than for the 50:50 one, proving that the former contains the highest content of polymerized Th_3-PEG_{2000} macromonomer. This feature is fully consistent with the intensity of the antisymmetric CH_3 band at 2925 cm^{-1}, which is also higher for the 75:25 copolymer.

In order to obtain a rough estimation of the composition of the two prepared PTh_5-*g*-PEG_{2000} copolymers, the ratios of the areas associated to the absorptions band at 2925 cm^{-1} (antisymmetric CH_3) and 1630 cm^{-1} (C=C stretching vibration of the Th ring) were evaluated. Results indicate that the copolymers derived from 50:50 and 75:25 Th_3-PEG_{2000}:Th_3 weight ratios present, respectively, ~4 and ~2 Th_3 units per Th_3-PEG_{2000} unit. This estimation is in good agreement with previously discussed XPS observations. Unfortunately, the insolubility of the copolymers precludes a more quantitative determination of their final composition by other techniques, as for example NMR.

Surface properties

The surface morphology of PTh_3*-*g*-PEG_{2000} and PTh_3 films was examined by SEM (Figure 3.2.7). Low and medium resolution micrographs reveal the formation of agglomerates onto the surface of PTh_3*-*g*-PEG_{2000} films, perturbing the very compact aspect detected at the level surface of graft copolymer films. The frequency and dimensions of these aggregates increase with the content of Th_3 in the generation medium, which is corroborated by examining the surface morphology of PTh_3 films (Figure 3.2.7). Thus, PTh_3 shows a very high concentration of large aggregates at the surface. High resolution SEM micrographs (Figure 3.2.7) indicate that the texture of these aggregates is similar to that of the levelled surface for PTh_3. In contrast, the textures of the levelled surface and the aggregates deposited onto it are very different for PTh_3*-*g*-PEG_{2000} films, this feature being especially remarkable for copolymer derived from the 75:25 ratio.

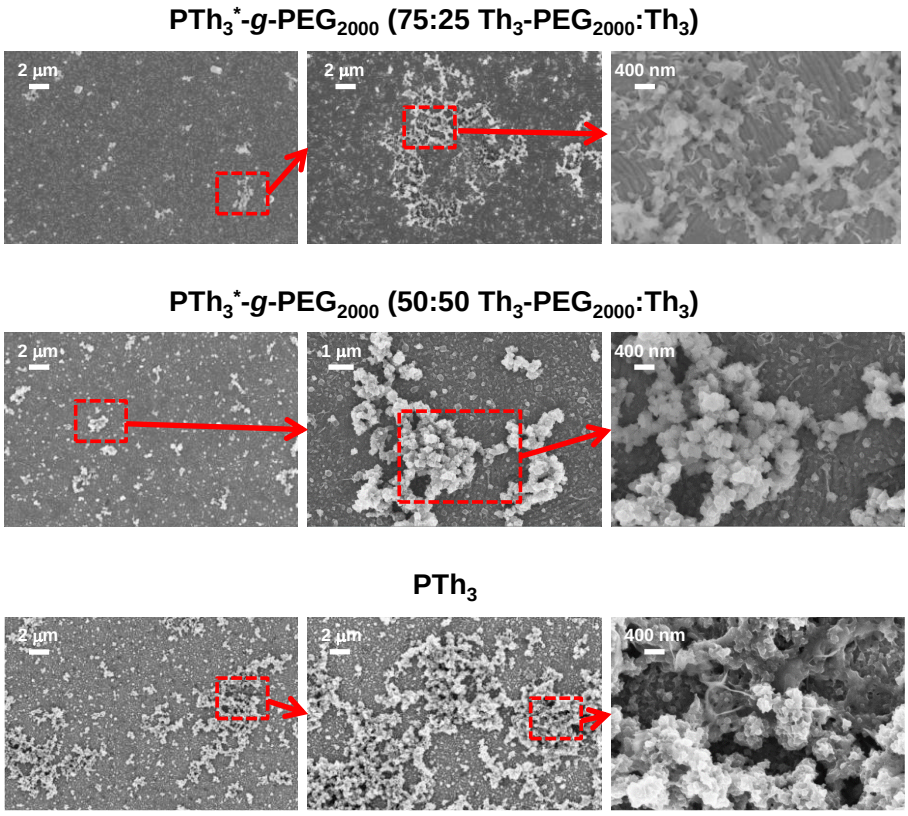

Figure 3.2.7 Low, medium and high resolution SEM micrographs of PTh_3*-*g*-PEG_{2000} (75:25 and 50:50 Th_3-PEG_{2000}: Th_3) and PTh_3.

2D and 3D AFM height images are displayed in figure 3.2.8. The topography of the 75:25 PTh_3*-*g*-PEG_{2000} film consists on a distribution of sharp, narrow and relatively low peaks. Both the width and height of these peaks increase significantly in the 50:50 PTh_3*-*g*-PEG_{2000} film, which has been attributed to the incorporation of the Th_3 macromonomers. This provokes a significant enhancement of R_q, which increases from 56±35 to 74±15 nm with the concentration of Th_3 in the generation medium. These features are magnified in PTh_3 films, which show not only the widest and highest peaks but also an R_q= 137±52 nm. The overall of these results, which are in very good agreement with previous SEM observations, suggest that Th_3 units do not incorporate homogeneously. Indeed, the roughness determined for PTh_5-g-PEG_{2000} films was of only R_q= 12.1±2.1 nm.

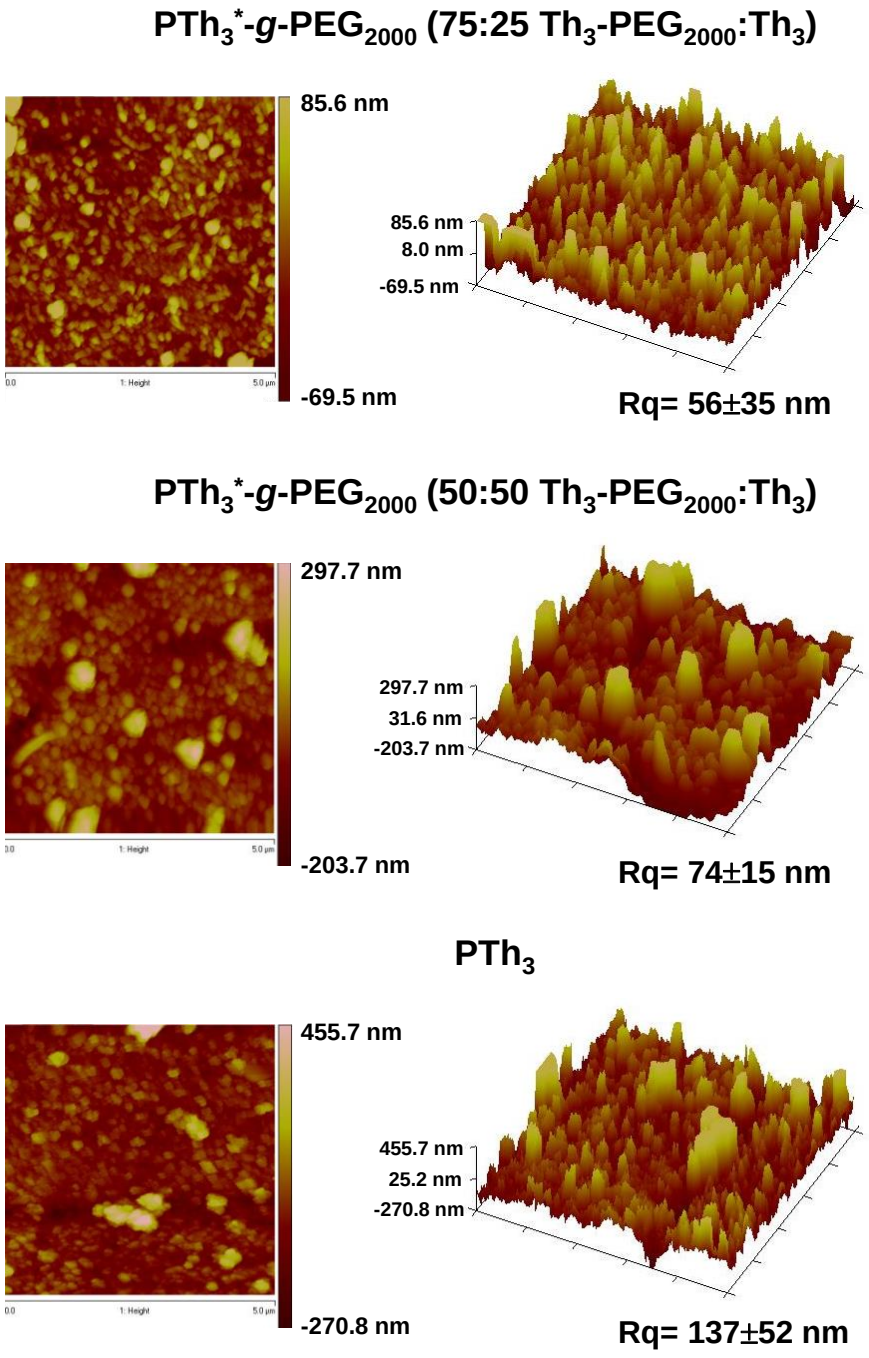

Figure 3.2.8 AFM height image of PTh_3*-*g*-PEG_{2000} (75:25 and 50:50 Th_3-PEG_{2000}: Th_3) and PTh_3.

Contact angle values determined for 50:50 PTh_3*-*g*-PEG_{2000} and PTh_3 are 90º±4º and 89º±2º, respectively, evidencing the hydrophobic nature of the thiophene rings. These values suggest that the 50:50 copolymer incorporates a high amount of Th_3 at the latter steps of the electrochemical polymerization process, hydrophilic PEG chains remaining inside the films. In contrast, the contact angle obtained for 75:25 PTh_3*-*g*-PEG_{2000}, 67º±5º, indicates an enhancement of the surface hydrophilicity due the PEG chains. The contact angle reported for PTh_5-g-PEG_{2000}, 76º±5º [22], is intermediate between those measured for 75:25 and 50:50 PTh_3*-*g*-PEG_{2000} films.

Optical and electrochemical properties

Figure 3.2.9a compares the UV-vis spectra of 75:25 and 50:50 PTh_3*-*g*-PEG_{2000}. The shapes of the two spectra are similar, showing a broad absorption band with λ_{max} at 458 and 501 nm, respectively. This band, which corresponds to the π-π* transition, have been used to approximate the optical π-π* lowest transition energy (ε_g) by estimating the onset wavelength (λ_{onset}= 573 and 566 nm for the 75:25 and 50:50 copolymer respectively), the resulting values being 2.16 (75:25) and 2.19 eV (50:50). These ε_g gaps are slightly lower than those reported for PTh_5-*g*-PEG_{1000} and PTh_5-*g*-PEG_{2000} doped with ClO_4^- (2.25 and 2.29 eV, respectively), which were estimated using the same methodology [22]. Accordingly, the π-electron delocalization in graft copolymers made of PTh and PEG increases with decreasing PEG / Th ratio.

The UV-vis spectrum recorded for PTh_3 is included in Figure 25. The ε_g estimated for π-π^* lowest transition energy (λ_{max}= 458 nm) is 2.28 eV (λ_{onset}= 543 nm). This gap is higher than those described for PTh derivatives with small substituents at the β-position (e.g. poly(thiophene-3-methyl acetate), 1.98-2.17 eV [26]; poly(3-chlorothiophene), 2.14 eV [27]; and poly(3-bromothiophene), 1.93-1.97 eV [28]). This feature suggests that Th_3 repeat units may polymerize forming, in addition to the expected α-α linkages, α-β and/or β-β linkages. On the other hand, the

PTh_3 spectrum shows a broad absorption tail between ~500 and ~700 nm ascribed to the polaronic band of the conductive quinoid form. This is considerably smaller for the 50:50 graft copolymer and practically inappreciable for the 75:25 one.

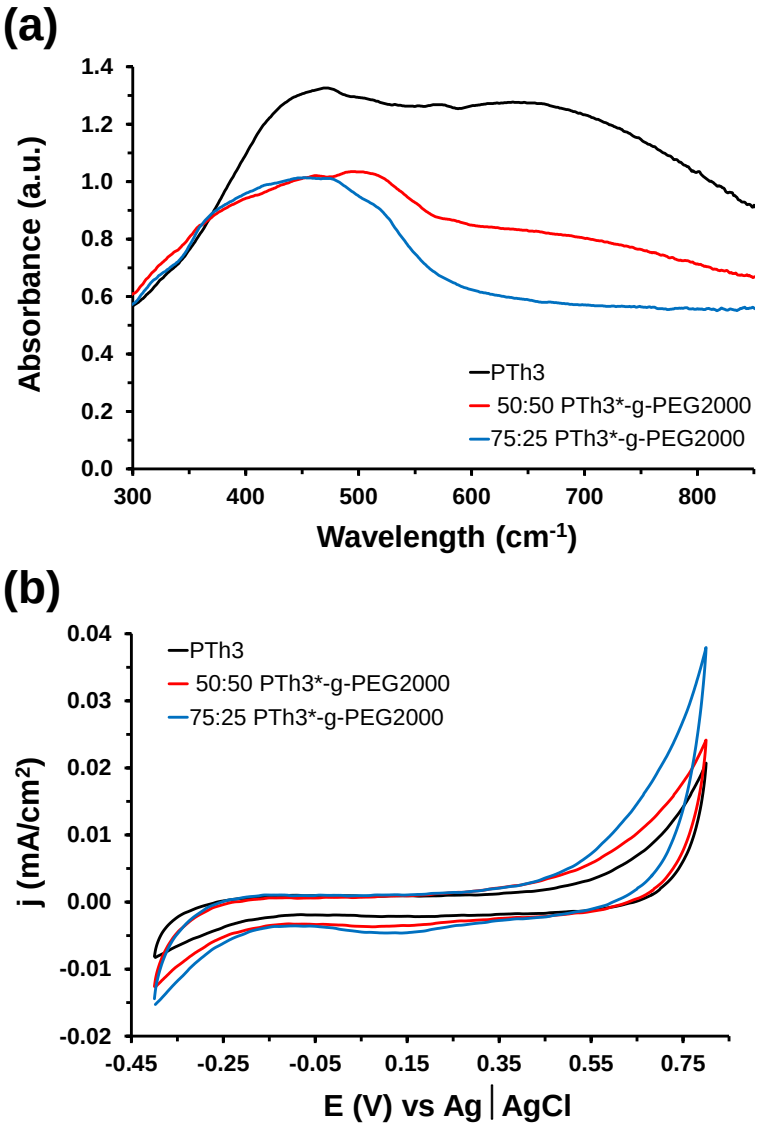

Figure 3.2.9 (a) UV-vis spectra and (b) cyclic voltammograms in PBS of PTh_3*-*g*-PEG_{2000} (75:25 and 50:50 Th_3-PEG_{2000}: Th_3) and PTh_3 doped with ClO_4^-.

Figure 3.2.9b compares the cyclic voltammograms recorded for PTh_3*-*g*-PEG_{2000} and PTh_3. The 75:25 PTh_3*-*g*-PEG_{2000} copolymer shows the highest electrochemical activity (electroactivity), which refers to the ability to exchange charge reversibly and increases with the similarity between the anodic and cathodic areas. Thus, the electroactivity of PTh_3 and 50:50 PTh_3*-*g*-PEG_{2000} is around 30% and 20% lower than that of the 75:25 graft copolymer. This feature may be attributed to two different reasons:

- the conjugation length in PTh_3 is relatively small due to the formation of cross-linking (i.e. polymer chains grow not only through α-α linkages between units but also through α-β and β-β linkages);
- the structure becomes more compact with increasing amount of Th_3 units, making more difficult the access and escape of the dopant ions into the dopant ions during the redox processes.

The degree of cross-linking is typically determined by the number of electrons consumed to incorporate a monomer into the polymer and to oxidize the resulting chain (n_{ox}), this information being determined through the electropolymerization kinetics (i.e. by considering different polymerization for the generation of polymer films under a constant potential) [29,30]. After discounting the oxidation charge used to compensate the charge of the dopant ion (i.e. doping level), the average number of electrons per monomer (n_{av}) incorporated into a linear polymer chain obtained from a typical condensation should be $n_{av} \approx 2.0$ (i.e. two protons and two electrons are involved in the formation of the α-α bond between the terminal repeat unit of the chain and the incorporated monomer [29,30]. Thus, cross-links are proved when $n_{av} > 2.0$.

The value of n_{ox} for PTh_3 has been determined using the following equation [29,30]:

$$n_{ox} = \frac{MQ_{pol}}{FW_{ox}(1 - W_{dop})} \qquad \text{(Eqn. 3.2.1)}$$

where M is the molar mass of PTh_3, Q_{pol} is the polymerization charge consumed in each process (in mC/cm^2) calculated from the chronoamperograms, F is the Faraday constant, W_{ox} is the film weight (in mg/cm^2) and W_{dop} is the mass of ClO_4^- per polymer unit of mass. The doping level (DL) of PTh_3 and, therefore, W_{dop} were estimated electrochemically using the following equation:

$$DL = \frac{2Q_0}{Q_D - Q_0} \times 100 \qquad \text{(Eqn. 3.2.2)}$$

where Q_D is the total charge used for the nanocomposite deposition and Q_0 is the total charge of oxidized species in the nanocomposite films. The value of dl is used to obtain n_{av}:

$$n_{av} = n_{ox} - DL \qquad \text{(Eqn. 3.2.3)}$$

The electrochemical doping level for PTh_3 is 0.12, this value being even lower than that roughly estimated by EDX (i.e. 0.23). This corresponds to a ClO_4^- molecule every ~8.3 Th_3 repeat units (i.e. every 25 thiophene rings). On the other hand, the values of n_{ox} and n_{av} are 2.08 and 1.96, respectively. This feature indicates that the PTh_3 matrix is formed by linear chains in which Th_3 units are attached though α-α linkages.

The porosity of PTh_3*-*g*-PEG_{2000} and PTh_3 was quantified through the parameter Δ [32], which is calculated as follows:

$$\Delta = \frac{\ell_0 - \ell_{10}}{\ell_0} \times 100 \qquad \text{(Eqn. 3.2.4)}$$

where ℓ_0 and ℓ_{10} refer to the thickness before applying any redox cycle (as prepared samples) and after 10 consecutive oxidation-reduction cycles, respectively. Although all samples experience a reduction after 10 redox cycles (Figure 3.2.10), the porosity being significantly higher for the graft copolymers (Δ= 18.9% and 14.8% for 75:25 and 50:50 PTh_3*-*g*-PEG_{2000}, respectively) than for PTh_3 (Δ= 7.1%). This remarkable difference, which explains the higher ability to store charge of the copolymers, should be attributed to the molecular architecture of PTh_3*-*g*-PEG_{2000} and PTh_3.

Thus, PTh_3 forms linear chains that adopt a compact aligned disposition due to the geometric constraints associated to the heterocyclic rings [33].

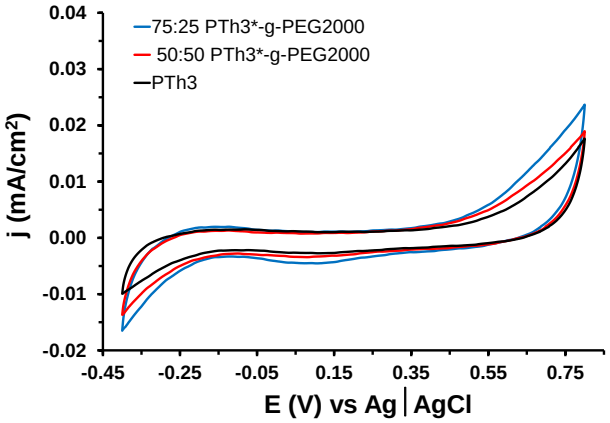

Figure 3.2.10 Cyclic voltammograms recorded after 10 consecutive oxidation-reduction cycles in PBS for PTh_3*-*g*-PEG_{2000} (75:25 and 50:50 Th_3-PEG_{2000}:Th_3 ratios) and PTh_3 films.

In contrast, the grafted architecture of PTh_3*-*g*-PEG_{2000} molecules, in which PEG side chains present coiled or extended conformations depending on environment [22], while PTh backbones adopt a linear disposition, favors an organization with cavities. The cavities of these porous matrices tend to disappear upon aggressive consecutive oxidation-reduction cycles, provoking a significant reduction in the thickness of the films (Table 3.2.1).

The electrochemical stability (electrostability), which has been evaluated through the LEA against the number of oxidation-cycles (Figure 3.2.11), decreases with the oxidation and reduction areas of consecutive control voltammograms. Cyclic voltammograms recorded after 10 consecutive oxidation-reduction cycles (Figure 3.2.10) results in LEA values of 25% and 15% for the 75:25 and 50:50 copolymers, and of 35% for PTh_3. Thus, the compactness of the films increases with the number of redox cycles and, therefore, the access and escape of dopant anions into the polymeric matrix become less favored when the number of these Faradaic processes increases. In spite of this, the most stable material after 10 redox cycles is the 75:25 PTh_3*-*g*-PEG_{2000} copolymer, the electroactivities of 50:50

PTh_3*-*g*-PEG_{2000} and PTh_3 being very similar and ~20% smaller. It is worth nothing that the LEA measured for PTh_5-*g*-PEG_{2000} after 10 redox cycles was of 35% [22], indicating it is less electrostable than 75:25 PTh_3*-*g*-PEG_{2000}.

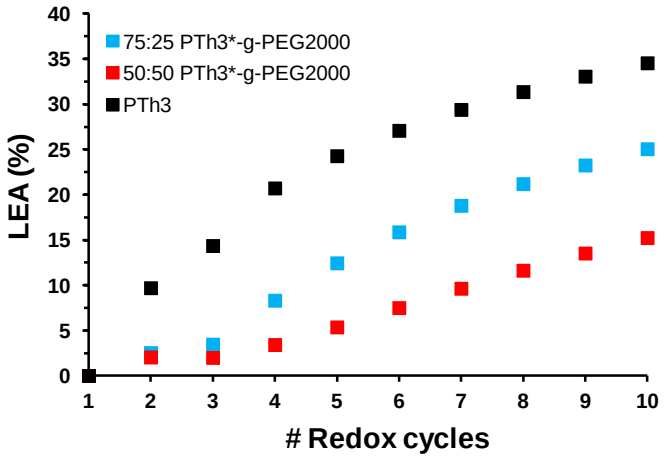

Figure 3.2.11 LEA (in %) against the number of consecutive oxidation-reduction cycles in PBS for PTh_3*-*g*-PEG_{2000} (75:25 and 50:50 Th_3-PEG_{2000}:Th_3 ratios) and PTh_3 films.

Cytoxicity

The potential cytotoxicity of PTh_3*-*g*-PEG_{2000} and PTh_3 was elucidated by culturing Cos-7 cells in plate wells containing steel sheets covered by these organic materials.

Cytotoxicity was determined after 24h using the MTT assay and quantifying all viable cells contained in the wells, which allowed us to consider the toxic effects associated not only to the polymeric matrix but to small molecules (e.g. acetonitrile, monomer and dopant molecules) or oligomers that could be eventually released from the polymeric matrix.

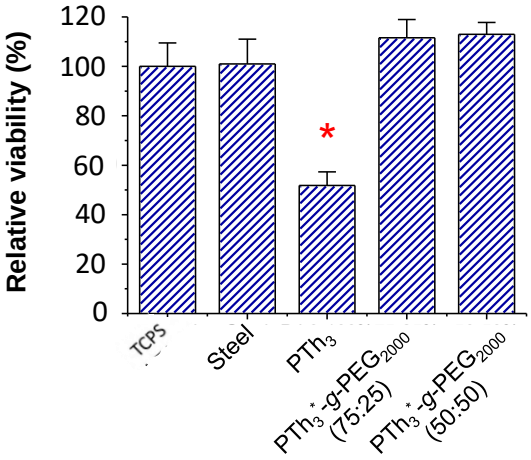

Figure 3.2.12 Cytotoxycity of PTh_3*-*g*-PEG_{2000} (75:25 and 50:50 Th_3-PEG_{2000}: Th_3) and PTh_3 doped with ClO_4^-. Three samples were analyzed for each group. Bars represent the mean standard deviation. The relative viability of Cos-7 cells was established in relation to the TCPS control. Steel was also considered as a control substrate because PTh_3*-*g*-PEG_{2000} and PTh_3 were deposited on this material. The asterisk (*) indicates a significant difference with the control, Tukey's test ($p<0.05$).

Results displayed in Figure 3.2.12 reflect the cytotoxic effects of PTh_3, which reduces the cells viability about 50% with respect TCPS and steel controls. In contrast, this negative effect is not observed for 75:25 and 50:50 copolymers, showing viabilities that are slightly higher than those of the controls This behavior should be attributed to oligomers and medium size harmful molecules that are leaching out from the PTh_3 films. This effect does not occur in PTh_3*-*g*-PEG_{2000} matrices because the size and flexibility of PEG side chains contribute to the immobilization of such medium size components, making difficult or even precluding their delivery to the medium.

In order to check if monomers and small oligomers, which are typically retained in a small fraction within polymeric matrices, may affect the cellular viability if they are released to the culture medium, toxicity curves were determined for Cos-7 cells cultured in presence of the Th_3 monomer during 24 h.

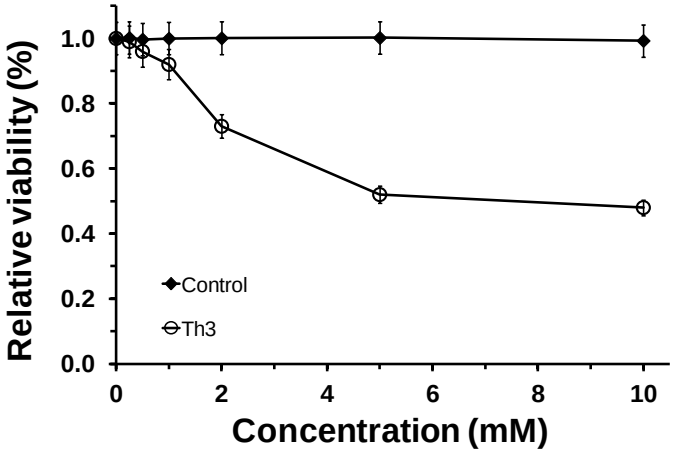

Figure 3.2.13 Toxicity curve for Cos-7 cells of the Th_3 monomer in acetonitrile. The toxicity of the solvent was subtracted from the cytotoxicity of the monomer. Four replicates were analyzed for each concentration of monomers after 24 h of culture. Each point represents the mean ± standard error.

Results, which are displayed in Figure 3.2.13, were obtained by subtracting the toxic effect of the acetonitrile solvent from the curve of the monomer to obtain reliable information about its own toxicity. As it can be seen, the maximum of toxicity is reached when the concentration of Th_3 is around 5×10^{-5} M becoming stable at higher concentrations. The overall of the results obtained in this subsection demonstrates that Cos-7 cells can be cultured on the PTh_3*-*g*-PEG_{2000} copolymers because the PEG chains avoids the exposition of the cells to concentrations of monomer and small oligomer large enough to affect their viability. Unfortunately, this is not possible for possible in PTh_3, which requires from alternative strategies, like that described below, to avoid the release of the entrapped toxic compounds.

Cellular adhesion and proliferation

The biocompatibility of PTh_3*-*g*-PEG_{2000} and PTh_3 was examined by comparing the abilities of these organic matrices to enhance cellular adhesion and proliferation onto the prepared films. In this case steel was considered as the control substrate since polymeric films were directly

deposited on this material. Quantitative results for cellular adhesion are displayed in Figure 3.2.14a. As expected, cellular adhesion on PTh_3 is severely conditioned by the cytotoxicity of this matrix (Figure 3.2.12), relatively viability of Cos-7 cells onto the film after 24 h being very low (~30%). In opposition, quantification of cell adhesion onto 75:25 and 50:50 PTh_3*-*g*-PEG_{2000} films reveals activities of 60% and 70%, respectively, which are higher than those of the steel control substrate.

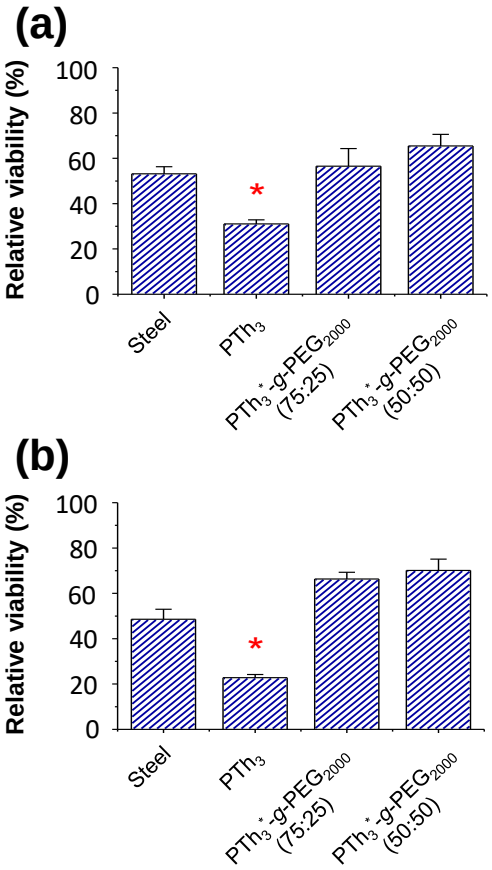

Figure 3.2.14 Cellular adhesion (a) and cellular proliferation (b) on PTh_3*-*g*-PEG_{2000} (75:25 and 50:50 Th_3-PEG_{2000}: Th_3) and PTh_3 films. Three samples were analyzed for each group. Bars represent the mean standard deviation. The relative viability of Cos-7 cells was established in relation to the steel control, which was the substrate used to deposit the films. The asterisk (*) indicates a significant difference with the control, Tukey's test ($p<0.05$).

Cell adhesion affects cell proliferation (Figure 3.2.14b), the number of cells on the surface of the films after 72 h being significantly higher for the two graft copolymers (~70%) than for PTh_3 (~25%). Indeed, the relative viability per unit of area determined for steel (~50%) is also significantly higher than for PTh_3. These results support the negative effect associated to the release of medium size oligomers from the PTh_3 matrix. Comparison of these results with those reported for PTh_5-*g*-PEG_{2000} [22] reveals that PTh_3*-*g*-PEG_{2000} is more biocompatible. Thus, the relative viabilities determined for PTh_5-*g*-PEG_{2000} using steel as the control reference are ~60% and ~65% for cellular adhesion and proliferation assays, respectively. Thus, the biocompatibility of PTh_n-*g*-PEG increases with decreasing PEG / Th ratio. Although PEG is a well-known biocompatible polymer [34,35], the ion exchange ability of the electroactive backbone also plays a crucial role. Therefore, the biocompatibility of PTh_n-*g*-PEG results from the balance between the benefits induced by the PEG side chains and the length of the PTh backbone.

Electrocompatibility

Control voltammograms of PTh_3*-*g*-PEG_{2000} and PTh_3 coated with Cos-7 cells are displayed in Figure 3.2.15a. Comparison with the voltammograms recorded for the uncoated films (Figure 3.2.9b) indicates that cells provoke in all cases a significant increase of the maximum value of anodic current density (j_{max}), which corresponds to that obtained at the reversal potential. More specifically, j_{max} increases from 0.38 / 0.24 to 0.74 / 0.55 mA/cm^2 for 75:25 / 50:050 copolymer films and from 0.21 to 0.47 mA/cm^2 for PTh_3. Moreover, Cos-7 cells enhance considerably the ability of PTh_3*-*g*-PEG_{2000} and PTh_3 films to store charge, even though electroactivity follows the same relative order that without cells: 75:25 copolymer > 50:50 copolymer > PTh_3. More specifically, the electroactivity of PTh_3*-*g*-PEG_{2000} and PTh_3 increases ~165% and ~120%, respectively, upon coating will cells. This feature is consistent with the exchange of ions between the PTh-containing matrix and the cells.

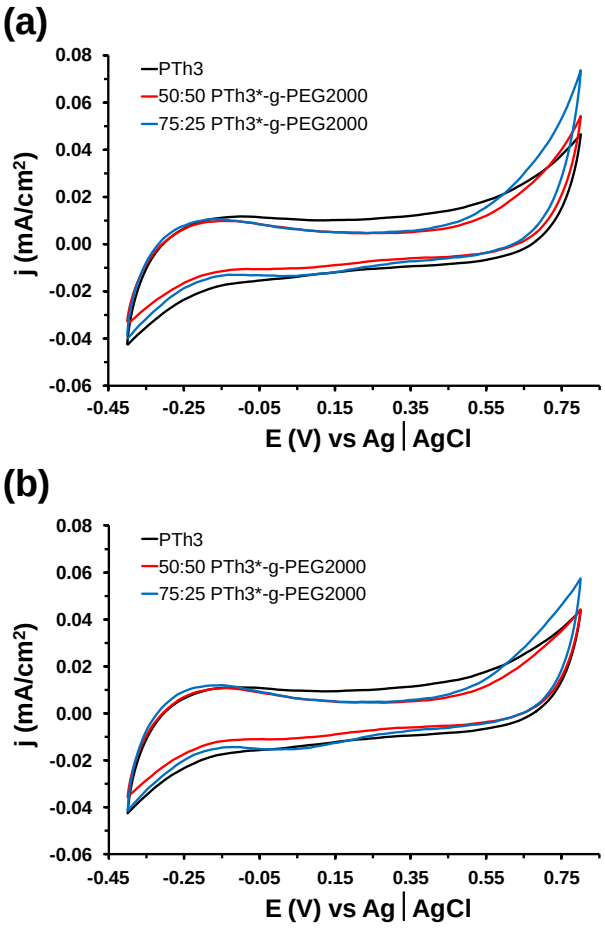

Figure 3.2.15 Cyclic voltammograms of PTh_3*-*g*-PEG_{2000} (75:25 and 50:50 Th_3-PEG_{2000}: Th_3) and PTh_3 films coated with Cos-7 cells in PBS. Voltammograms of both the as prepared samples (a) and after ten consecutive oxidation-reduction cycles (b) are displayed.

Application of consecutive oxidation-reduction cycles led to a reduction of the electroactivity in all cases, as is clearly reflected in the voltammograms recorded after 10 redox cycles (Figure 3.2.15b). Thus, the electroactivity of the 75:25 and 50:50 copolymers and PTh_3 cells coated with cells underwent a reduction of LEA= 22%, 18% and 6%, respectively, after 10 cycles. In spite of this, it is worth noting that the electroactivity of polymeric films coated with cells when submitted to 10 redox cycles is around 85% - 100% higher than the electroactivity of as prepared films

without cells. Accordingly, application of oxidation and reduction potentials to the cells does not provoke a moderate reduction of the benefits induced by such living systems, the electrochemical behavior of coated films being better than that of films without cells.

These results evidence that the ability to exchange charge reversibly of the three coated materials depends on the interactions at the interface between the surface of the substrate and the cellular monolayer. This feature, which occurs similarly for 75:25 and 50:50 PTh_3-*g*-PEG and PTh_3, suggests that the contribution of polymer-cell interactions is more important than the chemical nature and intrinsic properties of the polymeric material.

Cytotoxicity and cellular adhesion of PTh_3*-*g*-PEG_{2000} / collagen platforms

Protein adsorption onto surfaces is the first stage that takes place in cell adhesion and proliferation processes when biomaterials contact living cells in the appropriated media. Type I collagen is the most common collagen isotype. In addition, type I collagen is one of the most abundant extra cellular matrix (ECM) proteins, which is known to bind fibronectin, another important ECM protein, for early adhesion [36]. The cellular response of polymeric materials has been shown to be influenced by the adsorption of collagen onto their surface [37-39]. In order to look for an improvement in the properties of PTh_n-*g*-PEG as bioactive platforms, in this work collagen has been adsorbed onto the surface of PTh_3*-*g*-PEG_{2000} and PTh_3 films using the procedure described in the Methods section.

The cytotoxicity of PTh_3*-*g*-PEG_{2000} / collagen and PTh_3 / collagen was evaluated through viability assays, as those described above, using Cos-7 cells. Results (Figure 3.2.16) indicate that collagen does not improve appreciably the cell viability of PTh_3*-*g*-PEG_{2000} copolymers, which was found to be relatively high for films without superficially absorbed protein (Figure 3.2.12). However, a very noticeable result is that adsorbed collagen inhibits the cytotoxicity of PTh_3 films, the relatively viability of

PTh_3 / collagen being practically identical to those of PTh_3*-*g*-PEG_{2000} and PTh_3*-*g*-PEG_{2000} / collagen. This result corroborates that the cytotoxicity of PTh_3 is due to the release of medium size harmful molecules from the polymeric matrix to the culture medium. This phenomenon is precluded in PTh_3 / collagen by the layer of protein deposited onto the polymeric surface, which acts as a stopper.

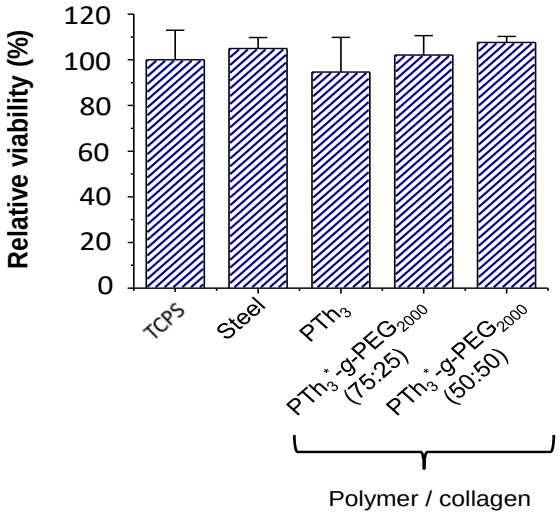

Figure 3.2.16 Cytotoxycity of PTh_3*-*g*-PEG_{2000} (75:25 and 50:50 Th_3-PEG_{2000}: Th_3) and PTh_3 coated with a thin layer of adsorbed collagen. Three samples were analyzed for each group. Bars represent the mean standard deviation. The relative viability of Cos-7 cells was established in relation to the TCPS control. Steel was also considered as a control substrate because PTh_3*-*g*-PEG_{2000} and PTh_3 were deposited on this material. The asterisk (*) indicates a significant difference with the control, Tukey's test ($p<0.05$).

Finally, the fibrous protein matrix on the top layer of PTh_3*-*g*-PEG_{2000} / collagen and PTh_3 / collagen favors cellular adhesion (Figure 3.2.17) with respect to that observed for same organic films but without protein coating (Figure 3.2.12). As expected, the increment is higher for PTh_3 (~30%) than for the graft copolymers (< 20%) because of the inhibition of cytotoxic effects in the former. The overall of these results allows us to conclude that, although the cellular response of bioactive platforms based graft copolymers with electroactive and hydrophilic characteristics is intrinsically very good, it can be easily enhanced by adding a top collagen layer. Thus, the role of this absorbed biolayer is not only to enhance cell

growth but also to act as a stopper, preventing eventual cytotoxic effects associated to the delivery of harmful molecules.

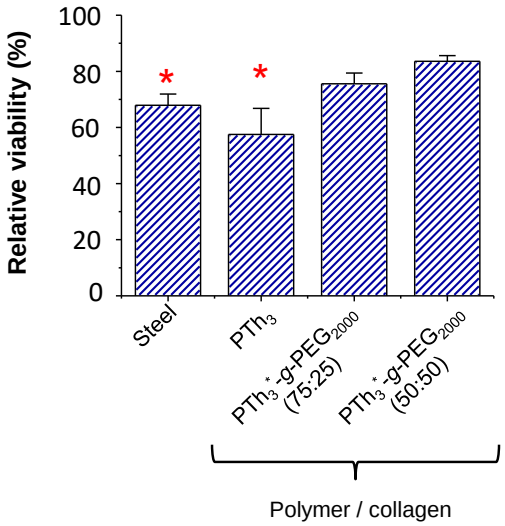

Figure 3.2.17 Cellular adhesion (a) and cellular proliferation (b) on PTh_3*-*g*-PEG_{2000} (75:25 and 50:50 Th_3-PEG_{2000}: Th_3) and PTh_3 films coated with a thin layer of adsorbed collagen. Three samples were analyzed for each group. Bars represent the mean standard deviation. The relative viability of Cos-7 cells was established in relation to the steel control, which was the substrate used to deposit the films. The asterisk (*) indicates a significant difference with the control, Tukey's test ($p<0.05$).

3.2.4 Conclusions

PTh_3*-*g*-PEG graft copolymers have been prepared by anodic copolymerization using a mixture of Th_3-PEG and Th_3 macromonomers. Although determination of the final composition is a very difficult task because of the insolubility of the copolymers, qualitative estimations obtained by FTIR suggest that materials derived from 50:50 and 75:25 Th_3-PEG_{2000}:Th_3 feeding compositions present ~4 and ~2 Th_3 units per Th_3-PEG_{2000} unit, respectively. The optical (ε_g) and electrochemical (electroactivity and electrostability) properties of these graft copolymers have found to be better than those of PTh_5-*g*-PEG and PTh_3. This behavior has been attributed to a combination of two factors: (1) conjugated chains

are longer in PTh_3*-*g*-PEG than in PTh_5-*g*-PEG; and (2) the porosity of graft copolymers facilitates the access and escape of dopant ions during Faradaic processes, which is not possible in compact structures formed by linear PTh_3 chains.

Analyses of cytotoxicity, cellular adhesion and proliferation and electro-compatibility of polymeric substrates covered by cells reveal that the behavior of PTh_3*-*g*-PEG as bioactive platform is better than those of PTh_5-*g*-PEG and PTh_3. More specifically, PTh_3 has been found to be cytotoxic, which have been attributed to the release of medium size harmful molecules from the polymeric matrix to the culture medium. Cellular adhesion and proliferation on the surface of graft copolymers have been found to increase with decreasing PEG / PTh ratio, while the biocompatibility of PTh_3 is very low because of its cytotoxic effects. PTh_3*-*g*-PEG copolymers have shown the highest electro-compatibility with cells. Thus, the electroactivity and electrochemical stability of PTh_3*-*g*-PEG coated with cells have been found to be significantly higher not only than those of all other examined substrates with and without cells but also than those of uncoated PTh_3*-*g*-PEG. Finally, the noxious cytotoxic effects of PTh_3 have been eliminated by incorporating a thin layer of collagen adsorbed onto the polymeric matrix, which acts as a stopper and enables cellular adhesion.

In summary, the behavior of PTh_3*-*g*-PEG copolymers, especially the 75:25, as electroactive substrates for biomedical applications is very good. Thus, these hydrophilic materials promote cell growth and are electro-compatible will cells. Current research is oriented towards cell regeneration onto 75:25 PTh_3*-*g*-PEG bioactive substrates through electrical stimulation for different advanced biomedical applications.

3.2.5 References

1. C. Feng, Y.J. Li, D. Yang, J.H. Hu, X.H. Zhang and X.Y. Huang; *Chem. Soc. Rev.*, vol. 3, pp. 1282-1295, 2011.
2. D. Neugebauer; *Polym. Int.*, vol. 56, pp. 1469-1498, 2007.
3. H.G. Borner, K. Matyjaszewski; *Macromol. Symp.*, vol. 177, pp. 1-15, 2002.
4. K. Nomura, M.M. Abdellatif; *Polymer*, vol. 51, pp. 1861-1881, 2010.
5. M. Zhang, A.H.E. Muller; *J. Polym. Sci., Part A: Polym. Chem.*, vol. 43, pp. 3461-3481, 2005.
6. S.S. Sheiko, B.S. Sumerlin, K. Matyjaszewski; *Prog. Polym. Sci.*, vol. 33, pp. 759-785, 2008.
7. H. Leea, J. Pietrasik, S.S. Sheiko, K. Matyjaszewski; *Prog. Polym. Sci.*, vol. 35, pp. 24-44, 2010.
8. J. Rzayev; *ACS Macro Lett.*, vol. 1, pp. 1146-1149, 2012.
9. I. Cianga, Y. Yagci; *Prog. Polym. Sci.*, vol. 29, pp. 387- 399, 2004.
10. E.H. Kang, I.H. Lee, T.L Choi; *ACS Macro Lett.*, vol. 1, pp. 1098-1102, 2012.
11. J. Shen, K. Ogino; *Chem. Lett.*, vol. 34, pp. 1616-1617, 2005.
12. J. Shen, K. Tsuchiya, K. Ogino; *J. Polym. Sci., Part A: Polym. Chem.*, vol. 46, pp. 1003-1013, 2008.
13. P.J. Costanzo, K.K. Stokes; *Macromol.*, vol. 35, pp. 6804-6810, 2002.
14. L. Qi, M. Sun, S. Dong; *J. Appl. Polym. Sci.*, vol. 102, pp. 1803-1808, 2006.
15. S.S. Balamurugan, G.B. Bantchev, Y. Yang, R.L. McCarley; *Angew. Chem. Int.*, vol. 44, pp. 4872-4876, 2005.
16. S. Das, S. Samanta, D.P. Chatterjee, A.K. Nandi; *J. Polym. Sci., Part A: Polymer Chem.*, vol. 51, pp. 1417-1427, 2013.
17. X. Chen, B. Gholamskhass, X. Han, G. Vamvouinis, S. Holdcro; *Macromol. Rapid Commun.*, vol. 28, pp. 1792-1797, 2007.
18. C.D. Grande, M.C. Tria, G. Jiang, R. Ponnapati, R. Advincula, *Macromol.*, vol. 44, pp. 966- 975, 2011.
19. L. Strover, C. Roux, J. Malmström, Y. Pei, D.E. Williams, J. Travas-Sejdic; *Synth. Met.*, vol. 162, pp. 381-390, 2012.

20. A.D. Bendrea, G. Fabregat, L. Cianga, F. Estrany, L.J. del Valle, I. Cianga, C. Alemán; *Polym. Chem.*, vol. 4, pp. 2709-2723, 2013.
21. A.D. Bendrea, G. Fabregat, J. Torras, S. Maione, L. Cianga, L.J. del Valle, I. Cianga, C. Alemán; *J. Mater. Chem. B*, vol. 1, pp. 4135-4145, 2013.
22. A.D. Bendrea, L. Cianga, E.G. Hitruc, I. Titorencu, I. Cianga; *Mater. Pastic*, vol. 2, pp. 71-78, 2013.
23. G. Fabregat, G. Ballano, E. Armelin, L.J. del Valle, C. Cativiela, C. Alemán; *Polym. Chem.*, vol. 4, pp. 1412-1424, 2013.
24. A.D. Bendrea, L. Cianga, I. Cianga; *Rev. Roum. Chim.*, vol. 58, pp. 153-160, 2013.
25. T. Mosmann; *J. Immunol. Methods*, vol. 65, pp. 55-63, 1983.
26. A.L. Gomes, J. Casanovas, O. Bertran, J.S. de C. Campos, E. Armelin, C. Alemán; *J. Polym. Res.*, vol. 18, pp. 1509-1517, 2011.
27. Y. Pang, X. Li, G. Shi, L. Jin; *Thin Solid Films*, vol. 516, pp. 6512–6516, 2008.
28. J. Casanovas, D. Aradilla, J. Poater, M. Solà, F. Estrany, C. Alemán; *Phys. Chem. Chem. Phys.*, vol. 14, pp. 10050-10062, 2012.
29. C. Ocampo, R. Oliver, E. Armelin, C. Alemán, F. Estrany; J. *Polym. Res.*, vol. 13, pp. 193-200, 2006.
30. D. Aradilla, D.S. Azambuja, F. Estrany, M. T. Casas, C. A. Ferreira, C. Alemán; *J. Mater. Chem.*, vol. 22, pp. 13110-13122, 2012.
31. V.S. Vashanta, K.L.N. Phani; *J. Electroanal. Chem.*, vol. 520, pp. 79-88, 2002.
32. E. Pal, V. Hornok, D. Sebo, A. Majzik, Dekany; *I. Colloids Surf., B*, vol. 79, pp. 276-283, 2010.
33. C. Alemán, D. Curcó; *J. Comput. Chem.*, vol. 28, pp. 1743-1749, 2007.
34. S.P. Zhong, Y.P. Zhang, C.T. Lim; *Tissue Engin. Part B, Reviews*, vol. 18, pp. 77-87, 2012.
35. C. Mangold, F. Wurm, H. Frey; *Polym. Chem.*, vol. 3, pp. 1714-1721, 2012.
36. J.S. Tjia, B.J. Aneskievich, P.V. Moghe; *Biomater.*, vol. 20, pp. 2223-2233, 1999.

37. N.M. Coelho, C. González-García, M. Salmerón-Sánchez, G. Altankov; *Biotechnol. Bioeng.*, vol. 108, pp. 3009-3018, 2011.
38. N.M. Coelho, M. Salmeron-Sanchez, G. Altankov; *Biomater. Sci.*, vol. 1, pp. 494-502, 2013.
39. M.M. Pérez-Madrigal, M.I. Giannotti, L.J. del Valle, L. Franco, E. Armelin, J. Puiggalí, F. Sanz, C. Alemán; *ACS Appl. Mater. Interf.*, vol. 6, pp. 9719-9732,2014.

CHAPTER 4

Poly(3,4-ethylenedioxythiophene)-peptide conjugates based on chemical similarity

4.1 ELECTRO-BIOCOMPATIBILITY OF CONJUGATES DESIGNED BY CHEMICAL SIMILARITY‡

4.1.1 Introduction

The implementation of peptides into synthetic polymer systems to form peptide-polymer conjugates can be carried out using different strategies, which are frequently categorized into four main approaches [1-4]:

- Coupling strategies, in which peptide segments are coupled to preformed synthetic molecules using one or more reactive sites;
- Grafting strategies, in which the polymer is grown from the peptide segment;
- Inverse conjugation strategy, where the peptide is sequentially assembled on an already formed polymer;
- Macromonomers strategies, which consist on the polymerization of short peptides with a polymerizable functionality.

In the particular case of incorporation of peptides into CPs, the most frequent is the incorporation of anionic peptides as dopant agents to produce biocomposites [5-12], even though modification of CPs via covalent bonds has been also explored using different techniques [13]. For example, the first oligothiophene directly conjugated to a β-sheet pentapeptide was reported in 2004 [14] while the modification of the β-position on PPy to create strong disulfide bonds with the Cys of Arg-Gly-Asp-Cys (RGDS) was described a few years above [15,16]. More recently, different strategies have been used to immobilize peptides at the surface of CPs through covalent bonds [17-20]. Within this context, in the last year we have reported [19,20] an alternative strategy for the preparation of peptide-CP hybrid materials, which is based on the chemical similarity of the two components of the hybrid. More specifically, methyl 2-(*N-tert-*

‡*Results discussed in section 4.1 were published in J. Pept. Sci., 2014, 20, 537-546.*

butoxycarbonyl)amino-3-(3,4-ethylenedioxy-2-thienyl) propanoate and 2-(*N*-*tert*-butoxycarbonyl)amino-2-(3,4-ethylenedioxy-2-thienyl) acetate (**I** and **II** in Figure 4.1.1), two synthetic amino acids bearing a 3,4-ethylenedioxythiophene (EDOT) side group, were designed and subsequently incorporated at the end of PEDOT chains to produce the hybrid PEDOT-I and PEDOT-II, respectively (figure 4.1.1).

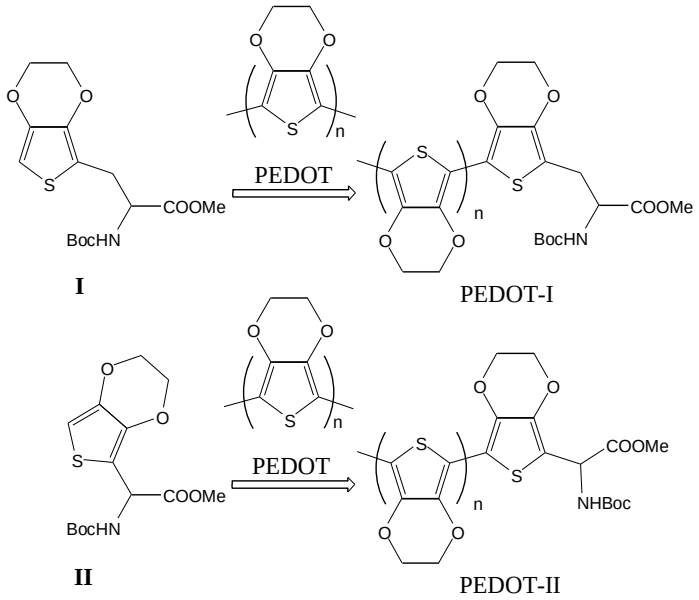

Figure 4.1.1 Chemical structure of PEDOT-I and PEDOT-II.

PEDOT-I and PEDOT-II were prepared by anodic polymerization using a two-steps strategy [19,20]. More specifically, in the first step PEDOT was prepared by electrochemical polymerization under a constant potential of 1.40 V in acetonitrile with $LiClO_4$. In the second step, the electrode coated with the PEDOT film was introduced in an acetonitrile containing $LiClO_4$ and **I** or **II**, a constant potential of 1.34 V being applied to transform PEDOT films into PEDOT-I or PEDOT-II, respectively. The advantage of peptide-CP conjugates based on chemical similarity is that this approximation avoids significant detriment in the electrical and electrochemical behavior of the bulk CP matrix, whereas drawbacks are typically observed in biocomposites made using peptides as dopant agents [5-7,21-24].

Although PEDOT-I and PEDOT-II behave much better than PEDOT as bioactive platforms, in this work we incorporate a variation in the synthetic approach that is expected to represent an improvement in the properties of these hybrids. The resulting hybrids have been denoted PEDOT-I* and PEDOT-II*, where the symbol used as super-index refers to the hybrids prepared using the new polymerization strategy. Specifically, we have examined the electrochemical, electronic, morphological and topographical properties, the wettability, and the behavior as the bioactive platform of PEDOT-I* and PEDOT-II*, results being compared with those previously obtained for PEDOT-I and PEDOT-II [19,20]. In addition, special emphasis has also been placed on the study of the electrocompatibility of the hybrids coated with cells and the surface energy, which were not studied before.

4.1.2 Methods

Materials

EDOT was purchased from Aldrich and used as received. Anhydrous $LiClO_4$, analytical reagent grade from Aldrich, was stored in an oven at 80 ºC before use in the electrochemical trials. **I** and **II** were synthesized using the procedures described in references 19 and 20.

Anodic polymerization and electrochemical assays

All electrochemical assays, including polymerizations, were carried out in a standard three electrode cell of 50 mL using steel AISI 316 sheets of 4 cm^2 area (surface roughness determined by atomic force microscopy: 11.4 Å) as working and counter electrodes. The reference electrode was an Ag|AgCl electrode containing a KCl saturated aqueous solution (E^0 = 0.222 V at 25ºC).

PEDOT-I* and PEDOT-II* were prepared by anodic polymerization using a two-steps strategy. In the first step, PEDOT films were obtained using a procedure identical to that employed for the electropolymerization

of PEDOT-I [19] and PEDOT-II [20]. More specifically, PEDOT was prepared by CA under a constant potential of 1.40 V using a 0.01 M EDOT solution in acetonitrile containing 0.1 M $LiClO_4$ as supporting electrolyte. The polymerization time was 10 s. The resulting PEDOT films, which showed the typical blue color, were washed with acetonitrile to eliminate the excess of monomer and dopant. In the second step, the electrode coated with the PEDOT film was introduced in a cell filled with 50 mL of an acetonitrile solution with 0.1 mM **I** (or **II**), 10 mM EDOT and 0.1 M $LiClO_4$. The resulting films were transformed into PEDOT-I* (or PEDOT-II*) applying a constant potential of 1.34 V during 5 s. Additionally, PEDOT-I* (PEDOT-II*) films were also prepared by increasing the concentration of **I** (**II**) in the acetonitrile solution used for the second step from 0.1 to 1 mM. Films produced using 0.1 and 1 mM amino acid concentration has been labelled as PEDOT-I*/0.1 and PEDOT-I*/1 (PEDOT-II*/0.1 and PEDOT-II*/1) for identification. All PEDOT-I* and PEDOT-II* films kept a blue color similar to that observed for PEDOT. For comparative purposes, PEDOT* films were prepared by immersing PEDOT-coated electrodes resulting from the first polymerization step into a cell filled with 50 mL of acetonitrile with 10 mM EDOT and 0.1 M $LiClO_4$ (*i.e.* without **I** or **II**) and applying a constant potential of 1.34 V during 5 s.

It should be remarked that in previous works [19,20] PEDOT films were transformed into PEDOT-I (or PEDOT-II) using an acetonitrile solution with 5 mM **I** (or **II**) and 0.1 M $LiClO_4$ and applying a constant potential of 1.34 V during 20 s. Accordingly, the main differences between the procedure used in this work for the preparation of PEDOT-I* and PEDOT-II* and that previously employed for the synthesis of PEDOT-I and PEDOT-II can be summarized as follow: a) the generation medium used in this work for the preparation of the conjugates contains both amino acid and EDOT monomer in the second step; and b) the polymerization time has been significant reduced (*i.e.* from 20 s to 5 s). These simple changes are expected to produce significant variations in the physical properties, especially in the roughness, which in turn are expected to enhance the bioactivity of the conjugates.

Contact profilometry

The thickness of the films was determined using a Dektak 150 stylus profilometer (Veeco, Plainview, NY). Different scratches were intentionally provoked on the films and measured to allow statistical analysis of data. Imaging of the films was conducted using the following optimized settings: tip radius= 2.5 μm; stylus force= 1.5 mg; scan length= 1 μm; speed= 1.5 nm/s. The thickness was measured using two different items: (i) the VD, which corresponds to the difference between the height polymer and the height of the steel substrate without any average; and (ii) the ASH, which measures the difference between the average height of the polymer and the average height of the steel substrate.

Scanning electron microscopy

SEM studies were performed to investigate the effect of the applied synthetic approach on the surface morphology of PEDOT-I* and PEDOT-II*. Dried samples were placed in a Focussed Ion Beam Zeiss Neon 40 scanning electron microscope operating at 5 kV, equipped with an EDX spectroscopy system. Samples were mounted on a double-side adhesive carbon disc and sputter-coated with a thin layer of carbon to prevent sample charging problems.

Atomic force microscopy

Topographic images were obtained with an AFM Dimension 3100 microscope and an AFM Multimode™ microscope using a NanoScope IV controller (Bruker) under ambient conditions in tapping mode. The R_q, which is the average height deviation taken from the mean data plane, was determined using the statistical application of the NanoScope Analysis software (1.20, Veeco). AFM measurements were performed on various parts of the films, which produced reproducible images similar to those displayed in this work. The scan window size was 25×25 μm^2.

UV-vis reflectance spectroscopy

Measurements were performed on a UV/Vis-NIR Shimadzu 3600 spectrophotometer, which contains a tungsten halogen visible source, a deuterium arc UV source, a photomultiplier tube UV-vis detector, and an InGaAs photodiode and cooled PbS photocell NIR detectors. The wavelength range is 200-800 nm. All the spectra were collected in the absorbance mode using the integrating sphere accessory (Model ISR-3100). Single-scan spectra were recorded at a scan speed of 60 nm min^{-1} using the UVProbe 2.31 software.

Cyclic voltammetry Electrochemical properties were studied by CV using a 0.1 M phosphate buffer saline solution (PBS; pH= 7.4 adjusted with NaOH). The initial and final potentials were -0.40 V while the reversal potential was 0.80 V. A scan rate of 50 mV/s was used in all cases. The ability to exchange charge reversibly (*i.e.* electroactivity) and the electrochemical stability (*i.e.* electrostability) were determined through direct measure of the anodic and cathodic areas in the control voltammograms using the GPES software. The electroactivity increases with the similarity between the anodic and cathodic areas of the first control voltammogram, whereas the electrostability decreases with the oxidation and reduction areas of consecutive control voltammograms. Specifically, the electrostability was expressed as the loss of electroactivity (LEA; in %) using the following Eqn:

$$\mathrm{LEA} = \frac{\Delta Q}{Q_{II}} \times 100 \qquad \text{(Eqn. 4.1.1)}$$

where ΔQ is the difference of voltammetric charges (in C) between the second and the last cycle, and Q_{II} is the voltammetric charge corresponding to the second cycle.

Contact angle measurements

Static contact angle measurements with the sessile drop method were recorded and analyzed at room temperature on an OCA-15EC contact angle meter from DataPhysics Instruments GmbH with SCA20 software (version 4.3.12 build 1037). The solvents, which were used as received, considered for this study were:

- distilled and deionized water;
- 1,2-propylencarbonate (Aldrich, Reagent Plus >99%);
- ethylene glycol (Merck >99.5%);
- formamide (Panreac, ultra-high purity);
- simulated body fluid (SBF) prepared by dissolving reagent-grade chemicals, NaCl, $NaHCO_3$, KCl, $K_2HPO_4 \cdot 3H_2O$, $MgCl_2 \cdot H_2O$, $CaCl_2$ and Na_2SO_4, in ion-exchanged and distilled water, buffered at pH= 7.25 and 37ºC with tris(hydroxymethyl)aminomethane, $(CH_2OH)_3CNH_2$, and 1M HCl;
- bovine serum albumin (BSA) (Gibco powder FR.5) was dissolved in SBF at pH 7.25 with a concentration of 10 mg/mL to be used for protein studies. Hereafter, this solvent is denoted SBF+BSA.

The sessile drop was gently put on the polished surface of PEDOT* and hybrid films using a micrometric syringe with a proper metallic needle (Hamilton 500μL). Initially, digital images of the drop were taken as a function of time, at regular intervals. The ellipse method was used to fit a mathematical function to the measured drop contour. This procedure consists on approximate the drop contour to the line of an ellipse, deviations from the true drop shape being in the range of a few %. The ellipse method provides accurate measure of the contact angle and holds the advantage that it is extremely fast. For each solvent and polymeric material, no less than 10 drops were examined.

Cellular adhesion and proliferation

MDCK (Madin-Darby canine kidney epithelial cell line) and Vero (African green monkey kidney epithelial cell line) cells were cultured in

DMEM supplemented with 10% fetal bovine serum, 1% penicillin/streptomycin and 2 mM L-glutamine at 37ºC in a humidified atmosphere of 5% CO_2 in air. The cultured media were changed every two days. For sub-culture, cell monolayers were rinsed with PBS and detached by incubating them with 0.25% trysin/EDTA for 5 min at 37ºC. Concentrations of cells were determined by counting at the Newbauer camera using 4% trypan blue as dye vital.

The detached cells were cultured following the conditions for the adhesion and proliferation assays. PEDOT,* PEDOT-I* and PEDOT-II* films deposited onto steel AISI 316 sheets of 1 cm^2 were placed in plates of 24 wells and sterilized using UV irradiation for 15 min in a laminar flux cabinet. An aliquot of 0.5 mL containing 5×10^4 cells (adhesion assays) or 2×10^4 cells (proliferation assays) was deposited on the substrate of each well. The plate was incubated under culture conditions for 60 min to promote the cell attachment to the film surface. Finally, 1 mL of the culture medium was added to each well. Controls of adhesion and proliferation were simultaneously performed by culturing cells on the surface of the TCPS plates and uncoated steel. Cell adhesion and proliferation were evaluated after 24 hours and 7 days of culture, respectively, using the MTT assay, which determines the cell viability [25]. This assay measures the ability of the mitochondrial dehydrogenase enzyme of viable cells to cleave the tetrazolium rings of the MTT and form formazan crystals, which are impermeable to cell membranes and, therefore, are accumulated in healthy cells. This process is detected by a colour change: the characteristic pale yellow of MTT transforms into the dark blue of formazan crystals. The viability results were normalized to TCPS control as relative percentages.

Results were derived from the average of four replicates (n= 4) for each independent experiment. ANOVA and Turkey tests were performed to determine the statistical significance, which was considered at a confidence level of 95% ($p < 0.05$).

Before the carbon coating for examination by SEM, samples covered with cells were fixed in a 2.5% glutaraldehyde PBS solution overnight at 4ºC. Then, they were dehydrated by washing in an alcohol battery (30º,

50º, 70º, 90º, 95º and 100º) at 4ºC for 30 minutes per wash. Finally, samples were air-dried, and sputter-coated with carbon before SEM observation.

4.1.3 Results and discussion

Polymerization and thickness

The two-steps process described in the Methods section was used for the preparation of PEDOT-I* and PEDOT-II*. Both the amino acid (**I** or **II**) and EDOT monomer were incorporated to the medium in the second step, allowing us to combine end-capping and polymer growing processes in the same step. This represents a significant change with respect to our previous strategy, in which the end-capping process was the only allowed. The combination of growing and end-capping processes in the same step is expected to affect the topography of the resulting films, enhancing the surface roughness (see below). The success of polymerization process and the successful incorporation of the amino acids were corroborated by FTIR and X-ray photoelectron spectroscopies. Obviously, results obtained for PEDOT-I* and PEDOT-II* were practically identical to those discussed for PEDOT-I and PEDOT-II in our previous works [19,20] and, therefore, have been omitted here. On the other hand, PEDOT* films were prepared (see Methods section) and used as a blank to identify the influence of **I** and **II** in the evaluated properties.

Table 4.1.1 lists the thicknesses of PEDOT,* PEDOT-I* and PEDOT-II* as determined by VD and ASH profilometry. As it can be seen, the thickness of PEDOT* films is $\ell \approx 0.8$ μm, whereas PEDOT-I* and PEDOT-II* are, in general, slightly thinner with $\ell \approx 0.7$ μm. In spite of the reduction of the polymerization time from 10 s to 5 s, these values are significantly higher than those previously obtained for PEDOT-I and PEDOT-II (also included in Table 4.1.1) using a different polymerization strategy (*i.e.* $\ell \approx$ 0.3 μm) [19,20]. This has been attributed to the incorporation of EDOT monomers to reaction medium in the second step of the

electropolymerization process, which favors the growing of the polymer chains.

Sample	Reference	Thickness (VL)[a]	Thickness (ASH)[b]	Roughness (Rq)
PEDOT*	This work	0.8±0.1	0.9±0.1	163±18
PEDOT-I*/0.1	This work	0.7±0.1	0.7±0.1	168±10
PEDOT-I*/1	This work	0.8±0.1	0.8±0.1	216±3
PEDOT-II*/0.1	This work	0.7±0.1	0.7±0.1	177±15
PEDOT-II*/1	This work	0.7±0.1	0.7±0.1	187±8
PEDOT	19	0.3±0.1	0.3±0.1	151±21
PEDOT-I	19	0.3±0.1	0.3±0.1	134±12
PEDOT-II	20	0.3±0.1	0.3±0.1	146±9

[a] Thickness measured by profilometry as the vertical line. [b] Thickness measured by profilometry as the average step height.

Table 4.1.1 Thickness (μm) and surface roughness (nm) of films made using the conjugates prepared in this and previous works.

Topography and Morphology

AFM and SEM images of PEDOT* are displayed in Figure 4.1.2a. 2D and 3D height AFM images indicate that polymer chains tend to organize in a dense distribution of sharp peaks forming two levels. The top one is constituted by a relatively small number of high and compact clusters formed from aggregation of peaks, whereas the bottom level involves individual peaks and low clusters of reduced dimensions, which can be associated to recently formed aggregates. The notable difference between the heights of the two levels indicates that PEDOT chains do not grow homogeneously, as is evidenced by the surface RMS roughness, R_q= 163±18 nm (Table 4.1.1). This topography is fully consistent with that previously reported for PEDOT sub-micrometric films [26,27]. High-resolution SEM micrographs show aggregation of sticks with a fiber-like morphology, which gives place to a homogeneous distribution of narrow

and tortuous pores that connect the bulk and the surface of the film. This particular morphology is in agreement with the AFM topography.

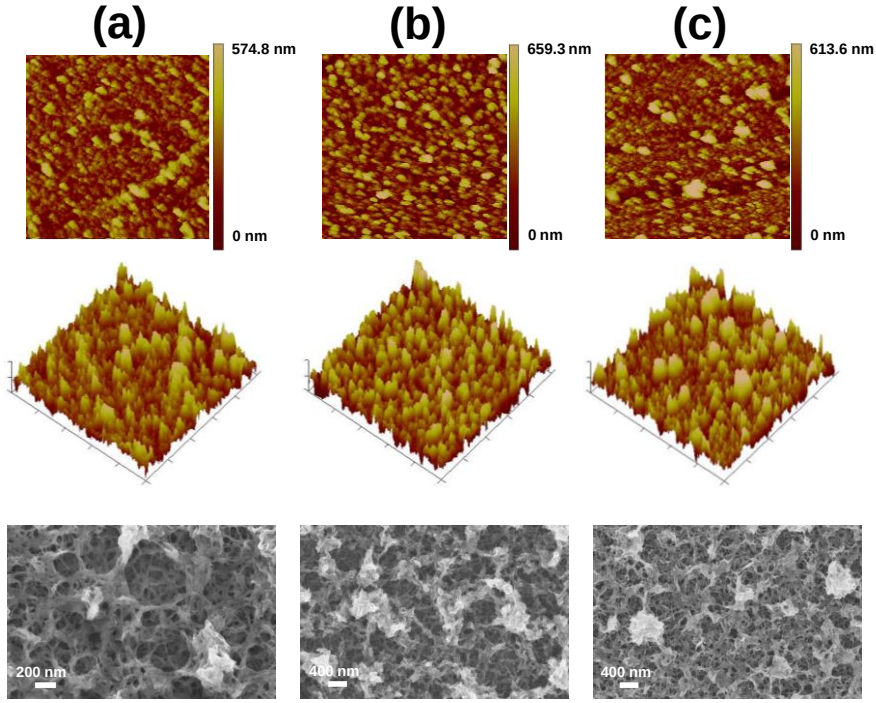

Figure 4.1.2 Representative 2D and 3D height (top and middle, respectively) AFM images (25 × 25 μm^2) and SEM micrograph (bottom) of (a) PEDOT*, (b) PEDOT-I*/1 and (c) PEDOT-II*/1. Magnification of SEM images: 120 kX for PEDOT* and 50 kX for PEDOT-I*/1 and PEDOT-II*/1.

Topographical and morphological images of PEDOT-I*/1 and PEDOT-I*/0.1 are displayed in Figures 4.1.2b and 4.1.3a, respectively. Although the topography of PEDOT-I*/1 is very similar to that observed for PEDOT*, the height of the aggregates located at the top level is significantly higher for the former than for the latter. As a result, the RMS roughness of PEDOT-I*/1 is 32% higher than that of PEDOT* (Table 4.1.1), and the maximum height of the peaks (R_{max}) is 1447±108 and 1656±90 nm for the former and latter, respectively. Moreover, the RMS roughness reported for PEDOT-I [19], R_q= 134±12 nm, was 38% lower than that obtained in this work for PEDOT-I*/1. AFM images of PEDOT-

I*/0.1 show similar features (Figures 4.1.3a). However, the topographical changes in PEDOT-I*/0.1 are much less prominent than for PEDOT-I*/1, as is also corroborated by the corresponding R_q value (Table 4.1.1). On the other hand, SEM micrographs of PEDOT-I*/1 and PEDOT-I*/0.1 do not present any appreciable change with respect to the morphology of PEDOT*. Obviously, PEDOT-II*/1 and PEDOT-II*/0.1 (Figures 4.1.2c and 4.1.3b, respectively) retains the topographical and morphological similarity with PEDOT* since these compounds only differ from the PEDOT-I* ones in one methylene group at the end-capping amino acid. As occurred above, the RMS roughness determined for PEDOT-II*/1 and PEDOT-II*/0.1, R_q= 187±8 nm and 177±155 nm, respectively, is around 25% higher than that reported for PEDOT-II (Table 4.1.1), reflecting the effect of the change implemented in the polymerization strategy.

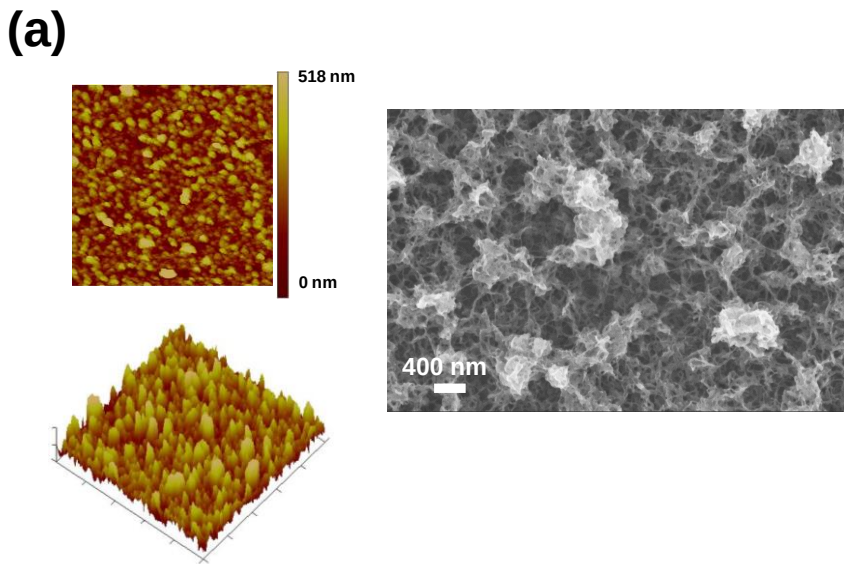

Figure 4.1.3a Representative 2D and 3D height (left) AFM images (25 × 25 μm^2) and SEM micrograph (right) of PEDOT-I*/0.1.

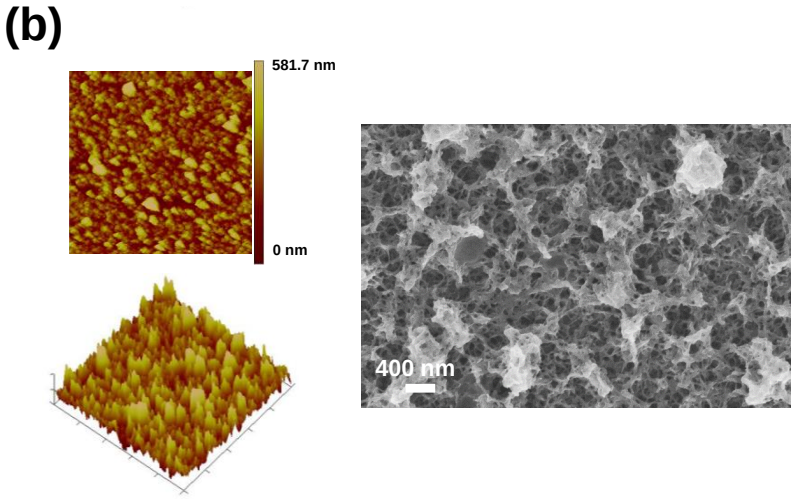

Figure 4.1.3b Representative 2D and 3D height (left) AFM images (25 × 25 μm^2) and SEM micrograph (right) of PEDOT-II*/0.1. Magnification of SEM images: 50 kX.

The overall of the results indicate that the incorporation of the EDOT monomers at the generation medium in the second step of the polymerization process provokes an enhancement of the surface roughness with respect to PEDOT-I and PEDOT-II. This effect, which increases with the concentration of **I** and **II**, has been attributed to the coexistence and competition of two chemical processes in the second step of polymerization: growing of the polymer chains by incorporating EDOT monomers and termination of polymer chains by incorporating **I** or **II**. In contrast, the termination process was the only present in the second step used to polymerize PEDOT-I and PEDOT-II [19,20]. In spite of the surface roughness changes, the morphology is neither altered by the incorporation of the amino acid or by the change in the polymerization strategy. The morphology of PEDOT is directly related with its the excellent electrochemical properties [26-28], this characteristic being expected to be preserved in PEDOT-I* and PEDOT-II*.

Electronic and electrochemical properties

Figure 4.1.4 compares the UV-vis spectra of PEDOT*, PEDOT-I*/1 and PEDOT-II*/1 films as prepared, whereas the spectra of the PEDOT-I*/0.1 and PEDOT-II*/0.1 films are displayed in figure 4.1.5. The highest energy band appears at λ_{max}=240 nm, which is typically assigned to the *n*-π^* transition in the polymer backbone [29], while the large absorption band at ~675 nm has been ascribed to the formation of polarons [30]. The slope of the tail that connects such two transition is similar, indicating that the doping level of the three systems is similar.

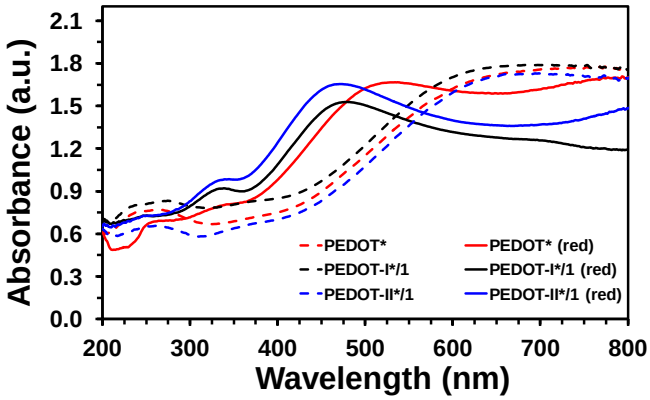

Figure 4.1.4 UV-vis spectra of PEDOT*, PEDOT-I*/1 and PEDOT-II*/1 in the doped (dashed lines) and reduced states (solid lines).

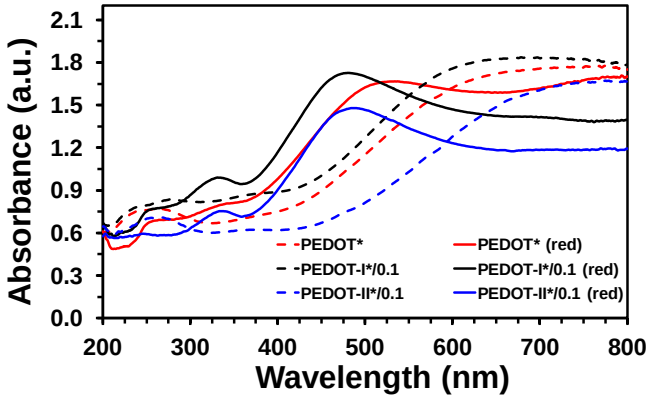

Figure 4.1.5 UV-vis spectra of PEDOT*, PEDOT-I*/0.1 and PEDOT-II*/0.1 in the doped (dashed lines) and reduced states (solid lines).

PEDOT*, PEDOT-I* and PEDOT-II* films were dedoped by reducing the pristine materials in acetonitrile with 0.1 M $LiClO_4$ applying a constant potential of -1.40 V for 100 s. The UV-vis spectra of the reduced films, which are included in Figures 4.1.4 and 4.1.5, were used to determine the optical ε_g from the λ^{onset}. The ε_g values of dedoped PEDOT*, PEDOT-I*/0.1, PEDOT-I*/1, PEDOT-II*/0.1 and PEDOT-II*/1 are 2.00 (λ^{onset}= 620 nm), 2.06 (λ^{onset}= 601 nm), 2.17 (λ^{onset}= 572 nm), 2.05 (λ^{onset}= 606 nm) and 2.07 eV (λ^{onset}= 597 nm), respectively. Accordingly, ε_g exhibits a slightly increment upon the incorporation of amino acid at the end of the polymer chains, this effect being more pronounced for the conjugates produced using a highest concentration of amino acid. Comparison with the ε_g values determined for PEDOT, PEDOT-I and PEDOT-II in our previous work (1.99, 1.99 and 1.86 eV, respectively) [20] indicates that the polymerization strategy used in this work provokes a more effective incorporation of end capping amino acids, which is consistent with the increment of ~0.1-0.2 eV in the band gap of PEDOT-I* and PEDOT-II*.

Control voltammograms in 0.1 M PBS of PEDOT*, PEDOT-I*/1 and PEDOT-II*/1, which are compared in Figure 4.1.6a, evidence that the incorporation of **I** and **II** to polymer chains provokes a loss of electroactivity. Thus, the ability to store charge of PEDOT* is ~20 % higher than that of PEDOT-I*/1 and PEDOT-II*/1. This reduction, which is practically identical to that obtained for PEDOT-I*/0.1 and PEDOT-II*/0.1 (Figure 4.1.7) is significantly higher than that previously reported for PEDOT-I and PEDOT-II (*i.e.* ~5%) [20]. This observation, which is fully consistent with the topographical and electronic changes mentioned above, has been attributed to the fact that the incorporation of amino acid at the end of polymer chains is more effective in PEDOT-I* and PEDOT-II* than in PEDOT-I and PEDOT-II. Therefore, the access and scape of dopant ions during the oxidation-reduction processes is more difficult with respect to doped PEDOT in the former than in the latter.

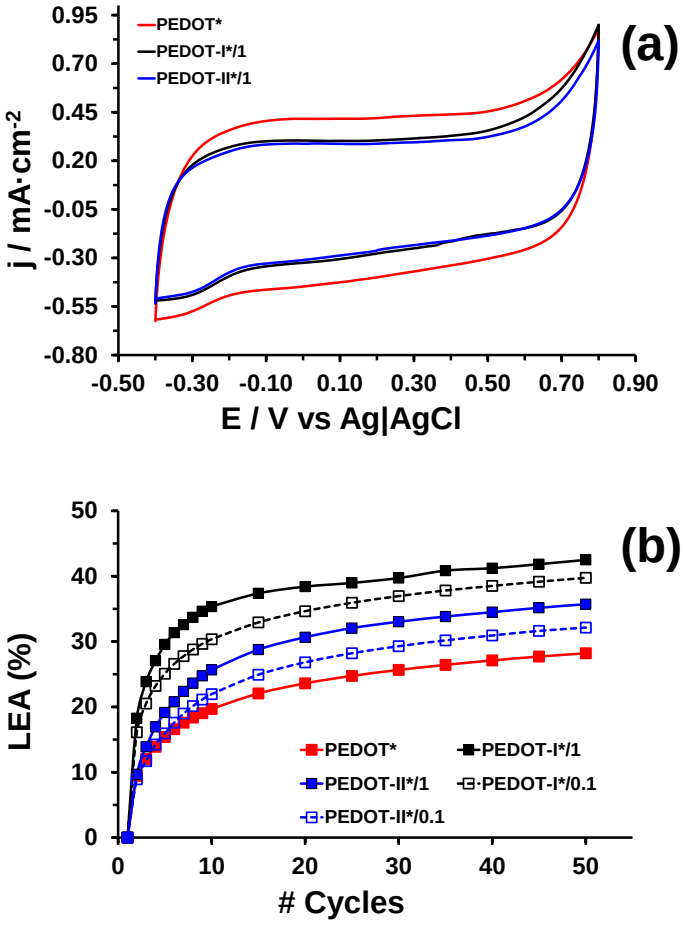

Figure 4.1.6 (a) Control voltammograms for the oxidation of PEDOT*, PEDOT-I*/1 and PEDOT-II*/1. Voltammograms were recorded in a 0.1 M PBS solution at 50 mV/s and 25 ºC. Initial and final potentials: -0.40 V; reversal potential: +0.80 V. (b) Variation of the LEA (in %) against the number of consecutive oxidation-reduction cycles for PEDOT*, PEDOT-I*/1, PEDOT-I*/0.1, PEDOT-II*/1 and PEDOT-II*/0.1 in water with 0.1 M PBS.

Although the influence of the concentration of amino acid in the generation medium and well as of the amino acid side chain composition (*i.e.* **I** shows a CH_2 unit in the side group that is not present in **II**) do not have any effect in the electroactivity (Figure 4.1.7), these factors have an appreciable impact on the electrostability. Figure 4.1.6b compares the

variation of the LEA (Eqn 1) against the number of consecutive oxidation-reduction cycles for PEDOT,* PEDOT-I*/1, PEDOT-II*/1, PEDOT-I*/0.1 and PEDOT-II*/0.1. After 50 cycles the loss of electroactivity is higher (~ 3%) for PEDOT-I*/1 and PEDOT-II*/1 than for PEDOT-I*/0.1 and PEDOT-II*/0.1, respectively, while the loss of electroactivity is higher (~ 8%) for PEDOT-I*/1 and PEDOT-I*/0.1 than for PEDOT-II*/1 and PEDOT-II*/0.1, respectively. Furthermore, PEDOT* shows the highest electrochemical stability, the LEA of the latter being 14% and 7% lower than those of PEDOT-I*/1 and PEDOT-II*/1, respectively.

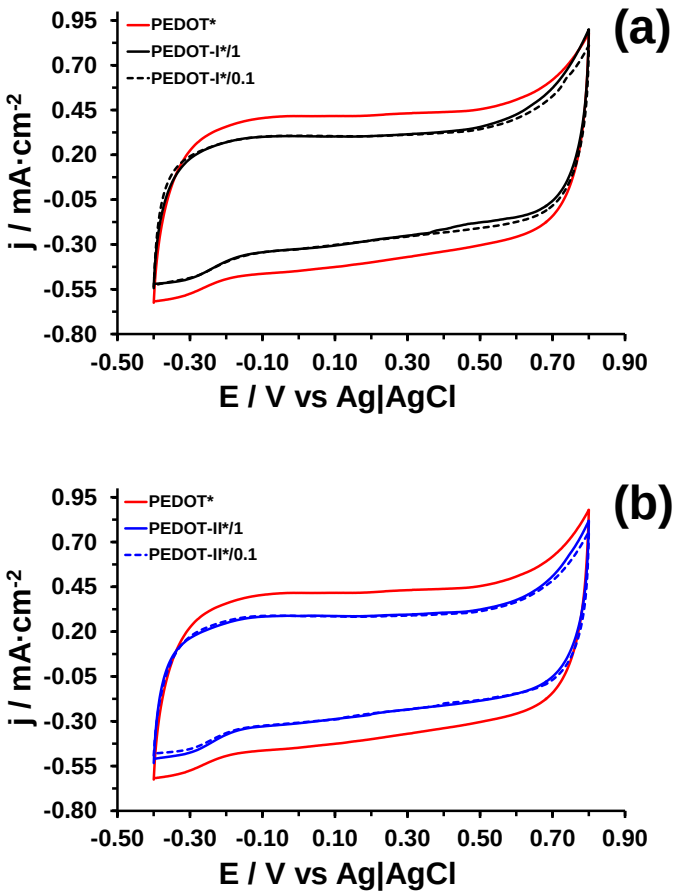

Figure 4.1.7 a) Control voltammograms for the oxidation of (a) PEDOT*, PEDOT-I*/1 and PEDOT-I*/0.1; and (b) PEDOT*, PEDOT-II*/1 and PEDOT-II*/0.1. Voltammograms were recorded in a 0.1 M PBS solution at 50 mV/s and 25 ºC. Initial and final potentials: -0.40 V; reversal potential: +0.80 V.

Application of consecutive oxidation-reduction cycles to films made of CPs typically provokes both reduction of the surface porosity and cross-linking in polymer chains [31,32]. These phenomena, which occur from the first Faradic process, are responsible of the loss of electroactivity since the access and scape of dopant ions during redox processes decrease with increasing number of cycles. As polymer chains in PEDOT*, PEDOT-I* and PEDOT-II* cannot undergo cross-linking processes because the β-positions of the thiophene ring are occupied by the dioxane ring, the loss of electroactivity has been exclusively attributed to the Faradaic-induced reduction of porosity. This phenomenon, which was explicitly investigated for PEDOT films [31], is higher for systems with end-capped polymer chains than for PEDOT*. Thus, the applied potential induces reactive processes in **I** and **II**, giving place to an enhancement of the surface compactness. These secondary processes increases with the amount of end-capping amino acid and are more effective for the systems having the amino acid with highest conformational flexibility (*i.e.* **I** > **II** due to the additional methylene unit [20]).

Wettability and surface energy

The θ values of the various solvents for the five materials prepared in this work are listed in Table 4.1.2. The contact angles measured in water indicate that all materials are hydrophilic (*i.e.* $\theta < 90^{o}$), even though water-wettability increases upon the incorporation of amino acids to the end of polymer chains. This effect is considerably more pronounced for PEDOT-II* than for PEDOT-I*, independently of the amino acid concentration ($\Delta\theta \approx -15^{o}$ and -7^{o} for 1 mM and 0.1 mM, respectively). The addition of salts to water for preparing SBF solvent does not provoke important changes in the surface wetting of the films. Thus, contact angles kept values similar to those obtained for distilled and deionized water ($\Delta\theta \leq 4.2^{o}$) in all cases with exception of PEDOT*, for which the contact angle decreased almost 7^{o}. In opposition, addition of BSA to SBF provoked a very significant increment of the contact angles with respect to both water and SBF. However, this increment was higher for PEDOT* ($\Delta\theta = 16.5^{o}$ with respect

to water) than for PEDOT-I* and PEDOT-II* ($\Delta\theta \approx 14^o$ and 10^o, respectively). Thus, the addition of BSA to SBF to produce SBF+BSA provokes a reduction of the surface hydrophilicity, which is more pronounced for the CP than for the conjugates. These results suggest that CP and hybrid films adsorb BSA at the surface, even though with different abilities. This hypothesis is supported by recent studies using CPs based on polypyrrole and polyaniline [33-35]. In order to provide indirect evidences of our assumption, PEDOT*, PEDOT-I* and PEDOT-II* samples were immersed in SBF+BSA for 3 minutes and, after drying, the contact angles for pure water were measured. and compared with those obtained without any previous treatment. Results, which are included in Table 4.1.2, reflect an increment of the surface hydrophilicity, which is particularly relevant for PEDOT and PEDOT-I (*i.e.* the contact angles decrease by about 17º-22º for both PEDOT and PEDOT-I, and about 6º-13º for PEDOT-II). Accordingly, this feature also points towards the adsorption of the BSA protein onto the surface of the polymeric and hybrid samples.

Solvent	PEDOT*	PEDOT-I*/1	PEDOT-I*/0.1	PEDOT-II*/1	PEDOT-II*/0.1
Water	80.4±2.2	74.6±3.6	72.1±3.6	64.6±1.2	66.1±5.7
1,2-Propylencarbonate	19.4±1.6	16.9±1.0	11.1±0.9	12.6±1.8	9.6±1.1
Ethylene glycol	23.9±l1.2	22.1±1.2	20.4±2.4	17.5±2.3	16.8±2.6
Formamide	11.2±0.5	12.2±1.0	12.0±3.7	11.0±2.2	8.7±0.9
SBF[a]	73.6±0.9	70.4±3.1	72.1±2.9	64.9±1.9	65.6±3.0
SBF+BSA[b]	96.5±1.9	87.5±0.9	86.8±1.9	76.0±2.7	75.1±0.9
Water[c] (modified)	63.2±2.5	52.6±2.9	55.1±4.4	51.5±1.9	59.6±1.6

[a] Simulated body fluid. [b] Bovine serum albumin. [c] Contact angles of water after immersion of the samples in SBF+BSA during 3 minutes.

Table 4.1.2 Overview of the measured contact angles of the solvents for the different materials prepared in this work.

Contact angle values for 1,2-propylencarbonate and ethylene glycol reveal wetting of the five substrates with $\theta < 24^o$, indicating that the five

substrates have a very high surface energy. In all cases the surface wettability increases upon the incorporation of end-capping amino acids, evidencing the impact of the biomolecule in the surface energy. This result, which is fully consistent with those obtained in water, SBF and SBF+BSA solvents, is expected to be advantageous for biomedical applications related with cell adhesion and proliferation (see next sub-sections). On the other hand, the five surfaces are highly wetted by formamide ($\theta \leq 12^{o}$ in all cases) indicating that the polarity of these materials and solvent are similar.

Contact angle measurements can be related to surface energies through the Young's equation [36]:

$$\gamma_{sv} = \gamma_{sl} + \gamma_{lv} \cos\theta \qquad \text{(Eqn. 4.1.2)}$$

where θ is the contact angle and γ is the surface energy of the solid-vapor (*sv*), solid-liquid (*sl*) and liquid-vapor (*lv*) interface. Although θ is experimentally measured and γ_{lv} can be determined using different techniques (*e.g.* pendant drop), γ_{sv} and γ_{sl} cannot be obtained separately. Therefore, different models have been proposed to establish further relationships [37]. In this work surface energies have been calculated using different models (*i.e.* Zismman [38], Owen-Wend-Kaelble [39,40], Wu [41] and Equation-of-State [42] models).

In the Zisman model [38] critical surface tensions (γ_{crit}) are derived from a plot of $\cos\theta$ versus γ (the test liquid's surface tension) for the various test liquids. The linear regression extrapolated value of γ at $\cos\theta$=1 equals γ_{crit}. This linear relationship between $\cos\theta$ and γ is based on the assumption proposed by Antonow one century ago [43] and practically only applies for purely disperse liquid–solid systems rendering the Zisman model rather limited and inaccurate. In general, the values obtained using the Zisman model indicate low-energy surfaces with similar γ_{crit} values for the five examined materials (Table 4.1.3). Thus, γ_{crit} ranges from 47.3 (PEDOT-I*/1) to 57.6 mN/m (PEDOT-I*/0.1), which are significantly lower than those reported for polar surfaces, like for example clean silicon dioxide (γ_{crit}= 143.5 mN/m) [44].

The model of Owen-Wend-Kaelble [39,40] (OWK) assumes that dispersive and polar intermolecular forces operate across the interface and, therefore, the value of the total surface tension is the sum of two components:

$$\gamma = \gamma^P + \gamma^D \qquad \text{(Eqn. 4.1.3)}$$

where γ^P and γ^D are the dispersive and polar components of the surface tension, respectively. The expression for γ_{sl} can be then written as:

$$\gamma_{sl} = \gamma_{sv} + \gamma_{lv} - 2\sqrt{\gamma_{sv}^D \gamma_{lv}^D} - 2\sqrt{\gamma_{sv}^P \gamma_{lv}^P} \qquad \text{(Eqn. 4.1.4)}$$

Combining Eqns (4.1.2) and (4.1.4) leads to:

$$\gamma_{lv}(\cos\theta + 1) = 2\sqrt{\gamma_{sv}^D \gamma_{lv}^D} + 2\sqrt{\gamma_{sv}^P \gamma_{lv}^P} \qquad \text{(Eqn. 4.1.5)}$$

From Eqns (4.1.2), (4.1.3) and (4.1.5), γ_{sv} and γ_{sl} can be obtained from the values of contact angles measured with a pair of testing liquids whose surface tension components are known. Inspection of Table 4.1.3 indicates that the dispersive component of the surface energy is higher for PEDOT* than for PEDOT-I* and PEDOT-II* while the opposite behavior is observed for the polar component. Furthermore, the polar contribution to the surface energy is very low compared to the dispersive contribution. These features are consistent with the fact that PEDOT-I* and PEDOT-II* essentially differ from PEDOT* in the dipole moments and hydrogen bonding abilities of the end-capping amino acids, which in turn are relatively small. Thus, the surface of PEDOT* is exclusively dominated by the dispersive interactions associated to the EDOT units, whereas the relative importance of such interactions decreases slightly in the conjugates, which show an enhancement of the polar interactions. The discrepancy between the tendencies showed by the surface energies derived from OWK and the Zisman models has been attributed to the limitation of the latter, which were discussed above.

The Wu model [41] uses a similar approach discerning between a dispersive and a polar component of the surface energies. However, Wu

claimed that the harmonic mean of these components is better suited for low energy surfaces, such as polymers:

$$\gamma_{sl} = \gamma_{sv} + \gamma_{lv} - 4\left(\frac{\gamma_{sv}^{D}\gamma_{lv}^{D}}{\gamma_{sv}^{D} + \gamma_{lv}^{D}} + \frac{\gamma_{sv}^{P}\gamma_{lv}^{P}}{\gamma_{sv}^{P} + \gamma_{lv}^{P}}\right) \quad \text{(Eqn. 4.1.6)}$$

Combining Eqns (4.1.2) and (4.1.6) yields:

$$\gamma_{lv}(\cos\theta + 1) = 4\left(\frac{\gamma_{sv}^{D}\gamma_{lv}^{D}}{\gamma_{sv}^{D} + \gamma_{lv}^{D}} + \frac{\gamma_{sv}^{P}\gamma_{lv}^{P}}{\gamma_{sv}^{P} + \gamma_{lv}^{P}}\right) \quad \text{(Eqn. 4.1.7)}$$

Although the surface energy provided by the harmonic mean is generally lower than that obtained using the geometric mean [43], comparison of values derived from OWK and Wu models (Table 4.1.3) indicates good qualitative and quantitative agreements. Thus, such reduction is only appreciate in the surface energy of PEDOT-I*/0.1 and PEDOT-I*/1, even though it is relatively small (*i.e.* ~ 6 mN/m). The most remarkable difference between the values estimated using OWK and Wu models refers to the relative importance of the polar and dispersive components. More specifically, the polar contribution exhibits a significant enhancement in the Wu model (*i.e.* in the range from 5.47 to 9.08 mN/m), which is in detriment of the dispersive contribution. This feature reflects that the role played by dipole-dipole and hydrogen bonding interactions promoted by **I** and **II** is underestimated by the OWK model. The relative weight of the polar contribution in the surface energies provided by the latter approximation ranges from 2.5% (PEDOT*) to 19.9% (PEDOT-II*/0.1) while it increases from 11.5% (PEDOT*) to 33.9% (PEDOT-II*/0.1) in the surface energies calculated using the Wu model.

The Equation-of-State (EOS) method [42] is based on an empirical expression for γ_{sl}:

$$\gamma_{sl} = \gamma_{sv} + \gamma_{lv} - 2\sqrt{\gamma_{lv}\gamma_{sv}}\,e^{-\beta(\gamma_{lv}-\gamma_{sv})^{2}} \quad \text{(Eqn. 4.1.8)}$$

where β is a constant with value $1.247\cdot10^{-4}$. If Eqn (4.1.8) is inserted into Eqn (4.1.2) a new expression is obtained to allow the calculation of the

surface tension of the solid from a single contact angle if the surface tension of the liquid is known:

$$\cos\theta = -1 + 2\sqrt{\gamma_{sv}/\gamma_{lv}}\, e^{-\beta(\gamma_{lv}-\gamma_{sv})^2} \qquad \text{(Eqn. 4.1.9)}$$

As it can be seen, EOS model uses the total surface tension of the test liquid without discern between polar and dispersive interactions. Therefore, this procedure is less accurate than the Wu model, especially for polar systems. This limitation is clearly reflected in Table 4.1.3, which shows that the surface energies derived from the EOS model for PEDOT* and PEDOT-I* are practically identical. In contrast, the rest of models clearly indicate that the surface energy of the former CP is higher than that of the hybrid.

	Zisman	**OWK**			**Wu**			**EOS**
	γ_{crit}	SE	Dispersive	Polar	SE	Dispersive	Polar	SE
PEDOT*	48.23±0.06	60.56±0.88	59.02±0.88	1.54±0.00	60.98±0.00	53.97±0.00	7.01±0.00	45.28±2.35
PEDOT-I*/0.1	57.65±0.06	59.23±0.03	56.47±0.03	2.76±0.00	53.05±0.00	41.96±0.00	11.09±0.00	45.7±1.,92
PEDOT-I*/1	47.33±1.57	55.57±0.03	51.31±0.03	4.26±0.00	49.28±0.00	35.95±0.00	13.34±0.00	45.11±1.18
PEDOT-II*/0.1	49.15±0.1	51.23±0.08	41.02±0.08	10.21±0.00	51.63±0.00	34.15±0.00	17.48±0.00	47.23±1.04
PEDOT-II*/1	50.6±0.07	54.12±0.05	46.57±0.05	7.58±0.00	54.07±0.00	38.73±0.00	15.33±0.00	46.47±1.28

Table 4.1.3 Surface energies (SE; in mN/m) calculated with the Zisman, OWK, Wu and EOS models (see text) for the different materials prepared in this work. The dispersive and polar components of the SE are indicated for the OWK and Wu models.

Cellular adhesion and proliferation

The response of PEDOT*, PEDOT-I*/0.1, PEDOT-I*/1, PEDOT-II*/0.1 and PEDOT-II*/1 to MCDK and Vero cell lines is represented in Figure 4.1.8, which also displays viability results for steel and TCPS (culture plate) controls. The number of cells per area unit adhered to the four hybrids surfaces is higher than that adhered onto the controls, especially onto steel that resulted the less biocompatible substrate. Moreover, cellular adhesion on PEDOT* is enhanced upon the incorporation of **I** and **II** amino acids, adhesion improving with the concentration of amino acid. For example, as compared with PEDOT*, the number of MCDK cells adhered to PEDOT-I*/1 and PEDOT-II*/1 increases by 54% and 37% , respectively, corroborating that functionalization of CPs with amino acids and peptides represents a promising approach to modify cell-biomaterial interfaces.

After seven days of culture, cellular viability was re-examined (Figure 4.1.7b). The behavior of PEDOT-I* and PEDOT-II* as supportive matrices for proliferation of the two cellular lines was found to be considerably better than those of controls and PEDOT*. Again, cell proliferation increases with the concentration of amino acid, independently of both the cellular line and the amino acid. In opposition to adhesion assays, the response of Vero cells to the hybrid organic materials after seven days was more pronounced than that of MCDK cells. Also, the behavior as bioactive matrix was clearly better for PEDOT-I* than for PEDOT-II*, reflecting the importance of the chemical structure of the biomolecule attached as end capping of CP chains.

Viability results reported in our previous work for PEDOT and PEDOT-I (*i.e.* PEDOT-II was not examined) are comparable to those displayed in Figure 4.1.7. Unexpectedly, physical changes induced by the new synthetic procedure used to prepare the conjugates, especially the increment of the surface roughness, do not enhance the cellular activity on the materials. More specifically, PEDOT-I and PEDOT-I* behave similarly in terms of cell adhesion and proliferation, the biocompatibility of these conjugates being higher than those PEDOT and PEDOT*.

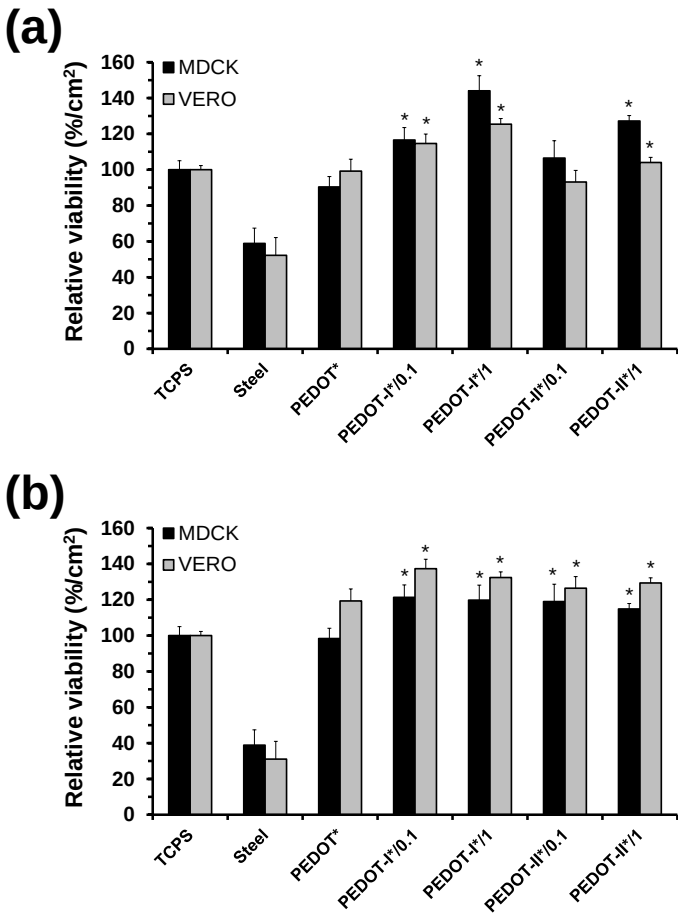

Figure 4.1.8 Cellular adhesion (a) and cellular proliferation (b) on PEDOT*, PEDOT-I*/0.1, PEDOT-I*/1, PEDOT-II*/0.1 and PEDOT-II*/1 using MDCK and Vero eukaryotic cell lines. The relative viability was established in relation to the TCPS control (tissue culture polystyrene). Steel was also considered as a control substrate because the individual polymers and the blend were deposited on this material. $p < 0.05$ *vs* [a)] TCPS, [b)] Steel, [c)] PEDOT, and [d)] doped PEDOT.

The abilities of the conjugates to behave as cellular matrix is clearly shown in the SEM micrographs displayed in Figures 4.1.9 and 4.1.10, which show the high density of adhered and proliferated cells. Furthermore, the zones covered by cells present a homogeneous spreading. The connection sites between the cells and the surface of the different substrates have been marked with arrows. These are extensions of

cytoplasm that form transient adhesions with the substrate. The abundance of these connection sites is similar on PEDOT-I* and PEDOT-II* surfaces.

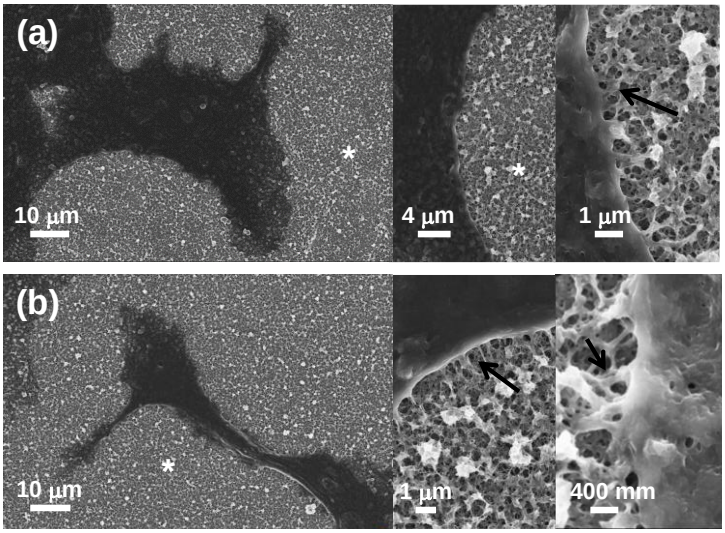

Figure 4.1.9 SEM micrographs of MDCK cells cultured for (a) 24 h and (b) 7 days on the surface of PEDOT-I*/1. The substrate surfaces (domains without cells) are marked with an asterisk (*). The connections of interactions between the cell and the surface are indicated by arrows.

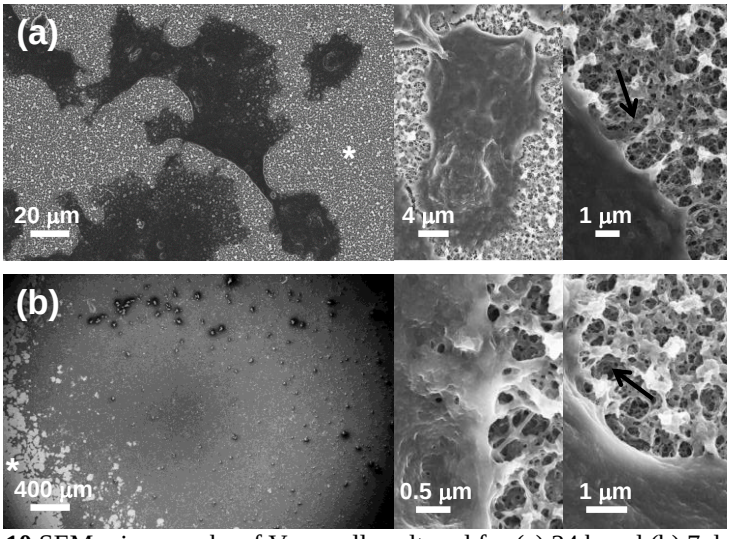

Figure 4.1.10 SEM micrographs of Vero cells cultured for (a) 24 h and (b) 7 days on the surface of PEDOT-II*/1. The substrate surfaces (domains without cells) are marked with asterisks (*). The connections or interactions between the cell and the surface are indicated by arrows.

Electro-compatibility of hybrids coated with cells

Control voltammograms of PEDOT*, PEDOT-I*/0.1, PEDOT-I*/1, PEDOT-II*/0.1 and PEDOT-II*/1 films coated with cellular mononolayers were registered in 0.1 M PBS. In all cases films were oxidized from -0.4 to 0.8 V, the resulting control voltammograms being displayed in Figure 4.1.11. Comparison with the voltammograms recorded for the uncoated films (Figures 4.1.6a and 4.1.7) indicates that cells provoke in all cases a significant increase of the j_{max}, which corresponds to that obtained at the reversal potential. More specifically, j_{max} increases from ~0.9 (for uncoated films) to ~1.6 and ~2.0 mA/cm^2 for films coated with MCDK and Vero cells, respectively. Moreover, the two cell lines enhance considerably the ability of PEDOT, PEDOT-I* and PEDOT-II* films to store charge, this increment being higher for films coated by Vero than by MCDK. This feature is consistent with the fact that Vero cells show the highest activity on all the studied films (Figure 4.1.8b) in terms of proliferation.

Comparison of the results obtained for the different materials covered with cells clearly indicate that the electroactivity increases as follows (Figure 4.1.9): PEDOT* < PEDOT-I*/0.1 < PEDOT-I*/1 ≈ PEDOT-II*/0.1 < PEDOT-II*/1 and PEDOT* < PEDOT-II*/0.1 ≈ PEDOT-I*/1 ≈ PEDOT-II*/1 < PEDOT-I*/0.1 for MCDK and Vero, respectively.

Indeed, the electroactivity of PEDOT* increases by 31% and 51% upon coating with MCDK and Vero cells, respectively. This remarkable enhancement has been attributed to the favorable interaction between the cellular monolayer and the surface of the CP, which facilitates the reversible exchange of ions between the two species and the electrolytic environment. The electroactivity of PEDOT-I*/1 and PEDOT-II*/1 coated with MCDK cells is 44% and 63% higher than that of uncoated PEDOT*, respectively, this increment being of ~100% for the two hybrids coated with Vero cells.

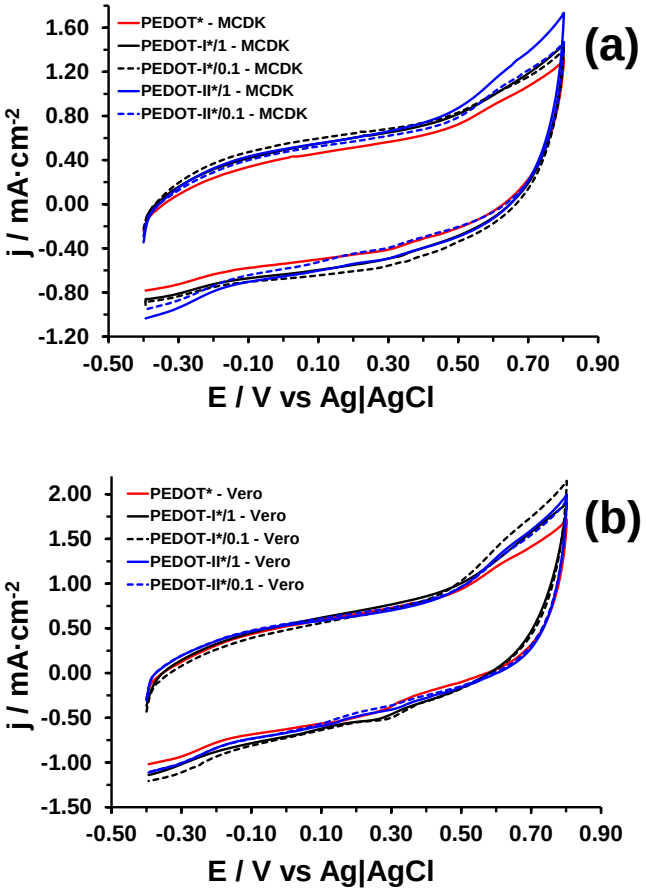

Figure 4.1.11 Control voltammograms for the oxidation of PEDOT*, PEDOT-I*/0.1, PEDOT-I*/1, PEDOT-II*/0.1 and PEDOT-II*/1 films coated with (a) MDCK and (b) Vero cells in a 0.1 M PBS solution at 50 mV/s and 25 ºC. Initial and final potentials: -0.40 V; reversal potential: +0.80 V.

Application of consecutive oxidation-reduction cycles led to a reduction of the electroactivity in all cases, as is clearly reflected in the voltammograms recorded after 5 redox cycles (Figure 4.1.12). Thus, the electroactivity of PEDOT* and the four examined conjugated coated with MCDK / Vero cells underwent a reduction of ~20% / ~24% after such amount of redox cycles. These values are relatively similar to the loss of electroactivity observed for uncoated films after 5 redox cycles, which ranged from 15% (PEDOT*) to 29% (PEDOT-I*/1). Accordingly, application of oxidation and reduction potentials to the cells does not

provoke a drastic elimination of the benefits induced by such living systems, the behavior of coated and uncoated films in PBS being very similar.

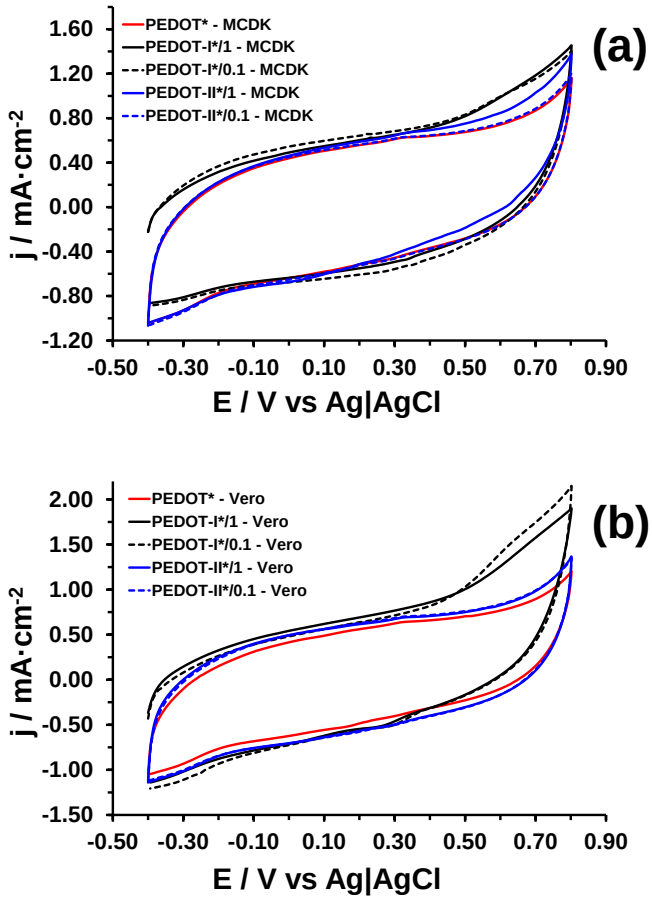

Figure 4.1.12 Voltammograms after 5 consecutive oxidation-reduction cycles for PEDOT*, PEDOT-I*/0.1, PEDOT-I*/1, PEDOT-II*/0.1 and PEDOT-II*/1 films coated with (a) MCDK and (b) Vero cells in a 0.1 M PBS solution at 50 mV/s and 25 ºC. Initial and final potentials: -0.40 V; reversal potential: +0.80 V.

Results displayed in Figures 4.1.11 and 4.1.12 evidence that the interactions at the interface between the conjugates films and the cellular monolayers produce an increment in the ability to exchange charge reversibly of the materials, which depend on the cell type. Indeed, the bioelectroactivity of these two-component substrates (*i.e.* cells + conjugate

or PEDOT*) is essentially controlled by the cell type, the contribution of the latter being significantly more important than that of the material. Thus, although the electrochemical response of coated PEDOT* is clearly worse than those of the four examined coated conjugates, the response of PEDOT-I*/0.1, PEDOT-I*/1, PEDOT-II*/0.1 and PEDOT-II*/1 is relatively similar. This feature suggests that the enhancement of the electroactivity by the cellular monolayer is a phenomenon that mainly depends on the interaction between the cells and the surface of the substrate.

4.1.4 Conclusions

A new synthetic approach, which is based on the incorporation of both amino acid and EDOT monomer in the generation medium of the second polymerization step used to produce conjugates, has been successfully employed to prepare PEDOT-I* and PEDOT-II*. This approach enhanced significantly the roughness of the films, which has been attributed to the competition between the polymer growing and end-capping processes, and provoked a more effective incorporation of the amino acid at the end of the polymer chains, as clearly evidenced the electronic and electrochemical properties (*i.e.* transition energy, electroactivity and electrochemical stability). Thus, amino acids affect those properties in which by chemical structure of the surface plays an important role.

The hydrophilicity of PEDOT increases upon the incorporation of **I** and **II**, the contact angle of water decreasing as follows: PEDOT* > PEDOT-I* > PEDOT-II*. The observed formamide-wettability suggests that the polarity of the CP, the conjugates and such solvent are similar. The surface energy, which has been evaluated using four different models, has been found to be higher for PEDOT* than for the two conjugates. Furthermore, the surface energy is dominated in all cases by the dispersive component, even although the polar contribution is higher for the conjugates than for the CP. This feature clearly indicates that by dipole-dipole and hydrogen

bonding interactions are promoted by the end amino acids located at PEDOT-I* and PEDOT-II*.

On the other hand, the roughness increment promoted by synthetic approach used in this work does not affect the biocompatibility of the hybrid conjugates. Thus, viability of cultured cells indicates that the behavior of PEDOT-I* and PEDOT-II* as cellular matrix is similar to that reported for PEDOT-I. Analysis of the electroactivity of PEDOT*, PEDOT-I* and PEDOT-II* coated with cellular monolayers indicate that all materials are electrocompatible with cells. Thus, the ability to exchange charge reversibly increases significantly in all cases, even though the response of all coated conjugates is higher than that of coated PEDOT*. The electrochemical response of these two-component substrates has been attributed to the interactions at the interface between the conjugate film surface and the cellular monolayer, which are more influenced by the cell type than by the material.

4.1.5 References

1. K.L. Heredia, H.D. Maynard; *Org. Biomol. Chem.*, vol. 99, pp. 45-53, 2007.
2. J.F. Lutz, H.G. Borner; *Prog. Polym. Sci.*, vol. 33, pp. 1-39, 2008.
3. M.A. Gauthier, H.A. Klok; *Chem. Commun.*, vol. 23, pp. 2591-2611, 2008.
4. H.G. Börner; *Prog. Polym. Sci.*, vol. 34, pp. 811-851, 2009.
5. N.K. Guimard, N. Gomez, C.E. Schmidt; *Prog. Polym. Sci.*, vol. 32, pp. 876-921, 2007.
6. X. Cui, J. Wiler, M. Dzaman, R.A. Altschuler, D.C. Martin; *Biomater.*, vol. 24, pp. 777-787, 2003.
7. R.A. Green, N.H. Lovell, L.A. Poole-Warren; *Biomater.*, vol. 30, pp. 3637-3644, 2009.
8. A.B. Sanghvi, K.P.H. Miller, A.M. Belcher, C.E. Schmidt; *Nat. Mater.*, vol. 4, pp. 496-502, 2005.
9. J.D. Nickels, C.E. Schmidt; *J. Mater. Chem. Part B*, vol. 1, pp. 1060-1066, 2013.
10. L. Zhang, W.R. Stauffer, E.P. Jane, P.J. Sammak, X.Y.T. Cui; *Macromol. Biosci.*, vol. 10, pp. 1456-1464, 2010.
11. J.D. Nickels, C.E. Schmidt; *J. Biomed. Mater. Res. A*, vol. 101, pp. 1464-1471, 2013.
12. W.R. Stauffer, X.T. Cui; *Biomater.*, vol. 27, pp. 2405-2413, 2006.
13. A. Jatsch, E.K. Schillinger, S. Schmid, P. Bäuerle; *J. Mater. Chem.*, vol. 20, pp. 3563–3578, 2010.
14. H.A. Klok, A. Rösler, G. Götz, E. Mena-Osteritz, P. Bäuerle; *Org. Biomol. Chem.*, vol. 2, pp. 3541–3544, 2004.
15. E. De Giglio, L. Sabbatini, P.G. Zambonin; *Polym. Ed.*, vol. 1, pp. 845-858, 1999.
16. E. De Giglio, L. Sabbatini, S. Colucci, P.G. Zambonin; *J. Biomater. Sci. Polym. Ed.*, vol. 11, pp. 1073-1083, 2000.
17. N. Gomez, C.E. Schmidt; *J. Biomed. Mater. Res. A*, vol. 81, pp. 135-149, 2007.
18. C.D. McTiernan, M. Chahma; *New J. Chem.*, vol. 34, pp. 1417-1423, 2010.

19. G. Fabregat, G. Ballano, E. Armelin, L.J. del Valle, C. Cativiela, C. Alemán; *Polym. Chem.*, vol. 4, pp. 1412-14124, 2013.
20. G. Fabregat, G. Ballano, J. Casanovas, A. Laurent, E. Armelin, L.J. del Valle, C. Cativiela, D. Jacquemin, C. Alemán; *RSC Adv.*, vol. 3, pp. 21069-21083,2013.
21. Y. Zhong, X. Yu, R. Gilbert, R.V. Bellamkonda; *J. Rehabil. Res. Dev.*, vol. 38, pp. 627-632, 2001.
22. B. Garner, A.J. Hodgson, G.G. Wallace, P.A. Underwood; *J. Mat. Sci. Mater. Med.*, vol. 10, pp. 19-27, 1999.
23. X.Y. Cui, D.C. Martin; *Sensors Actuators B*, vol. 89, pp. 92-102, 2003.
24. Y.H. Xiao, X.Y. Cui, J.M. Hancock, M. Bouguettaya, J.R. Reynolds, D.C. Martin; *Sensors Actuators B*, vol. 99, pp. 437-443, 2004.
25. T. Mosmann; *J. Immunol. Methods*, vol. 65, pp. 55-63, 1983.
26. D. Aradilla, F. Estrany, E. Armelin, C. Alemán; *Thin Solid Films*, vol. 520, pp. 4402-4409, 2012.
27. D. Aradilla, F. Estrany, E. Armelin, C. Alemán; *Thin Solid Films*, vol. 518, pp. 4203-4210, 2010.
28. D. Aradilla, D. Azambuja, F. Estrany, M.T. Casas, C.A. Ferreira, C. Alemán; *J. Mater. Chem.*, vol. 22, pp. 13110-13122, 2012.
29. D. Hohnholz, A.G. MacDiarmid, D.M, Sarno, W.E. Jones; *Chem. Commun.*, vol. 23, pp. 2444-2445, 2001.
30. S.L. McFarlane; B.A. Deore, N. Svenda, M.S. Freund; *Macromol.*, vol. 43, pp. 10241-10245, 2010.
31. D. Aradilla, F. Estrany, C. Alemán; *J. Phys. Chem.*, vol. 115, pp. 8430–8438, 2011.
32. C. Alemán, J. Casanovas, J. Torras, O. Bertran, E. Armelin, R. Oliver, F. Estrany; *Polymer*, vol. 49, pp. 1066-1075, 2008.
33. P.J. Molino, M.J. Higgins, P.C. Innis, R.M.I. Kapsa, G.G.Wallace; *Langmuir*,vol.28, pp. 8433-8445, 2012.
34. Z.H. Zhang, Y. Laing, P. Liang, Li C, S.M. Fang; *Polym. Int.*, vol.60, pp. 703-710, 2011.
35. L.P. Wang, W. Wang, L. Di, Y.N. Lu, J.Y. Wang; *Colloid Surf. B. Biointerf.*, vol. 80, pp. 72-78, 2010.

36. A.W. Adamso; *Physical chemistry of surfaces*, 5th ed, John Wiley: New York, 1990.
37. N.T. Correia, J.M. Ramos, B. Saramago, J. Calado; *J. Colloid Interface Sci*, vol.189, pp. 361-369, 1997.
38. W.A. Zisman; *Adv. Chem. Ser.*, vol. 43, pp. 1-51, 1964.
39. D.K. Owens, R.C. Wendt; *J. Appl. Polym. Sci.*, vol. 13, pp. 1741-1747, 1969.
40. D.H. Kaelble; *J. Adhes.*, vol. 2, pp. 66-81, 1970.
41. S. Wu; *J. Polym. Sci., Part C: Polym. Symp.*, vol. 34, pp. 19-30, 1971.
42. A.W. Neumann, R.J. Good, C.J. Hope, M. Sejpal; *J. Colloid Interface Sci.*, vol. 49, p. 291, 1974.
43. A.W. Neumann, R. David, Y. Zuo; *Applied Surface Thermodynamics Second Edition*, CRC Press (Taylor and Francis Group): New York, pp 424-426, 2011.
44. D. Janseen, R.D. De Palma, S. Verlaak, P. Heremans, W. Dehaen; *Thin Solid Films*, vol. 515, pp. 1433-1438, 2006.

4.2 ELECTROACTIVE POLYMER-PEPTIDE CONJUGATES FOR ADHESIVE BIOINTERFACES[§]

4.2.1 Introduction

The RGD (Arg-Gly-Asp) amino acid sequence is the unit of a cell adhesive activity domain in adherent proteins (*e.g.* fibronectin, fibrin and vitronectin) [1-3]. This cell adhesion motif has been widely used in the development of synthetic materials for bioengineering, different approaches being applied for such purpose (*e.g.* integration in larger peptide sequences [4-7], surface functionalized substrates [8-12] and polymer-peptide conjugates [12-15]). In all cases RGD-containing biomaterials increased the cellular adhesion with respect to the control when the adhesion motif was immobilized maintaining its biological activity.

Among advanced organic biomaterials, polymer-peptide conjugates, which result from the covalent integration of a peptide with a synthetic polymer block, are especially attractive because this kind of hybrid macromolecules combines unique properties that come from the precise chemical structure and functionality of peptides and the stability, functions and processability of synthetic polymers [16-19]. In order to take advantage of the electrochemical properties of electroactive CPs, different CP-peptide conjugates have been prepared during the last decade. For example, the first oligothiophene directly conjugated to a β-sheet pentapeptide was reported in 2004 [20], while the modification of the β-position on polypyrrole (PPy) to create strong disulfide bonds with the Cys of the RGDS sequence (Arg–Gly–Asp–Cys) was described in earlier works [21,22]. Within this context, we have recently reported a new strategy for the preparation of CP-peptide conjugates that is based on the chemical similarity of their two components [23,24]. This approach is

[§] *Results presented in section 4.2 were published in Biomaterials Science, 2015, 3, 1395-1405.*

based on the design of exotic synthetic amino acids bearing the main chemical groups of the polymer to facilitate the covalent conjugation between the components. Such methodology avoids the presence of long aliphatic linkers, which are typically used to join the two components of the polymer-peptide conjugate. The absence of linkers is expected to promote the extension of the polymer properties towards the peptide surface region, which is an important limitation typically found in CP-peptide conjugates.

In this work we have used a strategy based on chemical similarity to design an electroactive RGD-based CP-peptide conjugate. The polymer selected for this purpose is PEDOT, which is among the most successful CPs due to its excellent electrochemical and thermal properties, high conductivity, good environmental stability in its doped state, mechanical flexibility, relative ease of preparation, and fast doping-undoping process [25,27]. Regarding to the peptide, the Gly residue of the RGD sequence has been replaced by GlE, which consists of an amino acid bearing a 3,4-ethylenedioxythiophene as side group attached to an additional methylene group. The resulting sequence, hereafter denoted $RG^{E}D$, has been attached to end of PEDOT chains forming the PEDOT-$RG^{E}D$ conjugate (Figure 4.2.1). After chemical characterization, the physical properties of the conjugate have been investigated at different length scales. Finally, benefits induced by conjugation in tissue regeneration have been investigated by comparing the behavior of PEDOT and PEDOT-$RG^{E}D$ as soft bioelectroactive supports for cell attachment.

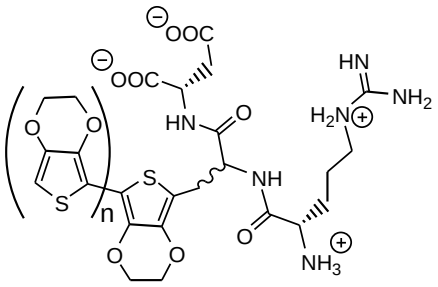

PEDOT-$RG^{E}D$

Figure 4.2.1 Chemical structure of the PEDOT-$RG^{E}D$ conjugate.

4.2.2 Methods

Chemical characterization of RG^{E}D

Melting points were determined on a Gallenkamp apparatus and are uncorrected. IR spectra were registered on a Nicolet Avatar 360 FTIR spectrophotometer; n_{max} is given for the main absorption bands. ^{1}H and ^{13}C NMR spectra were recorded on a Bruker AV-500, AV-400, ARX-300 or Varian Gemini 300 instrument at room temperature unless otherwise indicated, using the residual solvent signal as the internal standard, chemical shifts (δ) are expressed in ppm and coupling constants (*J*) in Hertz. High-resolution mass spectra were obtained on a Bruker Microtof-Q spectrometer.

Synthesis of PEDOT-RG^{E}D

Steps 1 and 2 of the synthetic process described in the text were carried out in a standard three electrode cell of 50 mL using steel AISI 316 sheets of 4 cm^2 area (surface roughness determined by atomic force microscopy: 11.4 nm) as working and counter electrodes. The reference electrode was an Ag|AgCl electrode containing a KCl saturated aqueous solution (E^0 = 0.222 V at 25ºC). The preparation of PEDOT and PEDOT-(protected RG^{E}D) films was performed by CA using a constant potential of 1.40 and 1.37 V, respectively. In all cases cells were filled with 50 mL of the corresponding acetonitrile solution. All electropolymerizations and cyclic voltammetry assays were conducted on a PGSTAT302N AUTOLAB potenciostat–galvanostat (Ecochimie, The Netherlands) equipped with the ECD module, which was connected to a PC computer controlled through the NOVA 1.6 software.

Contact profilometry

The thickness of PEDOT and conjugate films prepared in this work was determined using a Dektak 150 stylus profilometer (Veeco, Plainview, NY). Different scratches were intentionally provoked on the films and

measured to allow statistical analysis of data. Imaging of the films was conducted using the following optimized settings: tip radius= 2.5 μm; stylus force= 1.5 mg; scan length= 1 μm; speed= 1.5 nm/s. The thickness was measured using the ASH, which measures the difference between the average height of the polymer and the average height of the steel substrate.

FTIR spectroscopy

FTIR spectra of PEDOT and PEDOT-I were recorded on a Nicolet 6700 spectrophotometer. For this purpose, films were scrapped off from the electrode and dried under vacuum. FTIR spectra were recorded using KBr discs at 6 cm^{-1} resolution (60 scans).

X-ray photoelectron spectroscopy

XPS analyses were performed in a SPECS system equipped with a high-intensity twin-anode X-ray source XR50 of Mg/Al (1253 eV/1487 eV) operating at 150 W, placed perpendicular to the analyzer axis, and using a Phoibos 150 MCD-9 XP detector. The X-ray spot size was 650 mm. The pass energy was set to 25 and 0.1 eV for the survey and the narrow scans, respectively. Charge compensation was achieved with a combination of electron and argon ion flood guns. The energy and emission currents of the electrons were 4 eV and 0.35 mA, respectively. For the argon gun, the energy and the emission currents were 0 eV and 0.1 mA, respectively. The spectra were recorded with a pass energy of 25 eV in 0.1 eV steps at a pressure below $6 \cdot 10^{-9}$ mbar. These standard conditions of charge compensation resulted in a negative but perfectly uniform static charge. The C1s peak was used as an internal reference with a binding energy of 284.8 eV. High-resolution XPS spectra were acquired by Gaussian/Lorentzian curve fitting after S-shape background subtraction. The surface composition was determined using the manufacturer's sensitivity factors.

Standard ion chromatography

The percentage of doping ClO_4^- in PEDOT was obtained from reduction of approximately 2 mg of sample with carbon, followed by determination of the amount of chloride ions released by standard ion chromatography. This analysis was performed with a Kontron 600 HPLC liquid chromatograph fitted with a Waters IC-Pak anion column at 30 ºC and equipped with a Wescan conductimetric detector.

Scanning electron microscopy

SEM studies were performed to examine the effect of RG^ED on the surface morphology of PEDOT, respectively. Dried samples were placed in a Focussed Ion Beam Zeiss Neon 40 scanning electron microscope operating at 5 kV, equipped with an EDX spectroscopy system. Samples were mounted on a double-side adhesive carbon disc and sputter-coated with a thin layer of carbon to prevent sample charging problems.

Atomic force microscopy

Topographic AFM images were obtained with an AFM Dimension 3100 microscope and an AFM Multimode^{TM} microscope using a NanoScope IV controller (Bruker) under ambient conditions in tapping mode. The R_q, which is the average height deviation taken from the mean data plane, was determined using the statistical application of the NanoScope Analysis software (1.20, Veeco). AFM measurements were performed on various parts of the films, which produced reproducible images similar to those displayed in this work. The scan window size was 25×25 μm^2.

The AFM scratching technique was used to measure the thickness of the films. Specifically, contact mode AFM was used to intentionally scratch the films deposited on the steel substrate. Thus, the force was set to completely remove the layer in a scratch area of 0.7× 0.7 μm^2. After scratching, a topographic image was then obtained with tapping mode AFM and used to determine the films thickness from the depth of the

scratch. It should be noted that such a topographic image was taken of a big region to accurately measure the step between the coated and the uncoated surfaces.

Wettability

Contact angle measurements were carried out using the water sessile drop method. Images of 0.5 μL distillated water drops were recorded after stabilization with the equipment OCA 15EC (Data-Physics Instruments GmbH, Filderstadt). SCA20 software was used to analyze the images and determine the contact angle value, which was obtained as the average of at least six independent measures for each sample.

Cyclic voltammetry

The electrochemical behavior of PEDOT and PEDOT- RG^ED was determined by CV considering two different environments: films directly obtained from electropolymerization (*i.e.* as prepared samples) and films covered will cells. For this purpose, a sterilized PBS solution (pH = 7.2) was used as the electrolyte in the three electrode cell. All CV assays were performed with an Autolab PGSTAT302N equipped with the ECD module (Ecochimie, The Netherlands) using a three-electrode cell under a nitrogen atmosphere (99.995% in purity) at room temperature. The working compartment was filled with 50 μL of the electrolyte solution. Steel AISI 316 sheets of 1 cm^2 were used as both the working and the counter electrodes, and an Ag|AgCl electrode was used as the reference electrode which contained a KCl saturated aqueous solution (offset potential versus the standard hydrogen electrode, E^0 = 0.222 V at 25 °C). All potentials given in this report are referenced to this electrode. Cyclic voltammograms were registered at a scan rate of 50 mV/s in the potential range from −0.4 to + 0.8 V.

The electroactivity, which indicates the ability to exchange charge reversibly, was evaluated by examining the similarity between the anodic

and cathodic areas of the control voltammogram. The electrochemical stability (*i.e.* LEA), which decreases with the oxidation and reduction areas of consecutive control voltammograms, was determined using the following expression:

$$LEA = \frac{\Delta Q}{Q_{ii}} 100 \qquad \text{(Eqn. 4.2.1)}$$

where ΔQ is the difference of voltammetric charge between the second cycle and the last cycle and Q_{ii} is the voltammetric charge corresponding to the second cycle. In this work all values of *LEA* were referred to 10 consecutive oxidation-reduction cycles.

Conformational analyses

Density Functional Theory (DFT) calculations at the B3LYP/6-31+G(d,p) level were performed in aqueous solution. The solvent was described as a dielectric medium using a well stablished Self-Consistent Reaction Field (SCRF), that is, the Polarizable Continuum Model (PCM) of Tomasi and co-workers [28].

The conformational potential energy surface of the RG^ED peptide was systematically explored using a procedure inspired in the build-up method early developed by Scheraga and coworkers [29]. This approach is based on the assumption that short-range interactions play a dominant role in determining the conformation of a given peptide. Accordingly, the accessible conformations of a given peptide result from the combination of *N* independent rotamers (*i.e.*, the rotational isomeric approximation [30]), in which each independent rotational state corresponds to the most favored conformations of each residue. In practice, accessible starting geometries of RG^ED were constructed by combining all the minima identified for each of the three involved residues (*i.e.* Arg, GlE and Asp). Specifically, the minima of GlE and Asp were taken from the literature [31,32] while those of Arg were explicitly calculated in this work. For this purpose, starting geometries for calculations on Arg were constructed

using the minima previously obtained for *homo*-Arginine, that is, the Arg homologue containing one more methylene unit [33].

Starting from the five conformers computed with PCM(water)-B3LYP/6-31++G(d,p) and lying in a 5 kcal/mol energetic gap, a re-optimization has been performed in the experimental condition (in acetonitrile) using a PCM(acetonitrile)-ωB97XD/6-311++G(d,p) level of theory that has already shown satisfying results to study conformational preferences of dipeptides [34] and EDOT residues [31]. No negative frequencies were detected. For each conformer the forty first excited states were evaluated with the CAM-B3LYP/6-311++G(d,p) level of theory and the electronic density difference (EDD) between the excited state and the ground state have been plotted to qualitatively understand the variation of the maximum absorption wavelength (λ_{max}) depending on the conformation. All Quantum mechanics computations have been realized with Gaussian09 software [35].

Clustering analysis

The list of unique minimum energy conformations was generated by comparing each of the 552 minimized structures among themselves. First, the list of minimized conformations was organized by rank ordering all them in an increasing energy. Unique minimum energy conformations were identified based on φ and ψ dihedral angles, which characterize the peptide backbone conformation and on hydrogen-bond and salt-bridge interactions. Four dihedral angles were defined for the whole peptide: ψ for Arg, φ and ψ for GlE and φ for Asp. The existence of interactions was accepted on the basis of the following geometric criterion: (a) for salt bridges, the distance between the centers of the interacting groups is shorter than 4.50 Å; (b) for hydrogen bonds, the H···O distance is shorter than 2.50 Å. Two structures were considered different when differing in at least one of their dihedral angles by more than 60° or in at least one of the above interactions. All the structures classified as different were subsequently clustered based on salt bridges and hydrogen bonds.

UV-vis spectroscopy

UV-vis absorption spectra were obtained using a UV-vis-NIR Shimadzu 3600 spectrophotometer equipped with a tungsten halogen visible source, a deuterium arc UV source, a photomultiplier tube UV-vis detector, and a InGaAs photodiode and cooled PbS photocell NIR detectors. Spectra were recorded in the absorbance mode using the integrating sphere accessory (model ISR-3100), the range wavelength being 200-900 nm. The interior of the integrating sphere was coated with a highly diffuse $BaSO_4$ reflectance standard. Single-scan spectra were recorded at a scan speed of 60 $nm \cdot min^{-1}$. Measurements, data collection and data evaluation were controlled by the computer software UVProbe version 2.31.

Cell adhesion

Cos-7 (African green monkey kidney fibroblast cell line), Vero (African green monkey kidney epithelial cell line), MRC-5 (Human fetal lung fibroblast cell line) and Saos-2 (Human sarcoma osteogenic epithelial cell line) cells were cultured in Dulbecco's modified Eagle medium (DMEM) supplemented with 10% fetal bovine serum, 1% penicillin/streptomycin and 2 mM L-glutamine at 37ºC in a humidified atmosphere of 5% CO_2 in air. The cultured media were changed every two days. For sub-culture, cell monolayers were rinsed with PBS and detached by incubating them with 0.25% trypsin/EDTA for 5 min at 37ºC. Concentrations of cells were determined by counting at the Neubauer camera using 4% trypan blue as dye vital.

PEDOT and PEDOT-RG^ED films deposited onto steel AISI 316 sheets of 1 cm^2 were placed in plates of 24 wells and sterilized using UV irradiation for 15 min in a laminar flux cabinet. An aliquot of 0.5 mL containing 5×10^4 cells was deposited on the substrate of each well. The plate was incubated under culture conditions for 60 min to promote the cell attachment to the film surface. Finally, 1 mL of the culture medium was added to each well. Controls of adhesion were simultaneously performed by culturing cells on the surface of the tissue culture polystyrene (TCPS)

plates. Cell adhesion was evaluated after 24 hours of culture using the MTT assay, which determines the cell viability [53]. This assay measures the ability of the mitochondrial dehydrogenase enzyme of viable cells to cleave the tetrazolium rings of the MTT and form formazan crystals, which are impermeable to cell membranes and, therefore, are accumulated in healthy cells. This process is detected by a colour change: the characteristic pale yellow of MTT transforms into the dark blue of formazan crystals. The viability results were normalized to TCPS control as relative percentages.

Results were derived from the average of four replicates (n= 4) for each independent experiment. ANOVA and Turkey tests were performed to determine the statistical significance, which was considered at a confidence level of 95% ($p < 0.05$).

Before the carbon coating for examination by SEM, samples covered with cells were fixed in a 2.5% glutaraldehyde PBS solution overnight at 4ºC. Then, they were dehydrated by washing in ethanol battery (30º, 50º, 70º, 90º, 95º and 100º) at 4ºC for 30 minutes per wash. Finally, samples were air-dried, and sputter-coated with carbon before SEM observation.

4.2.3 Results and discussion

Synthesis of the protected RG^{E}D peptide

The synthetic route used to obtain the RG^{E}D sequence, which was protected at the reactive positions by tert-butyl ester groups (tBu-COO) to avoid interferences during the coupling to PEDOT chains, is provided in Figure 4.2.2.

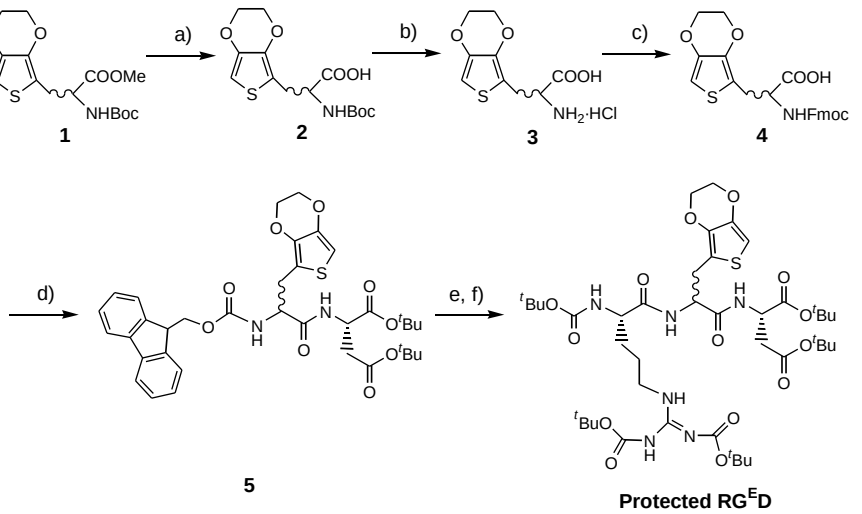

Figure 4.2.2 Reagents and conditions for the synthesis of protected RG^{E}D: (a) KOH 2N/MeOH, rt 2h, 99%; (b) HCl (3N)/AcOEt, rt 30 min, 100%; (c) FmocOsu, K_2CO_3, CH_3CN/H_2O 3/1, 80%; (d) HOBt, EDC·HCl, NMM, H-L-Asp(O^{t}Bu)-O^{t}Bu, CH_2Cl_2, 0ºC 30 min, rt 24h, 95%; (e) DEA, CH_2Cl_2, rt 4h, 100%; (f) HOBt, EDC·HCl, NMM, Boc-L-Arg(Boc)$_2$-OH, CH_2Cl_2, 0ºC 30 min, rt 24h, 90%.

The synthetic procedures used to obtain the intermediates 1-5 (Figure 4.2.2) required for the preparation of protected RG^{E}D can be described as follow:

(1) Methyl 2-(N-tert-butoxycarbonyl)amino-3-(3,4-ethylenedioxy-2-thienyl) propanoate

The synthesis of **1** was reported in reference 36.

(2) 2-(*N-tert*-butoxycarbonyl)amino-3-(3,4-ethylenedioxy-2-thienyl) propanoic acid

A 2N solution of KOH in methanol (15 mL) was added to **1** (1.44 g, 4.20 mmol) and the reaction mixture was stirred at room temperature for 2 hours. After evaporation of the solvent, the remaining residue was re-dissolved in water (15 mL), neutralized with HCl 2N and extracted with DCM (3×30 mL). The combined organic layers were dried over magnesium sulphate. Evaporation of the solvent gave **2**, a colourless oil that crystallized with a mixture of hexane/ether 2:1 v/v. The resulting white solid was collected by filtration under reduced pressure and washed several times with hexane (1.37 g, 4.16 mmol, 99% yield). Mp 132-133 ºC. IR (nujol) ν: 3341, 1704, 1676 cm^{-1}. ^{1}H NMR ($CDCl_3$, 400 MHz, 60 °C): δ 1.44 (s, 9H), 3.13 (dd, 1H, J = 15.0 Hz, J = 6.7 Hz), 3.23 (dd, 1H, J = 15.1 Hz, J = 5.0 Hz), 4.16 (m, 4H), 4.49 (m, 1H), 5.29 (m, 1H), 6.17 (s, 1H), 8.45 (bs, 1H). ^{13}C NMR ($CDCl_3$, 100 MHz, 60 °C): δ 28.5, 28.9, 54.4, 64.8, 64.9, 80.6, 97.8, 110.7, 139.8, 141.7, 155.7, 175.8. HRMS $C_{14}H_{19}NO_6NaS$ $[M+Na]^+$: calcd. 352.0825, found 352.0817.

(3) 2-Amino-3-(3,4-ethylenedioxy-2-thienyl) propanoic acid hydrochloride, [HCl·H-DL-GlE-OH]

A 3N solution of HCl in anhydrous ethyl acetate (10 mL) was added to **2** (750 mg, 2.28 mmol), and the reaction mixture was stirred at room temperature for 1 h. After evaporation of the solvent, the residue was taken up in water and lyophilized to afford pure **3** as a white solid (604 mg, 2.28 mmol, 100% yield). Mp 223-224 ºC (dec). IR (nujol) ν: 3300-2200, 1739 cm^{-1}. ^{1}H NMR (DMSO-d_6, 300 MHz): δ 3.07 (dd, 1H, J = 15.5 Hz, J = 5.8 Hz), 3.18 (dd, 1H, J = 15.3 Hz, J = 6.2 Hz), 3.97-4.07 (m, 1H), 4.11-4.23 (m, 4H), 6.48 (s, 1H), 8.39 (m, 2H). ^{13}C NMR (DMSO-d_6, 75 MHz): δ 26.7, 52.6, 64.3, 64.5, 97.9, 108.0, 140.3, 141.4, 170.0. HRMS $C_9H_{12}NO_4S$ $[M+H-HCl]^+$: calcd. 230.0482, found 230.0472.

(4) 2-(*N*-fluorenylmethoxycarbonyl)amino-3-(3,4-ethylenedioxy-2-thienyl) propanoic acid [Fmoc-DL-GlE-OH]

A solution of **3** (600 mg, 2.26 mmol) in water (15 mL) was cooled at 0 ºC and potassium carbonate (626 mg, 4.53 mmol) was added. Then, a solution of *N*-(9-fluorenylmethoxycarbonyloxy) succinimide (991 mg,

2.94 mmol) in acetonitrile (45 mL) was added and the reaction mixture was stirred at 0 ºC 1 hour and overnight at room temperature. The solvent was evaporated *in vacuo* and the remaining residue re-dissolved in water (15 mL) and extracted with diethyl ether (3×15 mL). The aqueous phase was neutralized with HCl 2N and extracted with DCM (3×15 mL). The combined organic layers were dried over magnesium sulphate, filtered and the solvent evaporated to dryness to give **4** as a white solid (815 mg, 1.81 mmol, 80% yield). Mp 201-202 ºC. IR (nujol) ν: 3303, 1695 cm^{-1}. ^1H NMR (Acetone-d_6, 400 MHz): δ 3.05 (dd, 1H, J = 15.0 Hz, J = 8.4 Hz), 3.34 (dd, 1H, J = 15.0 Hz, J = 4.6 Hz), 4.10-4.20 (m, 4H), 4.20-4.40 (m, 3H), 4.49 (ddd, 1H, J = 8.4 Hz, J = 8.4 Hz, J = 4.7 Hz), 6.25 (s, 1H), 6.64 (d, 1H, J = 8.4 Hz), 7.26-7.41 (m, 2H), 7.54-7.60 (m, 2H), 7.71 (d, 2H, J = 7.5 Hz), 7.85 (d, 2H, J = 7.5 Hz). ^{13}C NMR (Acetone-d_6, 100 MHz): δ 29.0, 48.1, 55.4, 65.5, 65.6, 67.3, 97.7, 112.4, 120.9, 126.3, 128.0, 128.6, 140.4, 142.2, 142.6, 145.2, 156.8, 172.8. HRMS $C_{24}H_{21}NO_6NaS$ $[M+Na]^+$: calcd. 474.0982, found 474.0972.

(5) Fmoc-DL-GlE-L-Asp(O^{t}Bu)-O^{t}Bu

To a solution of **4** (451 mg, 1 mmol) in DCM (60 mL) cooled to 0 ºC in an ice bath, was added 1-hydroxybenzotriazole hydrate (HOBt) (184.3 mg, 1.2 mmol) and *N*-[3-(dimethylamino)-propyl]-*N'*-ethylcarbodiimide hydrochloride (EDC·HCl) (230 mg, 1.2 mmol) followed by a solution of L-aspartic acid di-*tert*-butylester (338 mg, 1.2 mmol) and NMM (0.15 ml, 1.32 mmol) in DCM (10 mL) and finally NMM (0.11 ml, 1 mmol). The reaction mixture was stirred at room temperature for 24 hours. Then, the solution was washed with 5% $NaHCO_3$ (3×30 mL) followed by 5% $KHSO_4$. The organic phase was dried over magnesium sulfate and evaporated to dryness. The crude product was purified by column chromatography (eluent: hexane/ethyl acetate 7/3) to provide **5** (mixture of diastereoisomers) as a white solid (645 mg, 0.95 mmol, 95% yield).

IR (KBr) ν: 3321, 1733, 1683 cm^{-1}. ^1H NMR ($CDCl_3$, 400 MHz): δ 1.42 (sm 9H), 1.44 (s, 9H), 2.58-2.75 (m, 1H), 2.82-2.91 (m, 1H), 3.04-3.22 (m, 2H), 4.04-4.18 (m, 4H), 4.18-4.25 (m, 1H), 4.29-4.49 (m, 3H), 4.59-4.70 (m, 1H), 6.62-5.73 (m, 1H), 2.16 (2s, 1H), 7.00-7.10 (m 1H), 7.27-7.34

(m, 2H), 7.36-7.44 (m, 2H), 7.52-7.61 (m, 2H), 7.72-7.79 (m, 2H). ^{13}C NMR ($CDCl_3$, 125 MHz): δ 28.0, 28.15, 28.18, 29.3, 29.4, 37.45, 37.54, 47.3, 49.1, 49.4, 55.9, 64.7, 64.8, 67.2, 81.6, 81.7, 82.5, 97.6, 97.7, 111.2, 111.3, 120.1, 125.22, 125.24, 125.3, 127.2, 127.8, 139.31, 139.33, 141.4, 141.44, 143.9, 143.96, 144.03, 156.1, 169.4, 169.6, 170.2, 170.3, 170.4. HRMS $C_{36}H_{42}N_2O_9NaS$ $[M+Na]^+$: calcd. 701.2503, found 701.2516.

The procedure used to prepare the protected RG^ED peptide was as follows: to a solution of Boc-L-Arg(Boc)$_2$-OH (500 mg, 1.05 mmol) in DCM (60 mL) cooled to 0 ºC in an ice bath, was added 1-hydroxybenzotriazole hydrate (HOBt) (161 mg, 1.05 mmol) and *N*-[3-(dimethylamino)-propyl]-*N'*-ethylcarbodiimide hydrochloride (EDC·HCl) (201 mg, 1.05 mmol) followed by a solution of H-D,L-GlE-Asp(O^{t}Bu)-O^{t}Bu (1 mmol) [obtained by deprotection of **5** (678 mg, 1 mmol) with diethylamine (DEA; 5 mL, 50 mmol)] in DCM (10 mL) and finally *N*-methylmorpholine (NMM; 0.11 mL, 1 mmol). The reaction mixture was stirred at room temperature for 24 h. Then, the solution was washed with 5% $NaHCO_3$ (3×30 mL) followed by 5% $KHSO_4$ (3×30 mL). The organic phase was dried over magnesium sulfate and evaporated to dryness. The crude product was purified by column chromatography (eluent: hexane/ethyl acetate 6/4) to provide protected RG^ED (mixture of diastereoisomers) as a white solid (822 mg, 0.90 mmol, 90% yield).

IR (KBr) *ν*: 3381, 1715, 1610 cm^{-1}.^{1}H NMR ($CDCl_3$, 400 MHz): δ 1.37-1.85 (m, 4H), 1.43, 1.50, 1.51 (3s, 45H), 2.59-2.72 (m, 1H), 2.73-2.87 (m, 1H), 3.02-3.22 (m, 2H), 3.72-3.89 (m, 2H), 4.08-4.27 (m, 5H), 4.55-4.71 (m, 2H), 5.49-5.66 (m, 1H), 6.11, 6.12 (2s, 1H), 6.83-7.13 (m, 2H), 9.08-9.52 (m, 2H). ^{13}C NMR ($CDCl_3$, 125 MHz): δ 24.8, 24.9, 28.0, 28.18, 28.21, 28.4, 28.5, 28.8, 29.0, 29.8, 37.56, 37.59, 44.25, 44.29, 49.3, 49.5, 53.9, 54.0, 54.5, 54.7, 64.70, 64.72, 64.9, 79.1, 79.2, 81.5, 81.6, 82.29, 82.33, 84.0, 84.1, 97.3, 97.4, 111.26, 11.32, 139.3, 141.52, 141.54, 155.05, 155.08, 155.9, 160.7, 160.8, 163.71, 163.73, 169.4, 169.5, 169.92, 169.98, 170.1, 171.97, 172.22. HRMS $C_{42}H_{69}N_6O_{14}S$ $[M+H]^+$: calcd. 913.4587, found 913.4609.

Synthesis of the PEDOT-RGED conjugate

The PEDOT-RG^{E}D conjugate was prepared using two alternative strategies (A and B) of three steps each one, which are known to provide materials with different surface properties [37]. In the first step, which is the same for the two strategies (Figure 4.2.3), PEDOT films were deposited onto steel sheets by CA under a constant potential of 1.40 V and using a 10 mM 3,4-ethylenedioxythiophene (EDOT) solution in acetonitrile containing 100 mM $LiClO_4$ as supporting electrolyte. The polymerization time (θ_1) was only 10 s. After eliminating the excess of monomer and dopant from the prepared PEDOT films and washing with acetonitrile, the second step of each strategy was addressed (Figure 4.2.3).

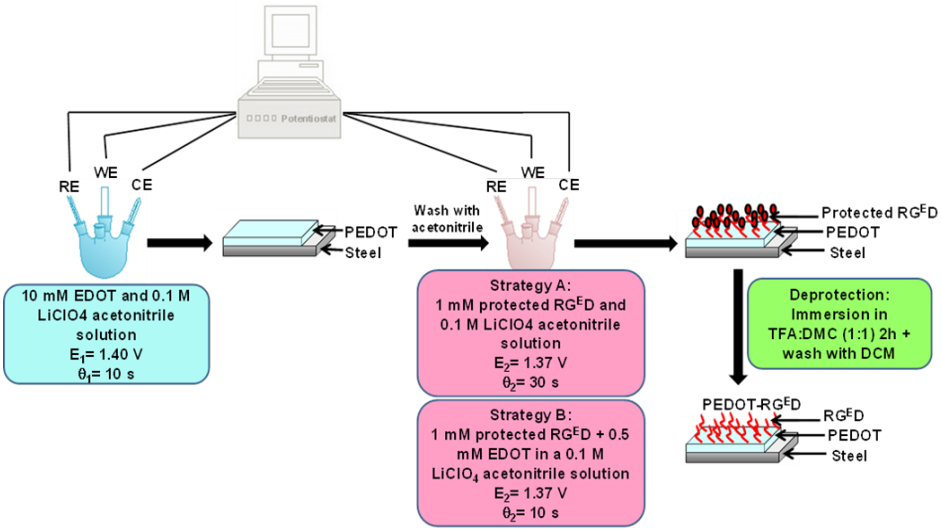

Figure 4.2.3. Scheme displaying the two synthetic strategies (A and B) used to prepare PEDOT-RG^{E}D. Each strategy involved a three-step process, even though A and B only differ in the conditions used for the intermediate step. RE, WE and CE refer to reference electrode, working electrode and counter electrode, respectively.

In strategy A, the electrode coated with the PEDOT was introduced in a cell containing an acetonitrile solution with 1 mM of protected RG^{E}D and 0.1 M $LiClO_4$, a constant potential of 1.37 V being applied during a time θ_2 = 30 s. In strategy B, the PEDOT film was introduced

in a cell filled with a 1 mM RG^ED, 0.5 mM EDOT and 0.1 M $LiClO_4$ acetonitrile solution. In this case, a constant potential of 1.37 V was applied during θ_2 = 10 s only. Accordingly, the main differences between strategies A and B can be summarized as follow:

- the generation medium used in B for the preparation of the conjugate contains both peptide and monomer in the second step, while that employed in A only contains peptide;
- the polymerization time, θ_2, is significantly larger in A than in B.

These modifications are expected to affect considerably the roughness and wettability of the surface [37]. Finally, in the last step, which was identical for strategies A and B (Figure 4.2.3), desired PEDOT-RG^ED conjugates were obtained by immersing electrodes coated with the PEDOT-(protected RG^ED) systems into a 1:1 trifluoroacetic acid:dichloromethane mixture (TFA:DCM) by 2 hours and, subsequently, washing with DCM. Thus, this step was exclusively focused on the deprotection of the peptide fragments once they have been attached to the CP chains. Hereafter, conjugates derived from strategies A and B have been labelled as PEDOT-RG^ED/A and PEDOT-RG^ED/B, respectively.

The average thickness, as determined by contact profilometry, of PEDOT-RG^ED/A and PEDOT-RG^ED/B films was 296±21 and 472±15 nm, respectively. On the other hand, PEDOT films used as a control during the whole work were prepared by immersing the films achieved in the first step into a cell containing an acetonitrile solution with 0.1 M $LiClO_4$ (i.e. without peptide and monomer) and applying a constant potential of 1.37 V during θ_2= 10 s. This methodology allowed us to obtain CP films with doping levels similar to that achieved for PEDOT-RG^ED/B. The average thickness of films derived from this process was 280±44 nm.

Comparison of the FTIR spectra of PEDOT, PEDOT-RG^ED/A and PEDOT-RG^ED/B (Figure 4.2.4) corroborates the incorporation of the

RG^{E}D peptide. Thus, the amide II and amide III bands, which arise from the coupling between the N−H in-plane bending and C−N stretching modes, are clearly recognizable at approximately 1520 and 1320 cm^{-1}, respectively, for the two conjugates. Unfortunately, the Arg and Asp side chain bands at around 1620 and 1708 cm^{-1} [38], respectively, are not identified because of the overlapping with the associated to the thiophene ring (C=C and C–C stretching) of PEDOT [23,39].

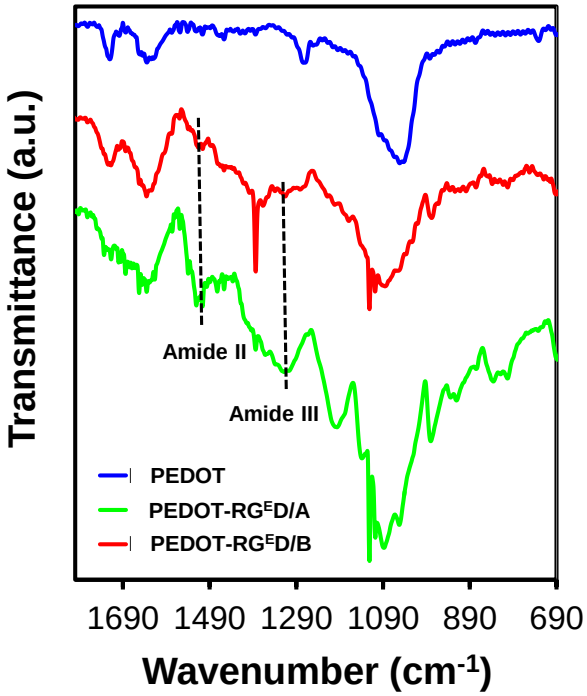

Figure 4.2.4 FTIR spectra of PEDOT, PEDOT-RG^{E}D/A and PEDOT-RG^{E}D/B.

The chemical structure of PEDOT-RG^{E}D films was further characterized by XPS. Table 4.2.1 compares the surface atomic compositions. The penetration of X-ray radiation using the conditions described in Methods section is expected to be ~10 nm, even though in this case the penetration is unknown because of both the nanometric thickness and porosity (next sub-section) of the films. This feature explains the detection of a small percentage of nitrogen

in PEDOT samples, which cannot be attributed to traces of acetonitrile since samples were stored for almost two weeks before XPS analyses. Thus, detailed interpretation of the N1s (see below) allowed us to conclude that the nitrogen detected in the composition of PEDOT comes from the AISI 316 steel substrate. However, the N1s increases from 0.43% in PEDOT to 0.81% and 1.58% in PEDOT-RG^{E}D/A and PEDOT-RG^{E}D/B, respectively, supporting the successful incorporation of the peptide. For PEDOT, the C/S ratio, 6.22, is close to the theoretical value of 6.00, while such ratio increases to 6.90 and 7.20 for PEDOT-RG^{E}D/A and PEDOT-RG^{E}D/B, respectively. This observation is consistent with the fact that the increment of the content of C in the two conjugates is due to the incorporation of the RG^{E}D peptide.

	C1s	N1s	O1s	S2p	Cl2p
PEDOT	50.56	0.43	36.90	8.12	3.99
PEDOT+TFA	57.74	0.47	31.62	8.80	1.17
PEDOT-RG^{E}D/A	62.01	0.81	27.85	8.98	0.35
PEDOT-RG^{E}D/B	61.54	1.58	27.78	8.55	0.55

Table 4.2.1 Atomic percent composition (C1s, O1s, N1s, S2p and Cl2p) obtained by XPS for PEDOT, PEDOT-RG^{E}D/A and PEDOT-RG^{E}D/B samples.

Figures 4.2.5a-d displays the high-resolution XPS spectrum in the C1s, N1s, O1s and S2p regions for PEDOT-RG^{E}D/B, the spectra for PEDOT-RG^{E}D/A being reported in the Figure 4.2.6. Before discussing the analysis, it should be mentioned that the peaks of the peptide may be influenced by those of PEDOT and vice versa, explaining the small deviations found in some peaks with respect to the values reported in the literature.

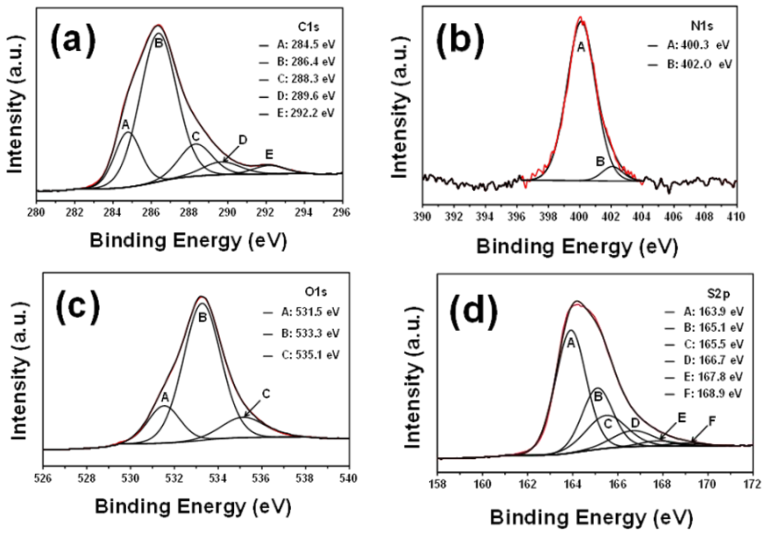

Figure 4.2.5 High-resolution XPS spectra for PEDOT-RG^{E}D/B: C1s (a), N1s (b), O1s (c) and S2p (d) regions. Peaks from deconvolution are also displayed. The red line corresponds to the experimental profile while the black line is the sum of the deconvoluted peaks.

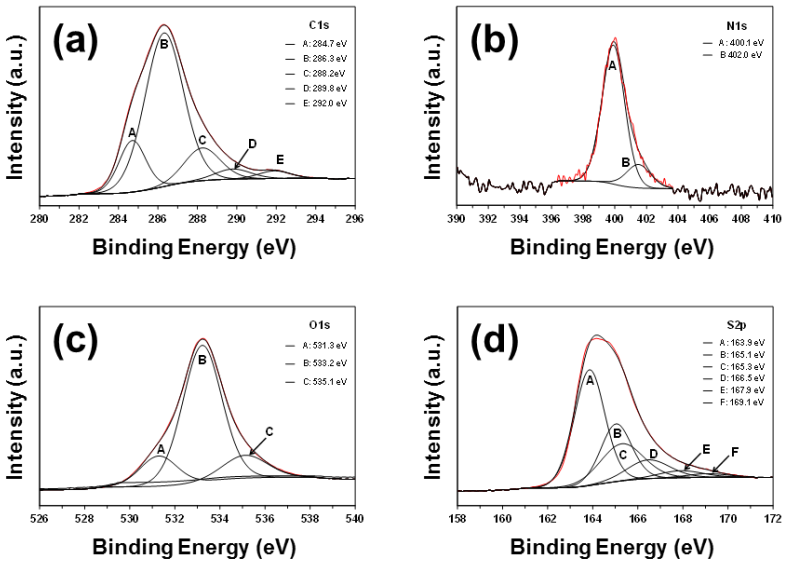

Figure 4.2.6 (a) High resolution XPS spectra and peaks from deconvolution for PEDOT-RG^{E}D/A: (a) C1s region, where the five Gaussian curves have been attributed to saturated and conjugated C–C (284.7 eV) and C=C–O (286.3 eV)

bonds of PEDOT chains, the C=O of amide (288.2 eV), the C–N bonds of the Arg gaunidinium group (289.8 eV) and the C–F_3 component of residual TFA molecules (292.0 eV) arising from the deprotection step in the synthesis; (b) N1s region, where the peak centered at 400.1 eV has been attributed to the guanidinium and amide groups while the peak at 402.0 corresponds to impurities of the substrate; (c) O1s region, where the three Gaussian curves have been attributed to the carboxylate groups in the conjugated RG^ED peptide (531.3 eV), the C–O–C bond in the ethylene bridge of PEDOT (533.2 eV) and C=O of contamination products produced during anodic polymerization (535.1 eV); and (d) S2p region, where the Gaussian curves have been assigned to the spin-split sulfur coupling $S2p_{3/2}$ and $S2p_{1/2}$ for the C–S–C bond of the thiophene ring (163.9 and 165.1 eV, respectively) in PEDOT, its homologous with positively charged sulfur (*i.e.* C–S^+–C at 167.9 and 169.1, respectively), and the C–S–C bond of the side chain of the GlE residue in the peptide (165.3 and 166.5 eV, respectively).

Deconvolution of the C1s peak led to five Gaussian curves that has been attributed to saturated and conjugated C–C (284.5 eV) and C=C–O (286.4 eV) bonds of PEDOT chains [39,40], the C=O of amide (288.3 eV) [41,42], the C–N bonds of guanidinium group in Arg (289.6 eV) [42] and the C–F bonds of residual TFA molecules (292.2 eV) [42] arising from the deprotection step in the synthesis (Figure 4.2.3). The high resolution N1s spectrum shows a peak centered at 400.3 eV, which seems to include both the guanidinium (400.1 eV) and the backbone amide (400.6 eV) signals identified for the RGD peptide sequence [42]. The peak at 402.0 eV, which was also detected in PEDOT samples, has been attributed to impurities of the substrate [23].

The O1s signal consists of three components, with the most intense one at 533.3 eV corresponding to the C–O–C bond in the ethylene bridge of PEDOT [39]. The component at 531.4 eV is assigned to the carboxylate groups in the conjugated RG^ED peptide [42] while the peak at 535.2 eV corresponds to the C=O of contamination products (*e.g.* CO_2 adsorbed from the atmosphere) [23,43]. The latter is typically found in PEDOT produced by anodic polymerization and doped with lithium perchlorate [23,43]. The high

resolution XPS of the S2p region of the conjugate shows the spin-split sulfur coupling $S2p_{3/2}$ and $S2p_{1/2}$, with a separation of 1.2 eV, for the C–S–C bond of the thiophene ring (163.9 and 165.1 eV, respectively) in PEDOT, its homologous with positively charged sulfur (*i.e.* $C–S^{+}–C$ 165.5 and 166.7 eV, respectively), and the C–S–C bond of the side chain of the GlE residue in the peptide (at 167.8 and 169.0 eV, respectively) [44,45].

Spectra in the Cl2p regions for PEDOT-$RG^{E}D$/B and PEDOT-$RG^{E}D$/A show peaks at 207.6 and 209.2 eV (Figure 4.1.7), which correspond to the spin-split chloride coupling $Cl2p_{3/2}$ and $Cl2p_{1/2}$, with a separation of 1.6 eV, for the Cl–O bond of the perchlorate dopant agent. The Cl/S ratios obtained using the atomic percent compositions displayed in Table 4.2.1 have been directly associated to the doping level (DL), which corresponds to the number of positive charges per thiophene ring. The DL is very high for PEDOT, DL= +0.49, indicating that the formula of the CP is: $[(EDOT^{0.49+})_n\ (ClO_4^-)_{0.49\cdot n}]_{solid}$.

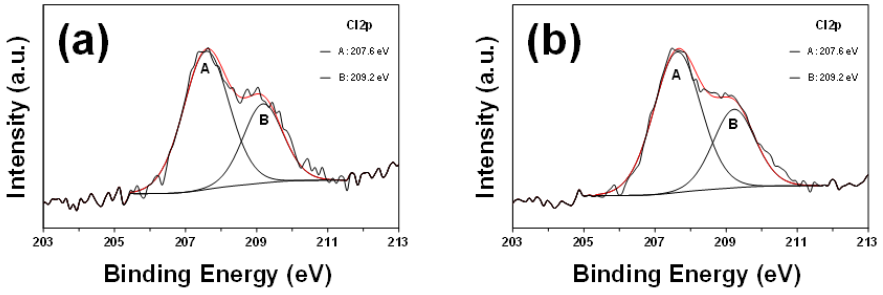

Figure 4.2.7 (a) High resolution XPS spectra in the Cl2p region and peaks from deconvolution for: (a) PEDOT-$RG^{E}D$/A and (b) PEDOT-$RG^{E}D$/B.

Very similar results (DL= +0.54) have been obtained by determining the amount of chloride with standard ion chromatography. In contrast, the DL of the two conjugates decreases to ~ +0.05, indicating a notable reduction of the salt structure behavior. In order to ascertain, one of the possible reasons of such drastic reduction, PEDOT films were immersed into a 1:1 TFA:DCM

by 2 hours and, subsequently, washed with DCM, emulating the step used to eliminate the protection of peptide fragments in PEDOT-(protected RG^ED) systems. XPS analyses of the resulting films (PEDOT+TFA in Table 4.2.1) indicate that the DL of PEDOT decreases by from +0.49 to +0.13 upon treatment with TFA.

Surface characterization

The surface morphology and topography of PEDOT-RG^ED conjugates were investigated using SEM and AFM, respectively. SEM micrographs of PEDOT-RG^ED/B (Figure 4.2.8a) indicate a structure formed by the aggregation of sticks with a fiber-like morphology, which facilitate the formation of narrow and tortuous pores. Comparison with micrographs obtained for PEDOT-RG^ED/A, as prepared PEDOT, and PEDOT treated with 1:1 TFA:DCM by 2 hours (Figure 4.2.9) indicates that the impact in the surface morphology of both end capping peptides and the applied deprotection treatment is practically negligible. Similarly, the surface topography of PEDOT-RG^ED/B (Figure 4.2.8b), that can be described as a dense and homogeneous distribution of sharp peaks grouped in clusters, is apparently indistinguishable from those of PEDOT and PEDOT-RG^ED/A (Figure 4.2.10). This topology, which is consequence of the linear growing of polymer chains (*i.e.* molecules are exclusively formed by α-α linkages because the β-positions of the thiophene ring are occupied by the dioxane ring) [46], is not altered by the incorporation of the RG^ED peptide at the ends.

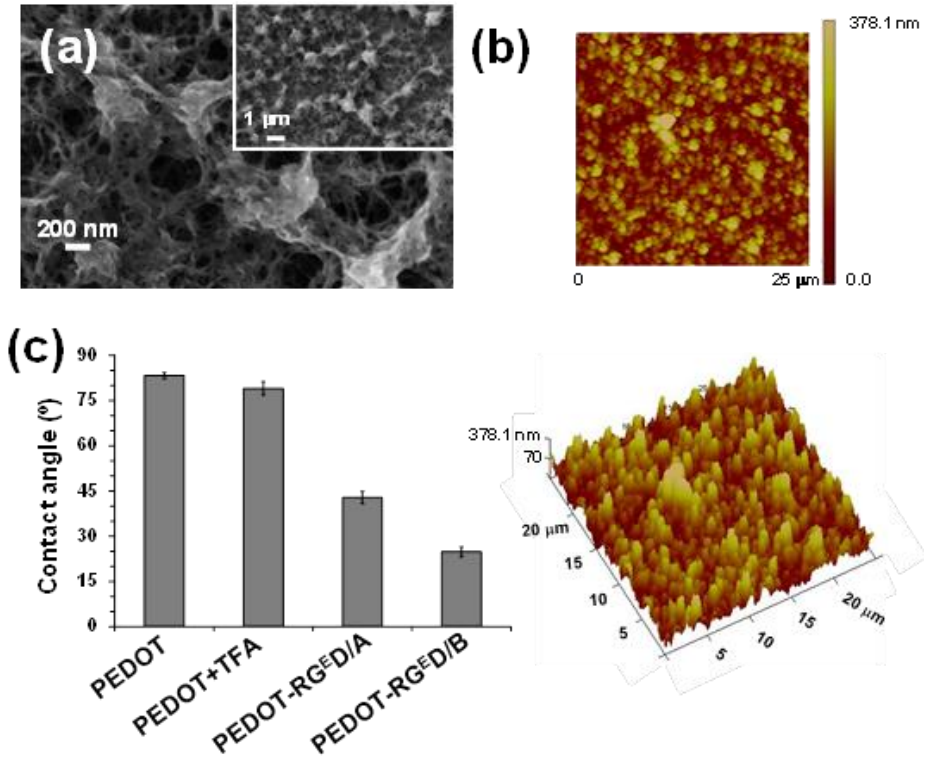

Figure 4.2.8 (a) SEM micrographs, high and low (inset) magnifications, and (b) 2D and 3D topographic images of PEDOT-RG^{E}D/B. (c) Contact angles of water (average and standard deviation of 14 independent measures) for as prepared PEDOT, PEDOT treated with 1:1 TFA:DCM by 2 hours and, subsequently, washed with DCM (PEDOT+TFA), emulating the step used to eliminate the protection of peptide fragments in PEDOT-(protected RG^{E}D) systems, and the two prepared conjugates.

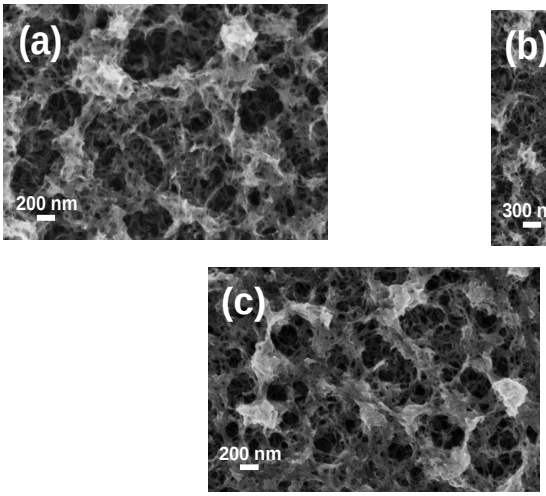

Figure 4.2.9 SEM micrographs of: (a) as prepared PEDOT; (b) PEDOT treated with 1:1 TFA:DCM by 2 hours and, subsequently, washed with DCM, emulating the step used to eliminate the protection of peptide fragments in PEDOT-(protected RG^ED) systems; and (c) PEDOT-RG^ED/A.

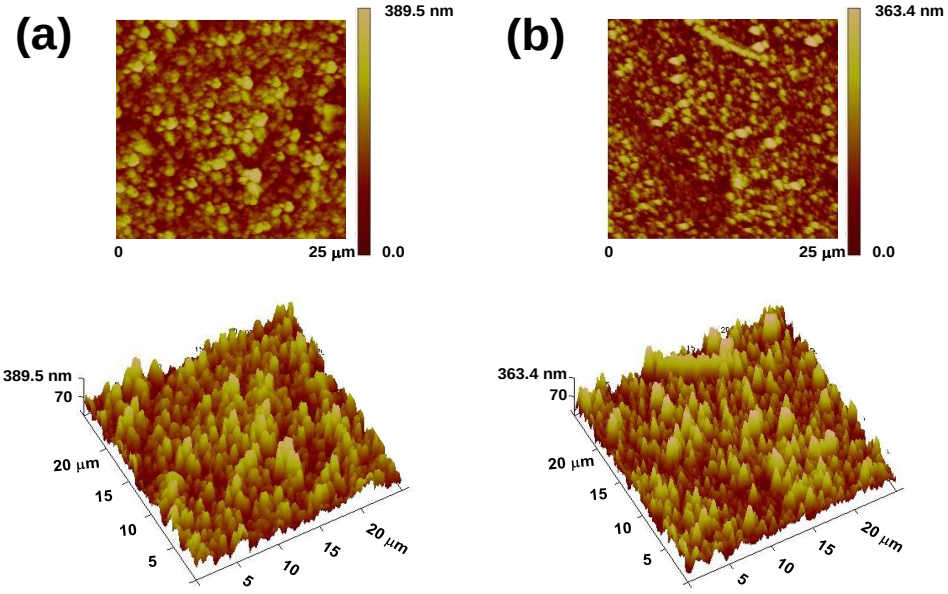

Figure 4.2.10 2D and 3D topographical AFM images: (a) as prepared PEDOT; and (b) PEDOT-RG^ED/A.

In spite of their morphological similarity, the surface roughness of PEDOT-RG^{E}D conjugates has been found to depend on the approach used in the intermediate step of the synthetic process. Thus, the R_q of PEDOT and PEDOT-RG^{E}D/A (R_q= 117±28 and 114±14 nm, respectively) are ~25% lower than that of PEDOT-RG^{E}D/B (R_q= 149±22 nm). This effect has been attributed to the coexistence and competition of two chemical processes in the intermediate step of strategy B: growth of polymer chains by incorporating EDOT monomers and termination of polymer chains by incorporating RG^{E}D. In contrast, the termination was the only process present in strategy A. On the other, the thickness determined by AFM scratching tests using the tip in contact mode (Figure 4.2.11) was 350±10, 361±15 and 443±7 nm for PEDOT, PEDOT-RG^{E}D/A and PEDOT-RG^{E}D/B, respectively, these values being fully consistent with those obtained by contact profilometry.

The contact angles (θ) measured in water (Figure 4.2.8c) indicate that PEDOT is a hydrophilic material (*i.e.* $\theta < 90^o$), which should be attributed to the oxygen atoms of the fused dioxane ring. The wettability increases significantly upon the incorporation of RG^{E}D to the end of polymer chains, independently of the strategy used in the synthetic process (*i.e.* $\Delta\theta > 40^o$ in all cases). However, the effect of the synthetic strategy is not negligible, the contact angle of PEDOT-RG^{E}D/B being 18º lower than that of PEDOT-RG^{E}D/A. The increment of both wettability and R_q suggest that the conjugate derived from synthetic strategy B is more appropriated for tissue engineering applications than that produced using A. On the other hand, the contact angle determined for PEDOT treated with 1:1 TFA:DCM by 2 hours (Figure 4.2.8c) indicates that the end capping peptide is responsible of the remarkable wettability of two conjugates, the impact of the changes produced by the acid treatment being practically null ($\Delta\theta \approx 4^o$).

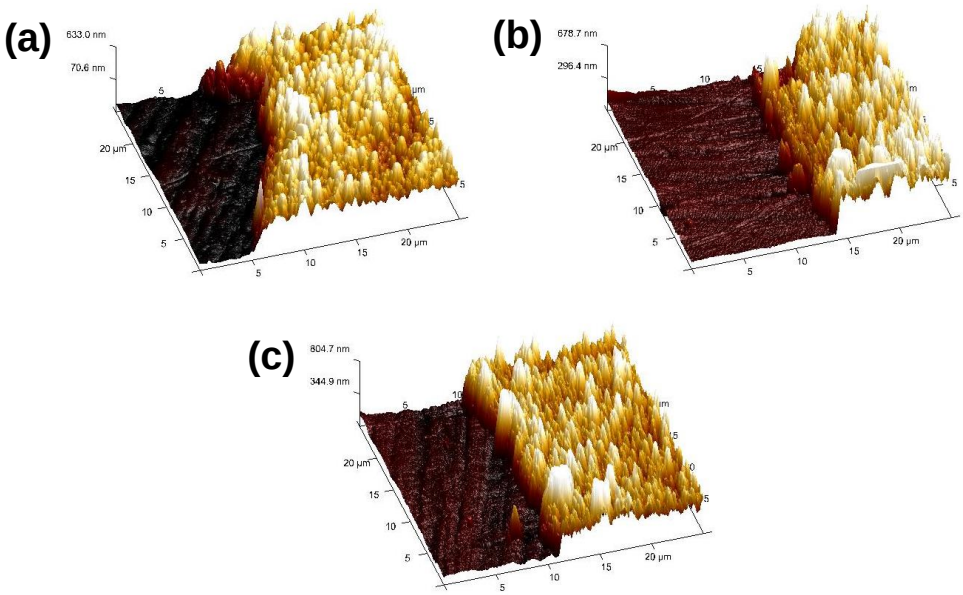

Figure 4.2.11 Determination of the thickness by scratch AFM for: (a) as prepared PEDOT; (b) PEDOT-RG^{E}D/A; and (c) PEDOT-RG^{E}D/B.

Electroactivity and electrostability

CV studies were conducted to determine the influence of the end capping peptide in the electrochemical properties of the CP. Control voltammograms recorded in PBS solution, which represents a physiological medium, are displayed in Figure 4.2.12a. The ability to exchange charge reversibly, hereafter denoted electroactivity, increases with the similarity between the anodic and cathodic areas of the control voltammogram. The electroactivity of PEDOT-RG^{E}D/A and PEDOT-RG^{E}D/B is, respectively, 57% and 75% higher than that of PEDOT. This feature points out the remarkable success of the strategy based on the design of CP-peptide conjugates by chemical similarity. Thus, conjugation between the two components through a synthetic amino acid bearing the repeat unit of PEDOT as side chain rather than using long and flexible linkers, as is frequently done, facilitates the movement of charge from the bulk to the film-solution interface during the oxidation process (or from the interface

to the bulk in the reduction process). Furthermore, charges located at ionized Arg and Asp residues, which are placed at the surface of film, also contribute to facilitate the access or escape of dopant ions during the redox processes. Consequently, the flow of ions is higher for PEDOT-RG^{E}D than for PEDOT. On the other hand, the ability to store charge is 11% higher for PEDOT-RG^{E}D/B than for PEDOT-RG^{E}D/A. This has been attributed to the accessibility of both PEDOT fragments and RG^{E}D peptides at the surface of films, which is promoted by synthetic strategy B (Figure 4.2.12b). These surface characteristics affect not only to the electroactivity, roughness and wettability but also to the electrochemical stability (electrostability).

The electrostability was evaluated by applying ten consecutive oxidation-reduction cycles in PBS. Figure 4.2.12c represents the LEA relative to the first cycle against the number of cycles. For PEDOT, the LEA stabilizes at 17% in the fourth cycle, reaching a plateau that reflects the high electrochemical stability of this CP. In contrast, the LEA grows progressively with the number of cycles for PEDOT-RG^{E}D/A, the observed value after 10 cycles being LEA= 29%. PEDOT-RG^{E}D/B exhibits an intermediate behavior. Thus, the LEA slowly increases with the number of redox cycles (*i.e.* LEA=22% after 10 cycles) and, simultaneously, tends to stabilize around a slightly higher value. According to these results, the conjugation of RG^{E}D has a negative effect in the electrochemical stability of PEDOT, which should be attributed to the degradation of the peptide during the oxidation and reduction processes. This undesirable effect is partially mitigated by the synthetic strategy B, which takes advantage of the excellent electrochemical properties of PEDOT (Figure 4.2.12b). Thus, negative effects on the electrostability caused by the peptide deterioration decrease with increasing surface reachability of PEDOT chains.

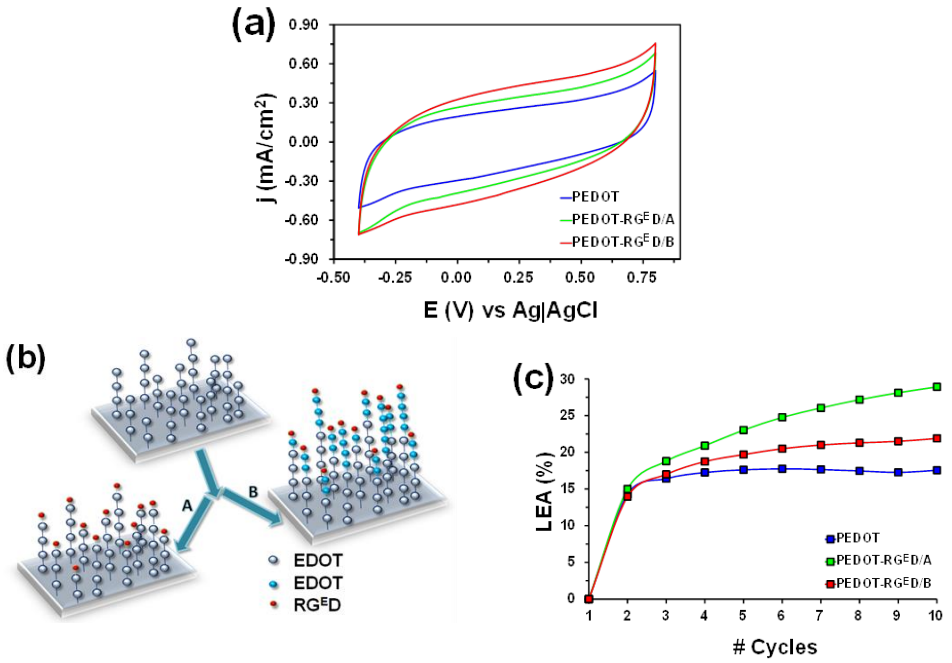

Figure 4.2.12 (a) Control voltammograms of PEDOT, PEDOT-RG^{E}D/A and PEDOT-RG^{E}D/B in PBS. Initial and final potentials, −0.40 V; reversal potential, 0.80 V; scan rate, 50 mV s^{-1}. (b) Scheme reflecting surface structural differences between PEDOT-RG^{E}D/A and PEDOT-RG^{E}D/B conjugates. (c) LEA against the number of consecutive oxidation and reduction cycles in 0.1 M PBS for PEDOT, PEDOT-RG^{E}D/A and PEDOT-RG^{E}D/B.

Molecular conformation and optical properties

The conformational potential energy surface of the RG^{E}D peptide was systematically explored using a procedure inspired in the build-up method early developed by Scheraga and coworkers [47]. This method uses the geometries of smaller peptide segments to build the structures of larger segments. Accordingly, 559 starting conformations were constructed by combining the most stable minima identified for each of the involved residues. The geometry of all these structures was optimized at the B3LYP/6-31+G(d,p) level of theory in aqueous solution, solvent effects being modeled by the Polarizable Continuum Model (PCM). The resulting 552 minima

were grouped in a list of 26 unique minimum energy conformations, which was constructed by assessing the similarities among the different structures (clustering of structures described in the Methods section). Figure 4.2.13a displays the distribution of such unique minima in the maps constructed using the backbone dihedral angles of Arg (ω,ψ), GlE (φ,ψ) and Asp (ω,φ) residues. As it can be seen, Arg and Asp tend to adopt an extended arrangement with ψ≈ 180º and φ≈ 180º, respectively, even though the latter also shows three minima with φ≈ 60º. Despite this apparent backbone homogeneity, both Arg and Asp present significant conformational variability at their side chains giving place to different networks of side chain···backbone interactions (Figure 4.2.13b). In contrast, the GlE residue exhibits remarkable conformational variability at the backone displaying minima in the α_R (φ,ψ≈ -70º,-20º), C_{7eq} (φ,ψ≈ -80º,80º) and β (φ,ψ≈ -150º, 60º) regions of the φ,ψ-map.

Figure 4.2.13b depicts the five unique minimum energy conformations with relative energy (ΔE) lower than 5 kcal/mol, which have labeled with letters A-E in increasing order of energy. The lowest energy minimum (A) is stabilized by a complex network of hydrogen bonds that include:

- two backbone···backbone (b-b) interactions involving the ionized N- and C-terminal group and the C=O and N-H moieties of the adjacent amide groups (*i.e.* known as C_5 interactions because atoms involved in such known define a five-membered ring);
- one side chain····backbone (sc-b) salt bridge between the carboxylate side group of Asp and the ionized N-terminus;
- one side chain···side chain (sc-sc) interaction between the guanidium group of Arg and the dioxane ring of GlE.

In addition, this structure is stabilized by a N–H···π interaction between the guanidium group of Arg and the thiophene ring of GlE. Such interaction has not been identified in any other unique

minimum with $\Delta E \leq 5$ kcal/mol. The next minimum (B), which is practically isoenergetic to A ($\Delta E < 0.1$ kcal/mol), exhibits the same b-b and sc-b interactions. Thus, the only difference between A and B refers to the sc-sc interaction that, in the latter, consists of a hydrogen bond between the guanidium group and the C=O of Arg.

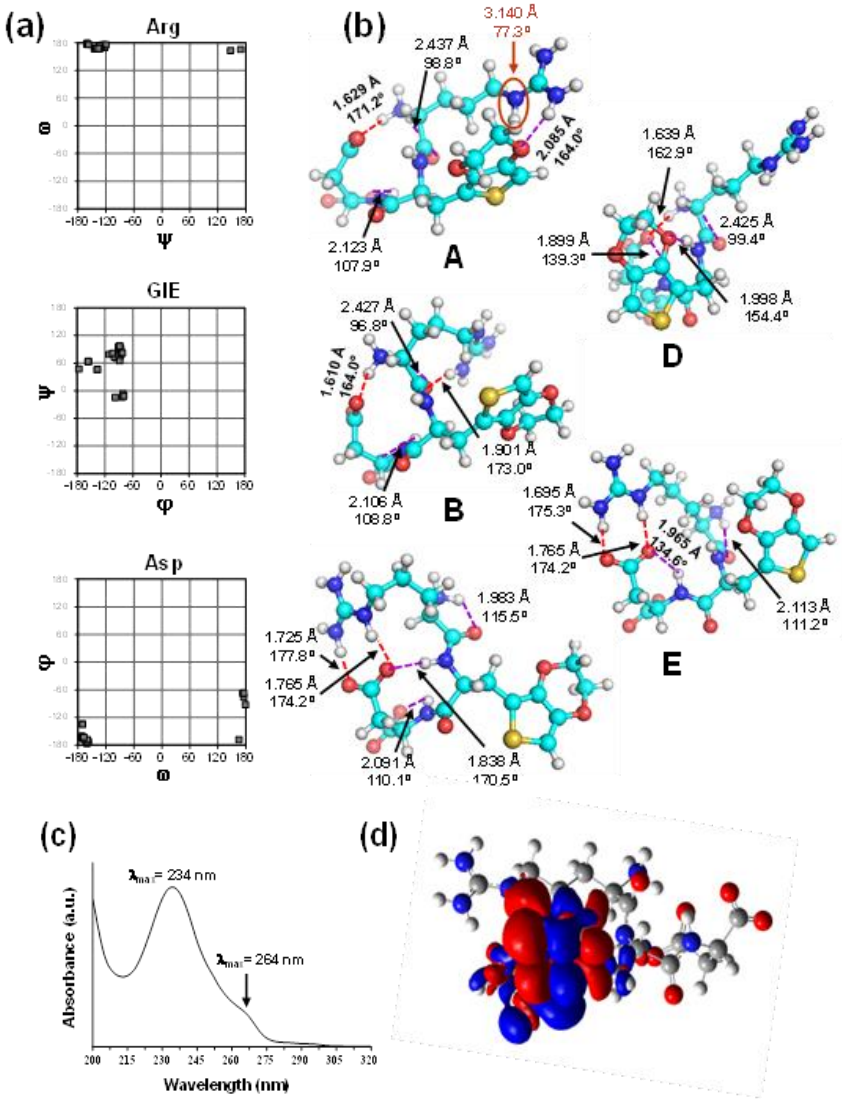

Figure 4.2.13 (a) Conformational maps constructed considering the backbone dihedral angles of the maps Arg (ω,ψ), GlE (φ,ψ) and Asp (ω,φ) residues, using

the 25 unique minimum energy conformations identified in the clustering analysis for $RG^{E}D$. (b) Representation of the five low-energy structures (labeled from A to E in increasing order of energy) found in the clustering analysis for $RG^{E}D$/B in PBS. Salt bridges and hydrogen bonds are indicated by red and violet dashed lines, respectively. The red circle in A indicates that the N–H group involved in the N–H$\cdots\pi$ interaction with the thiophene group. Distances and angles associated to each of these interactions are given in Å and degrees, respectively. (c) UV-vis spectrum recorded for acetonitrile dilute $RG^{E}D$ solution (37 μM). (d) Electronic density difference (excited – ground) corresponding to the first electronic transition ($\lambda^{(1)}_{max}$). Blue (red) regions indicate an increase (decrease9 of electron density upon electronic transition.

The most characteristic interaction in the next minimum (C), with ΔE= 1.5 kcal/mol, corresponds to a double sc-sc salt bridge between the guanidium and carboxylate groups of Arg and Asp, respectively. As a consequence of such interaction, charged side groups are less exposed to the solvent in C than in A and B. This conformer also presents b-b interactions between the charged ammonium-end group and the amide of Arg as well as between the carboxylate-end group and the amide of Asp. In minimum D (ΔE= 3.9 kcal/mol) the Arg side chain adopts a fully extended arrangement that precludes the participation of the guanidium group in the formation of sc-sc and sc-b intramolecular interactions. Thus, interactions observed in D are similar to those described for A-C. Finally, minimum E, with ΔE= 4.7 kcal/mol, exhibits a double sc-sc salt bridge between Arg and Asp as well as two sc-b interactions involving the charged end groups. These are similar to the interactions identified for C.

Results displayed in Figure 4.2.13b indicate that, in general, the overall shape of the unique minimum energy conformations with $\Delta E < 5$ kcal/mol is appropriate to form intermolecular interactions with the integrin receptor. Thus, the general shape adopted by these conformations can be simply described as a small and deformed hairpin with the charged groups pointing outwards. As PEDOT chains are connected to $RG^{E}D$ through the side group of the GlE residue, all these conformations are not expected to be affected by the formation of the conjugate. Accordingly, the functionality of the

RGD adhesive sequence is expected to the preserved in the peptide of PEDOT-RG^{E}D conjugates.

While EDOT absorption spectrum exhibits a broad peak characterized by a double hump (264 nm and 255 nm), the spectrum of RG^{E}D in similar conditions (diluted in acetonitrile solution) exhibits a clear transition maximum appears at 234 nm with a small shoulder at 264 nm (see Figure 4.2.13c). In a previous work [24] on EDOT, we showed the importance of accounting for several conformations of such flexible structure to reproduce the experimental data with computational means. In the same vein, optical properties were here simulated in acetonitrile for A-E conformations starting from the five above-mentioned structures. All conformations present similar spectra with two close maximum absorption wavelengths ($\lambda^{(1)}_{max}$ and $\lambda^{(2)}_{max}$) at 234 nm and 232 nm (associated oscillator strengths > 0.1). No significant variation was observed when selecting one conformation or another. Looking at the electronic density difference of these transitions of A conformation, it is crystal clear that the electronic transition occurs on the G^{E} moiety and is therefore not affected by Arg and Asp flexibility (Figure 4.2.13d, see Figure 4.2.14 for similar plots for B-D). Comparing the computational results with experiment, the computed peak at 234 nm reproduces the experimental main peak while the observed experimental shoulder at 264 nm could not be resolved using such methodology. The shoulder is therefore not the result of conformational effects but is related to the fine structure of G^{E}.

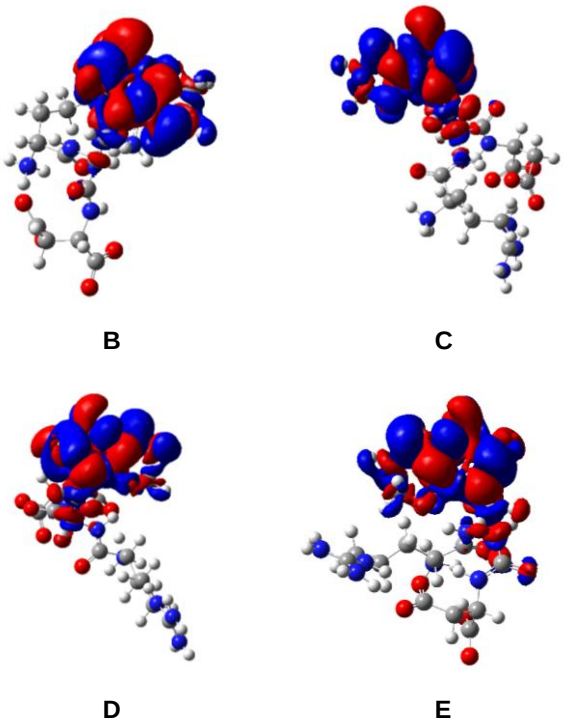

Figure 4.2.14 Electronic density difference (excited - ground) corresponding to the first and second electronic transition ($l^{(1)}_{max}$) of conformation B-E. Blue (red) regions indicate an increase (decrease) of electron density upon electronic transition.

Monitoring the influence of $RG^{E}D$ in cell adhesion

The effect of the peptide in cell adhesion was evaluated by considering two epithelial (Vero and Saos-2) and two fibroblast (Cos-7 and MRC-5) cell lines. Vero and Cos-7 are cell lines derived from monkey kidney, while the origin of Saos-2 and MRC-5 was human bone and human lung, respectively. Quantitative results for cell adhesion assays are displayed in Figure 4.2.15a. These are expressed per area of substrate material and relative to those of TCPS, which was used as a control material. The number of cells adhered to the surface of PEDOT-$RG^{E}D$ is significantly higher than that of PEDOT and TCPS for all cell lines, evidencing cell-specific adhesion promoted via $RG^{E}D$ ligands conjugated to the PEDOT

chains. The RGD peptide has been recognized as a molecular activator of the integrin cell surface receptor, which can induce intracellular signaling pathways [48-50]. This ability is preserved in $RG^{E}D$, where the Gly of RGD has been replaced by GlE. Especially, the activation of the integrin receptor through the interactions with the $RG^{E}D$ peptide in the initial cell attachment step seems to affect subsequent cell spreading and survival through cell signaling molecules, such as focal adhesion kinase, as proposed for RGD [49]. Although this behavior is remarkable for the two conjugates, it is considerably more evident for PEDOT-$RG^{E}D$/B than for PEDOT-$RG^{E}D$/A. This has been attributed to the benefits produced by the synthetic strategy B in the properties of the resulting conjugate (*i.e.* enhancement of the roughness, wettability and electroactivity). In general, the relative viability of Saos-2 and MRC-5 human cell lines are higher favored than that of Vero and Cos-7 monkey kidney cell lines, independently of the substrate surface.

Figure 4.2.15b, which displays low magnification SEM micrographs of cells cultured onto both PEDOT-$RG^{E}D$/A and PEDOT-$RG^{E}D$/B, reveals not only the high density of adhered cells but also their homogeneous spreading onto the surface of the two conjugate films. Details about the adhesion of MRC-5 and Saos-2 cells onto the surface of PEDOT-$RG^{E}D$/B are provided in Figure 4.2.15c. As it can be seen, the cellular mechanism operating for the adhesion of the cells onto the conjugate films is the connection to the surface with filopodia. Thus, spreading of the cells is achieved through an intimate contact between cells and the surface of the films.

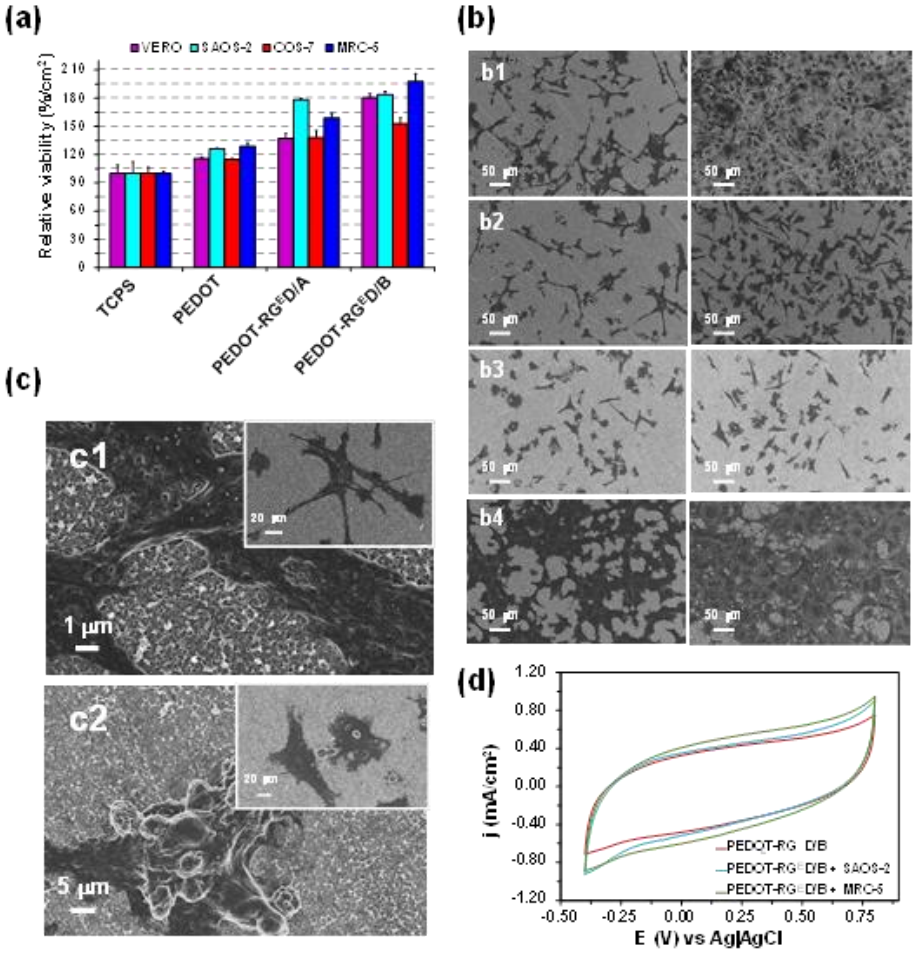

Figure 4.2.15 (a) Cellular adhesion on the surface of PEDOT, PEDOT-RG^{E}D/A and PEDOT-RG^{E}D/B. TCPS was used as a control substrate. Vero, Saos-2, Cos-7 and MRC-5 cells were cultured during 24 h. The experiments were performed using six samples for each substrate. (b) Adhesion of Vero, Saos-2, Cos-7 and MRC-5 cells (b1-b4) onto PEDOT-RG^{E}D/B. SEM micrographs reflect the homogeneous cell spreading. (c) High and low (inset) magnification SEM micrographs of Saos-2 and Cos-7 cells (c1 and c2, respectively) attached to PEDOT-RG^{E}D/B. (d) Control voltammograms in PBS of PEDOT-RG^{E}D/B uncoated and coated with Saos-2 and MRC-5 cells.

On the other hand, the particular electrochemical properties of PEDOT, which exhibits higher cell viability than inert TCPS, also contribute to the superior cell attachment of PEDOT-RG^{E}D. Thus,

the ability of this ECP to exchange ions with the cell through the cellular membrane is known to favor the formation of cell-surface interactions [51]. In order to evaluate the influence of cultured cells in the electrochemical activity of the conjugates, PEDOT-RG^{E}D/A and PEDOT-RG^{E}D/B films coated with cell monolayers were investigated by CV in PBS. Figure 4.2.15d compares the control voltammograms recorded for PEDOT-RG^{E}D/B coated with Saos-2 and MRC-5 cells with that obtained for the uncovered material (results obtained for PEDOT-RG^{E}D/A samples coated with are displayed in Figure 4.2.16). Cells do not affect the profile of the voltammograms, even though they provoke an enhancement of both the anodic current density at the reversal potential and of the electroactivity, which reflect the electrobioactivity of the prepared conjugates. Thus, cell monolayers increase the mobility of ions at the interfaces, the electroactivity increasing by about 10-25% with respect to the uncoated conjugates. According to these results, adhered cells promote the exchange of ions at the conjugate–cell interface rather than block the channels that allow the access and escape of ions.

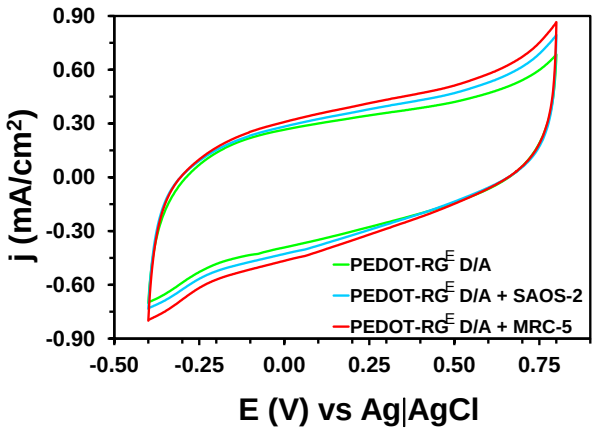

Figure 4.2.16 Control voltammograms in PBS of PEDOT-RG^{E}D/A uncoated and coated with Saos-2 and MRC-5 cells.

4.2.4 Conclusions

The $RG^{E}D$ peptide, which is an analogue of the adhesive RGD sequence, has been designed by chemical similarity with PEDOT and, subsequently, prepared through chemical synthesis. After this, PEDOT-$RG^{E}D$ has been obtained by anodic polymerization, the EDOT side group of the GlE residue acting as a linker between the peptide and the polymer. Two different strategies have been used to produce materials with different surface roughness, wettability and electrochemical activity. Control onto these properties has been found to modulate the behavior of PEDOT-$RG^{E}D$ conjugates as soft bioelectroactive supports for cell attachment.

Because the cell recognition abilities of the RGD motif remain in the $RG^{E}D$ sequence, cell attachment and spreading on PEDOT-$RG^{E}D$ have been significantly promoted with respect to PEDOT. Furthermore, the electrochemical activity of the CP is preserved in the conjugate because both the small size of the peptide and the utilization of an EDOT ring as linker between the CP and the peptide, do not affect the transport of charge. Indeed, the electrochemical activity of the conjugates increases upon the adhesion of cell monolayers. The successful design and controlled preparation of effective CP-peptide conjugates open new and varied possibilities within the biomedical field. For example, the fabrication of multifunctional biomedical platforms for regenerative medicine, combining the presence the $RG^{E}D$ adhesive sequence with other functional peptides in the same platform, and the development of artificial skin based on ECPs that, in addition, promote the regeneration of natural skin [52].

4.2.5 References

1. E. Ruoslahti, M.D. Pierschbacher; *Science*, vol. 238, pp. 491–497, 1987.
2. M.D. Pierschbacher, E. Ruoslahti; *Nature*, vol. 309, pp. 30–33, 1984.
3. R.O. Hynes; *Cell*, vol. 69, pp. 11–25, 1992.
4. G. Cheng, V. Castelletto, R.R. Jones, C.J. Connon, I.W. Hamley; *Soft Matter*, vol. 7, pp. 1326–1333, 2011.
5. A. Li, A. Hokugo, A. Yalom, E.J. Berns, N. Stephanopoulos, M.T. McClendon, L.A. Segovia, I. Spigelman, S.I. Stupp, R. Jarrahy, *Biomater.*, vol. 35, pp. 8780–8790, 2014.
6. K. Fukunaga, H. Tsutsumi, H. Mihara; *Biopolymers*, vol. 100, pp. 731–737, 2013.
7. K.M. Galler, L. Aulisa, K.R. Regan, R.N. D'Souza, J.D. Hartgerink; *J. Am. Chem. Soc.*, vol. 132, pp. 3217–3223, 2010.
8. E.S. Gil, B.B. Mandal, S.H. Park, J.K. Marchant, F.G. Omenetto, D.L. Kaplan; *Biomater.*, vol. 31, pp. 8953–8963, 2010.
9. J. Wu, J. Rnjak-Kovacina, Y. Du, M.L. Funderburgh, D.L. Kaplan, J.L. Funderburgh; *Biomater.*, vol. 35, pp. 3744–3755, 2014.
10. B.J. Kim, Y.S. Choi, H.J. Cha; *Angew. Chem. Int. Ed.*, vol. 51, pp. 675–678, 2012.
11. T.J. Dennes, G.C. Hunt, J.E. Schwarzbauer, J. Schwartz; *J. Am. Chem. Soc.*, vol. 129, pp. 93–97, 2007.
12. G. Oyman, C. Geyik, R. Ayranci, M. Ak, D. Odaci Demirkol, S. Timur, H. Coskunol; *RSC Adv.*, vol. 4, pp. 53411–53418, 2014.
13. V. Castelletto, R.J. Gouveia, C.J. Connon, I.W. Hamley; *Eur. Polym. J.*, vol. 49, pp. 2961–2967, 2013.
14. P. Viswanathan, E. Themistou, K. Ngamkham, G.C. Reilly, S.P. Armes, G. Battaglia; *Biomacromol.*, vol. 16, pp. 66–75, 2015.
15. Z. Yang, S. Yuan, B. Liang, Y. Liu, C. Choong, S.O. Pehkonen; *Macromol. Biosci.*, vol. 14, pp. 1299–1311, 2014.
16. G.M. Whitesides; *Small*, vol. 1, pp. 172–179, 2005.
17. S. Zhang; *Nat. Biotechnol.*, vol. 21, pp. 1171–1178, 2003.

18. T.Y. Liu, W.M. Hussein, Z. Jia, Z.M. Ziora, N.A.J. McMillan, M.J. Monteiro, I. Toth, M. Skwarczynski; *Biomacromol.*, vol. 14, pp. 2798–2806, 2013.
19. M. Morell, J. Puiggalí; *Polymers*, vol. 5, pp. 188–224, 2013.
20. H.A. Klok, A. Rösler, G. Götz, E. Mena-Osteritz, P. Bäuerle; *Org. Biomol. Chem.*, vol. 2, pp. 3541–3544, 2004.
21. E. De Giglio, L. Sabbatini, P.G. Zambonin; *J. Biomater. Sci. Polym. Ed.*, vol. 10, pp. 845–858, 1999.
22. E. De Giglio, L. Sabbatini, S. Colucci, G. Zambonin; *J. Biomater. Sci. Polym. Ed.*, vol. 11, pp. 1073–1083, 2000.
23. G. Fabregat, G. Ballano, E. Armelin, L.J. del Valle, C. Cativiela, C. Alemán; *Polym. Chem.*, vol. 4, pp. 1412–1424, 2013.
24. G. Fabregat, G. Ballano, J. Casanovas, A.D. Laurent, E. Armelin, L.J. del Valle, C. Cativiela, D. Jacquemin, C. Alemán; *RSC Adv.*, vol. 3, pp. 21069–21083, 2013.
25. L. Groenendaal, G. Zotti, P.H. Aubert, S.M. Waybright, J.R. Reynolds, *Adv. Mater.*, vol. 15, pp. 855–879, 2003.
26. L. Groenendaal, F. Jonas, D. Freitag, H. Pielartzik, J.R. Reynolds, *Adv. Mater.*, vol. 12, pp. 481–494, 2000.
27. S. Kirchmeyer, K. Reuter; *J. Mater. Chem.*, vol. 15, pp. 2077–2088, 2005.
28. J. Tomasi, M. Persico; *Chem. Rev.*, vol. 94, pp. 2027–2094, 1994.
29. K.D. Gibson, H.A. Scheraga; *J. Comput. Chem.*, vol. 8, pp. 826–834, 1987.
30. P.J. Flory; *Mechanics of Chain Molecules*, Interscience Publishers, New York, 1969.
31. G. Fabregat, G. Ballano, J. Casanovas, A.D. Laurent, E. Armelin, L.J. del Valle, C. Cativiela, D. Jacquemin, C. Alemán; *RSC Adv.*, vol. 3, pp. 21069, 2013.
32. J.C.P. Koo, J.S.W. Lam, G.A. Chass, L.L. Torday, A. Varro, J.G. Papp; *J. Mol. Struct. THEOCHEM*, vol. 620, pp. 231–255, 2003.
33. D. Zanuy, A. Flores-Ortega, A.I. Jiménez, M.I. Calaza, C. Cativiela, R. Nussinov, E. Ruoslahti, C. Alemán, *J. Phys. Chem. B*, vol. 113, pp. 7879–7889, 2009.

34. Y.K. Kang, B.J. Byun; *J. Comput. Chem.*, vol. 31, pp. 2915–2923, 2010.
35. M.J. Frisch, G.W. Trucks, H.B. Schlegel, G.E. Scuseria, M.A. Robb, J.R. Cheeseman, G. Scalmani, V. Barone, B. Mennucci, G.A. Petersson, H. Nakatsuji, M. Caricato, X. Li, H.P. Hratchian, A.F. Izmaylov, J. Bloino, G. Zheng, J.L. Sonnenberg, M. Hada, M. Ehara, K. Toyota, R. Fukuda, J. Hasegawa, M. Ishida, T. Nakajima, Y. Honda, O. Kitao, H. Nakai, T. Vreven, J.A. Montgomery, Jr., J.E. Peralta, F. Ogliaro, M. Bearpark, J.J. Heyd, E. Brothers, K.N. Kudin, V.N. Staroverov, R. Kobayashi, J. Normand, K. Raghavachari, A. Rendell, J.C. Burant, S.S. Iyengar, J. Tomasi, M. Cossi, N. Rega, J.M. Millam, M. Klene, J.E. Knox, J.B. Cross, V. Bakken, C. Adamo, J. Jaramillo, R. Gomperts, R.E. Stratmann, O. Yazyev, A.J. Austin, R. Cammi, C. Pomelli, J.W. Ochterski, R.L. Martin, K. Morokuma, V.G. Zakrzewski, G.A. Voth, P. Salvador, J.J. Dannenberg, S. Dapprich, A.D. Daniels, Ö. Farkas, J.B. Foresman, J.V. Ortiz, J. Cioslowski, D.J. Fox; *Gaussian, Inc.*, Wallingford CT, Gaussian 09, Revision E.01, 2009.
36. G. Fabregat, G. Ballano, E. Armelin, L.J. del Valle, C. Cativiela, C. Alemán; *Polym. Chem.*, vol. 4, pp. 1412–1424, 2013,.
37. S. Maione, G. Fabregat, L.J. Del Valle, G. Ballano, C. Cativiela, C. Alemán; *J. Pept. Sci.*, vol. 20, pp. 537–546, 2014.
38. V. Castelletto, C.M. Moulton, G. Cheng, I.W. Hamley, M.R. Hicks, A. Rodger, D.E. López-Pérez, G. Revilla-López, C. Alemán; *Soft Matter*, vol. 7, pp. 11405–11415, 2011.
39. G. Fabregat, B. Teixeira-Dias, L.J. del Valle, E. Armelin, F. Estrany, C. Alemán; *ACS Appl. Mater. Interfaces*, vol. 6, pp. 11940–11954, 2014.
40. S.A. Spanninga, D.C. Martin, Z. Chen; *J. Phys. Chem. C*, vol. 114, pp. 14992–14997, 2010.
41. D. Bhattacharyya, K.K. Gleason; *Chem. Mater.*, vol. 23, pp. 2600–2605, 2011.
42. J.S. Stevens, A.C. de Luca, M. Pelendritis, G. Terenghi, S. Downes, S.L.M. Schroeder; *Surf. Interface Anal.*, vol. 45, pp. 1238–1246, 2013.

43. N. Sakmeche, S. Aeiyach, J.J. Aaron, M. Jouini, J.C. Lacroix, P.C. Lacaze; *Langmuir*, vol. 15, pp. 2566–2574, 1999.
44. J. Chastain, Handbook of X-ray Photoelectron Spectroscopy: A Reference Book of Standard Spectra for Identification and Interpretation of XPS Data, Eden Prairie; *MN: Perkin-Elmer*, 1992.
45. G. Zotti, S. Zecchin, G. Schiavon, F. Louwet, L. Groenendaal, X. Crispin, W. Osikowicz, W. Salaneck, M. Fahlman; *Macromol.*, vol. 36, pp. 3337–3344, 2003.
46. D. Aradilla, F. Estrany, E. Armelin, C. Alemán; *Thin Solid Films*, vol. 518, pp. 4203–4210, 2010.
47. K.D. Gibson, H.A. Scheraga; *J. Comput. Chem.*, vol. 8, pp. 826–834, 1987.
48. E. Ruoslahti; *Annu. Rev. Cell Dev. Biol.*, vol. 12, pp. 697–715, 1996.
49. F.G. Giancotti; *Science*, vol. 285, pp. 1028–1033, 1999.
50. R.O. Hynes; *Cell*, vol. 110, pp. 673–687, 2002.
51. L.J. del Valle, F. Estrany, E. Armelin, R. Oliver, C. Alemán; *Macromol. Biosci.*, vol. 8, pp. 1144–1151, 2008.
52. T.F. Otero, J.G. Martínez, J. Arias-Pardilla; *Electrochim. Acta*, vol. 84, pp. 112-128, 2012.
53. T. Mosmann; *J. Immunol. Methods*, vol. 65, pp. 55–63, 1983.

CHAPTER 5

Biodegradable Nanofibrous Scaffolds as Smart Delivery Vehicles for Amino Acids

5.1 Introduction[**]

Coded AAs are not only building blocks of proteins but also play a variety of functions [1]. Among the most relevant are their actions to support the metabolism (*e.g.* glutathione is synthesized from its constituent amino acids by the sequential action of γ-glutamylcysteine synthetase [2,3] and Tyr synthesizes thyroid hormones [4]) and their role to protect the cardiovascular system (*e.g.* the body uses Arg to produce nitric oxide [5,6], which in turn reduces blood pressure by relaxing muscles in blood vessels [7,8]). From a physiological point of view, AAs are typically classified into three groups: (1) Essential AAs, which cannot be synthesized by the body (*i.e.* His, Ile, Leu, Lys, Met, Phe, Thr, Trp and Val); (2) Non-essential AAs, which are produced by the body (*i.e.* Ala, Asn, Asp and Glu); and (3) Conditional AAs, which are non-essential AAs that transform into essential under conditions of illness and/or stress (*i.e.* Arg, Cys, Gln, Tyr, Gly, Pro and Ser). Essential and conditional AAs come from the diet.

When added to the food of humans and animals, peptides and proteins are typically encapsulated to overcome some of the negative attributes observed when these biomolecules are directly furnished in the food matrix (*e.g.* loss of bioactivity, bitter taste and poor stability) [9]. Within this context, systems such as liposomes, cyclodextrins and hydrogels result in appropriate encapsulation matrices that facilitate oral delivery [10-12]. Although many studies related with the immobilization of small peptides (with even only five residues) have been reported [9,13-15], research on the encapsulation of individual AAs is very scarce [16,17]. In fact, this is an extremely complex task because of the small size of these compounds, which undergo uncontrolled release from the carrier matrix almost immediately through simple diffusive processes. From a practical point of view, the correct encapsulation and controlled release of AAs is very relevant in the livestock and fisheries sectors: a safe and nutritionally

[**] *Results presented in chapter 5 were published in J. Appl. Pol. Sci., 2017, 134, 44883.*

improved animal and fish feed supply ensures healthy animals and people. For example, microparticulate diets with crystalline AAs have embedded into bio-organic matrices (*e.g.* alginate, carrageenan and zein microparticles) loose up to 80% of their AAs within the first minute after suspending the particles in water [16,17]. Lipid-based systems (*i.e.* liposomes and lipid spray beads) are fragile, making difficult microparticles preparation [18,19].

In a different approach, Mezzenga and co-workers [20] claimed that oleoylethanolamide-based lyotropic liquid crystals are promising vehicles for the controlled release of hydrophilic AAs. More recently, Wenke and co-workers loaded D-AAs in polyurethane scaffolds (*i.e.* cylindrical foams of 3 mm diameter × 6.5 mm height), for local delivery [21]. Loaded D-AAs protected the scaffold from contamination, preventing biofilm formation, which may represent a treatment strategy for infections caused by bacteria contamination. However, although numerous studies focus on the drug or peptide loading-release behaviour of nanofibrous scaffolds [22-24], no attempt to load electrospun fibres with AAs has been made yet. It is worth noting that the nanofibers can be processed with cattle feed, enabling the delivery of the AAs upon ingestion.

The main aim of this work is to study the loading of AAs into biodegradable non-toxic PE44 NFs using the electrospinning technique. Appropriated incorporation of fibre-based formulations to cattle feed may be an attractive way to supply AAs, thus improving their bioavailability through controlled delivery. More specifically, non-polar (Ala and Phe), polar (Cys and Asn) and charged (Lys and Asp) AAs have been loaded at concentrations of 1% and 10% w/w into PE44 NFs. After this, the effect of the AAs on the wettability and the morphological, topographical and thermal properties of PE44 fibres have been investigated, paying specific attention to the chemical nature of the AA in the variation of such properties. Finally, release and degradation assays in different environments have been performed to ascertain the advantages and limitations of this AA-loading technology.

5.2 Methods

Materials

PE44 was prepared by bulk thermal polycondensation of 1,4-butanediol and succinic acid (diol/diacid molar ratio of 2.2/1) [25]. The synthetic route is summarized in Figure 5.1 Chemical characterization, viscosity and molecular masses were reported in our previous study [26].

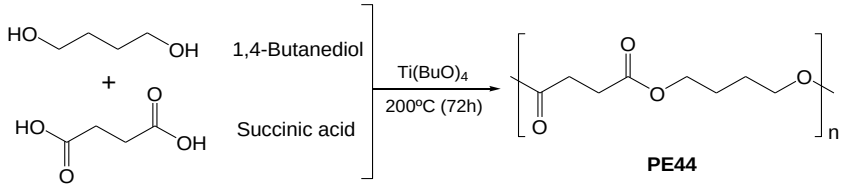

Figure 5.1 Synthesis of PE44.

L-Alanine (Ala), L-Phenylalanine (Phe), L-Cysteine hydrochloride (Cys), L-Asparagine (Asn), L-Aspartic acid (Asp), and L-Lysine hydrochloride (Lys) were purchase from Sigma-Aldrich. Dichloromethane (ACS reagent, ≥99.5%; each amino acid includes 40-150 ppm amylene as stabilizer), chloroethanol (99% by GC), trifluoroacetic acid (for HPLC, ≥99.0%), and ninhydrin reagent solution were purchased from Sigma-Aldrich. Lipase from *Rhizopus oryzae* (with activity ≥30 U/mg protein) and lipase from porcine pancreas (Type VI-S, ≥20,000 U/mg protein) were purchase from Sigma-Aldrich.

Electrospinning

This method provides a simple and versatile method for generating fibers from a rich variety of materials, including polymers, as has been extensively reported [27-29]. Mixtures of PE44 at concentration 8% w/w and AAs (Ala, Phe, Cys, Asn, Lys or Asp) at concentration 1% or 10% w/w were electrospun. Samples will be named indicating both the AA code and weight percentage (*e.g.* PE44/Ala-10 and PE44/Phe-1 corresponds to

a mixture of PE44 with 10% Ala and 1% Phe, respectively). Mixtures were prepared as follows. PE44 was dissolved in a 7:3 dichloromethane: chloroethanol solution, while AAs were dissolved in 200 µL trifluoroacetic acid (TFA). Solutions were kept under stirring for 24 hours at 37 ºC and, finally, they were mixed and loaded in a 5 mL BD plastic syringe for delivery through an 18G × 1.1/2'' needle at a mass-flow rate of 0.5 mL/h using an KDS100 infusion pump. The applied voltage was 20 kV in all cases with exception of Asn-containing mixtures, for which the applied voltage was 15 kV. Thus, for Asn-containing fibres the formation of droplets and electrospun beads was minimized at 15 kV rather than at 20 kV. All electrospun NFs were obtained using a needle tip-collector distance of 18 cm.

FTIR spectroscopy

FTIR spectroscopy was used to assess the composition of the electrospun PE44/AA NFs. Infrared absorption spectra were recorded with a Fourier Transform FTIR 4100 Jasco spectrometer in the 4000-600 cm^{-1} range. A Specac model MKII Golden Gate attenuated total reflection (ATR) with a heated Diamond ATR Top-Plate was used.

Morphology of electrospun fibres

Optical microscopy studies were performed with a Zeiss Axioskop 40 microscope. Micrographs were taken with a Zeiss Axios Cam MRC5 digital camera. Detailed inspection of texture and morphology of electrospun samples was conducted by scanning electron microscopy using a Focus Ion Beam Zeiss Neon 40 instrument (Carl Zeiss, Germany). Carbon coating was accomplished using a Mitec K950 Sputter Coater fitted with a film thickness monitor *k*150x. Samples were visualized at an accelerating voltage of 5 kV. The diameter of electrospun NFs was measured with the SmartTiff software from Carl Zeiss SMT Ltd using at least 300 values.

Atomic Force Microscopy

AFM was conducted to obtain topographic and phase images of the surface of NFs using silicon TAP 150-G probes (Budget Sensors, Bulgaria) with a frequency of 150 kHz and a force constant of 5 N/m. Images were obtained with an AFM Dimension microscope using the NanoScope IV controller under ambient conditions in tapping mode. The row scanning frequency was set between 0.4 and 0.6 Hz. The root mean square roughness (Rq), which is the average height deviation taken from the mean data plane, was determined using the statistical application of the NanoScope Analysis software (1.20, Veeco).

Calorimetry and thermal degradation

Calorimetric data were obtained by differential scanning calorimetry (DSC) with a TA Instruments Q100 series equipped with a refrigeration cooling system (RCS). Experiments were conducted under a flow of dry nitrogen with a sample weight of approximately 5 mg and temperatures ranges between 20 and 250 ºC. Calibration was performed with indium. Heating runs were carried out at a rate of 20 ºC/min. DSC experiments were performed on PE44 and two representative AA-loaded samples.

Thermogravimetric analyses (TGA) for studying thermal degradation were performed at a heating rate of 20 ºC/min (sample weight *ca.* 5 mg) with a Q50 thermogravimetric analyser of TA Instruments and under a flow of dry nitrogen. Test temperatures ranged from 50 to 600 ºC.

X-Ray diffraction (XRD)

The crystallinity of loaded and unloaded NFs was analysed by WAXD using the X'Pert Pro System (PANalytical, Netherland). Diffraction patterns were obtained using Cu Kα (λ= 0.154 nm) X-ray source operating at 30 kV and 30 mA.

Wettability

Contact angle measurements were carried out using the water sessile drop method. Images of milliQ water drops (0.5 μL) were recorded after stabilization with the equipment OCA 15EC (Data-Physics Instruments GmbH, Filderstadt). SCA20 software was used to analyse the images and determine the contact angle value, which was obtained as the average of at least six independent measures for each sample.

Release experiments

AA-loaded mats were cut into small square pieces (20×20×0.1 mm^3) which were weighed (~25 mg) and placed into polypropylene tubes. PBS, pH 7.4, and PBS supplemented with 70 *v/v*-% of ethanol (PBS-EtOH) were considered as release media. As PBS-EtOH is more hydrophobic than PBS, comparison of the results in such two environments will provide information about the influence of the hydrophilicity / hydrophobicity of the medium in the release process. More specifically, the addition of ethanol to hydrophilic PBS is expected to cause some swelling effect in the electrospun mats favoring the release of hydrophobic AAs [30].

Samples (30 mL) were incubated at 37 ºC in an orbital shaker at 80 rpm in tubes of 50 mL. Aliquots of 1 mL were taken at *t*= 0, 0.5, 1, 2, 6, 8, 24, 32, 48, 120, 144 and 168 h for the quantification of released AAs using the ninhydrin reaction, which is described below. After *t*= 168 h, the remaining medium was aspirated quantify the amount of AA remaining in the polymeric matrix. For this purpose, the PE44 matrix was dissolved by placing electrospun samples in eppendorfs with 250 μL of 7:3 dichloromethane: chloroethanol under stirring. Once PE44 was completely dissolved, 1 mL of PBS was added, and the solution was stirred again for 1 hour. Then, solutions were centrifuged and the supernatants (~1 mL) were collected to quantify the amount of AA (see below) that was not released from the electrospun NFs after 168 h. It should be remarked that, in all cases, the sum of AA released along 168 h and the AA remaining at

the PE44 matrix corresponded to the amount of AA loaded during the electrospinning process.

Additional release assays were carried out using an enzymatic solution (lipase from *Rhizopus oryzae*) as release medium. PE44/AA-10 samples (*i.e.* mats weighting approximately 20 mg) were incubated in 1 mL of lipase solution (3.3 mg/mL, $MgCl_2 \cdot 6H_2O$ 0.056% in PBS, pH= 7.2) at 37 ºC and 80 rpm. After *t*= 1, 6 and 24 h, the solutions were centrifuged and the supernatant was removed. The remaining polymeric matrices were washed three times with milliQ water and subsequently dried during 24 h at 37 ºC. After this, matrices were re-dissolved with chloroform (200 µL) to extract the remaining AA. It should be noted that, in this case, the quantification of AAs was performed considering the loaded PE44 matrix rather than the release medium to avoid the interferences induced by the building blocks of the lipase enzyme.

For all release assays, quantification of AAs was carried out using the ninhydrin reaction, which is based on the fact that AAs with a free α-amino group yield a purple (Ala and Asn), blue (Phe and Asp), yellow (Cys) or orange (Lys) coloured product when treated with an excess of ninhydrin. Under appropriate conditions, the colour intensity produced is proportional to the AA concentration. In quantitative estimation of AA using ninhydrin reagent, AA concentration is determined by comparison of the absorbance at 570 nm readings to the standard curve for each AA. Standard curves were performed with stock solutions of AAs prepared at concentrations ranging from 0 to 0.2 mM in milliQ water. Then, 200 µL of nihydrin reagent was added to the stock solution (200 µL). The mixtures were heated at 95 ºC for 15 min and, after this time, they were allowed to cool down at room temperature. Subsequently, the reaction was stopped by adding 300 µL of ethanol (50%) in water. The absorbance was read at 570 nm using aliquots of 30 µL that were previously diluted with 270 µL of milliQ water. The same process was used to determine the concentration of AAs from release assays, 200 µL of AA-containing solution and 200 µL of nihydrin reagent being employed in those cases.

All AA release tests were carried out using three replicates and the results were averaged.

Hydrolytic, enzymatic and accelerated degradation experiments

AA-loaded mats were cut into small square pieces (20×20×0.1 mm^3) which were weighed (~25 mg) and placed into polypropylene tubes. The hydrolytic (PBS) and enzymatic (porcine lipase at 1 mg/mL PBS) degradation of AA-loaded mats were studied at 37 ºC. For this purpose, samples placed in a volume of 5 mL were incubated in an orbital shaker at 80 rpm in tubes of 15 mL during four weeks. To prevent microbial degradation, media were supplemented with 0.2 mg/mL sodium azide. In addition, the media were changed to refresh weekly. The accelerated degradation medium consisted of 5 mL of a 1 N NaOH solution and the samples were evaluated at t= 30, 60, 90, 120, 150 and 180 min. The weight loss was evaluated using the following expression:

$$Weight\ loss\ (\%) = \frac{W_0 - W_t}{W_0} \qquad \text{(Eqn. 5.1)}$$

where W_0 is the dry weight before degradation and W_t is the dry weight at time t. All degradation assays were run in triplicate and the results were averaged. The morphology of the samples after degradation was examined by SEM.

5.3 Results and discussion

Preparation and characterization of loaded nanofibers

Figure 5.2 shows the FTIR spectrum of PE44 and representative PE44/AA-10 NFs in the 1450-1800 cm^{-1} region. The main absorption band, which appears at 1714 cm^{-1}, has been assigned to the C=O stretching of the PE44 ester group. Furthermore, a significant band corresponding to CH_2 asymmetric and symmetric bending stretching of PE44 is observed at

1470 cm^{-1}. The two characteristic bands of AAs and peptides emerge in the 1700-1600 and 1600-1500 cm^{-1} regions in all the spectra of PE44/AA-10 NFs, thus confirming the presence of entrapped AAs in the electrospun mats. Furthermore, the C=O stretching modes of AAs appear at relatively low wavenumbers (< 1630 cm^{-1}) indicating the formation of intermolecular hydrogen bonds, which have been related with the formation of crystals (see below). Unfortunately, the low concentration of AA in PE44/AA-1 NFs precluded their identification in the corresponding FTIR spectra.

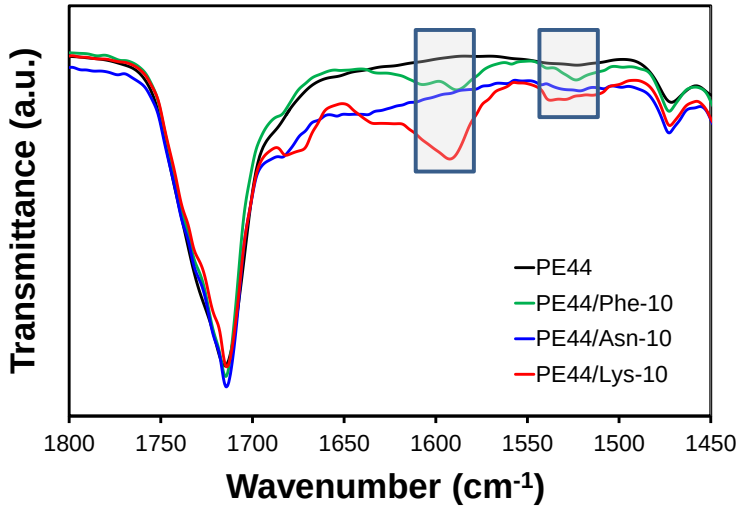

Figure 5.2 FTIR spectra of electrospun PE44, PE44/Phe-10, PE44/Asn-10 and PE44/Lys-10 fibres in the range 1800-1450 cm^{-1}. Absorption bands marked with boxes have been used to identify the AA in the loaded fibres (see text).

Optical micrographs comparing the morphology of unloaded and loaded PE44 NFs are displayed in Figure 5.3: unloaded PE44 mats consisted in continuous well-defined fibres of homogeneous size, while small beads and heterogeneity appeared after loading AAs.

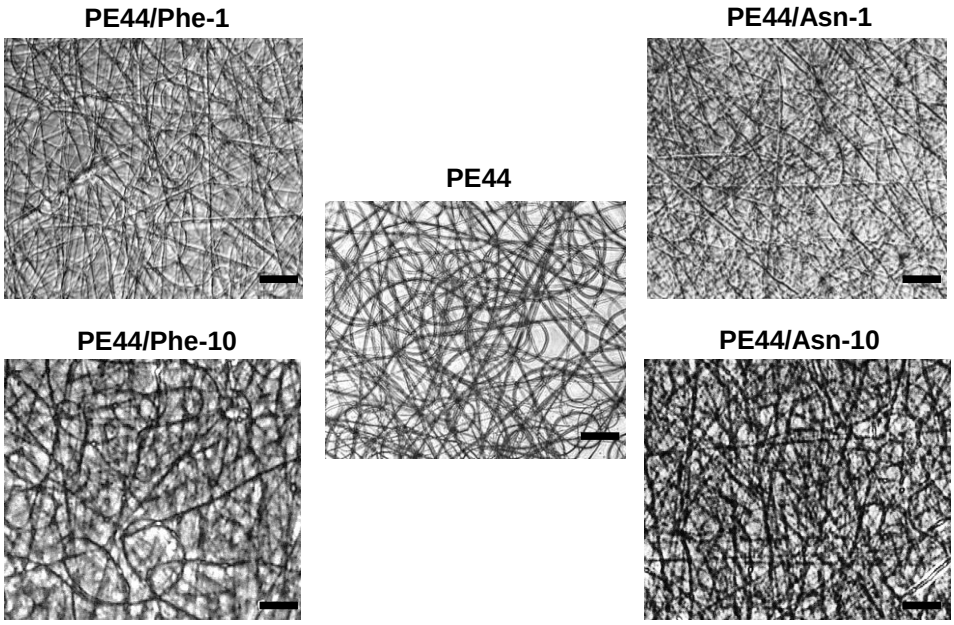

Figure 5.3 Optical micrographs of PE44 and some representative PE44/AA nanofibres obtained using with 1% and 10% w/w of AA. Scale bar: 20 μm.

These features were particularly important for the highest AA concentration, as it was corroborated by SEM micrographs (Figure 5.4). Moreover, AAs caused not only small defects but, in some cases, important morphological changes. For example, the cylindrical shape of PE44 NFs was preserved in matrices loaded with non-polar AAs (Ala and Phe), while a relatively flat ribbon-like morphology was obtained upon the incorporation of Asn and, especially, Cys. In fact, for PE44/Cys samples this effect was detected upon the incorporation of only 1% w/w Cys. These phenomena have been related with the interaction of the AAs with the solvent during the electrospinning process. Thus, velocity of the solvent evaporation, which plays a critical role in fibre formation, is probably affected by AA⋯solvent interactions that in turn depend on the chemical nature of the AA and its affinity by the different solvents participating in the mixture (*i.e.* dichloromethane, chloroethanol and TFA).

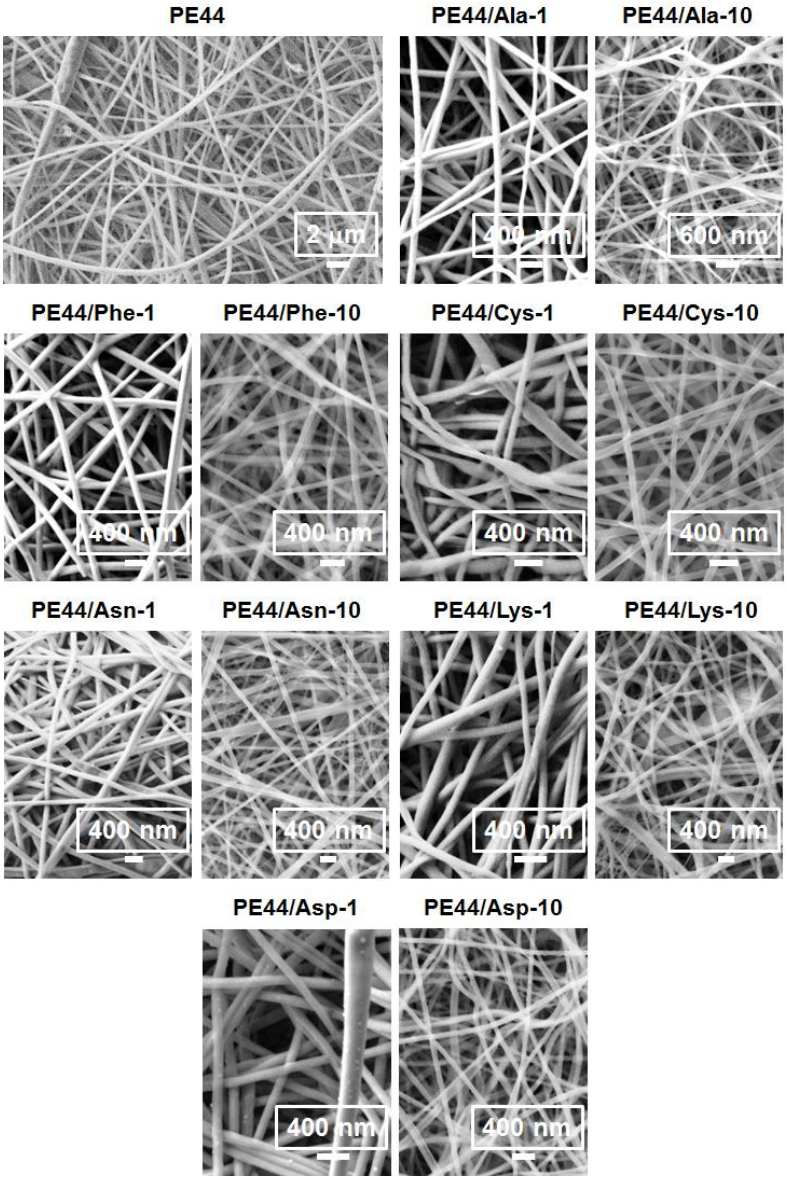

Figure 5.4 Representative SEM micrographs of PE44, PE44/Ala, PE44/Phe, PE44/Cys, PE44/Asn, PE44/Lys and PE44/Asp electrospun fibres.

Figures 5.5 and 5.6 display the diameter distributions of electrospun fibers containing 1% and 10% w/w AAs, respectively, while Table 5.1 lists the average diameter (D_{av}) and the corresponding standard deviation (σ). The diameter distribution of PE44 fibres is relatively wide with $D_{av} \pm \sigma$ =

386 ± 121 nm. However, the incorporation of AAs not only significantly reduced the fibre diameter (*i.e.* D_{av} ranges from 99 to 140 nm and from 83 to 130 nm for PE44/AA-1 and PE44/AA-10, respectively) but also enhanced in their uniformity (*i.e.* σ ranges 19 to 31 nm and from 13 to 37 nm for PE44/AA-1 and PE44/AA-10, respectively). The reduction of the fibre diameter has been attributed to the influence of the AAs in the chain entanglement of the solution mixture. Thus, both the incorporation of low-molecular weight AAs and the formation of PE44···AA interactions decreases the degree of chain entanglement in the feeding solution, which is a parameter that significantly influence the fibre diameter [31].

System	D_{av} (nm) ± σ (nm)	System	D_{av} (nm) ± σ (nm)
PE44	386 ± 121	-	
PE44/Ala-1	120 ± 24	PE44/Ala-10	108 ± 30
PE44/Phe-1	140 ± 31	PE44/Phe-10	91 ± 16
PE44/Cys-1	109 ± 28	PE44/Cys-10	91 ± 13
PE44/Asn-1	119 ± 26	PE44/Asn-10	116 ± 29
PE44/Lys-1	99 ± 19	PE44/Lys-10	130 ± 37
PE44/Asp-1	108 ± 20	PE44/Asp-10	83 ± 16

Table 5.1 Average diameter and standard deviation (D_{av} ± σ) of electrospun fibres prepared in this work.

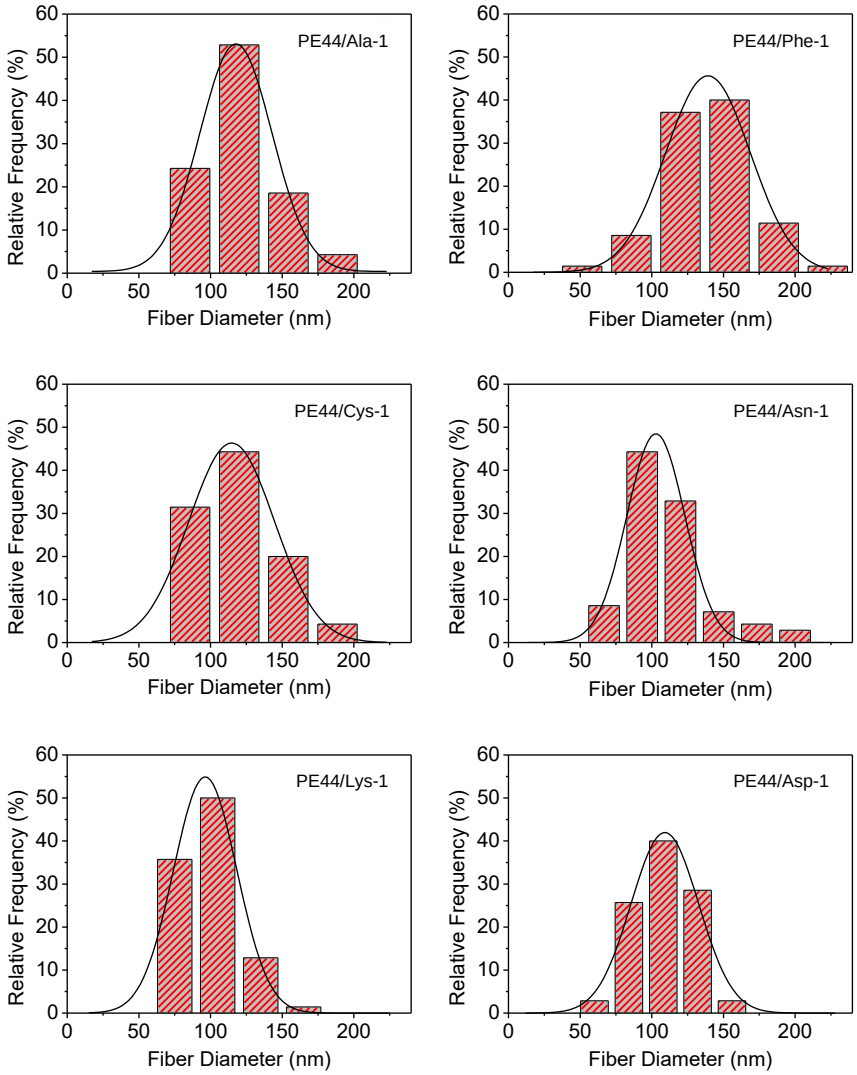

Figure 5.5 Diameter distribution of electrospun nanofibers of PE44/AA-1 samples.

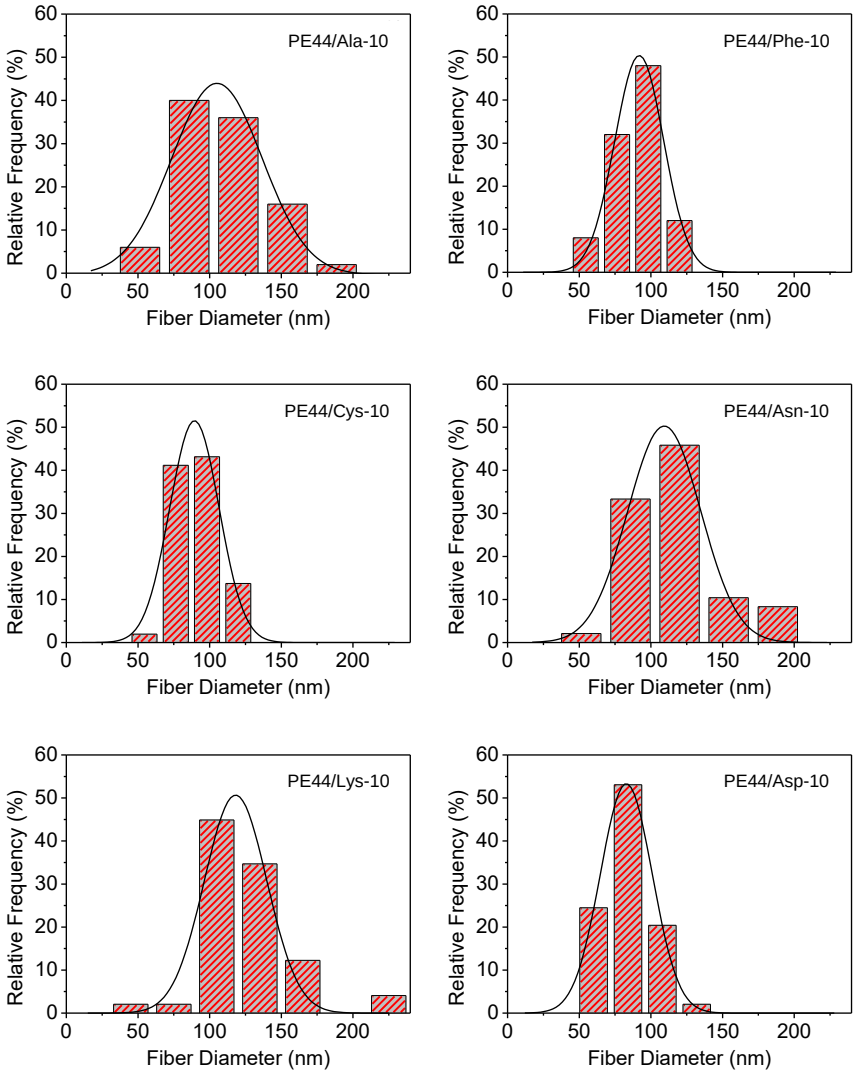

Figure 5.6 Diameter distribution of electrospun nanofibers of PE44/AA-10 samples.

AFM topography and phase images of the different PE44/AA-1 NFs (Figures 5.7 and 5.8), which are consistent with SEM images, suggest that the distribution of the loaded AAs depends on their chemical nature. Thus, PE44/Ala-1 (Figure 5.7a) and PE44/Phe-1 (Figure 5.8a) NFs present a smooth surface, no separation between the polymer matrix and the AA

being distinguished in corresponding phase images. Accordingly, both Ala and Phe are apparently immobilized inside the polymeric matrix. This is not an unexpected result since electrospun PE44 fibers are very hydrophobic (see discussion of the contact angles below), which facilitate the integration and immobilization of hydrophobic AAs, such as Phe and Ala, through the formation of non-specific van der Waals interactions. In contrast, Lys and Asp are easily observed at the surface of PE44/Lys-1 (Figure 5.7c) and PE44/Asp-1 (Figure 5.8c), respectively. Hence, irregular particles of ~30 nm, which have been attributed to crystalized AAs, are embedded at the surface of the NFs following homogeneous distribution. Finally, the characteristics of PE44/Asn-1 (Figure 5.7b) and PE44/Cys-1 (Figure 5.8b) are intermediate between those of fibres loaded with hydrophobic and charged AAs. Although Asn- and Cys-containing NFs show particles at the surface, these are significantly smaller and partially immersed into the polymeric matrix. As it was expected, all these trends are more pronounced for PE44/AA-10 NFs. Figure 5.7 displays the AFM images of PE44/Phe-10 and PE44/Asn-10. The former shows a very smooth surface morphology while the latter exhibits Asn particles partially immersed in the polymeric phase. Overall, these results reflect that AA⋯solvent interactions during the electrospinning process are responsible for the distribution of AA particles into the resulting polymeric NFs. Accordingly, non-polar AAs are totally immersed into the polymeric matrix, whereas polar and charged AAs form crystalline domains that remain at the surface of the fibres.

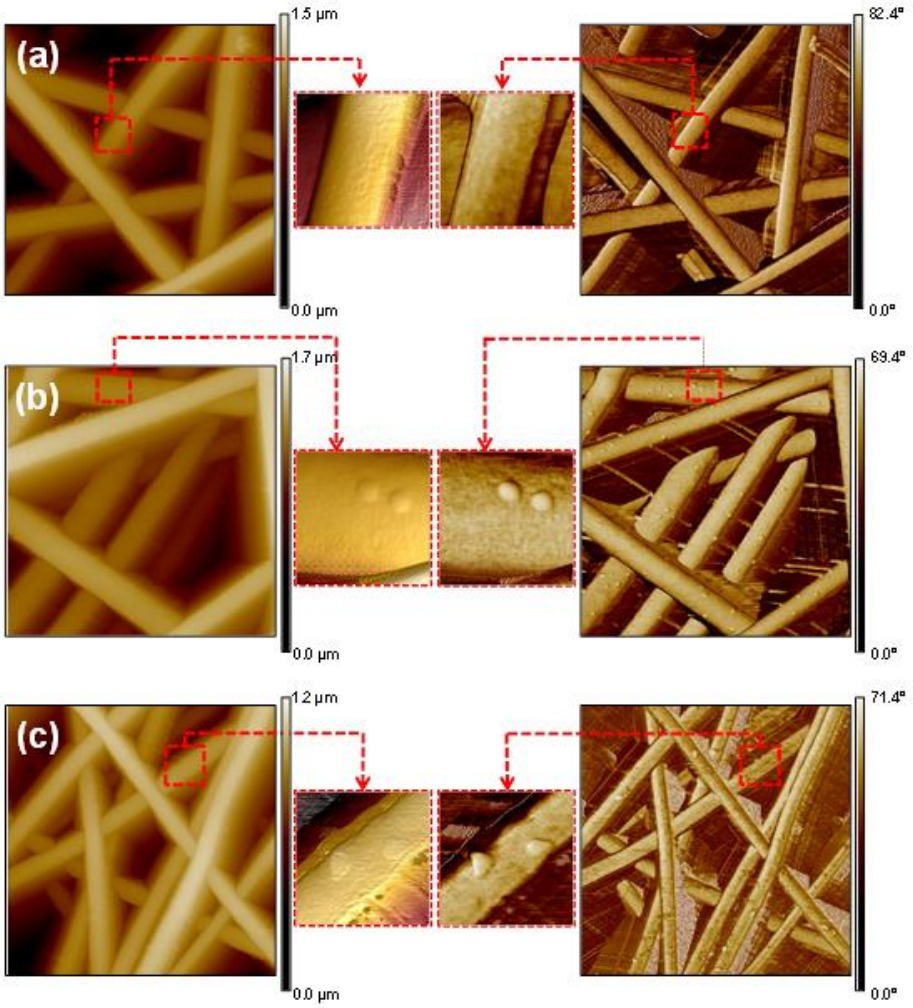

Figure 5.7 AFM images of (a) PE44/Ala-1, (b) PE44/Asn-1 and (c) PE44/Lys-1: 2D topography (left) and phase (right) images. The scan window sizes were 2×2 µm2, whereas zoomed areas correspond to 250×250 nm2 windows.

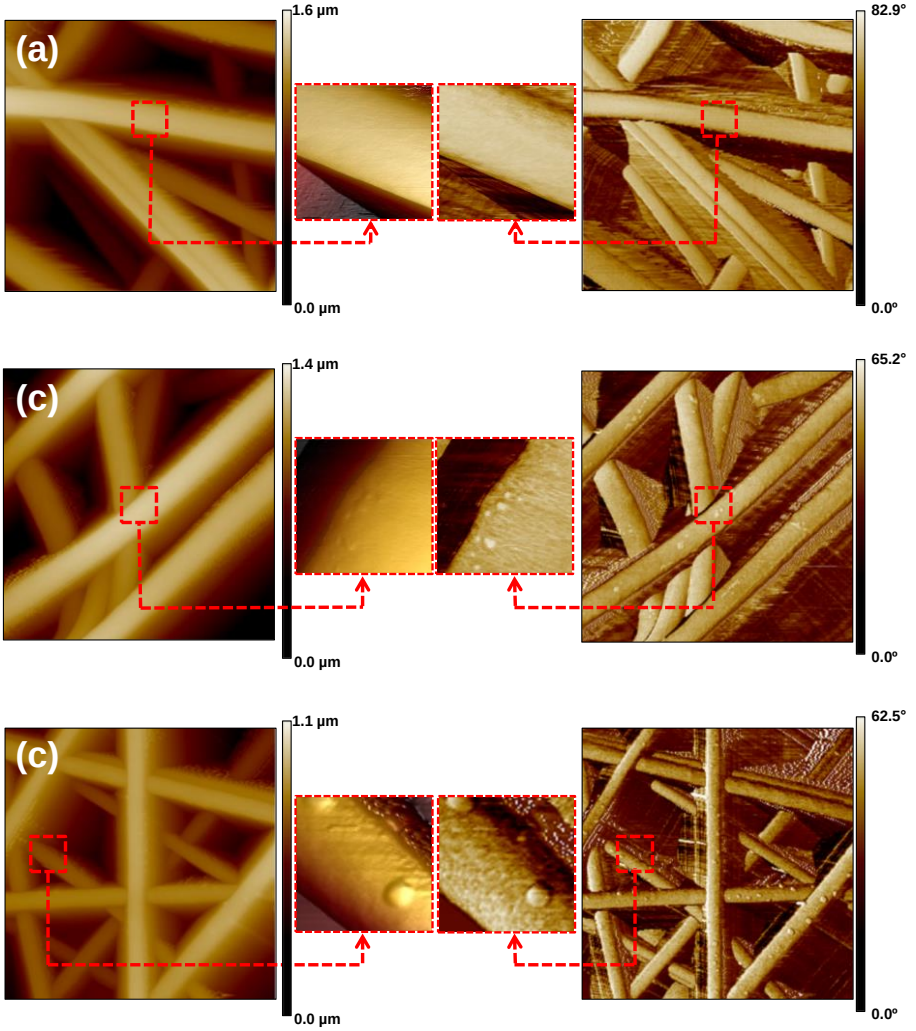

Figure 5.8 AFM micrographs of (a) PE44/Phe-1, (b) PE44/Cys-1 and (c) PE44/Asp-1 nanofibres: 2D topography (left) and phase (right) images. The scan window sizes were 2×2 µm^2, whereas the zooms correspond to 250×250 nm^2 windows.

Table 5.2 presents the Rq of PE44/AA fibres displayed in Figures 5.7 and 5.9. The lowest Rq value corresponds to unloaded PE44, increasing for loaded fibres as follows: non-polar AAs (Ala and Phe) < polar AAs (Cys and Asn) < charged AAs (Lys and Asp).

System	Rq (nm) ± σ (nm)	System	D_{av} (nm) ± σ (nm)
PE44	3.2 ± 1.1	-	
PE44/Ala-1	6.4 ± 1.7	PE44/Lys-1	10.2 ± 2.4
PE44/Phe-1	5.3 ± 1.1	PE44/Asp-1	9.5 ± 2.4
PE44/Cys-1	8.5 ± 2.8	PE44/Phe-10	4.3 ± 1.2
PE44/Asn-1	7.7 ± 1.7	PE44/Asn-10	6.3 ± 1.8

Table 5.2 Root mean square roughness and standard deviation (D_{av} ± σ) values for the fibre surface of the electrospun samples displayed in Figure 5.4 and 5.6.

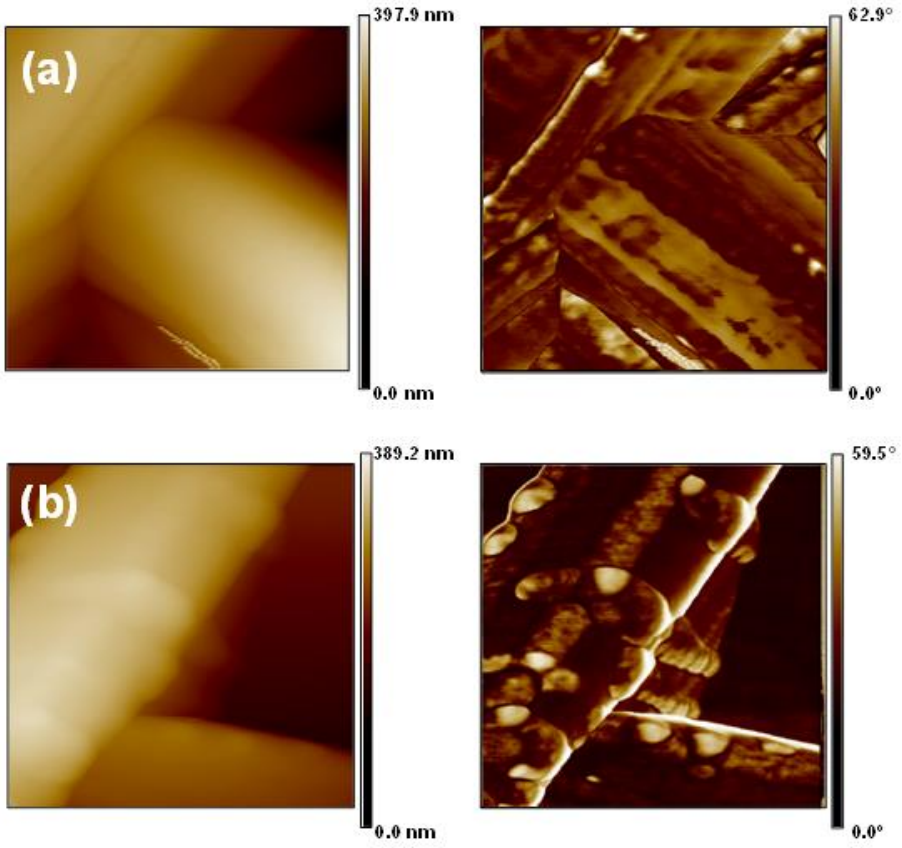

Figure 5.9 AFM images of (a) PE44/Ala-10 and (b) PE44/Asn-10: 2D topography (left) and phase (right) images. The scan window sizes were 500×500 nm^2.

Thermogravimetric analyses (Figure 5.10 and Table 5.3) evidenced that all samples are stable up to a temperature 80 ºC higher than the melting point of the PE44 matrix (T_m= 112.8 ºC). Incorporation of the AA led to a first degradation step that started at a temperature comprised between 184 ºC and 222 ºC, depending on the AA , which is clearly lower that the initial degradation temperature of PE44 (e.g 299 ºC for 1% weight loss). This first step involved a maximum weight loss of 10%, which is in full agreement with the amount of loaded AA. This step was also detected for the other amino acids although weight loss was lower (i.e. between 3 and 5%). Specifically the maximum temperatures of differential thermal gravimetric analysis (DTGA) curves were between 213-221 ºC range. It should be point out that a continuous degradation was subsequently observed until degradation of PE 44 was predominant.

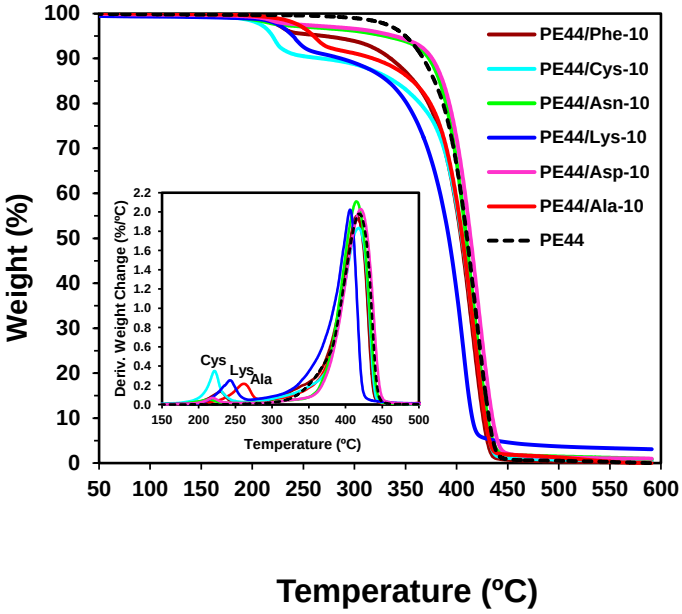

Figure 5.10 TGA and DTGA curves (shown in inset) of all studied samples.

The degradation behaviour of the PE44/AAs systems differ depending on the loaded AA, as it is deduced from the DTGA curves shown in the inset of Figure 5.10. Thus, a pronounced degradation step was observed

for Cys, Lys and Ala, the maximum temperature of DTGA curves increasing from Cys to Ala. A complex degradation occurs for Phe, whereas Asn and Asp exhibit a continuous weight loss after an initial process that involved a weight loss lower than 3%. No significant char (*i.e.* less than 0.3%) was observed at temperatures higher than 500 ºC, except for the sample loaded with Lys that rendered a char weight of 3% at 580 ºC.

Sample	$T_{1\%}$ **(ºC)** [a]	$T_{3\%}$ **(ºC)** [a]	T_{max} **(ºC)** [b]	T_{max} **(ºC)** [b]	$\%W_{(500ºC)}$ [a]
PE44	299	337	-	419	0.52
PE44/Ala-10	222	249	261	417	1.27
PE44/Phe-10	203	228	229	415	0.33
PE44/Cys-10	185	212	221	417	0.77
PE44/Asn-10	189	256	213	414	1.47
PE44/Lys-10	184	229	243	405	3.72
PE44/Asp-10	209	280	218	421	1.27

Table 5.3 Thermogravimetric data of PE44 and PE44/AAs samples.

The second degradation step (*i.e.* that associated with PE44) also depends on the loaded AA: (i) degradation is clearly accelerated with respect to the pure polymer (maximum of DTGA curve at 419 ºC) by the previous decomposition of the cationic form of Lys; (ii) slightly accelerated when Asn or Phe are present; (iii) practically not influenced when Cys and Ala were loaded; and (iv) delayed by the incorporation of Asp, which in fact should correspond to a trifluoroacetate salt.

Thermal properties were analysed by DSC following a three run protocol that consisted on a first heating run (20 ºC/min) of the as-processed samples, a cooling run (10 ºC/min) of previously melted samples after wiping out thermal history for three minutes and finally a third heating run (20 ºC/min) of samples crystallized from the melt. Table 5.4 summarizes the main data for PE44 and two representatives AA loaded samples, whereas Figure 5.11 displays the characteristic heating and cooling DSC traces of the studied samples.

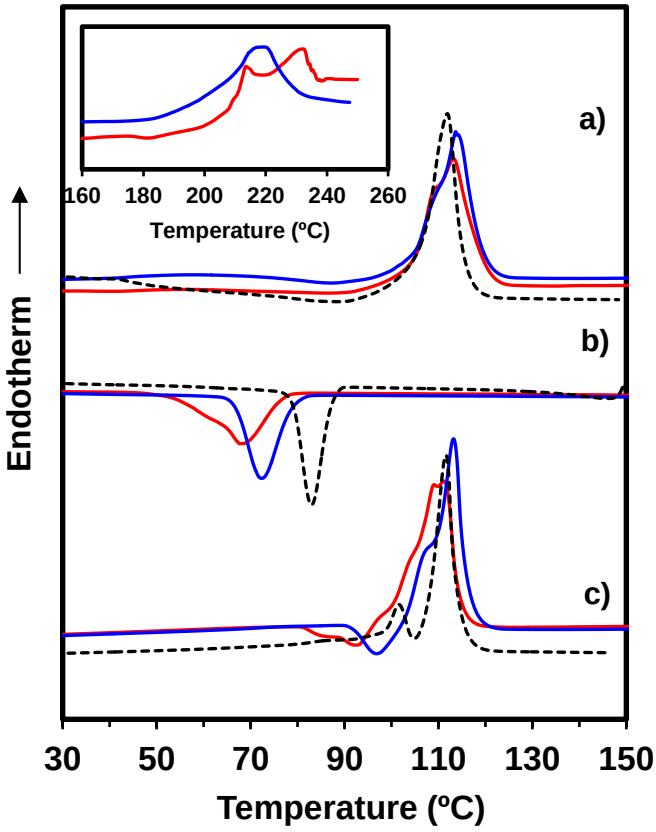

Figure 5.11 DSC curves indicating the first heating run (a), the cooling run (b) and the third heating run (c) of PE44 (dashed black line) , Pe44/Phe-10 (solid red line) and Pe44/Asn-10 (solid blue line). Inset shows endothermic peaks associated to AAs degradation process.

Sample	1st Heating run		Cooling run		2nd Heating run	
	T_m (ºC)	ΔH_m (J/g)	T_c (ºC)	ΔH_c (J/g)	T_m (ºC)	ΔH_m (J/g)
PE44	111.9	70.8	82.0	72.0	101.6, 111.6	74.0
PE44/Asn-10	113.7, 108.6[a]	71.1	72.4	67.3	113.2	70.9
PE44/Phe-10	113.2, 108.8[a]	68.8	68.0	67.5	111.1	72.4

Table 5.4 Calorimetric data of the PE44, PE44/Asn-10 and PE44/Phe-10 samples.

The second heating run of PE44 (Figure 5.11c) exhibits the typical behaviour reported by Yoo *et al.* [32] with an endotherm at 102 ºC prior to the high endotherm at 112 ºC. Double melting peaks have been associated with the fusion of original and thinner crystallites and recrystallized lamellae during the heating process. The total enthalpy is 74.0 J/g, which represents a crystallinity of 67% if the value of 110.3 J/g for a 100% crystalline material is taken into account [33].

The DSC trace of the initial PE44 scaffold (Figure 5.11a) shows a single peak at 111.9 ºC, which means that thinner crystals were not thermally stable and underwent the typical reorganization process. Therefore PE44 was able to crystallize during the electrospinning process but lamellae were less organized that those obtained by crystallization from the melt. In fact, the melting enthalpy sligthly decreases up to 70.8 J/g, which represents a crystallinity of 64%. In contrast, the DSC trace of electrospun samples loaded with AAs exhibit a complex melting peak with a shoulder being clearly identified at 109 ºC and a higher peak at 113-114 ºC that is again associated with reorganized crystals. For these systems, crystallinities are high and close to 65%, which demonstrate the positive effect of the electric field on the molecular orientation. The inset in Figure 5.11 shows also small endothermic peaks at 213.6 and 231.3 ºC (PE44/Phe-10) and 218.6 ºC (PE44/Asn-10), which are related with the previous indicated degradation process of both AAs. In any case, crystals of AAs could not be deduced from DSC data. Nevertheless it should be pointed that the crystallinity of PE44 could increase up to 72% if the AA content is taken into account in the estimation.

Cooling runs (Figure 5.11b) reveal that AA-loaded samples crystallize with greater difficulty than pure PE44 since exothermic peaks are broader and appear at lower temperatures (*i.e.* 68 and 72.4 ºC with respect to 82 ºC). Crystallization is more difficult for the Phe-loaded sample than for that incorporating Asn, which is less voluminous and more polar. In addition, these DSC traces are highly complex and even show a hot-crystallization peak close to fusion, which shows the difficulty of samples to crystallize during the cooling run. Note also that PE44/Phe-10 presents

different endothermic peaks that can be related to phases with different content and also to recrystallization processes. The DSC trace of the PE44/Asn-10 sample illustrates that, after reorganization, thicker crystals with a melting temperature of 113 ºC are formed.

The contact angle values (θ) measured using water (Table 5.5) indicate that electrospun PE44 matrices are hydrophobic (θ= 129º ± 2º), which should be attributed to both the presence of aliphatic segments and their compact structure within the NFs. Such hydrophobic character decreases upon the addition of a small amount (1% w/w) of non-polar and polar AAs (*i.e.* θ comprised between 124º and 110º), whereas incorporation of charged AAs transforms the fibers into very hydrophilic (θ < 20º). In contrast, all fibres loaded with 10% w/w of AA are more hydrophilic, independently of the chemical nature of the AA. This has been attributed to the increment of the surface roughness caused with the loading (Table 5.1).

System	θ (º) ± σ (º)	System	θ (º) ± σ (º)
PE44	129 ± 2	-	
PE44/Ala-1	124 ± 2	PE44/Ala-10	< 20
PE44/Phe-1	114 ± 7	PE44/Phe-10	< 20
PE44/Cys-1	110 ± 7	PE44/Cys-10	< 20
PE44/Asn-1	113 ± 11	PE44/Asn-10	< 20
PE44/Lys-1	< 20	PE44/Lys-10	< 20
PE44/Asp-1	< 20	PE44/Asp-10	< 20

Table 5.5 Average contact angle and standard deviation (θ ± σ) of electrospun PE44, PE44/AA-1 and PE44/AA-10 fibres prepared in this work.

Both 10 % w/w loaded (*i.e.* no clear response was expected from samples loaded with 1% w/w) and unloaded PE44 fibres were characterized by XRD (Figure 5.12). For unloaded fibres the main peaks correspond to the (020), (021), and (110) reflections, which appear at 2θ= 19.8°, 22°, and 22.6°, respectively (Figure 5.12a, left) [34,35]. Detailed structural analysis was obtained by deconvoluting the XRD spectrum into their three main crystalline peaks and two amorphous halos (Figure 5.12a, right).

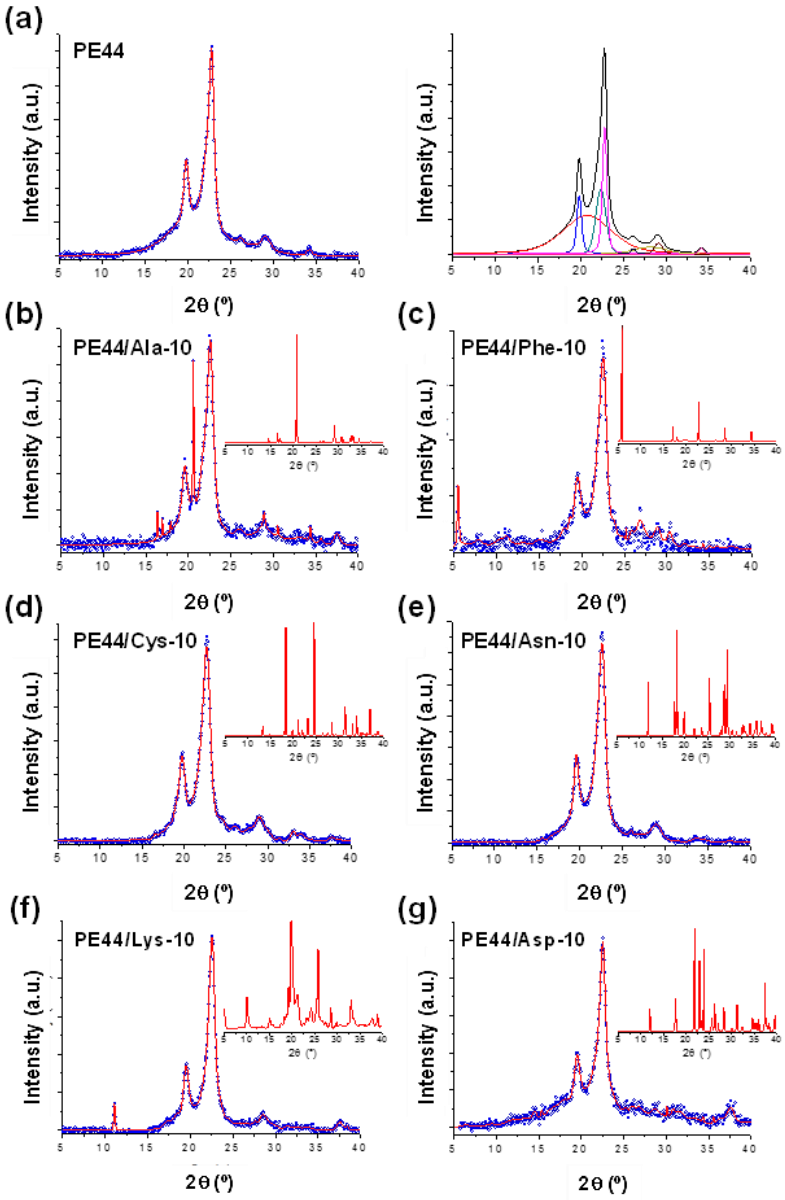

Figure 5.12 WAXD patterns of unloaded and loaded fibres matrices: (a) unloaded PE44; (b) PE44/Ala-10; (c) PE44/Phe-10; (d) PE44/Cys-10; (e) PE44/Asn-10; (f) PE44/Lys-10 and (g) PE44/Asp-10. Circles correspond to the observed XRD profiles while red lines are calculated profiles. Insets in (b)-(g) correspond to the XRD profiles of crystallized AAs. The deconvolution of the XRD profile (right) is also displayed for unloaded PE44 (a).

The degree of crystallinity (χ_c) of the PE44 matrix was estimated by fitting the XRD profile with the Lorentzian function and, subsequently, applying the following expression [36]:

$$\chi_c = \frac{A_c}{A_c + A_a} \qquad \text{(Eqn. 5.2)}$$

where A_c and A_a are the crystalline and amorphous diffraction areas, respectively, derived from the deconvoluted profiles. The average crystallite size, $L_{(hkl)}$, in the direction perpendicular to the representative (*hkl*) planes of loaded and unloaded samples was derived from the X-ray diffraction line broadening measurement using the Scherrer equation [37]:

$$L_{hkl} = \frac{0.9\lambda}{\beta \cos\theta} \qquad \text{(Eqn. 5.3)}$$

where λ is the wavelength (CuKα), β is the full width at half maximum height of the (211) line, θ is the diffraction angle and 0.9 is a shape factor. The $L_{(hkl)}$ values for the crystallites perpendicular to the planes (020), (021) and (110) are listed in Table 5.6.

The degree of crystallinity of unloaded PE44 is χ_c= 0.47 (Table 5.6), which is consistent with other values reported in the literature [38,39]. For example, PE44 fibres prepared from chloroform : chloroethanol and dichloromethane : dimethylformamide solutions displayed χ_c values ranging from 0.38 to 0.42 [38] and from 0.43 to 0.46 [39], respectively. Therefore, fiber crystallinity decreases with increasing solvent volatility [40].

The χ_c values determined for PE44/AA-10 fibers (Table 5.6) range from 0.55 (PE44/Ala-10) to 0.74 (PE44/Asn-10), thus revealing crystallinities significantly higher than those observed for unloaded fibers. This feature has been associated with the crystallization of AAs among the polymeric chains, as it is proved by comparing the diffractograms recorded for PE44/AA-10 with those of individual crystallized AAs (Figures 5.12b-g). Thus, XRD profiles for loaded samples exhibit not only the peaks

attributed to the polymeric matrix but also some of the peaks identified for the crystallized AAs (insets in Figures 5.12b-g). Overall, XRD and DSC results suggest that AA crystals form initially, subsequently affecting the crystallization and morphology of the polymeric matrix. This observation is supported by changes in the crystallite sizes of loaded samples with respect to the unloaded (Table 5.6).

	χ_c	$L_{(020)}$ (nm)	$L_{(021)}$ (nm)	$L_{(110)}$ (nm)
PE44	0.47	11.67	5.29	11.59
PE44/Ala-10	0.55	10.49	7.18	9.94
PE44/Phe-10	0.66	9.31	5.87	8.70
PE44/Cys-10	0.67	10.75	4.93	8.02
PE44/Asn-10	0.74	11.54	5.91	8.47
PE44/Lys-10	0.72	11.10	9.26	10.50
PE44/Asp-10	0.58	9.68	4.55	10.62

Table 5.6 Crystallinity degree (χ_c; Eqn 5.2) and crystallite size in the direction perpendicular to the representative (*hkl*) planes ($L_{(hkl)}$; Eqn 5.3) for unloaded PE44 and PE44/AA-10 fibres.

Amino acid release from PE44 fibres

Quantitative AA release assays were performed with PE44/AA-10 samples (*i.e.* expected uncertainty was too high for assays with 1% w/w AA-loaded fibres) in PBS, PBS-EtOH and an enzymatic environment.

Release in PBS

Figure 5.13a compares the AA accumulated release behavior of all PE44/AA-10 samples when they were exposed to PBS. Release proceeds in a similar way for all samples. Thus, after 1 h an important amount of AA is released to the medium, even though such amount highly depends on the AA. For example, the highest and lowest release after 1 h corresponds to the two polar AAs (78% and 19% for Cys and Asn, respectively). A similar difference was detected for non-polar AAs (57% and 33% for Ala and Phe, respectively) as well as for charged AAs (52%

and 33% for Lys and Asp, respectively). After this initial stage, the amount of released AA grows during a few hours for all the systems, even though the stabilization is rapidly reached. The amount of released AA after 168 h comprised between 35% (Phe) and 98% (Cys). Accordingly, Figure 5.13b which represents the amount of AA retained into the PE44 fibres after 168 h in PBS at 37 ºC, reflecting that the release process cannot be simply related to the polarity of the loaded AA.

Release in PBS-EtOH

The AA release profiles in PBS-EtOH for all PE44/AA-10 loaded fibres are displayed in Figure 5.13c. Amazingly, the more hydrophobic PBS-EtOH environment did not significantly alter the release of Ala and Phe, for which the retention after 168 h increased 11% and 7%, respectively, with respect to PBS (Figure 5.13b). This feature has been attributed to the fact that these two AAs are immersed into the polymeric matrix. Furthermore, PBS-EtOH also affected the release of Asn, Lys and Asp: the amount of Asn and Asp retained after 168 h increased 20% and 24%, respectively, with respect to PBS, while that of Lys decreased 28%. The only AA that exhibits similar results in PBS and PBS-EtOH is Cys, which experienced an almost complete release after 48 h in both environments. In spite of those differences, the release kinetics of all AAs is similar in PBS and PBS-EtOH, which can be explained by the Higuchi and first-order models. The Higuchi model, which provides a linear behavior when the cumulative percentage of AA release is represented against the square root of time, indicates that the concentration of AA in the matrix is much higher than the AA solubility, the AA particles (*i.e.* crystals) are smaller than the system thickness, the PE44 swelling and diffusivity are very low and the AA diffusivity is constant. On the other hand, the first order model provides a straight line when the data are plotted as the logarithm of the cumulative percentage of AA release *versus* time, this first order kinetics release reflecting that PE44 can be considered as porous matrix. It is worth noting that the Higuchi and the first-order models are usually combined to describe the first very fast releasing stage and the second very slow releasing stage of the complete profile [38].

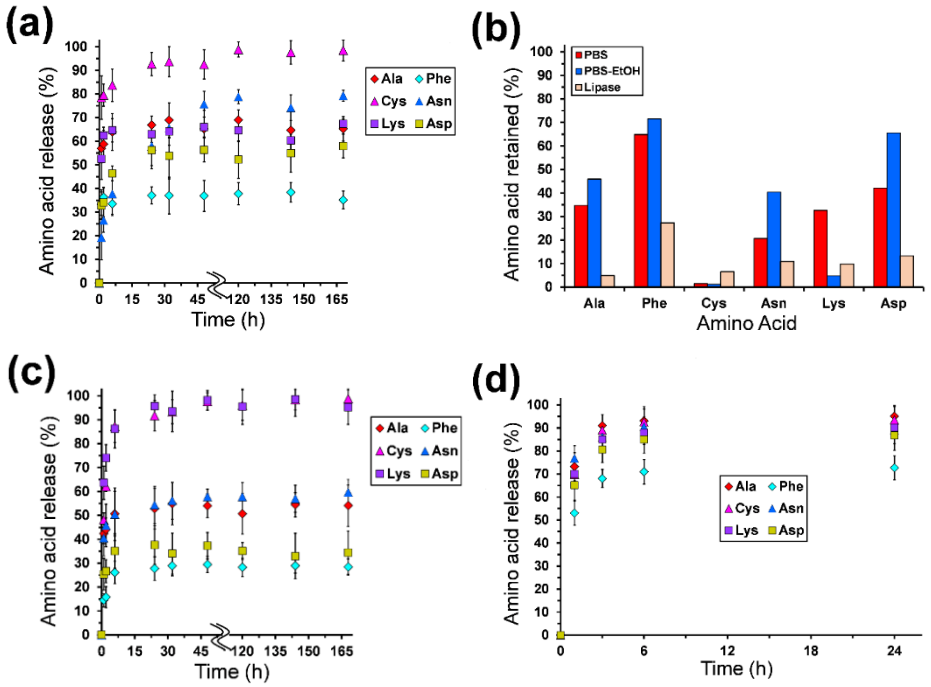

Figure 5.13 Accumulated release profiles of AAs from PE44/AA-10 NFs in (a) PBS, (c) PBS-EtOH and (d) a lipase-containing medium. The amount of AA retained after 168 h (PBS and PBS-EtOH) or 24 h (lipase-containing medium) is represented in (b).

Figure 5.13 indicates that in many cases the release of AAs is not total. This should be attributed to the delicate but complex balance among interactions. More specifically, in a molecular distribution of AAs inside the fibers, the release would be exclusively affected by the balance between AA···polymer and AA···solvent interactions, the former and the latter being against and in favor, respectively, of the release. However, in this case AAs are not distributed at the molecular level (*i.e.* as individual molecules) but as crystals, as proved by both phase AFM images and XRD. Accordingly, AA···AA interactions, which in turn are affected by the geometry of the crystal, play a crucial role in the release process. It is worth noting that in many cases the latter interactions are expected to be strong because of their polar/charged nature. In addition, the strength of AA···solvent interactions in PE44/AA systems with AA crystals embedded inside polymeric matrix are expected to be restricted by the

penetrability of the solvent into the fibers. Such two factors affect negatively to the release and explain the uncomplete release after 168 h. However, it should be emphasized that, in all cases, it was checked that the sum of AA released along 168 h and the AA remaining at the PE44 matrix corresponded to the amount of AA loaded during the electrospinning process (see Methods).

Release in enzymatic medium

Profiles obtained using a lipase-containing medium evidences a very fast AA release (Figure 5.13d). The amount of AA retained after only 1 h is lower than 30% in all cases with the exception of Phe and Asp, which display values not very far from that value (47% and 35%, respectively). This should be attributed to a burst effect that is probably more pronounced for PE44/AA systems with AA crystal near the surface. Thus, in such systems the specific surface that is contact with the enzymatic medium is high, favoring the instability of AA particles. All the AAs reach the maximum release is reached after only 6 h, and it remains stable for the following 18 h. Furthermore, it is worth noting that the amount of AA retained in the fibre mats after 24 h is very small (Figure 5.13b), ranging from 5 % (Ala) to 27% (Phe). This represents a very remarkable difference with respect to the AA release in PBS and, especially, PBS-EtOH (Figure 5.13b).

In summary, results from release experiments in PBS, PBS-EtOH and the enzymatic solution prove that PE44 fibers are a very promising vehicle to supply AAs. Thus, the AAs are retained at the polymeric matrix not only in PBS but also in PBS-EtOH, which is a powerful extraction medium. In contrast, lipase, which is a key enzyme in the digestion process, favors a fast release. Overall, these results are consistent with the use of electronspun fibers as carriers for the contribution of AAs to the feed.

Hydrolytic, enzymatic and accelerated degradation of loaded nanofibers

In order to prove that PE44/AA NFs resist hydrolysis, accelerated degradation assays were performed by incubating unloaded PE44 and PE44/AA-10 mats in an aggressive 1 N NaOH solution for 30 min. It is worth noting that accelerated assays in acidic conditions are not required since the pH in the digestive system is < 7 and, therefore, preservation of the loading under such conditions is not required. In opposition, the delivery of loaded AAs should be prevented in basic conditions, which could be accidentally reached by food-containing PE44/AA fibers (*e.g.* during the storage). Representative SEM micrographs of the NFs after such incubation time are displayed in Figure 5.14. Unloaded PE44 NFs underwent a very fast hydrolytic degradation that produced erosion phenomena at their surface. This feature is corroborated in Figure 5.15, which shows a SEM micrograph of unloaded NFs after 3 h in the same basic solution. In opposition, PE44/AA-10 fibers remained unaltered in the NaOH solution. This feature has been attributed to the buffering capacity of the positively charged N-terminal group of the AA, which protects the polymeric matrix from the attack of hydroxyl groups. Similar buffering activity has been previously observed in other materials with charged groups [42]. The overall of these results is fully consistent with the AAs retention determined from release assays in PBS and PBS-EtOH.

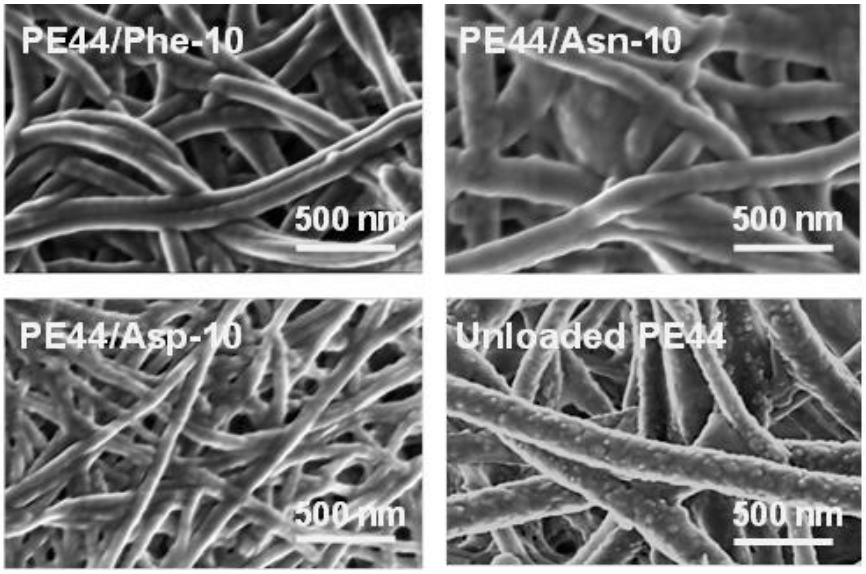

Figure 5.14 SEM micrographs of PE44/Phe-100, PE44/Asn-10, PE44/Asp-10 and unloaded PE44 after 30 min of immersion in 1 N NaOH.

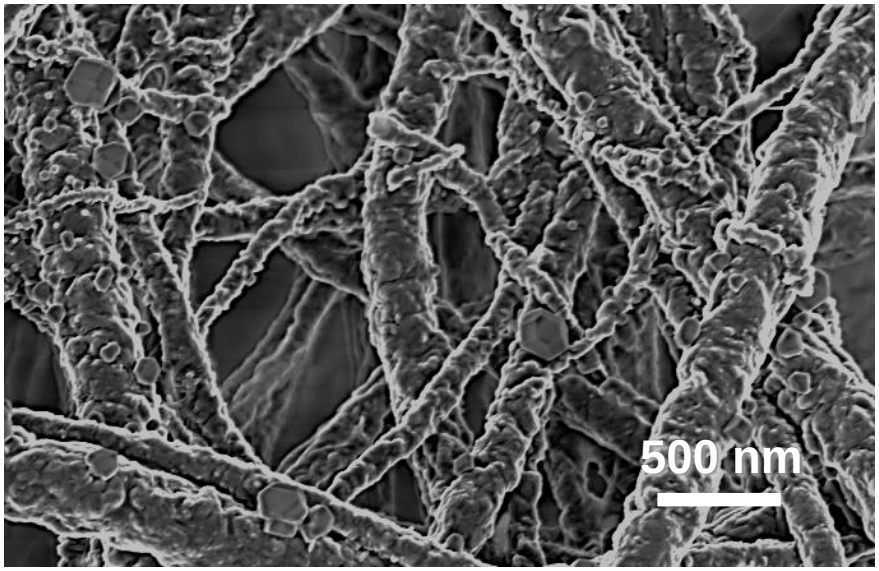

Figure 5.15 SEM micrographs of unloaded PE44 after 3 h of immersion in 1 N NaOH.

On the other hand, the enzymatic degradation of the PE44/AA-10 mats was performed by incubating the samples in a lipase-containing medium. Analysis of the resulting profiles, which are displayed in Figure 5.16a, reflects a relatively fast degradation stage after the first two days: the weight loss (Eq. 5.1) ranges from 7% (PE44/Cys-10) to 16% (PE44/Lys-10) after such short period. However, the weight loss increases by less than 3% during the following 26 days evidencing that, after the initial degradation stage, the enzymatic degradation of PE44 NFs is very slow (*i.e.* the weight loss after 28 days ranges from 9% to 19% only). SEM micrographs displayed in Figure 5.16b correspond to PE44/AA-10 NFs after 2 days of incubation in the lipase-containing solution. Although erosion is not evident in many cases (*e.g.* Phe and Cys loaded NFs), some morphological changes are detected at the surface of PE44/Lys-10, which experienced the highest weight loss. Hence, the enzymatic release of AAs from PE44 loaded NFs cannot be attributed to a fast and unspecific lipase-induced decomposition of the polymeric matrix. On the contrary, the enzymatic attack preferentially affected the ester bonds that keep the AA domains into the biphasic system, thus promoting their release. Probably, the morphological defects at the boundary limits between phases induced this specificity due to the higher accessibility of the enzyme into the polymeric fragments that retain the AA domains. This hypothesis is consistent with the fact that the highest weight loss in the enzymatic degradation assays corresponds to NFs loaded with charged AAs (*i.e.* SEM micrographs and AFM images revealed that Lys and Asp domains are preferentially embedded at the surface of NFs).

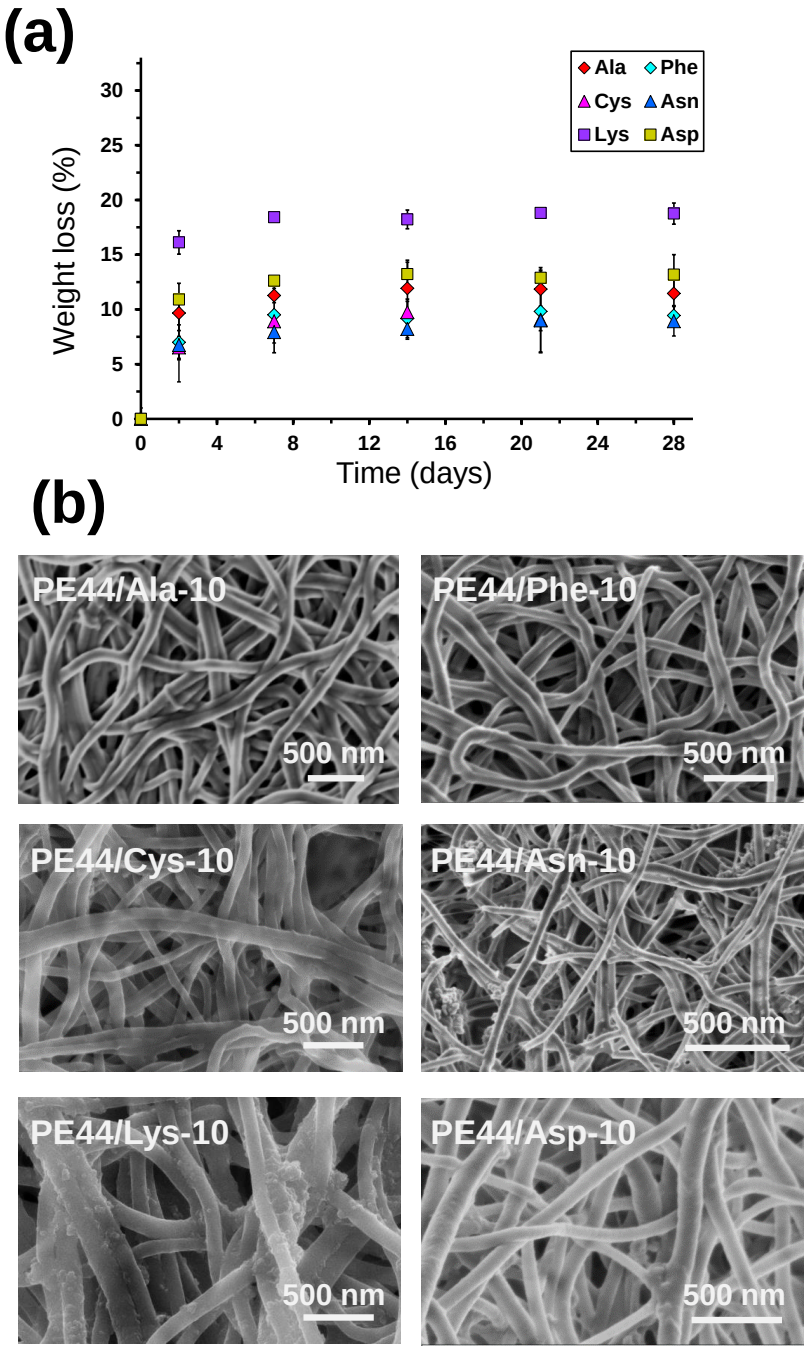

Figure 5.16 (a) Weight loss profiles of PE44/AA-10 NFs in 1 N NaOH solution. (b) SEM micrographs of PE44/AA-10 after 2 days of incubation in the lipase-containing solution.

5.4 Conclusions

In the light of the difficulties associated with AAs retention in delivery vehicles exposed to humid environments and their effective release after ingestion, we propose the loading of AAs into PE44 NFs using an electrospinning process as a reliable approach. Electrospun PE44/AA NFs can be described as biphasic systems made of AA crystals distributed into a polymeric matrix. The chemical nature of the AA has a deep impact on the distribution of such crystals, affecting also the properties of electrospun NFs. PE44 NFs have been proved to be very stable systems, able to retain loaded non-polar, polar and charged AAs in aqueous environments of different polarities and to deliver them very rapidly in enzymatic media. The physical characteristics of loaded PE44/AA NFs as well as their behaviour to effectively supply essential and conditional AAs suggest that they can be incorporated into the diets of livestock and fish in farms for administration.

It should be noted that electrospun fibres of biodegradable polymers loaded with biomolecules (*e.g.* growth factor, biocides, antibiotics and anticoagulants) are typically used in the biomedical field as scaffolds for cell regeneration. However, our approach can be used in the agro-food biotechnology field, solving an important problem like is the contribution of essential and conditional AAs to the feed. Obviously, the use of this strategy is not restricted to PE44 but it can be extended to other biodegradable polymers and biopolymers, such as for example poly(lactic acid) and poli(γ-glutamic acid). We are currently investigating the influence of this extrapolation on the release of loaded AAs.

5.5 References

1. A.B. Hughes; Amino Acids, Peptides and Proteins in Organic Chemistry, vol 1-5, *Wiley-VCH, Weinheim*, 2009-2013.
2. O.W. Griffith; *Free Radic. Biol. Med.*, vol. 27, pp. 922–935, 1999.
3. S.C. Lu; *B.B.A.-Gen. Subjects*, vol, 1830, pp. 3143–3153, 2013.
4. M.C. Nlend, D.M. Cauvi, N. Venot, O. Chabaud; *Endrocrinol.*, vol. 146, pp. 4834–4843, 2005.
5. S. M. Morris; *J. Nutr.*, vol. 137, pp. 1602S–1609S, 2007.
6. S. Nagase, K. Takemura, A. Ueda, A. Hirayama, K. Aoyagi, M. Kondoh, A. Koyama; *Biochem. Biophys. Res. Commun.*, vol. 233, pp. 150–153, 1997.
7. N.W. Rajapakse, D.L. Mattson; *Curr. Opin. Nephrol. Hypertens.*, vol. 22, pp. 45–50, 2013.
8. J. Yan, G. Tie, L. M. Messina; *Mol. Med.*, vol. 18, pp. 1220–1230, 2012.
9. B. Hernández-Ledesma, M.M. Contreras, I. Recio; *Adv. Colloid Interface Sci.*, vol. 165, pp. 23–35, 2001.
10. J. Renukuntla, A.D. Vadlapudi, A. Patel, S.H.S. Boddu, A.K. Mitra; *Int. J. Pharm.*, vol. 447, pp. 75–93, 2013.
11. X. Gao, C. He, C. Xiao, X. Zhuang, X. Chen; *Polymer*, vol. 54, pp. 1786–1793, 2013.
12. C. Dai, B. Wang, H. Zhao; *Colloids Surf. B Biointerfaces*, vol. 41, pp. 117–120, 2005.
13. D. Hennig, S. Schubert, H. Dargatz, E. Kostenis, A. Fahr, U.S. Schubert, T. Heinzel, D. Imhof; *Macromol. Biosci.*, vol. 14, pp. 69–80, 2014.
14. L. Li, Q. Wang, H. Li, M. Yuan, M. Yuan; *PLOS one*, vol. 9, e100809, 2014.

15. G. Fabregat, B. Teixeira-Dias, L.J. del Valle, E. Armelin, F. Estrany, C. Alemán; *ACS Appl. Mater. Interfaces*, vol. 6, pp. 11940–11954, 2014.

16. C.J. Langdon; *Aquaculture*, vol. 227, pp. 259–275, 2003.

17. J. López-Alvarado, C.J. Langdon, S.I. Teshima, A. Kanazawa; *Aquaculture*, vol. 122, pp. 335–346, 1994.

18. S.K. Tonheim, W. Koven, I. Rønnestad; *Aquaculture*, vol. 190, pp. 223–235, 2000.

19. C. Langdon, B. Clack, U. Önal; *Aquaculture*, vol. 268, pp. 143–148, 2007.

20. S.Z. Mohammady, M. Pouzot, R. Mezzenga; *Biophys. J.*, vol. 96, pp. 1537–1546, 2009.

21. C.J. Sánchez Jr., E.M. Prieto, C.A. Krueger, K.J. Zienkiewicz, D.R. Romano, C.I. Ward, K.S. Akers, S.A. Guelcher, J.C. Wenke; *Biomaterials*, vol. 34, pp. 7533-7543, 2013.

22. S. Maione, L.J. del Valle, M.M. Pérez-Madrigal, C. Cativiela, J. Puiggalí, C. Alemán; *RSC Adv.*, vol. 6, pp. 73045–73055, 2016.

23. M.M. Pérez, E. Llorens, L.J. del Valle, J. Puiggalí, E. Armelin, C. Alemán; *Express Polym. Lett.*, vol. 10, pp. 628–646, 2016.

24. I. Sebe, P. Szabó, B. Kállai-Szabó, R. Zelko, *Int. J. Pharm.*, vol. 494, pp. 516–530, 2015.

25. A. Díaz, R. Katsarava, J. Puiggalí; *Int. J. Mol. Sci.*, vol. 15, pp. 7064–7123, 2014.

26. E. Armelin, A.L. Gomes, M.M. Pérez-Madrigal, J. Puiggalí, L. Franco, L.J. del Valle, A. Rodríguez-Galán, J.S. de C. Campos, N. Ferrer-Anglada, C. Alemán; *J. Mat. Chem.*, vol. 22, pp. 585–594, 2012.

27. E. Llorens, E. Armelin, M.M. Pérez-Madrigal, L.J. del Valle, C. Alemán, J. Puiggalí; *Polymers*, vol. 5, pp. 1115–1157, 2013.

28. K. Ghosal, A. Manakhov, L. Zajickova, S. Thomas; *AAPS Pharm. Sci. Tech.*, in press. doi:10.1208/s12249-016-0500-8, 2016.

29. D. Li, Y. Xia; *Adv. Mater.*, vol. 16, pp. 1151–1170, 2004.

30. L.J. del Valle, R. Camps, A. Díaz, L. Franco, A. Rodríguez-Galán, J. Puiggalí; *J. Polym. Res.*, vol. 18, pp. 1903–1917, 2011.

31. S.L. Shenoy, W.D. Bates, H.L. Frisch, G.E. Wnek; *Polymer*, vol. 46, pp. 3372-3384, 2005.

32. E.S. Yoo, S.S. Im; *J. Polym. Sci. Polym. Phys.*, vol. 37, pp. 1357–1366, 1999.

33. V.M. Correlo, L.F. Boesel, E. Pinho, A.R. Costa-Pinto, M.L. Alves da Silva, M. Bhattacharya, J.F. Mano, N.M. Neves, R.L. Reis; *J. Biomed. Mater. Res.*, vol. 91A, pp. 489–504, 2009.

34. Z. Qiu, W. Yang; *Polymer*, vol. 47, pp. 6429–6437, 2006.

35. L. Song, Z. Qiu; *Polym. Degrad. Stab.*, vol. 94, pp. 632−637, 2009.

36. J. Hay, J. Langford, J. Lloyd; *Polymer*, vol. 30, pp. 489−493, 1989.

37. H. Klug, L. Alexander; X-Ray Diffraction Procedure for Polycrystallite and Amorphous Materials, 2nd. Edition, *John Wiley and Sons, New York*, 1974.

38. E.H. Jeong, S.S. Im, J.H. Youk; *Polymer*, vol. 46, pp. 9538−9543, 2005.

39. V. Tserki, P. Matzinos, E. Pavlidou, D. Vachliotis, C. Panayiotou; *Polym. Degrad. Stab.*, vol. 91, pp. 367−376, 2006.

40. X .Zong, K. Kim, D. Fang, S. Ran, B.S. Hsiao, B. Chu; *Polymer*, vol. 43, pp. 4403−4412, 2002.

41. R. Baker; Controlled release of biologically active agents, *Wiley & Sons, Eds., New York*, Chapter 4, 1987.

42. L.J. del Valle, O. Bertran, G. Chaves, G. Revilla-López, M. Rivas, M.T. Casas, J. Casanovas, P. Turon, J. Puiggalí, C. Alemán; *J. Mater. Chem. B*, vol. 2, pp. 6953–6966, 2014.

CHAPTER 6

Loading and release of hydrophobic gramicidin in micro- and nanostructured polyester

6.1 ELECTROSPRAY LOADING AND RELEASE OF HYDROPHOBIC GRAMICIDIN IN POLYESTER MICROPARTICLES††

6.1.1 Introduction

Linear gramicidin (GA-L) is a hydrophobic pentadecapeptide produced by *Bacillus brevis* [1] with sequence formyl-L-Xxx-Gly-L-Ala-D-Leu-L-Ala-D-Val-L-Val-D-Val-L-Trp-D-Leu-L-Yyy-D-Leu-L-Trp-D-Leu-L-Trp-ethanolamine, where Xxx and Yyy depend on the GA-L molecule type. For example, commercial samples of GA-L usually contain types A, B and C, in which Xxx can be either Val or Ile for the three species and Yyy= Trp, Phe and Tyr for type A, B and C, respectively. This unique sequence of alternating L- and D-amino acids renders GA-L sensitive to the environment [2-7]. More specifically, the pitch, handedness and dimeric configuration of the helix adopted by GA-L depends on the dielectric constant of its environment.

From a functional point of view, GA-L is well known because of its ability to kill pathogenic microorganisms. For example, it exhibits activity against gram-positive bacteria, even though its mechanism of action is not entirely understood [8-12]. GA-L is also used as antibiotic but its toxicity due to hemolytic characteristics limited that application [13,14]. In the last few years, GA-L has been proposed as a potential therapeutic agent for different carcinomas [15,18]. Thus, studies *in vivo* revealed that GA-L effectively reduces the growth of renal cell carcinoma (RCC) cells [15], which are highly resistant to conventional treatments. The peptide blocks ATP generation by inhibiting oxidative phosphorylation and glycolysis, leading to cellular energy depletion and nonapoptotic cell death. Form these works it was concluded that GA-L reduced the growth of human RCC xenograft tumors without causing significant toxicity [16]. GA-L

†† *Results presented in section 6.1 were published in RSC Advances, 2016, 6, 73045-73055.*

treated tumors also displayed physiologic and molecular features consistent with the inhibition of hypoxia-inducible factor-dependent angiogenesis. Wijesinghe and co-workers [17] reported that GA-L channels inserted into the cancer cells open flux of protons into the cytoplasm and disrupt balance of other monovalent cations, which induces cell apoptosis. Rao *et al.* [18] introduced a strategy to kill selectively multi-drug-resistant cells that express the breast cancer resistance protein (BCRP). This approach was based on specific stimulation of ATP hydrolysis by BCRP transporters with subtoxic doses of curcumin combined with stimulation of ATP hydrolysis by Na^+, K^+-ATPase with subtoxic doses of GA-L. More biomedical applications of GA-L have been recently reviewed by Gurnev and Nestorovich [19], who also summarized the role of channel-forming peptides for cancer therapy.

In spite of its biomedical interest, encapsulation of GA-L, which represents a major challenge due to the insolubility of this peptide, has been scarcely studied [20]. In a very recent study, Fu and coworkers [20] used graphene oxide (GO) as nanocarrier to load and deliver GA-L. In spite of the effective antibacterial activity exhibited by GA-L loaded GO nanoparticles, other studies [21] evidenced that GO exhibits dose-dependent toxicity to cells and living systems. Accordingly, the use of GO as a biocompatible material was suggested to be controversial when this material is applied for biomedical engineering. On the other hand, solid peptide nanoparticles have been prepared using amino acid sequences related with those of GA-L [22,23]. Within this context, Dittrich and Meier [22] obtained solid spherical particles with diameters of around 500 nm and low-size polydispersity using a highly hydrophobic peptide decamer made of acetylated L-Lys, L-Trp and D-Leu. Also, Meier and coworkers [23] prepared peptide particles, which were hypothesized to be multicompartment micelles, using an undecamer made of a repetitive L-Trp-D-Leu motif in a hydrophobic block and an N-terminally attached hydrophilic (Lys) section. Nevertheless, the potential biomedical applications of the peptides used to prepare such nano- and micro-structures have not been examined and, indeed, is not expected to be similar to those of parent GA-L.

In this work we report a simple strategy to prepare PE44 microspheres loaded with GA-L by means of the electrospraying technique. After comparison of the chemical, morphological and thermal properties of GA-L loaded and unloaded PE44 microspheres (*i.e.* PE44 microspheres without GA-L), hereafter denoted PE44-GA and U-PE44, respectively, the delivery of the peptide has been examined in two media. Results indicate that the release behaviour is highly dependent on the hydrophilicity of the medium.

6.1.2 Methods

Materials

PE44 is a commercial product (Bionolle® 1001) supplied by Showa Denko K.K. (Germany). The polymer has a melt flow index of 1.6 g/10 min (measured at 190 ºC under a load of 2.16 kg according to ASTM-D1238). GA-L was purchased from Sigma-Aldrich (G5002), containing 80-85%, 6-7%, 5-14% and < 1% of type A, B, C and D, respectively.

Electrospraying

PE44 and GA-L were dissolved in chloroform and ethanol, respectively, by stirring at 80 rpm overnight. The two solutions were mixed in a resalable glass vial to prepare the electrospray solution, which was homogenized by stirring at 80 rpm for 1 h. The weight percentages of PE44 and GA-L in the resulting electrospray solution were 2.5 wt.% and 0.25 wt.% (*i.e.* 10% respect to the polymer weight), respectively. Operational conditions for the preparation of PE44-GA microspheres by electrospraying were optimized, even though results obtained using the selected processing conditions are the only displayed in this work. Electrosprayed PE44-GA microspheres were collected on a target placed at 25 cm from the needle tip (18 G, inside diameter 0.84 mm). A voltage of 30 kV was applied to the target using a high-voltage supply (Gamma

High Voltage Research, ES30-5W). Polymer solutions were delivered via a KDS100 infusion syringe pump (KD Scientific, USA) to keep the flow rate at 1 mL/h. All electrospraying experiments were carried out at room temperature. The procedure and the parameters used to prepare blank samples, which consist of U-PE44 microspheres, were identical to those described for PE44-GA with the obvious exception that ethanol did not contain GA-L.

Characterization

Detailed inspection of texture and morphology of microspheres was conducted by SEM using a Focus Ion Beam Zeiss Neon 40 instrument (Carl Zeiss, Germany). Carbon coating was accomplished using a Mitec K950 Sputter Coater fitted with a film thickness monitor *k*150x. Samples were visualized at an accelerating voltage of 5 kV. The diameter of the microspheres was measured with the SmartTiff software from Carl Zeiss SMT Ltd.

AFM was conducted to obtain topographic and phase images of the surface of microspheres using silicon TAP 150-G probes (Budget Sensors, Bulgaria) with a frequency of 150 kHz and a force constant of 5 N/m. Images were obtained with an AFM Dimension microscope using the NanoScope IV controller under ambient conditions in tapping mode. The row scanning frequency was set between 0.4 and 0.6 Hz. The RMS Rq, which is the average height deviation taken from the mean data plane, was determined using the statistical application of the NanoScope Analysis software (1.20, Veeco).

Aggregation phenomena in raw materials (*i.e.* PE44 and GA-L) were studied by dynamic light scattering (DLS) using the conditions (solvent and concentration) selected for the processing by electrospraying. Measurements were performed using a NanoBrook Omni Zeta Potential Analyzer from Brookheaven Instruments Corporation.

The specific surface area of U-PE44 and PE44-GA was determined by the Brunauer–Emmett–Teller (BET) technique under standard conditions

using a Micromeritics Tristar 3000 analyzer and using N_2 as adsorption gas. Prior to the measurement, the sample was outgassed at 40°C for 240 minutes (~0.15 mbar).

The degree of crystallinity of the PE44 and the electrosprayed microspheres was analyzed by means of WAXD using the X'Pert Pro System (PANalytical, Netherland). The diffraction patterns were obtained using Cu Kα (λ = 0.1542 nm) X-ray source operating at 30 kV and 30 mA. Samples were examined using the powder form. The degree of crystallinity was estimated using PeakFit v4.0 software (Jandel Scientific Software, AISN Software Inc.) according to Hindeleh and Johnson's method and the following equation:

$$\chi_c = \frac{A_C}{A_C + A_A} \qquad \text{(Eqn. 6.1.1)}$$

where: A_A and A_C are the calculated area under amorphous and crystalline curves of deconvoluted X-ray pattern, respectively.

Additionally, approximated theoretical curves allow calculating crystalline size using the Scherrer equation:

$$L_{(hkl)} = \frac{K\lambda}{B \cdot \cos\theta} \qquad \text{(Eqn. 6.1.2)}$$

where $L_{(hkl)}$ is the average crystallite size in the orthogonal direction to the plane (*hkl*), θ is the Bragg angle, λ is the X-ray wavelength, B is the FWHM of the diffraction peak for the plane (*hkl*) and *K* is the Scherrer constant (*K*= 0.9 for polymers).

A UV-3600 (Shimadzu) UV-vis/ NIR spectrophotometer controlled by the UVProbe V2.31 software was used to record UV-vis spectra of GA-L at room temperature in the 200-400 nm range, with a bandwidth of 2 mm, a scan speed of 600 nm/min, and a sampling interval of 1 nm

FTIR spectroscopy was used to assess the presence of peptide in PE44-GA samples. Absorption spectra were recorded with a Fourier Transform FTIR 4100 Jasco spectrometer in the 4000-600 cm^{-1} range. A Specac

model MKII Golden Gate attenuated total reflection (ATR) with a heated Diamond ATR Top-Plate was used. FTIR spectroscopy was also used to examine the secondary structure of GA-L in prepared PE44-GA microspheres. This information was derived from the peaks in the amide I and amide II regions, which were deconvoluted and fitted to Gaussian functions using the PeakFit 4 (Jandel Scientific Software, AISN Software Inc.) and OriginPro 8 software, respectively.

Circular dichroism (CD) measurements were carried out in a Jasco J-810 spectropolarimeter at 22 ºC using a quartz cuvette. The CD data were recorded with standard sensitivity (100 mdeg), in the 150–260 nm range, with bandwidth of 2 mm, response time of 0.5 s and scanning speed of 500 nm/min. The reported spectra correspond to the average of five scans, the raw spectra being smoothed by the Savitsky–Golay algorithm and deconvolutioned for analysis and interpretation.

XPS analyses were performed in a SPECS system equipped with a high-intensity twin-anode X-ray source XR50 of Mg/Al (1253 eV/1487 eV) operating at 150 W, placed perpendicular to the analyzer axis, and using a Phoibos 150 MCD-9 XP detector. The X-ray spot size was 650 mm. The pass energy was set to 25 and 0.1 eV for the survey and the narrow scans, respectively. Charge compensation was achieved with a combination of electron and argon ion flood guns. The energy and emission currents of the electrons were 4 eV and 0.35 mA, respectively. For the argon gun, the energy and the emission currents were 0 eV and 0.1 mA, respectively. The spectra were recorded with a pass energy of 25 eV in 0.1 eV steps at a pressure below $6 \cdot 10^{-9}$ mbar. These standard conditions of charge compensation resulted in a negative but perfectly uniform static charge. The C1s peak was used as an internal reference with a binding energy of 284.8 eV. High-resolution XPS spectra were acquired by Gaussian/Lorentzian curve fitting after S-shape background subtraction. The surface composition was determined using the manufacturer's sensitivity factors.

Thermal degradation was studied at a heating rate of 20 ºC/min (sample weight *ca.* 5 mg) with a Q50 thermogravimetric analyser of TA

Instruments and under a flow of dry nitrogen. Test temperatures ranged from 30 to 600 ºC.

Contact angle measurements were obtained using the sessile water drop method at room temperature and controlled humidity. Images of 0.5 µL distillate water drops on surfaces collecting the microspheres were recorded after stabilization (10 s) with the equipment OCA 20 (DataPhysics Instruments GmbH, Filderstadt). The software SCA20 was used to analyze the images and acquire the contact angle value. Contact angle values were obtained as the average of 15 independent measures for each sample.

GA-L release experiments

Mats with GA-L loaded microspheres were cut into small squares (2×2 cm^2 and around 15-20 mg of weight) which were weighed and placed into polypropylene tubes. PBS (pH 7.4) and PBS-EtOH were considered as release media. The addition of ethanol to hydrophilic PBS increases the hydrophobicity of the medium and provokes some swelling effect, both favoring the release of hydrophobic drugs as GA-L [24]. The released GA-L was quantified using the Bradford reagent. Assays were carried out by immersing sample mats in 30 mL of the release medium at 37 ºC for 1 week. Aliquots (1 mL) were drawn from the release medium at predetermined intervals, and an equal volume of fresh medium was added to the release vessel. The Bradford reaction was performed in microtiter plate mode and the absorbance measurement in a reader plate. Calibration curves were obtained by plotting the absorbance measured at 595 nm against drug concentration. Finally, the mats were dissolved in chloroform and the residual drug was extracted in ethanol for quantification. All tests were performed in triplicate to control the homogeneity of the release, and the results were averaged.

Antimicrobial test: Inhibition of bacterial growth

Escherichia coli (*E. coli*) and *Staphylococcus aureus* (*S. aureus*) were selected to evaluate the activity of loaded GA-L against bacteria. The bacteria were previously grown aerobically by exponential phase in Luria-Bertani (LB) broth (at 37 ºC and agitated at 80 rpm). In addition to PE44-GA samples, U-PE44 (negative control) and gentamicin (GM) discs (positive control), an antibiotic used to treat many types of bacterial infections, were also considered for antimicrobial assays.

The agar diffusion test was performed in Petri dishes of 90 mm. A standardized 0.5 McFarland of the test strain culture was inoculated homogeneously on the surface of LB agar using a sterile nylon swab. Then, samples were pasted onto the agar plate. Bacteria were incubated at 37 ºC for 24 hours and the inhibition zone for each sample on the plate was observed.

Cytotoxicity and cell adhesion

Madin Darby canine kidney (MDCK) cells were cultured in DMEM high glucose supplemented with 10% FBS, penicillin (100 units/mL), and streptomycin (100 µg/mL). The cultures were maintained in a humidified incubator with an atmosphere of 5% CO_2 and 95% O_2 at 37ºC. Culture media were changed every two days. When the cells reached 80-90% confluence, they were detached using 1-2 mL of trypsin (0.25% trypsin/EDTA) for 5 min at 37 °C. Finally, cells were re-suspended in 5 mL of fresh medium, their concentration being determined by counting in a Neubauer camera using 0.4% trypan blue as a dye vital.

U-PE44 and PE44-GA samples were placed in plates of 24 wells and sterilized using UV-light for 15 min in a laminar flux cabinet. Controls were simultaneously performed by culturing cells on the surface of the TCPS plates. For adhesion assays, an aliquot of 50 µL containing 5×10^4 cells was deposited onto each sample. Then, cell attachment was promoted by incubating under culture conditions for 30 min. Finally, 500 µL of the culture medium were added to each well. After 24 h, non-attached cells

were washed out, while attached cells were quantified. Cytotoxicity was also determined after 24 h of culture. All viability measures were relative to TCPS used as control (*i.e.* 100%).

Viability for cytotoxicity and cellular adhesion were evaluated by the colorimetric MTT assay. This assay measures the ability of the mitochondrial dehydrogenase enzyme of viable cells to cleave the tetrazolium rings of the MTT and form formazan crystals, which are impermeable to cell membranes and, therefore, are accumulated in healthy cells. This process is detected by a colour change: the characteristic pale yellow of MTT transforms into the dark-blue of formazan crystals. Specifically, 50 µL of MTT solution (5 mg/mL in PBS) were added to each well. After 3 h of incubation, samples were washed twice with PBS and stored in clean wells. In order to dissolve formazan crystals, 200 µL of DMSO/methanol/water (70/20/10 % v/v) was added. Finally, the absorbance at 570 nm was measured using a microplate reader (Biochrom EZ Read 400, Biochrom). The resulting viability results were normalized to TCPS control as relative percentages. Results were derived from the average of six replicates (n= 6) for each independent experiment. ANOVA and Tukey tests were performed to determine statistical significance, which was considered at a confidence level of 95 % ($p < 0.05$).

6.1.3 Results and Discussion

PE44 has been reported to be perfectly soluble in chloroform, this solvent being previously used to process different nano- and microstructures with the same polyester [25,26]. Although hydrophobic GA-L is hardly soluble in water and tends to form colloidal suspensions in this solvent, it is soluble in a number of organic solvents including those used in the electrospray solution. Initially, the impact of different solvents on the stability of GA-L was examined by absorption spectroscopy. Although the UV-vis spectrum of GA-L is not characteristic of its entire structure [27], uncharacteristic absorbance at 200-300 nm should be clearly detected due to the chromophoric units of the molecule (*i.e.* the four Trp of GA-L of

type A, which is the most abundant in the purchased sample) [28-30]. Results, which are displayed in Figure 6.1.1a, indicated that the spectrum of GA-L remains practically unaltered when the ethanol solvent is replaced by methanol, chloroform, acetonitrile, formic acid and dichloromethane while important changes occur in water. Thus, the absorption peaks at around 280 and 288 nm observed for organic solvents become a shoulder in water. In addition, the solubility of the peptide in aqueous solution was observed to be very low in comparison to the other solvents.

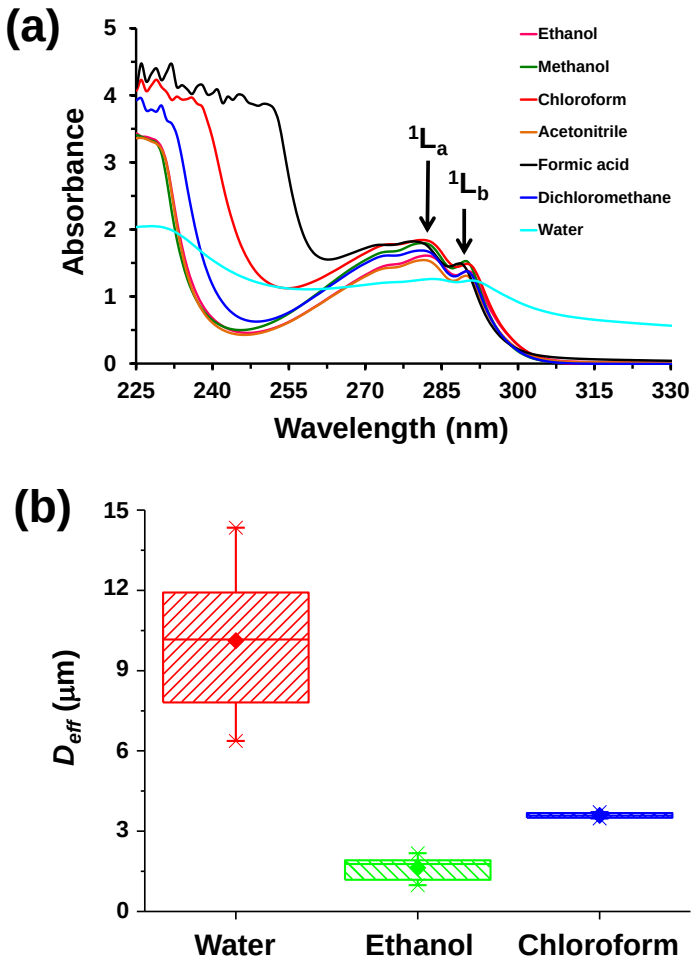

Figure 6.1.1 (a) Absorption (absorbance expressed with arbitrary units) spectra of GA-L determined in different solvents (dilute solution). (b) Effective diameter (D_{eff} , in μm) as measured by DLS of GA-L aggregates in different solvents.

These results are fully consistent with DLS measures for GA-L in water, ethanol and chloroform (Figure 6.1.1b). As it can be seen, the lowest and highest effective particle diameter (D_{eff}) was obtained in ethanol (D_{eff}= 1.6 μm) and water (D_{eff}= 10.1 μm), respectively, while the size of the aggregates in chloroform (D_{eff}= 3.5 μm) was similar to that in ethanol. According to these results, the electrospray solution described in the Methods section, which was obtained by mixing PE44 and GA-L solutions in chloroform and ethanol, respectively, was appropriated for loading the peptide.

Once the solvents were selected, operational parameters (*i.e.* applied voltage, tip-collector distance and flow rate) and solution properties (*i.e.* viscosity, surface-tension, volatility and concentration) were optimized to obtain regular microparticles of well-defined diameter. In general, the charge density on the droplet increases with the voltage, favouring the breakup of the liquid jet when the polymer concentration is low. However, high voltages promote the formation of microparticles with a broad distribution of sizes since multi-jets become irregular. The particle diameter increases with the distance between the tip and the collector because breakup becomes insufficient. The flow rate, which affects the charge density, is typically used to control the sphericity (*i.e.* high flow rates are characteristic of a poor sphericity). Solution properties also affect the fission of droplets, which is hampered when the surface tension is too high. Solution viscosity, which depends on the solvent, temperature and, especially, the polymer concentration and molecular weight, affects both the size and shape of the particles. Thus, breakup and deformation are hampered when the viscosity is high, fibres or particles being obtained from high or low viscosity solutions, respectively. These criteria were used to optimize the electrospraying conditions used in this work, which are summarized in the Methods section.

SEM micrographs of U-PE44 and PE44-GA electrosprayed particles are compared in Figure 6.1.2 In both cases microspheres were abundant and present some irregularities, which have been attributed to different degrees of collapse provoked by the low PE44 concentration (*i.e.* 2.5 wt.%). In

spite of these similarities, the peptide induces some important differences between the loaded and unloaded microspheres. Thus, U-PE44 particles present a wrinkled surface with well-defined folds homogeneously distributed onto it. These folds are placed at higher levels than the core of the particle, resulting in a homogeneous distribution of small cavities at the surface. In contrast, the cavities defined by the folds are filled in PE44-GA samples, indicating that peptide is loaded at the surface. This feature was corroborated by the AFM images displayed in Figure 6.1.3. Thus, comparison between phase and height images recorded for U-PE44 and PE44-GA samples clearly indicate that GA-L particles are located on the surface of the microspheres. The diameter of GA-L particles, which was estimated by analysing the cross-sectional profiles displayed in Figure 6.1.4, varied between 50 nm and 114 nm. AFM images also evidenced that the RMS Rq was slightly higher for U-PE44 than for PE44-GA.

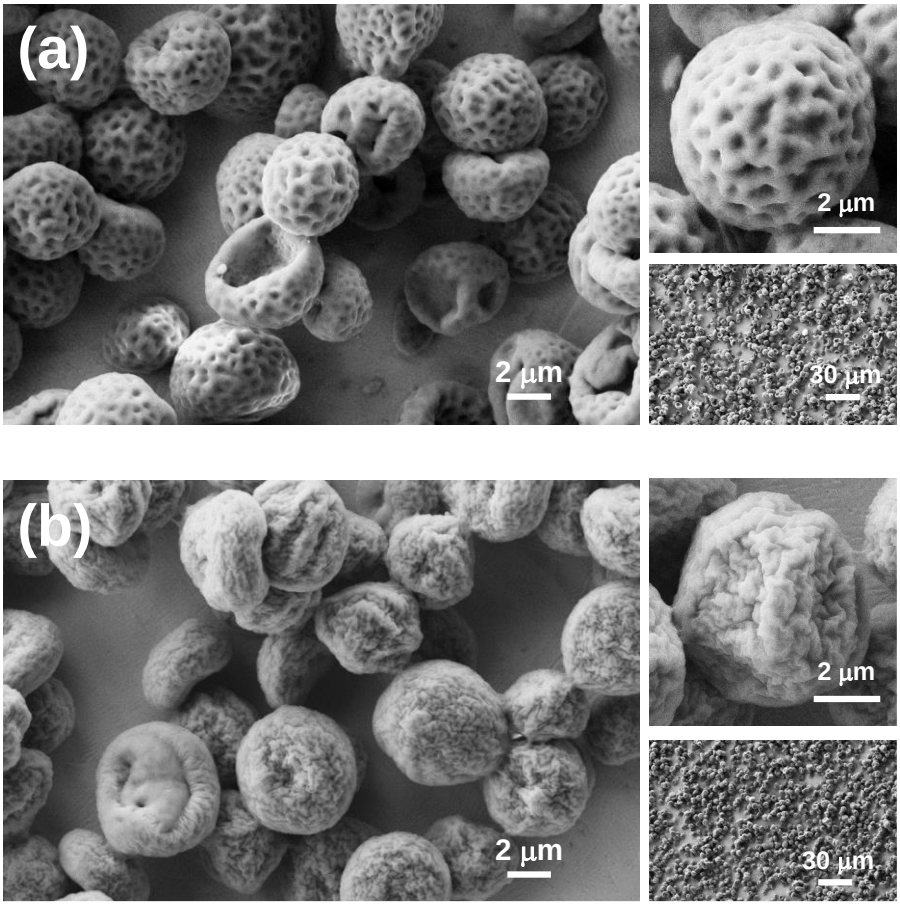

Figure 6.1.2 High and low magnification SEM micrographs of (a) U-PE44 (blank sample) and (b) PE44-GA electrosprayed microspheres.

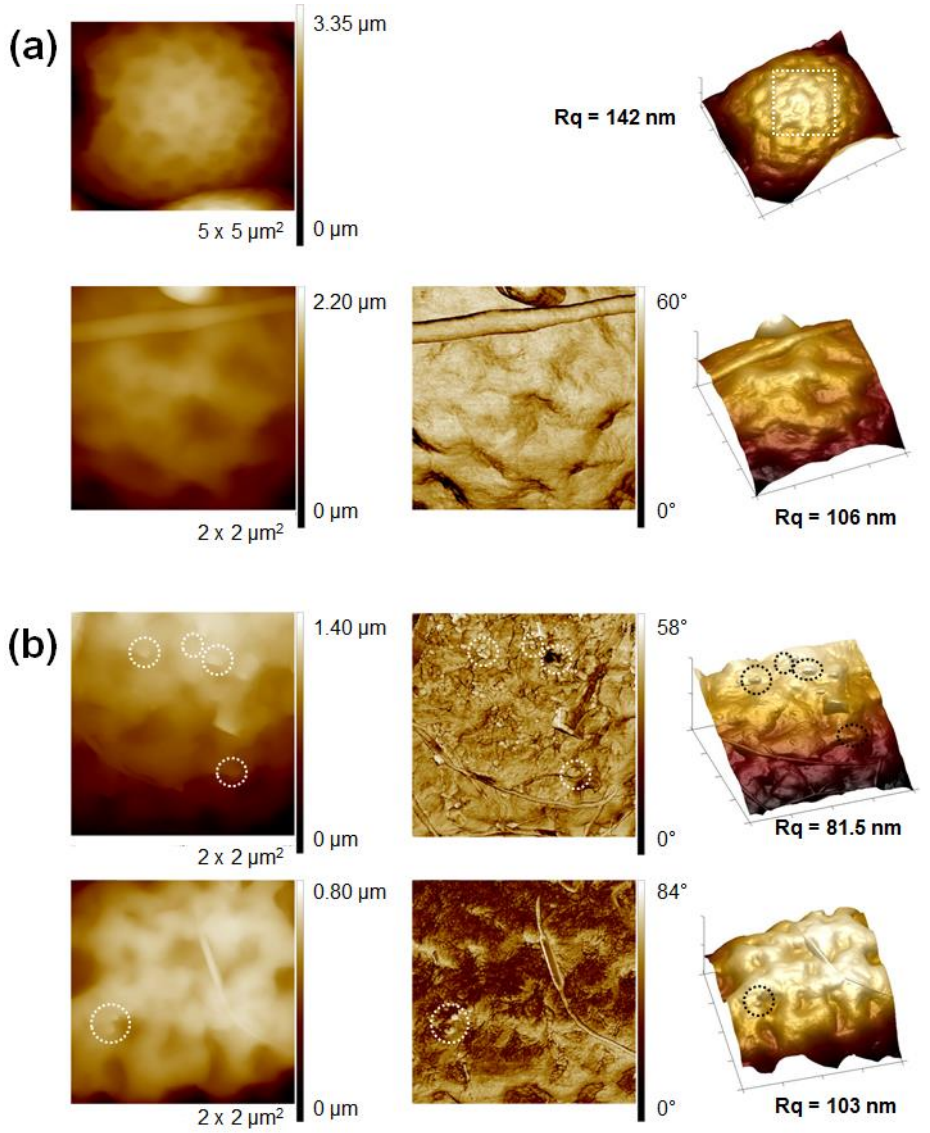

Figure 6.1.3 AFM images of (a) U-PE44 (blank sample) and (b) PE44-GA electrosprayed microspheres: 2D height images (left column), 2D phase images (middle column), and 3D height images (right column). Pointed circles in images displayed in (b) indicate GA-L aggregates (cross-section profiles of these particles are shown in Figure 6.1.4).

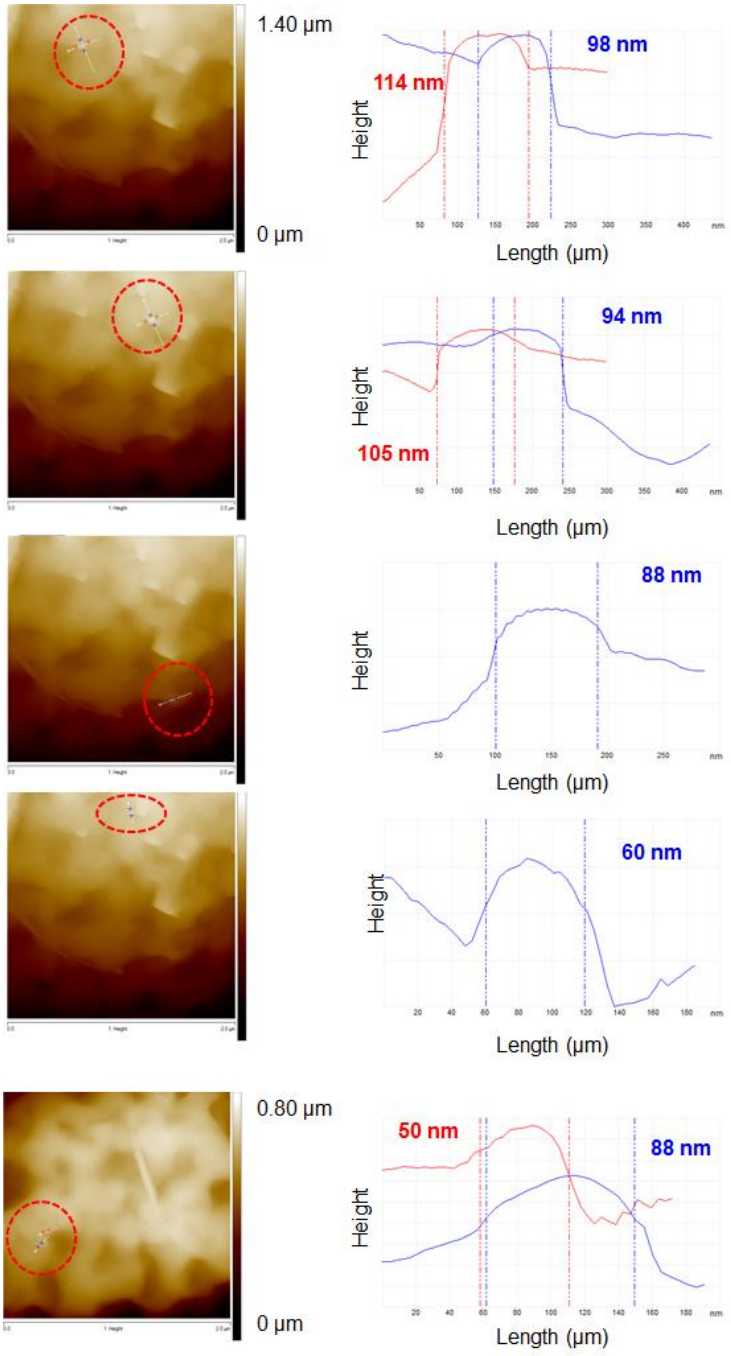

Figure 6.1.4 Cross-section profiles of GA-L particles located on the surface of PE44-GA electrosprayed microspheres.

It was not possible to have straightforward evidences of the morphology at the interior of the microspheres. Unfortunately, application of FIB-SEM led to the melting of the microparticles, while the application of alternative methodologies, like the one proposed by Wang *et al.* [31] and Zhang *et al.* [32], was not feasible because it requires the sample to be dissolved in water (*i.e.* both U-PE44 and PE44-GA microspheres tend to aggregate when interacting in aqueous solutions). However, the preparation process and the surface morphology of samples displayed in Figure 6.1.2 is similar to that of electrosprayed aluminum microspheres [33], which were found to be denser in the surface region than in the interior. This phenomenon, which should be attributed to the electrospraying process, is presumable due to the fact that aggregates on the surface have more opportunity to move and re-arranged relative to the interior aggregates.

The generation of electrosprayed particles is widely accepted to be controlled by two main mechanisms: solvent evaporation from droplets *en route* from the tip to the collector, and contemporaneous polymer diffusion during evaporation [34]. Rapid polymer diffusion does not necessarily lead to spherical particles but will ensure solid, dense particles. Both these mechanisms are dictated by the characteristics of the electrosprayed polymer solution itself, which in turn depend on the molecular weight and polymer concentration. Theoretically, the GA-L should be distributed evenly throughout the electrosprayed PE44 microparticles, however, it was scattered throughout the microparticles in various sizes (*i.e.* from 50 nm to 114 nm). This distribution pattern is closely related to the structure and stability of water-in-oil emulsions [35,36]. The polar phase composed of GA-L dissolved in ethanol was dispersed into the organic phase, composed of PE44 dissolved in chloroform during the own electrospraying process. As a consequence, the drug was close to the surface the microparticles.

Although the average particle diameter (d) was very similar for both U-PE44 and PE44-GA (5.1±0.5 μm and 5.0±0.7 μm, respectively), addition of 0.25 wt.% GA-L to the electrospray solution slightly affects the diameter distribution (Figure 6.1.5). Thus, a narrow distribution with

kurtosis of 1.34 at a confidence interval (CI) of 95% in the range 4.9-5.2 μm is observed for U-PE44, while PE44-GA shows a broader distribution with kurtosis of 0.04 in the CI of 95% (4.9-5.2 μm). As the electrospray operational conditions were identical for both systems, the movement of the diameter distribution of PE44-GA towards higher values supports that the peptide is loaded in the microspheres and particularly at their surface. Processing has a notable effect on the the dimensions of polymer particles. Thus, the *d* value determined for U-PE44 electrosprayed microparticles is 20% higher than the effective diameter determined by DLS (D_{eff}= 4.1±0.6 μm) for the raw material (*i.e.* PE44 powder coming from synthesis). The surface area of the electrosprayed particles, which is relevant for the diffusion of the GA-L molecules from particle to solvent, was determined by BET. This area increased from 2.5705 $m^2/g \pm 0.0513$ m^2/g for U-PE44 to 6.1361 m2/g ± 0.2548 for PE44-GA, indicating that diffusion phenomena should be favoured in latter with respect to the former.

Figures 6.1.6 compares the WAXD patterns registered for U-PE44 and PE44-GA microspheres, respectively. Detailed analysis of the X-ray diffractograms reflects the PE44 monoclinic crystal lattice.[37] Thus, the X-ray diffraction peaks at 2θ = 19.7°, 22.1°, 22.8°, 26.2° and 29.1°, which correspond to $(11\bar{1})$/(002), (012), (110), $(12\bar{1})$ and (111) planes of PE44 monoclinic crystal lattice, respectively, are identified. Deconvolution of the X-ray diffraction patterns into the crystalline peaks and the amorphous halo reveals significant differences between electrosprayed microspheres and the raw-materials. According to Eqn 6.1.2, variations in the $L_{(hkl)}$ values are consistent with changes in crystalline structure of the PE44. Thus, although $L_{(hkl)}$ in the (110) plane is similar for all samples, $L_{(hkl)}$ in the $(11\bar{1})$/(002) plane direction is 12.4 nm in the reference PE44 film and of 13.4 nm in the U-PE44 microspheres. In the (012) plane, $L_{(hkl)}$ is 0.7 nm higher for U-PE44 than for the film. These results indicate that the electrospraying process affects the supramolecular structure of the polymer.

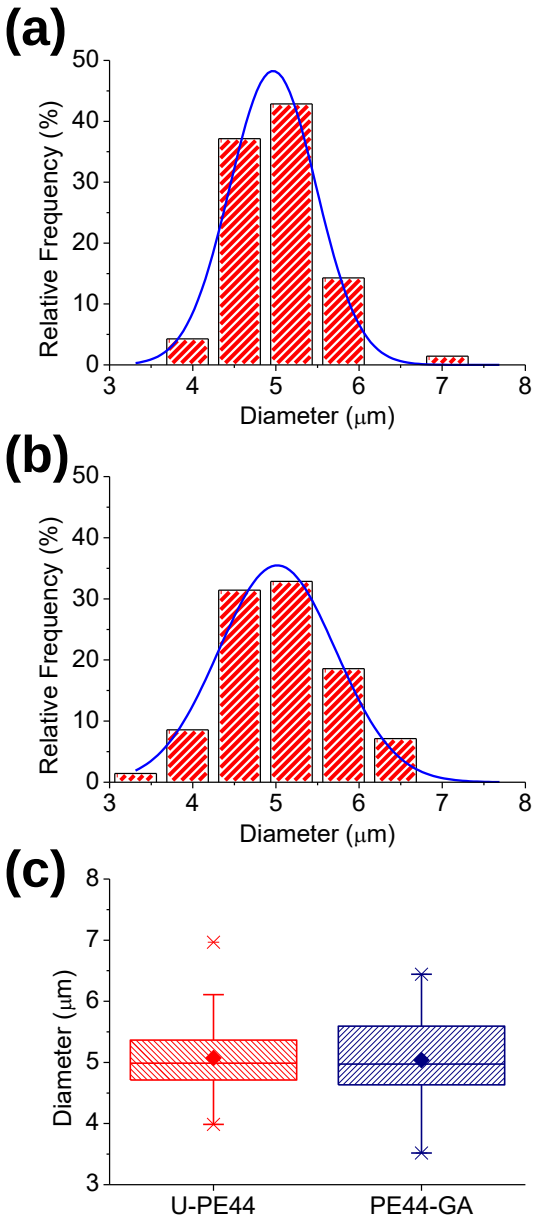

Figure 6.1.5 Diameter distribution of electrosprayed (a) U-PE44 and (b) PE44-GA microparticles. (c) Comparison of the diameters using a box-chart representation. The box range is determined by the 25th and 75th percentiles. The whiskers (×) are determined by the 1th and 99th percentiles. The (–) are the maximum and minimum values, (◆) corresponds to the mean, and the horizontal line into box is the median.

Deconvolution of the X-ray diffraction patterns into the crystalline peaks and the amorphous halo reveals significant differences between electrosprayed microspheres and the raw-materials (Table 6.1.1). As it can be seen, the crystallinity of the electrosprayed microparticles increases significantly upon the loading of GA-L (χ_c= 0.42 and 0.76 for U-PE44 and PE44-GA). Indeed, PE44-GA is more crystalline than the reference sample (χ_c= 0.63), even though the origin of their crystallinities are different. The sample prepared by solvent-casting allows a slow settlement of the polymer chains, resulting in a χ_c value higher than that of U-PE44. In contrast, for PE44-GA the increment in the χ_c value with respect to U-PE44 must be attributed to the contribution of the crystalline GA-L.

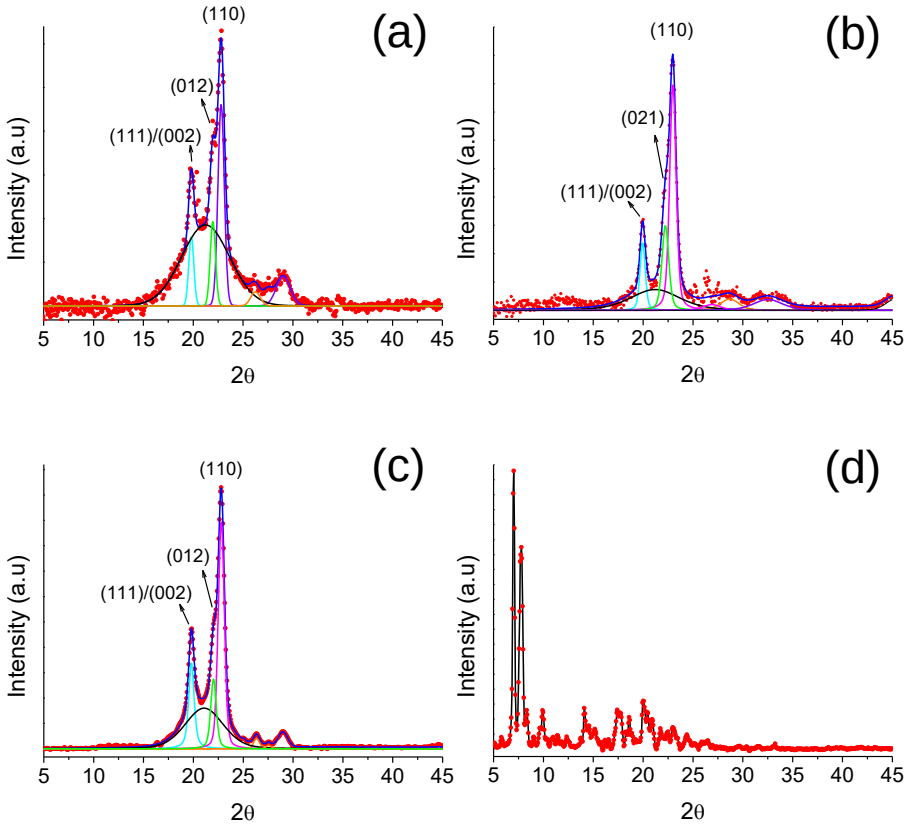

Figure 6.1.6 WAXD patterns of (a) U-PE44 and (b) PE44-GA electrosprayed microspheres, (c) PE44 film prepared by solvent-casting (reference sample), and (d) gramicidine.

Sample	χ_c	$L_{(11\bar{1})/(002)}$ (nm)	$L_{(012)}$ (nm)	$L_{(110)}$ (nm)
Reference (film)	0.63	12.4	12.2	11.0
U-PE44	0.42	13.4	12.9	10.7
PE44-GA	0.76	12.9	10.0	10.6

Table 6.1.1 Degree of crystallinity (χ_c) and crystallite size ($L_{(hkl)}$) of PE44 films prepared by solvent casting (reference sample) and both U-PE44 and PE44-GA electrosprayed microspheres.

Comparison of the FTIR spectra of U-PE44 and PE44-GA samples corroborates the loading of the peptide during the electrospraying process (Figure 6.1.7). Thus, the amide I band, which is governed by the stretching vibrations of the C=O and C–N groups, and the amide II band, which arises from the coupling between the N–H in-plane bending and the C–N stretching modes, are recognizable at approximately 1629 and 1535 cm^{-1}, respectively, for PE44-GA. These two amide bands are clearly distinguishable from the C=O stretching of aliphatic esters that appears as an intense and sharp band at 1712 cm^{-1} for both U-PE44 and PE44-GA.

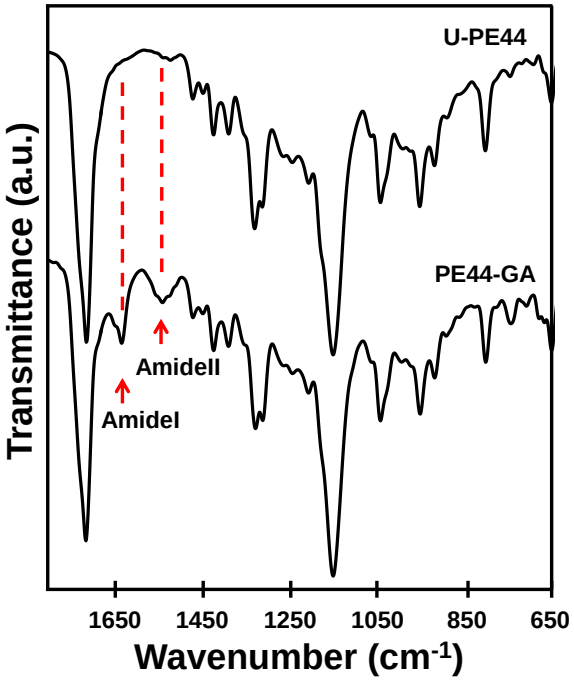

Figure 6.1.7 FTIR spectra of electrosprayed U-PE44and PE44-GA microparticles in the range 1850-1000 cm^{-1}.

Analysis of the FTIR amide I and amide II regions has been used to determine the structural characteristics of GA-L loaded into PE44 microspheres. Results, which are displayed in Figure 6.1.8 for unloaded and loaded GA-L, indicate that the amide I band correspond to the β-helix conformation. The component at 1632 cm^{-1} is present in the two samples and has been related with the $\beta^{6.3}$-helix [38]. The component at 1650 cm^{-1}, which corresponds to the $\beta^{5.6}$-helix [38], is clearly recognizable for the loaded peptide while it is only a shoulder in the spectrum of unloaded GA-L. These results suggest that two different β-helices coexist in PE44-GA while the $\beta^{6.3}$-helix is clearly the predominant for the GA-L in solution. The latter has been corroborated by comparing the CD spectrum acquired for GA-L dissolved in ethanol (Figure 6.1.9) with those reported in the literature [7]. The influence of the PE44 matrix in the peptide conformation is also supported by relative intensity changes in the four components of the FTIR amide II band (Figure 6.1.8).

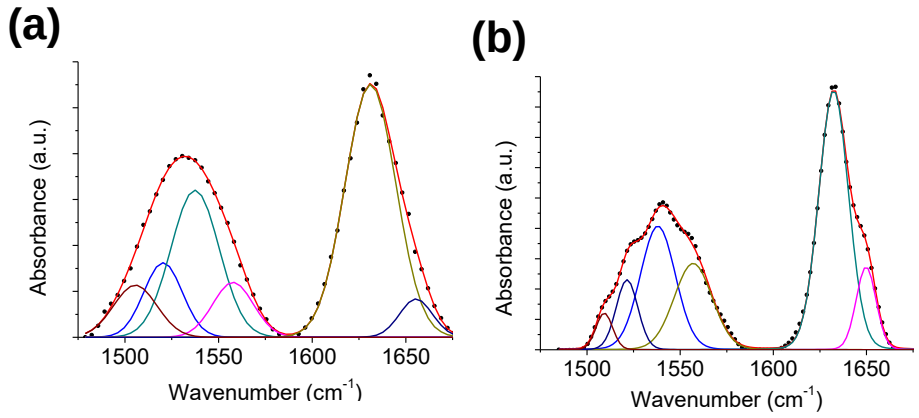

Figure 6.1.8 Deconvolution of the amide I and amide II absorption bands recorded by FTIR spectroscopy for (a) GA-L and (b) GA-L loaded into PE44 microspheres at room temperature.

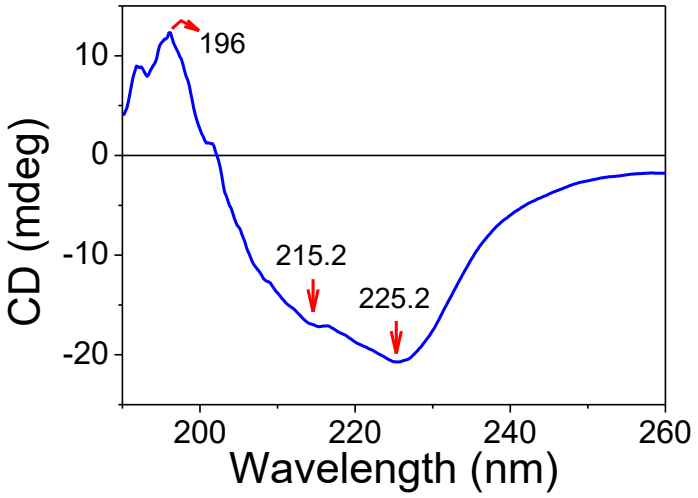

Figure 6.1.9 CD spectrum of GA-L dissolved in ethanol.

The chemical structure of U-PE44 and PE44-GA particles was further characterized by XPS, compositions being compared in Table 6.1.2. The penetration of X-ray radiation using the conditions described in Methods section is expected to be ~10 nm, even though in this case the penetration is unknown because of both the porosity (Figure 6.1.2a) of U-PE44 microspheres. In any case, radiation reaches the surface of the metallic

substrate (aluminum foil) used as collector, which is only partially covered by electrosprayed microspheres. This feature explains the detection of a small percentage of nitrogen in U-PE44 samples, which has been attributed to the aluminum foil substrate. It should be noted that we also detected nitrogen in the atomic composition of polymeric microstructures deposited onto metallic substrates, even though in those cases the substrate was stainless steel [39]. However, the N1s increases from 0.26% in U-PE44 to 4.57% in PE44-GA, supporting the successful incorporation of the peptide. For U-PE44 the C/O ratio, 2.27, is close to the theoretical value of 2.00, while such ratio increases to 2.49 for PE44-GA-L. Although the increment of the C/O ratio in the latter has been associated to the loading of peptide, it is important to point out that the experimental values of C/O ratio are influenced by the presence of hydrocarbon contamination. This is commonly present in samples subjected to XPS analysis and can be traced back to typical laboratory environment and the pumping system [40].

Sample	C1s	N1s	O1s
U-PE44	69.23	0.26	30.51
PE44-GA	68.09	4.57	27.34

Table 6.1.2 Atomic percent composition (C1s, N1s and O1s) obtained by XPS for U-PE44 and PE44-GA samples.

High-resolution XPS spectra in the C1s and O1s regions are displayed in Figure 6.1.10. Deconvolution of the C1s peak led to three and four Gaussian curves for U-PE44 and PE44-GA, respectively. Three of such curves have been attributed to saturated C–C / C–H (284.2 eV), C–O (286.1 eV) and C=O (288.7 eV) bonds of PE44 chains [41,42], while the fourth curve of PE44-GA corresponds to the (O=)C–NH peptide bonds (287.3 eV) [43,44]. The O1s signal consists of two components, which has been assigned to the C=O (531.87 eV) and C–O bonds (533.42) [39-44]. For U-PE44, the C=O component is less intense than the C–O one while

the opposite relative intensity order is obtained for PE44-GA due to the incorporation of peptide molecules.

Thermal degradation kinetics of PE44 was studied by Chrissafis *et al.* [45], a two-step decomposition process being reported. The first one was very small and could only be slightly distinguishable in DTGA thermograms. n^{th}-Order mechanisms were postulated as typical for degradation of polyesters [46]. Specifically n = 0.75 and 0.68 and activation energies of 128 and 189 k/mol were determined for the first and second decomposition steps of PE44, respectively. U-PE44 has a high thermal stability, being the onset degradation temperature higher than 300 ºC and, obviously, higher than its melting temperature (115 ºC).

.

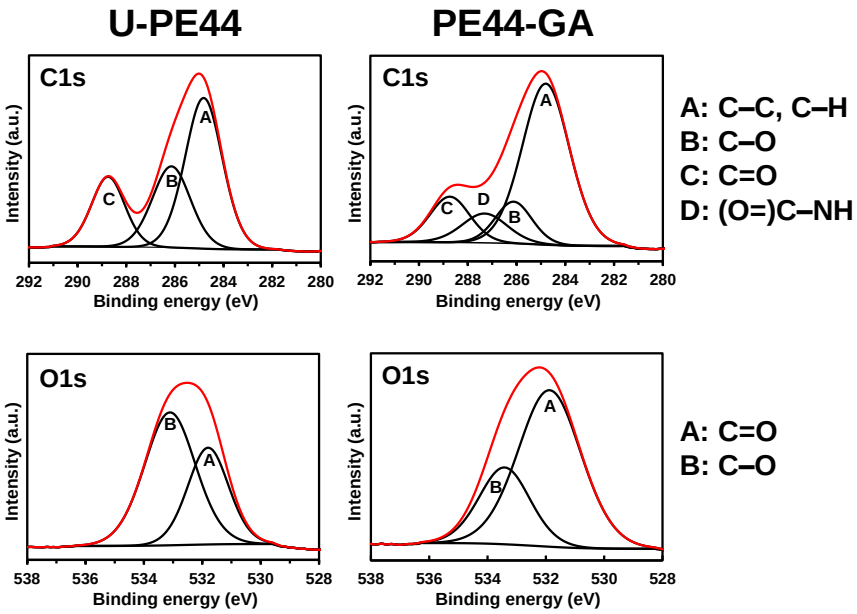

Figure 6.1.10 High-resolution XPS spectra for U-PE44 and PE44-PGA: C1s and O1s regions. The red line corresponds to the experimental profile while the black lines are the peaks from deconvolution. The bonds associated to the deconvoluted peaks are also displayed.

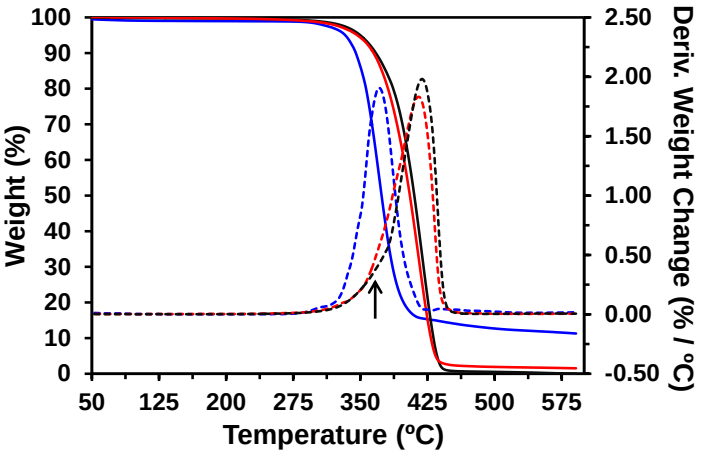

Figure 6.1.11. TGA (solid lines) and DTGA (dashed lines) curves for U-PE44 (black), GA-L (blue) and the PE44-GA (red). Arrow points out the first degradation step of PE44.

Incorporation of drugs may affect the thermal stability of the base polymer, a feature that has been considered due to the lower stability of GA-L. Thus, the temperature of the main DTGA peak for GA-L decreases by approximately 50 ºC with respect to PE44. In spite of this, minimum changes were detected between U-PE44 and PE44-GA samples (Figure 6.1.11). Thus, the second degradation step seems to proceed slightly faster in such a way that the two stages of degradation are practically not differentiated on the corresponding DTGA curve. In addition, the char yield of PE44-GA slightly increased with respect U-PE44, which is in agreement with the significant residue produced in the decomposition of GA-L as consequence of its aromatic content.

The water contact angle value determined for U-PE44 is 104º±3º (Figure 6.1.12) evidencing the hydrophobic nature of the polymeric matrix. The incorporation of GA-L enhances the hydrophobicity of the polymeric matrix, the contact angle increasing to 129º±2º for PE44-PGA. This is a very attractive result for peptide-release based applications since the low wettability of PE44-GA microspheres in water solvents is expected to be accompanied by a relatively slow delivery in polar environments like PBS.

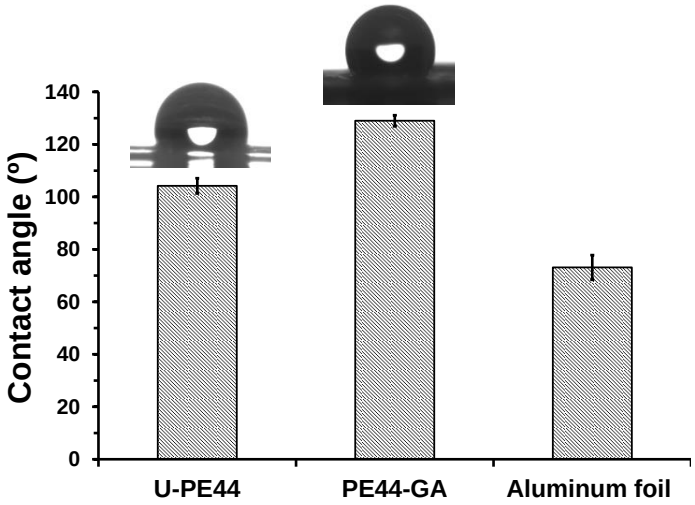

Figure 6.1.12 Contact angle values of U-PE44 and PE44-GA. The contact angle of the aluminum foil used to collect the microspheres is also displayed.

GA-L release from electrosprayed microparticles in a given medium is expected to depend on the intermolecular interactions between the peptide and the PE44 matrix. Quantitative release studies were performed considering PE44 microspheres loaded with GA-L. Both PBS and PBS-EtOH were used as release media. It should be noted that the physical characteristics in a place of the body (*e.g.* pH and hydrophilicity/hydrophobicity ratio) depends on the location. Therefore, comparison of the release rate in PBS and PBS-EtOH is a standard assay to ascertain how changes in the environment affect the drug release. According to previous studies [24,25], the ethanol supplement facilitates the delivery of highly hydrophobic molecules, such as GA-L, precluding the establishment of early equilibrium conditions that limit their release in PE44.

Figure 6.1.13 shows the release profile in PBS and PBS-EtOH for GA-L loaded in PE44 microparticles. The cumulative release plot in PBS for PE44 microspheres loaded with GA-L exhibits a massive initial burst release up to a maximum percentage (~87%) and a subsequent decrease of the release percentage until a constant value (~70%). The plateau region observed after 5 days is consistent with the achievement of that

equilibrium value. This behaviour suggests that a small amount of the initially delivered peptide was able to enter again inside the PE44 microparticles to meet the equilibrium condition. It should be remarked that the burst release, which is due to the rapid diffusion of PBS into the microparticles surface, is consistent with the location of the GA-L near the surface [47], as was evidenced by AFM and SEM. Also, it should be mentioned that measures about the release of GA-L in PBS exhibited very poor statistical precision (Figure 6.1.13a), which has been attributed to the poor interaction between GA-L and water discussed above (Figure 6.1.1).

The rate of GA-L release from PE44 microspheres is higher in PBS-EtOH than in PBS, which is consistent with hydrophobic sequence of the peptide. Thus, results displayed in Figure 6.1.13b indicate that, initially, the release of GA-L was very fast, reaching 92% and 98% of the loaded peptide after 6 hours and 7 days of exposure in PBS-EtOH, respectively. The delivery process in PBS-EtOH is explained by the diffusion of the peptide through the polymeric matrix, which is facilitated by the solvent-induced swelling of PE44 and the weak interactions and the polymeric matrix and peptide.

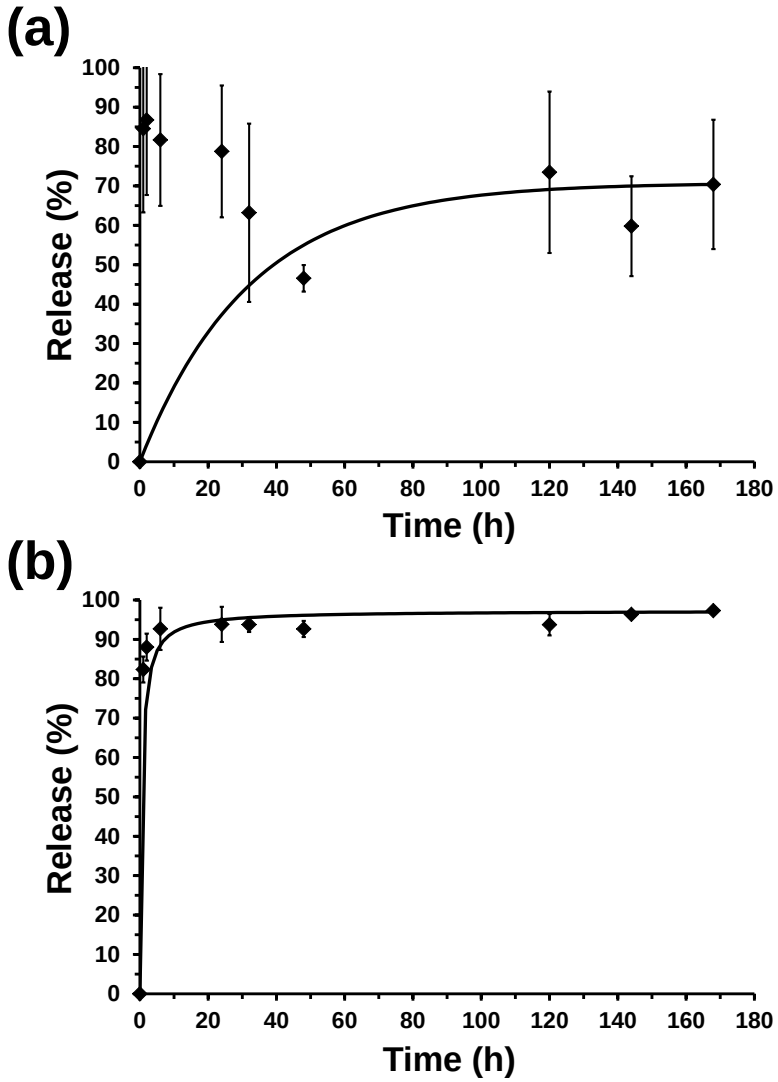

Figure 6.1.13 Release curves in (a) PBS and (b) PBS-EtOH media of GA-L from PE44-GA microspheres.

The loading efficiency (LE) was calculated on the basis of the following formula:

$$\%LE = \frac{[GA - L]_{final}}{[GA - L]_{initial}} \times 100 \quad \text{(Eqn. 6.1.3)}$$

where $[GA\text{-}L]_{final}$ is the sum of GA-L released in PBS-EtOH along 168 h and the GA-L remaining at the PE44 matrix after such time, and $[GA\text{-}L]_{initial}$ corresponds to the GA-L concentration in the electrospraying solution related to the content of polymer (w/w%). Results indicated that the average LE for this pentadecapeptide is 41%±10% (*i.e.* the LE determined for four replicas varied between 32% and 51%). Although very high drug loading efficiencies (up to ~90%) have been reported for microspheres obtained using electrospraying [48-50], it should be emphasized that the loading of GA-L in the polymeric matrix is a major challenge due to its insolubility. According to such circumstance, the LE reached in this work, which to the best of our knowledge is the greatest reached for GA-L (*i.e.* Dittrich and Meier [22] obtained LEs lower than 30%), should be considered relatively high. The LE obtained in the current work should be attributed not only to the electrospraying process but also to the appropriate choice of the polymeric matrix. More specifically, the charge distributions of the peptide and the PE44 matrix exhibit important similarities. Thus, the peptide and ester bonds are the only polar groups in the GA-L and PE44, respectively, while the charge in the rest of the molecular fragments is homogeneously low, which provides a high hydrophobic character. These similar trends facilitate the formation of stable mixtures that are subsequently used as electrospraying solutions.

The antibacterial activity of PE44 microspheres loaded with GA-Lwas tested against *E. coli* and *S. aureus* (as representative of Gram-positive and Gram-negative bacteria, respectively). Results from antimicrobial tests are displayed in Figure 6.1.14. An inhibition zone around both PE44-GA and GM samples is clearly identified for the two tested bacteria indicating that compounds with bactericidal activity diffuse outward from the samples. Thus, such clear zones are halos of inhibition that indicate the extent of the

test organism's inability to survive in the presence of the GM antibiotic and the GA-L released from the PE44 matrix. Obviously, the area of the clear zone is higher for GM than for PE44-GA since the bacterial growth inhibition promoted by GA-L depends on the release rate from the polymeric matrix. On the other hand, no inhibition zone has been detected for PE44 samples indicating that, as it was expected, the polymeric matrix is harmless to bacteria.

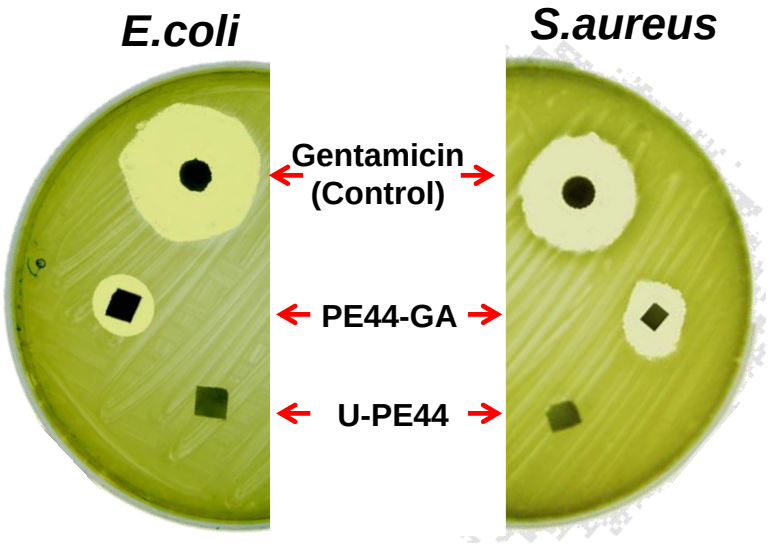

Figure 6.1.14 *E.coli* and *S.aureus* bacterial cultures showing the inhibition zones around PE44-GA and GM (positive control) samples. U-PE44 was also tested as negative control.

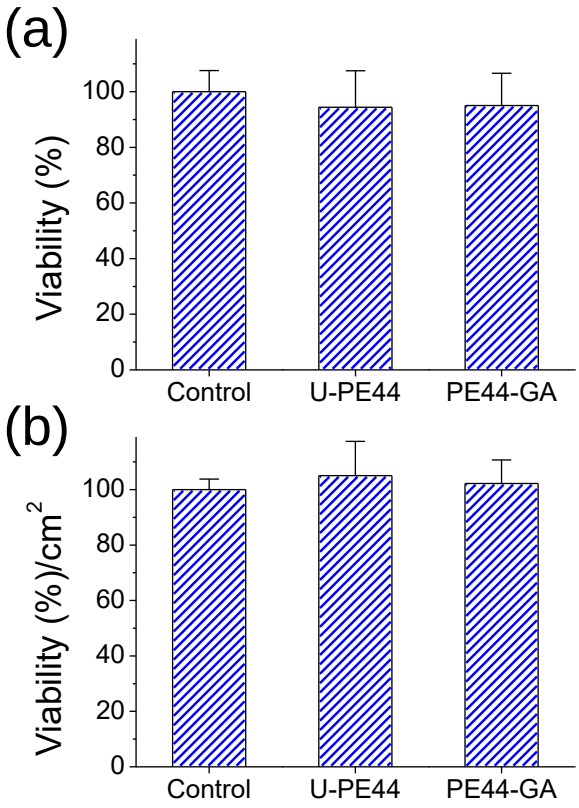

Figure 6.1.15 Viability of MDCK cells in presence of (a) U-PE44 and PE44-GA samples and (b) adhesion cellular onto the microsphere matrices.

The response of PE44-GA towards cells was compared with that of U-PE44. Cytotoxicity and cellular adhesion assays were performed considering MDCK epithelial cells. These carcinogenic cells were selected due to their fast growth. Quantitative results are displayed in Figure 6.1.15, TCPS being used as control substrates. As it can be seen, the reduction in the number of viable cells after 24 h of culture was similar for the U-PE44, PE44-GA and the control (Figure 6.1.15a). Similarly, the number of adhered cells by area of material was the same for the three species (Figure 6.1.15b). These results clearly indicate that the incorporation of GA-L does not alter the biocompatibility of the PE44 matrix, which is practically identical to that of TCPS.

6.1.4 Conclusions

The results reported above demonstrate that electrosprayed PE44 microspheres can be used to load GA-L, a highly hydrophobic pentadecapeptide that has been recently proposed as a potent therapeutic agent against different carcinomas. The loading efficiency is relatively high (41%), which has been attributed to the hydrophobic similarity between the GA-L and PE44 matrix resulting in a stable combination. The peptide, which is mainly loaded at the surface of the microparticles, enhances the hydrophobicity of the microparticles while the thermal stability remains practically unaltered. After seven days, the delivery in PBS and PBS-EtOH is 70% and 98%, respectively. Thus, the release rate of GA-L from PE44 microparticles is higher in PBS-EtOH than in PBS due to the remarkably hydrophobicity of this peptide. On the other hand, although FTIR studies suggest that GA-L undergoes some structural changes upon loading into PE44 microspheres, both the antibacterial activity of the peptide and the biocompatibility of the polymeric matrix are clearly maintained.

In summary, the delivery of therapeutic molecules is tantamount to the success of many medical treatments. With the development of new and superior medical treatment for many diseases, as for example cancer, there is a concomitant demand to encapsulate and release bioactive molecules in a safe, effective and reproducible manner. In this work we have proved that encapsulation and release of GA-L, a versatile bioactive molecule because of its multiple and varied therapeutic uses, is feasible despite its molecular size and very high hydrophobicity.

6.1.5 References

1. D.A. Kelkar, A. Chattopadhyay; *Biochim. Biophys. Acta, Biomembr.*, vol. 1768, pp. 2011-2025, 2007.
2. R.D. Hotchkiss, R. Dubos; *J. Biol. Chem.*, vol. 132, pp. 791-792, 1940.
3. F. O'Boyle, B.A. Wallace; *Protein Pept. Lett.*, vol. 10, pp. 9-17, 2003.
4. D.A. Doyle, B.A. Wallace; *J. Mol. Biol.*, vol. 266, pp. 963-977, 1997.
5. F. Heitz, A. Heitz, Y. Trudelle; *Biophys. Chem.*, vol. 24, pp. 149-160 ,1986.
6. N. Mobashery, C. Nielsen, O.S. Andersen; *FEBS Lett.*, vol. 412, pp. 15-, 1997.
7. J. A. Killian, K. U. Prasad, D. Hains and D. W. Urry, *Biochemistry*, 1988, 27, 4848.
8. G.N. Moll, V. van den Eertwegh, H. Tournois, B. Roelofsen, J.A.F. Op den Kamp, L.L.M. van Deenen; *Biochim. Biophys. Acta*, vol. 1062, pp. 206-210, 1991.
9. C. Gumila, M.L. Ancelin, A.M. Delort, G. Jeminet, H.J. Vial; *Antimicrob. Agents Chemother.*, vol. 41, pp. 523-529, 1997.
10. J.W. Liou, Y.J. Hung, C.H. Yang, Y.C. Chen; *PLOS One*, vol. 10, pp. e0117065, 2015.
11. J.F. Yala, P. Thebault, A. Hequet, V. Humblot, C.M. Pradier, J.M. Berjeaud; *Appl. Microbiol. Biotechnol.*, vol. 89, pp. 623-634, 2011.
12. S. Sek, T. Laredo, J.R. Dutcher , J. Lopkowski; *J. Am. Chem. Soc.*, vol. 131, pp. 6439-6445, 2009.
13. F. Wang, L.H. Qin, C.J. Pace, P. Wong, R. Malonis, J.M. Gao; *Chem.Bio.Chem.*, vol. 13, pp. 51-55, 2012.
14. J.D. Freedman, T.S. Novak, J.D. Bisognano, P.R. Pratap; *J. Gen. Physiol.*, vol. 104, pp. 961-983, 1994.

15. J.M. David, T.A. Owens, S.P. Barwe, A.K. Rajasekaran; *Mol. Cancer Ther.*, vol. 12, pp. 2296-2307, 2013.

16. J.M. David, T.A. Owens, L.J. Inge, R.M. Bremmer, A.K. Rajasekaran; *Mol. Cancer Ther.*, vol. 13, pp. 788-799, 2014.

17. D. Wijesinghe, M.C. Arachchige, A. Lu, Y.K, Reshetnyak, O.A. Andreev; *Sci. Rep.*, vol. 3, pp. 3650-3671, 2013.

18. D.K. Rao, H.Y. Liu, S.V. Ambudkar, M. Mayer; *J. Biol. Chem.*, vol. 289, pp. 31397-31410, 2014.

19. P.A. Gurnev, E.M. Nestorvich; *Toxins*, vol. 6, pp. 2483-2540, 2014.

20. H.N. Abdelhamid, M.S. Khan, H.F. Wu; *RSC Adv.*, vol. 4, pp. 50035, 2014.

21. K. Wang, J. Ruan, H. Song, J. Zhang, Y. Wo, S. Guo, D. Cui; *Nanoscale Res. Lett.*, vol. 6, pp. 8, 2011.

22. C. Dittrich, W. Meier; *Macromol. Biosci.*, vol. 10, pp. 1406-1415, 2010.

23. T.B. Schuster, D. de Bruyn Outboter, E. Bordignon, G. Jeschke, W. Meier; *Soft Matter*, vol. 6, pp. 5596-5604, 2010.

24. L.J. del Valle, R. Camps, A. Díaz, L. Franco, A. Rodríguez-Galán, J. Puiggalí; *J. Polym. Res.*, vol. 18, pp. 1903-1917, 2011.

25. S. Murase, M. Aymat, A. Calvet, L.J. del Valle, J. Puiggalí; *Eur. Polym. J.*, vol. 71, pp. 196-209, 2015.

26. M.M. Pérez-Madrigal, E. Armelin, L.J. del Valle, F. Estrany, C. Alemán; *Polym. Chem.*, vol. 3, pp. 979-991, 2012.

27. A. Aszalos, In "Modern Analysis of Antibiotics", *Marcel Dekker Inc, New York*, pp. 32-33, 1986.

28. J. Catalán; *Phys. Chem. Chem. Phys.*, vol. 18, pp. 15170-15176, 2016.

29. D.M. Rogers, N.A. Besley, P. O'Shea, J.D. Hirst; *J. Phys. Chem. B*, vol. 109, pp. 23061-23069, 2005.

30. D.W. Pierce, S.G. Boxer; *Biophys. J.*, vol. 68, pp. 1583-1591, 1995.

31. L. Wang, Q. Zhang, X. Wang, J. Liu, J. Yang; *J. Appl. Polym. Sci.*, vol. 122, pp. 2552-2556, 2011.

32. Q. Zhang, Y. Zhang, Q. Wei, X. Wang, J. Liu, J. Yang, C. Zhao; *J. App. Polym. Sci.*, vol. 120, pp. 2648-2653, 2011.

33. H. Wang, G. Jian, S. Yan, J. B. DeLisio, C. Huang, M.R. Zachariah; *ACS Appl. Mater. Interfaces*, vol. 5, pp. 6797-6801, 2013.

34. B. Almeria, W.W. Deng, T.M. Fahmy, A. Gomez; *J. Colloid Interface Sci.*, vol. 343, pp. 125-133, 2010.

35. X.Y. Yang , A. Leonard, A. Lemaire, G. Tian, B.L. Su; *Chem Commun*, vol. 47, pp. 2763-2786, 2011.

36. T. Takami, Y. Murakami; *Langmuir*, vol. 30, pp. 3329- 3336, 2014

37. M. S. Nikolic, J. Djonlagic; *Polym. Degr. Stab.*, vol. 74, pp. 263-270, 2001.

38. A. Nelson; *Biophys. J.*, vol. 76, pp. 1639, 1999.

39. G. Fabregat, G. Ballano, E. Armelin, L.J. del Valle, C. Cativiela, C. Alemán; *Polym. Chem.*, vol. 4, pp. 1412-1424, 2013.

40. G. C. Smith, *J. Electron. Spectrosc. Relat. Phenom.*, vol. 148, pp. 21-28, 2005.

41. E. Llorens, H. Ibañez, L. J. del Valle, J. Puiggalí; *Mater. Sci. Eng. C*, vol. 49, pp. 472-484, 2015.

42. H.Y. Wang, J.H. Ji, W. Zhang, Y.H. Zhang, J. Jiang, Z.W. Wu, S.H. Pu, P.K. Chu; *Acta Biomater.*, vol. 5, pp. 279-287, 2009.

43. J.F. Moulder, W.F. Stickle, P.E. Sobol, K.D. Bomben; Handbook of X-ray Photoelectron Spectroscopy, Perkin-Elmer Corp, *Eden Prairie, MN, USA*, 1992.

44. Z. Yang, S. Yuan, B. Liang, Y. Liu, C. Choong, S.O. Pehkonen; *Macromol. Biosci.*, vol. 14, pp. 1299-1311, 2014.

45. K. Chrissafis, K.M. Paraskevopoulos, D.N. Bikiaris; *Thermochim. Acta*, vol. 435, pp. 142-150, 2005.

46. H. Zhao, Y. Z. Wang, D.Y. Wang, B. Wu, D.Q. Chen, X.L. Wang, K.K. Yang; *Polym. Degrad. Stab.*, vol. 80, pp. 135-140, 2003.

47. Y. Wang, X. Yang, W. Liu, F. Zhang, Q. Cai, X. Deng; *J. Microencapsul.*, vol. 30, pp. 490-497, 2013.

48. J. Xie, W.J. Ng, L.Y. Lee, C.H. Wang; *J. Colloid Interface Sci.*, vol. 317, pp. 469-476, 2008.

49. Y.H, Lee, F. Mei, M. Bai, S. Zhao, D.R. Chao; *J. Control Release*, vol. 145, pp. 58-65, 2010.

50. A. Bohr, J. Kristensen, M. Dyas, M. Edirisinghe, E. Stride; *J. R. Soc. Interface*, vol. 9, pp. 2437-2449, 2012.

6.2 ANTIMICROBIAL ELECTROSPUN FIBERS OF POLYESTER LOADED WITH ENGINEERED CYCLIC GRAMICIDIN ANALOGUES‡‡

6.2.1 Introduction

On-demand release of drug molecules from biomedical devices enables precise targeted dosing that can be temporally tuned to meet the requirements of a variety of biomedical applications [1-3]. Although recent advances have facilitated the use of different stimuli, such as light, magnetic and electric fields, ultrasounds and electrochemical signals, to trigger drug release from smart material formulations (*e.g.* films, micro- and nanoparticles, and implant devices) [3-6], traditional systems based on the biodegradability of polymeric vehicles remain the most employed technology because of its efficiency, simplicity, and low cost [7-14]. Biodegradable polyester particles and fibers are widely employed for controlled and sustained targeted release of hydrophobic and poorly-water soluble drugs [15-21].

Among biomolecules with therapeutic applications, gramicidin (GA) deserves special mention because of its versatility. From a functional point of view, GA is well known because of its activity as bactericide [22,23], antibiotic [24], and potential therapeutic agent for different carcinomas [25-28]. In spite of its potential biomedical applications, encapsulation of GA has been scarcely studied due to the insolubility of this peptide, which represents a major limitation [19,29-31]. Abdelhamid *et al.* [29] loaded GA on the surface of GO for effective antibacterial treatments. Nevertheless, the utilization of GO for biomedical applications is controversial because of its dose-dependent toxicity to cells and living systems [32]. Also, peptide particles have been prepared using amino acid sequences related to those of GA [30,31]. Recently, we loaded

‡‡ Results submitted for publication.

hydrophobic GA produced by *Bacillus brevis* (*i.e.* a linear pentadecapeptide with sequence formyl-L-Xxx-Gly-L-Ala-D-Leu-L-Ala-D-Val-L-Val-D-Val-L-Trp-D-Leu-L-Yyy-D-Leu-L-Trp-D-Leu-L-Trp-ethanolamine, where Xxx can be either Val or Ile and Yyy is frequently Trp) into spherical microparticles (average diameter: 5.0±0.7 μm) of PE44, a biodegradable and biocompatible aliphatic polyester, by means of electrospraying [19]. Unfortunately, the release of GA in physiological media was severely limited by the very low solubility of the biomolecule in aqueous solution: a fast burst effect followed by the establishment of equilibrium after 5 days was observed in hydrophilic media. However, despite such limitation, biological tests demonstrated that GA retained its antimicrobial activity after loading and did not alter the biocompatibility of PE44 [19].

The high potential of peptides in diagnosis and therapeutics is sometimes hampered by their short-life times (*i.e.* endogenous proteases rapidly digest these biomolecules). Among the different strategies proposed to protect peptides from proteolytic cleavage, targeted replacements with non-coded amino acids is among the most successful ones [33-35]. In an early study, Cativiela and co-workers designed and synthetized two rigid GA analogues by introducing some chemical changes at the sequence of gramicidin soviet (GA-S) to enhance the antimicrobial activity of GA by stabilizing the bioactive conformations through steric and stereochemical constraints [36]. In addition, the incorporation of non-proteinogenic residues into GA-S should also impart stability against proteolytic cleavage. GA-S is a cyclic symmetrical cationic antimicrobial peptide of sequence *cyclo*(Val-Orn-Leu-D-Phe-Pro)$_2$ produced non-ribosomally by *Bacillus brevis* [37] and active against bacteria and fungi [38,39]. More specifically, in such two engineered peptides the D-Phe was replaced by D-Pro while the L-Pro was changed by two conformationally restrained residues. In the first peptide, hereafter denoted GA-S1 [with sequence *cyclo*(Val-Orn-Leu-D-Pro-Ac$_3$c)$_2$], L-Pro was replaced by 1-aminocyclopropanecarboxylic acid (Ac$_3$c in Figure 6.2.1), an α,α-dialkylated amino acid with strong stereochemical constraints [40,41]. The second peptide [with sequence *cyclo*(Val-Orn-Leu-D-Pro-*S,S*-c$_3$diPhe)$_2$],

hereafter denoted GA-S2, was designed using an Ac_3c derivative with two vicinal phenyl substituents in a *trans* relative disposition (*S,S*-$c_3$diPhe in Figure 6.2.1) to replace L-Pro. It is worth noting that *S,S*-$c_3$diPhe is much more constrained and hydrophobic than Ac_3c because of two additional phenyl rings [42]. Moreover, the substitutions introduced in GA-S1 and GA-S2 are expected to have a severe impact in the capacity of the peptides to be loaded in polymeric matrices since they reduced the molecular flexibility and alters the wettability.

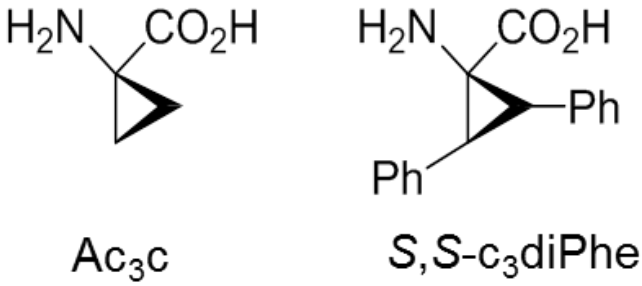

Figure 6.2.1 Chemical structure of Ac_3c and *S,S*-$c_3$diPhe.

In this work we prepared ultrathin fibers loaded with GA-S1 and GA-S2 using electrospinning. This electrostatic technique involves the use of a high voltage field to charge the surface of a polymer solution droplet, which is held at the end of a capillary tube, inducing the ejection of a liquid jet towards a grounded target (collector) [43-45]. After characterizing the morphology, chemical structure, and properties of the resulting GA-loaded PE44 fibers, we examined their antibiotic potency and biocompatibility as well as the peptide release in different environments. In all cases, results were compared with those obtained from PE44 fibers loaded with linear GA pentadecapeptide, hereafter denoted GA-L. PE44 fibers stabilize the bioactive conformation of the two cyclic peptides and regulate the peptide release in hydrophilic environments, which is of crucial importance for biomedical applications. Furthermore, PE44/GA-S2 is more effective than PE44/GA-S1 in terms of antimicrobial response because of the disposition of the phenyl rings in *S,S*-$c_3$diPhe.

6.2.1 Methods

Materials

PE44 is a commercial product (Bionolle® 1001) supplied by Showa Denko K.K. (Germany). The polymer has a melt flow index of 1.6 g/10 min (measured at 190 ºC under a load of 2.16 kg according to ASTM-D1238). Linear GA was purchased from Sigma-Aldrich (G5002), while GA-S1 and GA-S2 were prepared as previously reported [46].

Electrospinning

Mixtures of PE44 and GA peptides (*i.e.* GA-S1, GA-S2 and GA-L) were electrospun, samples being named PE44/GA-# (where GA-# indicates the loaded peptide). Mixtures were prepared as follows. PE44 was dissolved in chloroform while peptides were dissolved in ethanol. Solutions were kept under stirring at 80 rpm overnight. Finally, the solutions were mixed and loaded in a 5 mL BD plastic syringe for delivery through an 18G × 1.1/2'' needle at a mass-flow rate of 2 mL/h using a KDS100 infusion pump. The PE44 concentration was 13.0 wt% in the electrospinning mixtures with GA-L and 2 wt% in mixtures with GA-S1 and GA-S2. The concentrations of peptides were 1.3 wt% for GA-L and 0.2 wt% for both GA-S1 and GA-S2. As a control, fibers of pure PE44 were produced using a 13 w/v% concentration of polymer. The applied voltage was 15 kV for PE44/GA-S1 and PE44/GA-S2 while for unloaded PE44 (control) and PE44/GA-L fibers the applied voltage was 25 kV. All electrospun nanofibers were obtained using a needle tip-collector distance of 18 cm. It should be mentioned the choice of these conditions (*i.e.* concentrations, distance between the syringe tip and the collector, voltage and the flow rate) were selected on the basis of preliminary experiments devoted to optimize the morphology of the fibers. Thus, appropriate selection of the processing conditions is required to avoid the formation of droplets and electrospun beads. The procedure used for such optimization, which was

individually applied for each mixture, was detailed in previous works [47,48].

Circular dichroism (CD)

CD measurements were carried out in a Jasco J-810 spectropolarimeter at 22 ºC using a quartz cuvette. The CD data were recorded with standard sensitivity (100 mdeg), in the 190–350 nm range, with bandwidth of 2 mm, response time of 0.5 s and scanning speed of 500 nm/min. The reported spectra correspond to the average of five scans, the raw spectra being smoothed by the Savitsky–Golay algorithm. Spectra were analyzed in the DicroWeb software [49-51].

Microscopy

Optical microscopy (OM) studies were performed with a Zeiss Axioskop 40 microscope. Micrographs were taken with a Zeiss AxiosCam MRC5 digital camera.

Detailed inspection of texture and morphology of microspheres was conducted by SEM using a Focus Ion Beam Zeiss Neon 40 instrument (Carl Zeiss, Germany). Carbon coating was accomplished using a Mitec K950 Sputter Coater fitted with a film thickness monitor *k*150x. Samples were visualized at an accelerating voltage of 5 kV. The diameter of the nanofibers was measured with the SmartTiff software from Carl Zeiss SMT Ltd.

AFM was conducted to obtain topographic and phase images of the surface of fibers using silicon TAP 150-G probes (Budget Sensors, Bulgaria) with a frequency of 150 kHz and a force constant of 5 N/m. Images were obtained with an AFM Dimension microscope using the NanoScope IV controller under ambient conditions in tapping mode. The row scanning frequency was set between 0.4 and 0.6 Hz. The RMS R_q, which is the average height deviation taken from the mean data plane, was

determined using the statistical application of the NanoScope Analysis software (1.20, Veeco).

Chemical characterization

FTIR spectroscopy was used to assess the presence of peptide in PE44/GA-S1, PE44/GA-S2 and PE44/GA-L samples. Absorption spectra were recorded with a Fourier Transform FTIR 4100 Jasco spectrometer in the 4000-600 cm^{-1} range. A Specac model MKII Golden Gate attenuated total reflection (ATR) with a heated Diamond ATR Top-Plate was used.

XPS analyses were performed in a SPECS system equipped with a high-intensity twin-anode X-ray source XR50 of Mg/Al (1253 eV/1487 eV) operating at 150 W, placed perpendicular to the analyzer axis, and using a Phoibos 150 MCD-9 XP detector. The X-ray spot size was 650 mm. The pass energy was set to 25 and 0.1 eV for the survey and the narrow scans, respectively. Charge compensation was achieved with a combination of electron and argon ion flood guns. The energy and emission currents of the electrons were 4 eV and 0.35 mA, respectively. For the argon gun, the energy and the emission currents were 0 eV and 0.1 mA, respectively. The spectra were recorded with a pass energy of 25 eV in 0.1 eV steps at a pressure below $6 \cdot 10^{-9}$ mbar. These standard conditions of charge compensation resulted in a negative but perfectly uniform static charge. The C 1s peak was used as an internal reference with a binding energy of 284.8 eV. High-resolution XPS spectra were acquired by Gaussian/Lorentzian curve fitting after S-shape background subtraction. The surface composition was determined using the manufacturer's sensitivity factors.

Properties

Thermal degradation was studied at a heating rate of 20 ºC/min (sample weight *ca.* 5 mg) with a Q50 thermogravimetric analyzer of TA

Instruments and under a flow of dry nitrogen. Test temperatures ranged from 30 to 600 ºC.

Contact angle measurements were carried out using the water sessile drop method. Images of milliQ water drops (0.5 μL) were recorded after stabilization with the equipment OCA 15EC (Data-Physics Instruments GmbH, Filderstadt). SCA20 software was used to analyze the images and determine the contact angle value, which was obtained as the average of at least six independent measures for each sample.

Release experiments

Mats with peptide-loaded fibers were cut into 2×2 cm^2 squares (around 15-20 mg of weight) which were weighed and placed into polypropylene tubes. Phosphate buffer saline (PBS, pH 7.4) and PBS supplemented with 70 *v/v*-% of ethanol (PBS-EtOH) were considered as release media. The addition of ethanol to hydrophilic PBS increases the hydrophobicity of the medium and provokes some swelling effect, both favoring the release of hydrophobic drugs. The released peptide was quantified using the Bradford reagent. Assays were carried out by immersing sample mats in 30 mL of the release medium at 37 ºC for 1 week. Aliquots (1 mL) were drawn from the release medium at predetermined time intervals, and an equal volume of fresh medium was added to the release vessel. The Bradford reaction was performed in microtiter plate mode and the absorbance measurement in a reader plate. Calibration curves were obtained by plotting the absorbance measured at 595 nm against drug concentration. Finally, the mats were dissolved in chloroform and the residual drug was extracted in ethanol for quantification. All tests were performed in triplicate to control the homogeneity of the release, and the results were averaged.

Inhibition of bacterial growth

E. coli and *S. aureus* were selected to evaluate the antibacterial activity of peptides loaded in fibers. The bacteria were previously grown aerobically to exponential phase in broth culture (5 g/L beef extract, 5 g/L NaCl, 10 g/L tryptone, pH 7.2).

Growth experiments were performed placing five pieces (area: 0.5 cm^2) of each sample in tubes of 15 mL. After this, 2 mL of broth culture containing 10^3 CFU was seeded in each samples-containing tube. The cultures were incubated at 37 °C and agitated at 100 rpm. Aliquots of 100 µL were taken at predefined time intervals for absorbance measurement at 650 nm in a plate reader. Thus, turbidity was directly related to bacterial growth. The bacterial growth in broth culture alone (in absence of any material) was considered as the maximum growth (control) and it was used to calculate the relative growth of the bacteria in presence of the samples. Values were averaged considering the five replicas.

Agar diffusion tests were performed in Petri dishes of 90 mm, and seeded separately with 1.5×10^8 UFC/mL of each bacterium. Disks of 0.5 cm of diameter for each sample were placed onto an agar diffusion plate. In addition to PE44/GA-S1, PE44/GA-S2 and PE44/GA-L samples, assays were carried out using discs of GM, an antibiotic used to treat many types of bacterial infections, as positive control. Inhibition halos images were taken after incubation of samples with bacteria for 24 h at 37 ºC.

Cytotoxicity and cell adhesion

MDCK cells were cultured in DMEM high glucose supplemented with 10% FBS, penicillin (100 units/mL), and streptomycin (100 µg/mL). Cultures were maintained in a humidified incubator with an atmosphere of 5% CO_2 and 95% O_2 at 37ºC. Culture media were changed every two days. When the cells reached 80-90% confluence, they were detached using 1-2 mL of trypsin (0.25% trypsin/EDTA) for 5 min at 37 °C. Finally, cells were re-suspended in 5 mL of fresh medium, their concentration being

determined by counting in a Neubauer camera using 0.4% trypan blue as a dye vital.

Unloaded PE44, PE44/GA-S1, PE44/GA-S2 and PE44/GA-L samples were placed in plates of 24 wells and sterilized using UV-light for 15 min in a laminar flux cabinet. Controls were simultaneously performed by culturing cells on the surface of the tissue culture polystyrene (TCPS) plates. For adhesion assays, an aliquot of 50 µL containing 5×10^4 cells was deposited onto each sample. Then, cell attachment was promoted by incubating under culture conditions for 30 min. Finally, 500 µL of the culture medium were added to each well. After 24 h, non-attached cells were washed out, while attached cells were quantified. Cytotoxicity was also determined after 24 h of culture. All viability measures were relative to TCPS used as control (*i.e.* 100%).

Viability for cytotoxicity and cellular adhesion were evaluated by the colorimetric MTT assay. This assay measures the ability of the mitochondrial dehydrogenase enzyme of viable cells to cleave the tetrazolium rings of the MTT and form formazan crystals, which are impermeable to cell membranes and, therefore, are accumulated in healthy cells. This process is detected by a color change: the characteristic pale yellow of MTT transforms into the dark-blue of formazan crystals. Specifically, 50 µL of MTT solution (5 mg/mL in PBS) were added to each well. After 3 h of incubation, samples were washed twice with PBS and placed in clean wells. In order to dissolve formazan crystals, 200 µL of DMSO/methanol/water (70/20/10 % v/v) was added. Finally, the absorbance at 570 nm was measured using a microplate reader (Biochrom EZ Read 400, Biochrom). The resulting viability results were normalized to TCPS control as relative percentages. Results were derived from the average of six replicates (n= 6) for each independent experiment. ANOVA and Tukey tests were performed to determine statistical significance, which was considered at a confidence level of 95 % ($p < 0.05$).

6.2.3 Results and discussion

Electrospinning of PE44 and peptide mixtures

Firstly, we aimed to load GA-S1 and GA-S2 in electrosprayed PE44 microspheres, as we successfully did for GA-L [19]. However, despite the high peptide-loading efficiency (41%) and well-defined morphology of PE44/GA-L microspheres (Figure 6.2.2a), PE44/GA-S1 and PE44-GA-S2 microspheres were not feasible, even after optimization of the processing conditions. This important drawback, which was mainly attributed to the conformational rigidity of the two modified cyclic peptides, led us to consider the use of electrospun fibers as the most suitable system for the loading and sustained delivery of GA-S1 and GA-S2.

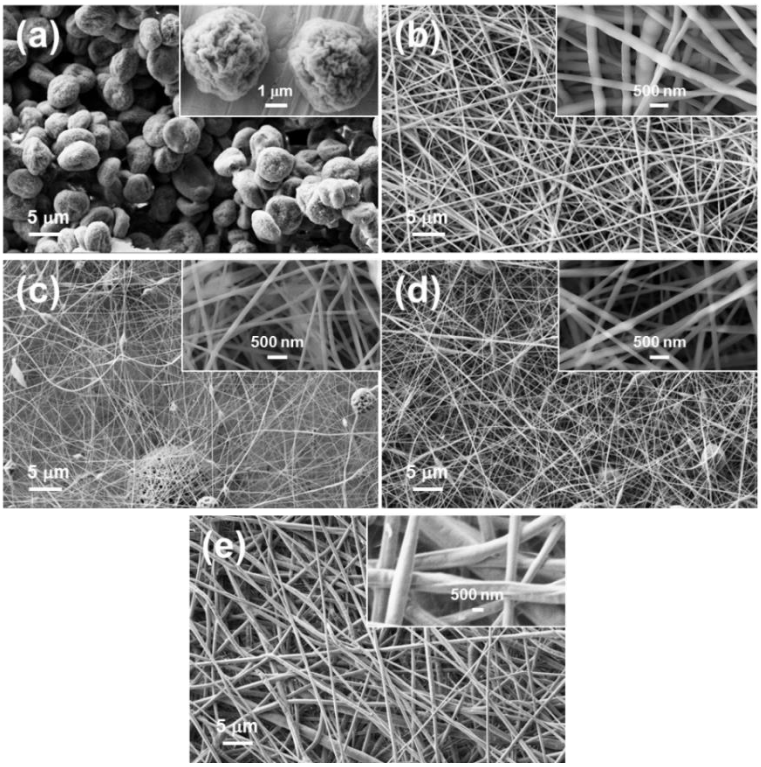

Figure 6.2.2 High and low magnification SEM micrographs of (a) PE44/GA-L electrosprayed microspheres (experimental conditions defined in reference 19); (b) unloaded PE44, (c) PE44/GA-S1, (d) PE44/GA-S2 and (e) PE44/GA-L electrospun fibers.

PE44 and GA peptides (*i.e.* GA-S1, GA-S2, and GA-L) were dissolved in chloroform and ethanol, respectively, for the electrospinning process. Accordingly, in a first stage, we examined the stability of the three peptides in both solvents using CD spectroscopy, and the recorded spectra were interpreted using the on-line Dichroweb software [52-54]. In ethanol the three peptides exhibit secondary structures (Figure 6.2.3a). More specifically, the spectrum of GA-S2 was interpreted as a combination of β-sheet (83%), β-turn (9%), and disordered (8%) motives, which was fully consistent with the reported 2D NOESY spectra recorded in H_2O/D_2O 9:1 v/v [36]. In contrast, GA-S1 and GA-L exhibited a combination of regular and distorted α-helical structures with a small fraction of disordered motives (< 5%). It is worth noting that the antibiotic activity of GA-S and GA-L is associated to β-sheet and α-helical conformation, respectively [24,38,39]. Therefore, the antimicrobial potency of GA-S2 and GA-L is expected to be preserved in ethanol, while that of GA-S1 could be affected by peptide···solvent interactions. In the following sections we demonstrate that the antibiotic potency is higher for GA-S2 than for GA-S1, even though the microbicide activity of the latter is not negligible. Unfortunately, the complexity of the CD spectra recorded in chloroform (Figure 2b) precluded their analysis, thus suggesting a complex mixture of ordered structures [55].

Mixtures of PE44 and GA peptides (*i.e.* GA-S1, GA-S2 and GA-L) were electrospun to obtain PE44/GA-# fibers, where GA-# indicates the loaded peptide. For each case, the processing conditions (*i.e.* concentrations, distance between the syringe tip and the collector, voltage, and flow rate) were optimized to avoid the formation of droplets and electrospun beads. The feeding mixture essentially depended on the peptide to be accommodation within the polymeric matrix, which is conditioned by the peptide conformational flexibility. After optimization, the PE44 concentration in the electrospinning mixtures was 13.0 wt% for unloaded and GA-L loaded fibers, while it decreased to 2 wt% for GA-S1 and GA-S2 loaded fibers. The concentrations of peptides were 1.3 wt% for GA-L and 0.2 wt% for both GA-S1 and GA-S2. It is worth noting that the amount

of peptide used in the feeding solution is completely incorporated into the fibers.

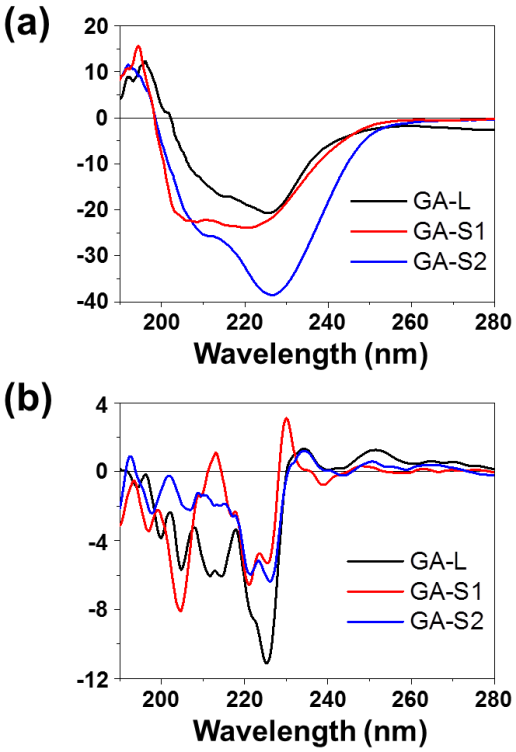

Figure 6.2.3 Circular dichroism spectra of GA-S1, GA-S2 and GA-L recorded in (a) ethanol and (b) chloroform. The peptide concentration was 5 mg/mL in all cases.

Figures 6.2.4 and 6.2.2b-e compare representative OM and SEM micrographs, respectively, of unloaded PE44, PE44/GA-S1, PE44/GA-S2 and PE44/GA-L, while their average diameters (*D*) are listed in Table 6.2.1. Although both unloaded PE44 and PE44/GA-L resulted in well-defined fibers, the loading of GA-L caused some important changes. Specifically, unloaded PE44 fibers presented a cylindrical morphology with *D*= 246±68 nm, while the linear peptide induced a flatter morphology (ribbon-like fibers) and a significant increment in the fiber thickness (*D*= 590±156 nm). In contrast, PE44/GA-S1 and PE44/GA-S2 fibrous mats

displayed a high amount of droplets and beads, even after optimization of the processing conditions. Furthermore, the cylindrical fibers experienced a drastic reduction in diameter (*D*= 106±25 and 146±34 nm for PE44/GA-S1 and PE44/GA-S2, respectively). These phenomena have been attributed to the low concentrations of both polymer and peptide, which affect the viscosity of the feeding solution.

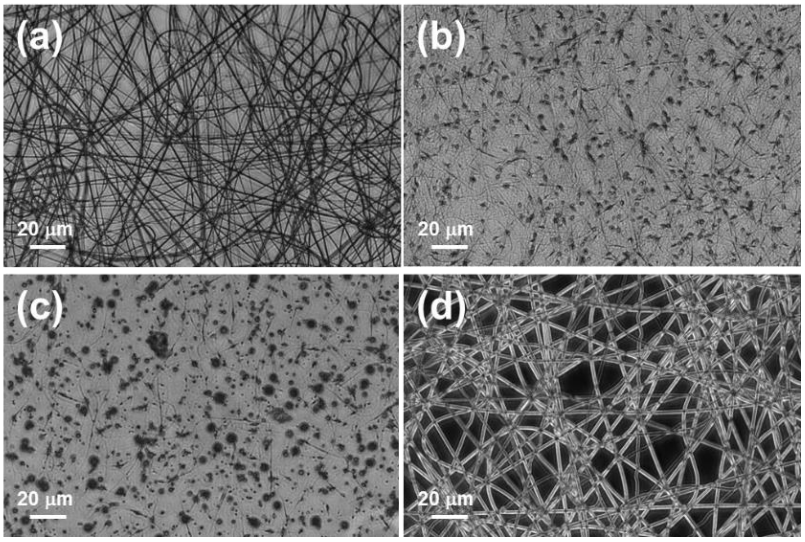

Figure 6.2.4 Optical microscopy micrographs of (a) unloaded PE44, (b) PE44/GA-S1, (c) PE44/GA-S2 and (d) PE44/GA-L electrospun nanofibers.

	D **(nm)**	**RMS R_q (nm)**	**$T_{50\%}$ (ºC)**	**$T_{70\%}$ (ºC)**	**T_{max} (ºC)**	***θ*** **(º)**
Unloaded PE44	246±68	36.2±8.7	410	420	419	125±6
PE44/GA-S1	106±25	6.1±2.4	400	410	412	128±4
PE44/GA-S2	146±34	5.0±1.7	387	400	401	47±1
PE44/GA-L	590±156	36.8±3.6	405	416	415	68±2

Table 6.2.1 Average diameter (*D*), root-mean-square roughness (RMS R_q), temperatures for 50% and 70% weight loss ($T_{50\%}$ and $T_{70\%}$, respectively), maximum temperature (T_{max}) and contact angle (*θ*).

3D topographic AFM images, which are displayed in Figure 6.2.5, are in good agreement with SEM observations. In addition, comparison between the topographic and phase AFM images indicates that the peptides are not located as particles or aggregates on the surface of the fibers.

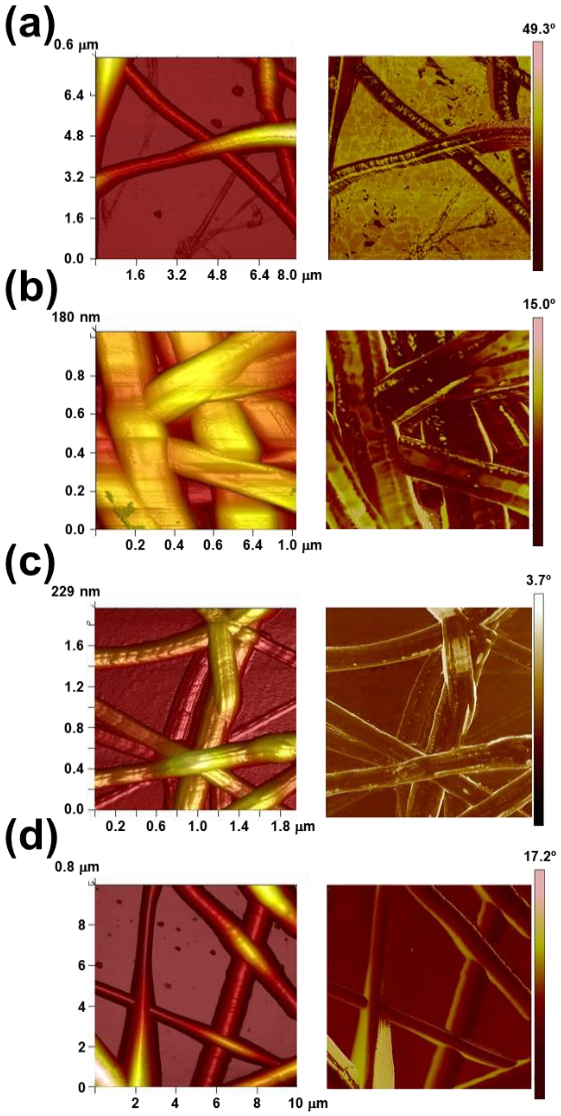

Figure 6.2.5 AFM images of (a) unloaded PE44, (b) PE44/GA-S1, (c) PE44/GA-S2 and (d) PE44/GA-L electrospun fibers: 3D topography (left) and phase (right) images. The scan window size was adjusted in each case according to the diameter of the fibers (see Table 6.2.1): (a) 8×8 μm^2; (b) 1×1 μm^2; (c) 2×2 μm^2; and (d) 10×10 μm^2

Besides, the RMS R_q values, which are included in Table 6.2.1, evidenced that PE44/GA-S1 and PE44/GA-S2 nanofibers are ultra-smooth, while the texture of PE44 fibers is not altered by GA-L.

.

Chemical characterization

Figure 6.2.6a displays the FTIR spectra of unloaded PE44, PE44/GA-S1, PE44/GA-S2 and PE44/GA-L samples. In the spectrum of PE44, the peaks corresponding to the C=O and C–O–C vibrations of the ester bond are detected at 1712, 1150 (sharp and strong absorption bands) and 1044 cm^{-1} (sharp and medium absorption band). These important bands are also clearly identified in the spectra of the three peptide-loaded PE44 samples (red rectangles in Figure 6.2.6a). Other main absorption bands of PE44 appearing at 2964, 2946 and 2857 $cm^{-1}$are attributed to the C–H aliphatic stretching; CH_2 asymmetric and symmetric bending are shown between 1470 and 1390 cm^{-1}; $–(CH_2)_n–$ hydrocarbon chains are detected at 804 cm^{-1} (sharp) and 748 cm^{-1} (broad, CH_2 rock vibrations).

Most importantly, the successful loading of the peptide in PE44/GA-S1, PE44/GA-S2 and PE44/GA-L samples is evidenced in Figure 6.2.6a by the bands arising from the amide groups. The amide II band, which is due to the C–N stretching vibration in combination with N–H bending, is detected at ~1540 cm^{-1} (*i.e.* 1539, 1537 and 1541 cm^{-1} for PE44/GA-S1, PE44/GA-S2, and PE44/GA-L, respectively). The amide I band, which arises from the C=O stretching vibration of the peptide bond and is modulated by the peptide secondary structure, appears at 1629 cm^{-1} for the systems loaded with cyclic peptides and at 1635 cm^{-1} for PE44/GA-L. The C=O stretching of aliphatic esters, which corresponds to the intense and sharp band at 1712 cm^{-1} for unloaded and peptide-loaded PE44 samples, is clearly distinguishable from such two amide bands.

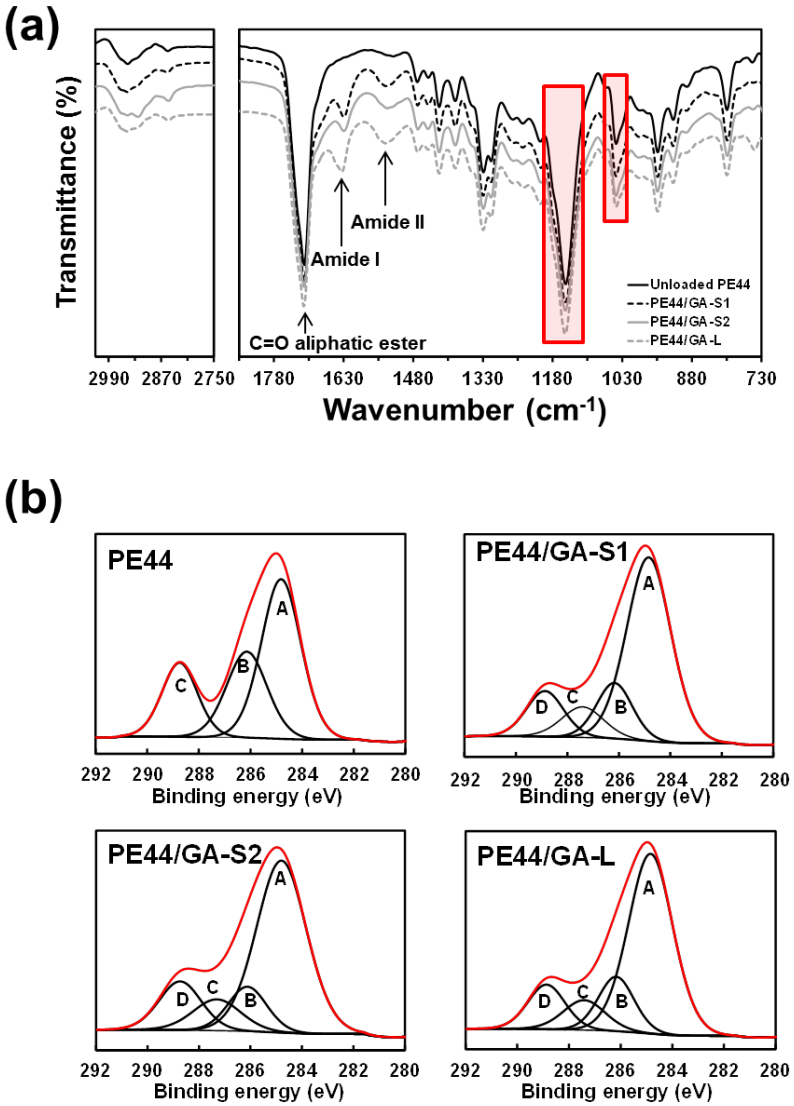

Figure 6.2.6 (a). FTIR spectra of electrospun unloaded and GA-loaded PE44fibres. The red rectangles indicate the C–O–C (1150 and 1044 cm^{-1}) vibrations of the ester bond in PE44. The C=O, amide I and amide II bands are explicitly indicated. (b) High-resolution XPS spectrum at the C 1s region for unloaded and GA-loaded PE44 fibers. The red line corresponds to the experimental profile while the black lines are the peaks from deconvolution. Unloaded PE44: C–C / C–H (A: 284.8 eV), C–O (B: 286.1 eV) and C=O (C: 288.7 eV). GA-S1, GA-S2 and GA-L loaded PE44: C–C / C–H (A: 284.9 eV), C–O (B: 286.2 eV), (O=)C–NH peptide bond (287.7) and C=O (C: 288.8 eV).

The chemical structure of the systems under study was further characterized by XPS. Table 6.2.2 compares the atomic composition of unloaded and peptide-loaded PE44 fibers. The detection of a small percentage of nitrogen in unloaded PE44 samples has been attributed to the substrate (aluminum foil) used to collect the fibers during electrospinning. However, the percentage of nitrogen increases from 0.26% in unloaded PE44 to 5.58%, 3.11%, and 6.52% in PE44/GA-S1, PE44/GA-S2, and PE44/GA-L, respectively, which further confirms the successful incorporation of the peptides. High-resolution XPS spectra in the C 1s region are displayed in Figure 6.2.6b, while those in the N 1s and O 1s regions are displayed in Figure 6.2.7. The three Gaussian curves derived from the deconvolution of the C 1s peak for unloaded polyester fibers correspond to the saturated C–C / C–H (284.8 eV), C–O (286.1 eV) and C=O (288.7 eV) bonds of the PE44 chains [56,57]. The three peptide-loaded PE44 fibers display an additional fourth Gaussian curve at 287.7 eV that has been attributed to the (O=)C–NH peptide bonds [58,59]. On the other hand, two Gaussian curves, which correspond to the C=O (531.87 eV) and C–O bonds (533.42), were derived from the O1s signal [56-60]. The intensity of the C=O component is lower than that of the C–O one for unloaded PE44, while the opposite is obtained for PE44/GA-S1, PE44/GA-S2, and PE44/GA-L due to the incorporation of peptides.

	C 1s (%)	**N 1s (%)**	**O 1s (%)**
Unloaded PE44	69.23	0.26	30.51
PE44/GA-S1	67.77	5.58	26.65
PE44/GA-S2	66.63	3.11	30.26
PE44/GA-L	70.13	6.52	23.35

Table 6.2.2 Atomic percent composition (C 1s, N 1s and O 1s) obtained by XPS for unloaded PE44, PE44/GA-S1, PE44/GA-S2 and PE44/GA-L.

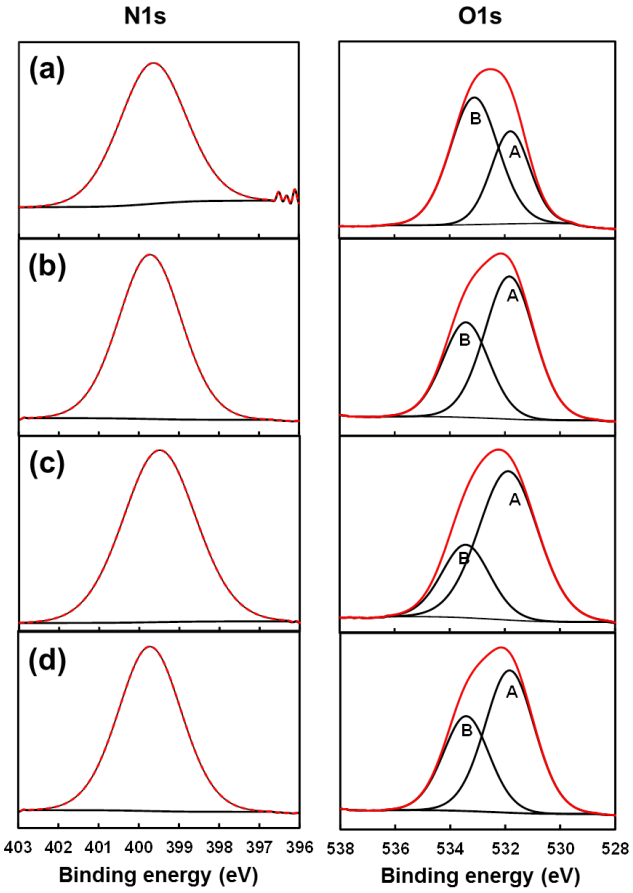

Figure 6.2.7 High-resolution XPS spectra for (a) unloaded PE44, (b) PE44/GA-S1, (c) PE44/GA-S2 and (d) PE44/GA-L: N 1s and O 1s regions. The red line corresponds to the experimental profile while the black lines are the peaks from deconvolution.

Properties

Thermogravimetric analyses (Figure 6.2.8a and Table 6.2.1) reflect the significant influence of the peptide in the thermal stability of PE44. Although all loaded samples are stable up to a temperature 40 ºC higher than the melting temperature of the PE44 matrix (T_m= 112.8 ºC) at least, the thermal stability of PE44/GA-S1 and, specially, PE44/GA-S2 is considerably lower than that displayed by PE44/GA-L and unloaded PE44, which are very similar. Thus, the temperatures at a 50% weight loss ($T_{50\%}$)

are around 10 and 23 ºC lower for PE44/GA-S1 and PE44/GA-S2, respectively, than for unloaded PE44. Moreover, these differences are preserved at a 70% weight loss ($T_{70\%}$, Table 6.2.1). DGTA curves show a pronounced degradation step for all peptide-loaded samples, the maximum temperature (T_{max}, Table 6.2.1) increasing as follows: GA-S2 < GA-S1 < GA-L. Furthermore, an initial degradation step at 224 and 241 ºC occurs for PE44/GA-S1 and PE44/GA-S2, respectively, which involved a weight loss lower that 5%. This degradation is probably induced by the severe molecular constraints of Ac_3c and *S,S*-$c_3$diPhe in the cyclic peptides, thus being less stable than GA-L. No significant char (*i.e.* less than 2.5%) was observed at temperatures higher than 500 ºC. Therefore, the peptide clearly influences the thermal stability of the polymeric matrix, which is practically independent of the morphology. For instance, the thermal parameters for unloaded PE44 and PE44/GA-L microspheres (average particle diameter: 5.1±0.5 μm and 5.0±0.7 μm, respectively), $T_{50\%}$= 410 and 405 ºC, $T_{70\%}$= 420 and 416 ºC, and T_{max}= 418 and 411 ºC [19], are similar to those listed in Table 6.2.1 for fibers.

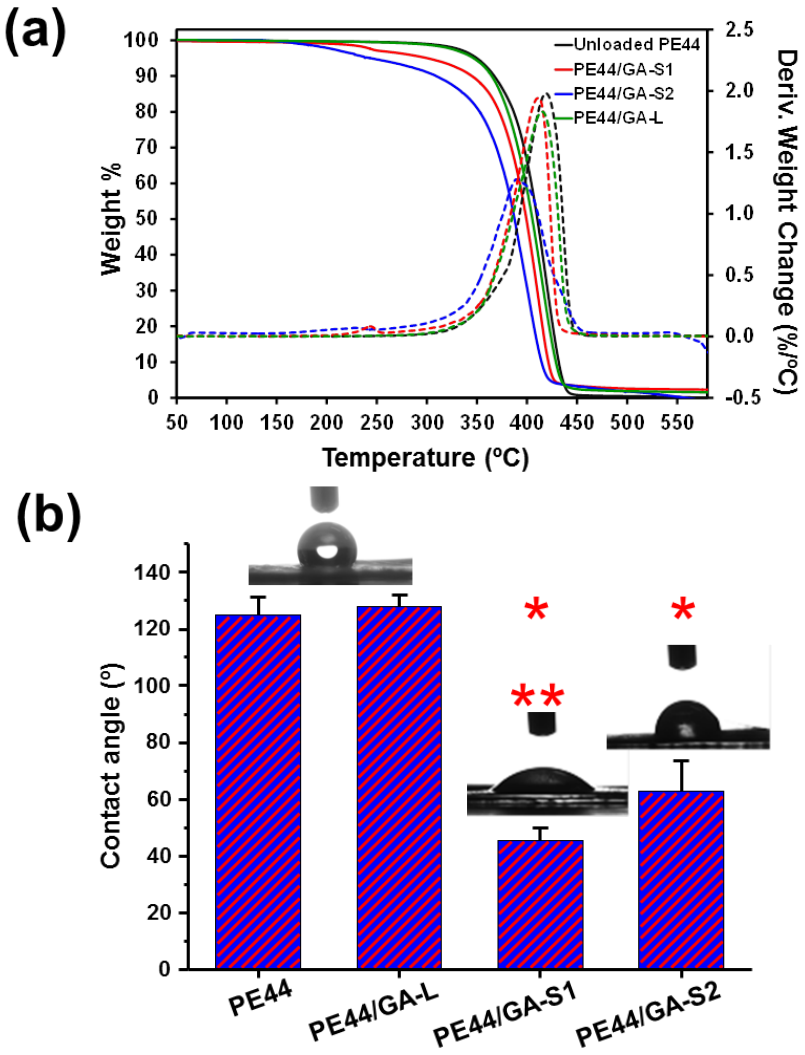

Figure 6.2.8 For unloaded PE44, PE44/GA-S1, PE44/GA-S2 and PE44/GA-L electrospun fibers: (a) TGA (solid lines) and DTGA (dashed lines) curves; and (b) contact angle. * Significantly different with respect to unloaded PE44 and PE44/GA-L with $p < 0.05$. ** Significantly different with respect to PE44/GA-S2 with $p < 0.05$.

The contact angle values measured using water (Figure 6.2.8b) indicate that unloaded PE44 matrices are hydrophobic (θ= 125º±6º) due to both the presence of aliphatic segments and the microfibrous structure of produced electrospun mats. In contrast, the water contact angle value determined for unloaded PE44 electrosprayed microspheres was significantly lower (θ= 104º±3º) [19], even though the surface RMS Rq was slightly higher for microspheres than for fibers. This feature proves that the wettability of structured polymeric matrices is influenced by morphology. Such hydrophobic character is retained after loading GA-L (*i.e.* θ= 128º±4º for PE44/GA-L), whereas the presence of GA-S1 and GA-S2 transformed the PE44 fiber mats into hydrophilic substrates (θ = 47º±1º and 68º±2º for PE44/GA-S1 and PE44/GA-S2, respectively). The Wenzel equation indicates that, if the surface is chemically hydrophobic, as that of PE44, it will become less hydrophobic when the surface roughness decreases [61]:

$$\cos\theta_m = r \cdot \cos\theta_\gamma \qquad \text{(Eqn. 6.2.1)}$$

where θ_m is the measured contact angle, θ_γ is the Young contact angle and r is the roughness ratio, the latter parameter increasing with the RMS R_q (Table 6.2.1). The Wenzel equation is based on the assumption that the liquid penetrates into the rough grooves, which occurs when the droplet is larger than the roughness scale by two or three orders of magnitude, as it is in this case. However, other factors are probably affecting the wettability of PE44/GA-S1 and PE44/GA-S2, since the reduction of the contact angle with respect to unloaded PE44 and PE44/GA-L is too high to be attributed exclusively to the surface roughness. Thus, the distribution of GA-S1 and GA-S2 peptides in the polymeric matrix is possibly another factor influencing the wettability of the PE44 fibers. More specifically, a homogeneous distribution of the cyclic peptides on the surface of fibers, forming aggregates small enough to be undetectable by phase imaging AFM, would result in a reduction of the contact angle due to the exposition of amide groups. This situation is completely different from that of hydrophobic PE44/GA-L fibers, for which their resemblance with unloaded PE44 fibers suggests that the peptide is inside the polymeric matrix.

Peptide release

The peptide release profiles in PBS, which is the simplest physiological medium, for GA-S1, GA-S2 and GA-L loaded fibers are displayed in Figure 6.2.9a. The cumulative release plots in PBS indicate a massive initial burst release up to a maximum percentage (65%±3%, 78%±1% and 74%±3% for GA-S1, GA-S2 and GA-L, respectively) and a subsequent decrease of the release percentage until a value of ~40-50%, depending on the peptide. This behavior suggests that, after an initial burst release caused by the rapid diffusion of PBS into PE44 fibers, a given amount of such delivered peptide re-enters in the PE44 fibers to meet equilibrium conditions. These observations, especially for PE44/GA-S1 and PE44/GA-S2, are consistent with the location of the peptide near the surface, as suggested by contact angle measurements. After the initial burst release, the shape of the cumulative profiles is similar regardless the loaded peptide, even though the release rate to the medium highly depends on the chemical structure of the peptide. For example, the release after 24 h reaches values of 55%±6%, 49%±2% and 35%±2% for GA-S1, GA-S2 and GA-L, respectively, increasing to 86%±1%, 70%±4% and 57%±2% after 48 h. The complete stabilization of the amount of released peptide, which was reached after ~5 days, occurred at 97%±1%, 78%±2% and 62%±4% for GA-S1, GA-S2 and GA-L, respectively.

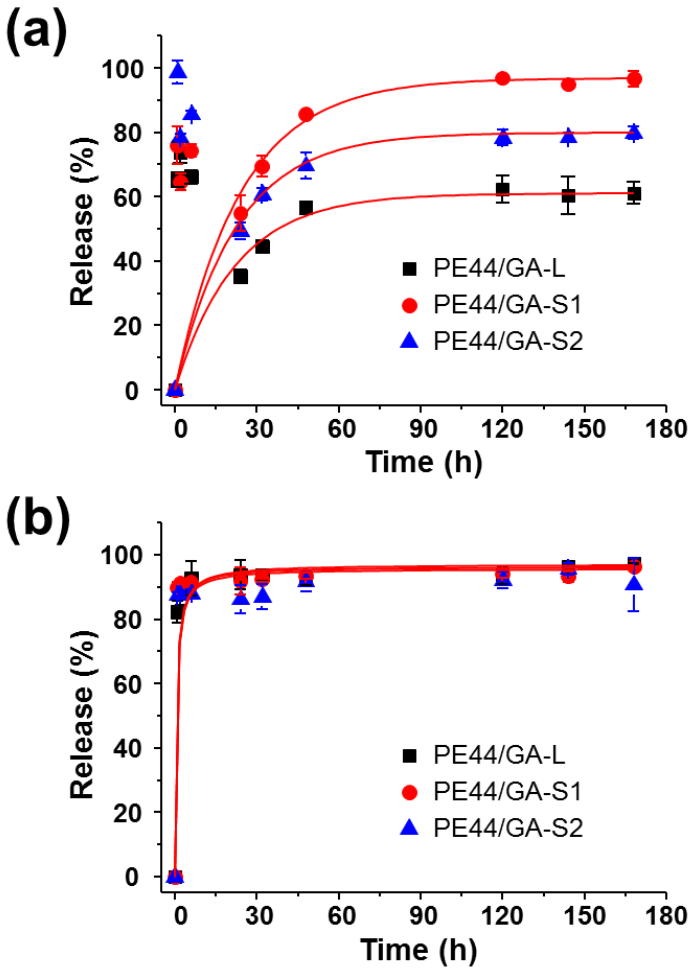

Figure 6.2.9 Accumulated release profiles of GA-S1, GA-S2 and GA-L peptides from loaded PE44 electrospun fibers in (a) PBS and (b) PBS-EtOH.

After the initial burst, the release kinetics can be explained in all cases by the Higuchi and first-order models. On the one hand, the Higuchi model, which provides a linear behavior when the cumulative percentage of peptide release is represented against the square root of time, indicates that:

(i) the concentration of peptide in the matrix is much higher than the peptide solubility;

(ii) the peptide aggregates are significantly smaller than the system thickness;
(iii) the PE44 swelling and diffusivity are very low;
(iv) the peptide diffusivity is constant.

On the other hand, the first order model results in a straight line when the data are plotted as the logarithm of the cumulative percentage of peptide release *versus* time, which reflects that the PE44 mat can be considered as a porous matrix. It is worth highlighting that the Higuchi and the first-order models are usually combined to describe the first very fast releasing stage and the second very slow releasing stage of the complete profile [62].

The release profiles in PBS and PBS-EtOH are frequently compared to examine the influence of the medium [63,64]. The peptide release profiles in PBS-EtOH for all PE44 loaded fibers are represented in Figure 6.2.9b. The more hydrophobic PBS-EtOH environment significantly alters the release of the three peptides, which display a very fast delivery. Specifically, the peptide retention after 6 h and 120 h was around 9% and 7%, respectively, in all cases. The differences observed between the profiles in PBS and PBS-EtOH have been attributed to the hydrophobicity of the three peptides, GA···solvent interactions being more favorable in the latter environment than in the former one. Accordingly, these attractive interactions are probably responsible for the diffusion of the peptides through the PE44 fibers and their subsequently delivery.

Antimicrobial activity

The results from susceptibility tests and bacterial growth of representative Gram-negative and Gram-positive bacteria (*E. coli* and *S. aureus*, respectively) are shown in Figure 6.2.10. The presence of inhibition halos in the agar plates reflects the diffusion of the compounds with antimicrobial activity, the size of the inhibition zone being related to the level of antimicrobial activity. Accordingly, the bactericidal response against *E. coli* is slightly greater for PE44/GA-S1 and PE44/GA-S2 than for PE44/GA-L, while the activity against *S. aureus* is apparently much higher for the latter than for the formers. Obviously, the inhibition zone around GM, which was used as positive control, is the greatest, while the antimicrobial activity of peptide-loaded PE44 samples depends on the release rate. No inhibition halo was observed around unloaded PE44 fibers (not shown), which were used as negative control, proving that such polymeric matrix has not antibiotic activity.

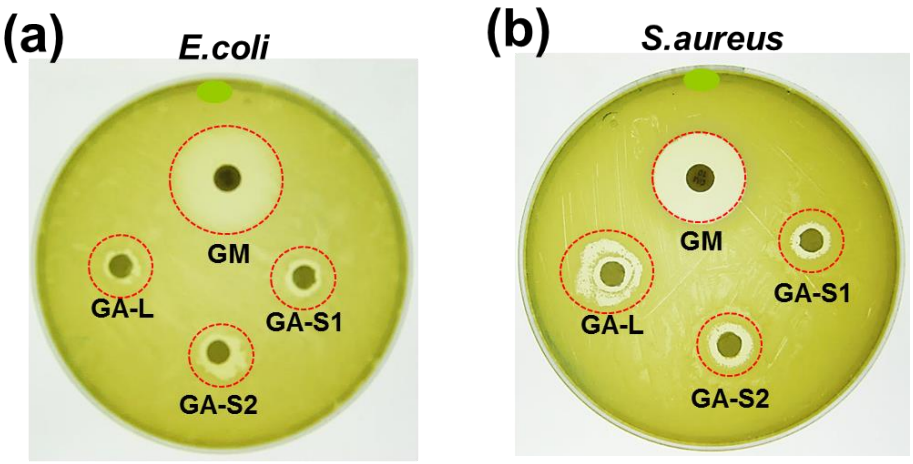

Figure 6.2.10 (a) *E. coli* and (b) *S. aureus* bacterial cultures showing the inhibition zones around PE44/GA-S1, PE44/GA-S2, PE44/GA-L and gentamicin (GM, positive control) samples. Unloaded PE44 (not shown) was tested as negative control.

Inhibition zones do not necessarily indicate that microorganisms have been killed by the antimicrobial product but just that they have been prevented from growing. In order to quantify the extent of the antimicrobial activity, the turbidity of bacteria cultures incubated in the presence of unloaded and loaded PE44 fibers was evaluated spectroscopically and was related to the bacterial growth. Figure 6.2.11 shows the bacterial growth in media containing unloaded and peptide-loaded PE44 fibers, relative to the growth in absence of any material (control). As it can be seen, PE44/GA-S1 and, especially, PE44/GA-S2 inhibit the growth of *E. coli*, whereas unloaded PE44 and PE44/GA-L fibers are harmless to such Gram-negative bacteria. It is worth noting that GA-L is active against Gram-positive bacteria and against a few selected Gram-negative microbial (*e.g.* Neisseria bacteria), explaining the inactivity displayed in Figure 6.2.11a. In contrast, GA-S is indistinctly effective against some Gram-positive and Gram-negative bacteria. Accordingly, the peptide-loaded PE44 fibers show antibiotic activity against *S. aureus*, which decreases as follows: GA-L > GA-S2 > GA-S1 (Figure 6.2.11b). Thus, after 24 hours, the microbicide activity of GA-S1 and GA-S2 against *E. coli* is 9±4 % and 16±4 % inhibition of bacterial growth and 12±3 % and 21±5 % inhibition of bacterial growth against *S. aureus*, respectively. Overall, the antimicrobial activity of GA-S2 is greater than that of GA-S1, indicating that *S,S*-$c_3$diPhe preserves better the bioactive conformation of the parent GA-S peptide than Ac_3c. This observation is in good agreement with the CD results discussed above.

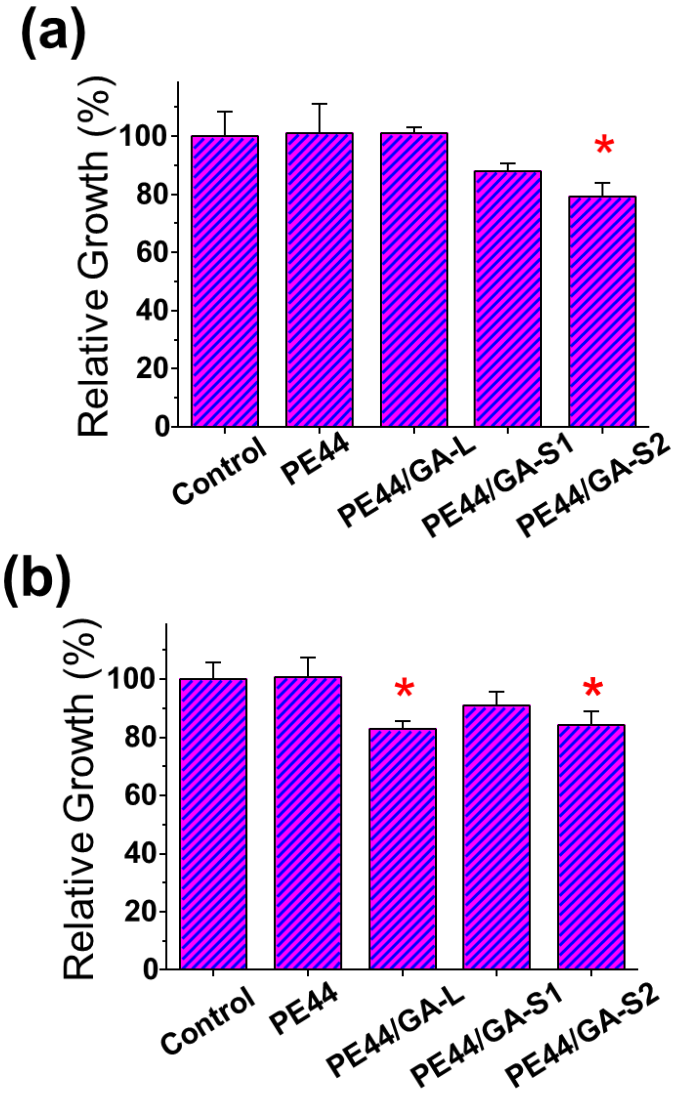

Figure 6.2.11 Bacterial growth in (a) *E. coli* and (b) *S. aureus* cultures after 24 h for unloaded and peptide-loaded PE44 fibers. Results are expressed with respect to the bacterial growth in absence of any material (control), which was considered as the maximum growth. * Significant differences with respect to the control and unloaded PE44 with $p < 0.05$.

Although the antimicrobial behavior of PE44 fibers loaded with GA-S1 and GA-S2 is limited by the peptide release rate, the activities displayed in Figure 8 are in good agreement with those reported for the peptides in solution [36]. More specifically, biological assays of such two peptides in solution using two Gram-negative (two different *Acinetobacter baummanii* strains) and two Gram-positive (*S. aureus* and *Listeria monocytogenes*) bacteria showed that GA-S1 was practically devoid of any antibiotic activity, while GA-S2 displayed low activity against Gram-negatives and some selectivity for Gram-positives. The inactivity of GA-S1 was attributed to the absence of an aromatic moiety in the Ac_3c residue (Figure 6.2.1), which destabilized the bioactive conformation of the GA-S parent peptide [36].

Biocompatibility

The biocompatibility of PE44/GA-S1 and PE44/GA-S2 fibers was evaluated by performing *in vitro* cytotoxicity and cell adhesion assays, and the results were compared with those obtained for unloaded PE44 and P44/GA-L fibers. Thus, in order to do so, samples from the electrospun mats were placed in contact with a MDCK epithelial cell line inside TCPS well plates and tested using the colorimetric MTT assay to evaluate the cell viability on each well after 24 h. Viability measures were relative to TCPS without fibers, which were used as control (*i.e.* 100% cell viability).

As it is displayed in Figure 6.2.12a, the cytotoxicity of the three peptide-loaded systems was higher than that of unloaded PE44, the biocompatibility of the latter being similar to that of TCPS. Hence, the possible cytotoxicity of GA-S1 and GA-S2 loaded fibers should be attributed to their non-proteinogenic residues. Interestingly, the cytotoxic behavior of PE44/GA-S1 and PE44/GA-S2 was completely different, while PE44/GA-S2 behaved similarly to PE44/GA-L. Although the concentration of loaded peptide is higher GA-L than for the GA-S2 (*i.e.* 1.3 wt% and 0.2 wt%, respectively), this result indicates that the incorporation of *S,S*-$c_3$diPhe is essentially harmless to eukaryotic cells. Thus, the phenyl substituents seem to be recognized by the cells even

though are tightly held in *S,S*-$c_3$diPhe, suggesting some similarity with the aromatic ring of L-Phe. This is probably ascribed to the proper orientation and location at different β-carbon atoms of the aromatic rings in *S,S*-$c_3$diPhe. In contrast, PE44/GA-S1 fibers are significantly more toxic to cells, which has been exclusively associated with the Ac_3c residue (*i.e.* two Ac_3c-containing antibiotics were reported to exhibit cytotoxic activity [65]).

Finally, Figure 6.2.12b represents the amount of cells adhered onto the surface of the examined materials (expressed by unit of area) after 24 h. As it can be seen, in comparison to the control TCPS, cell adhesion was promoted for unloaded PE44, whereas the difference between TCPS and both PE44/GA-S2 and PE44/GA-L is not statistically significant. These observations are fully consistent with the cytotoxicity of the system (Figure 6.2.12a), which indicates that the very high biocompatibility of PE44 is slightly reduced by the loading of GA-S2 and GA-L peptides. This effect is more pronounced for PE44/GA-S1, which exhibited the lowest biocompatibility.

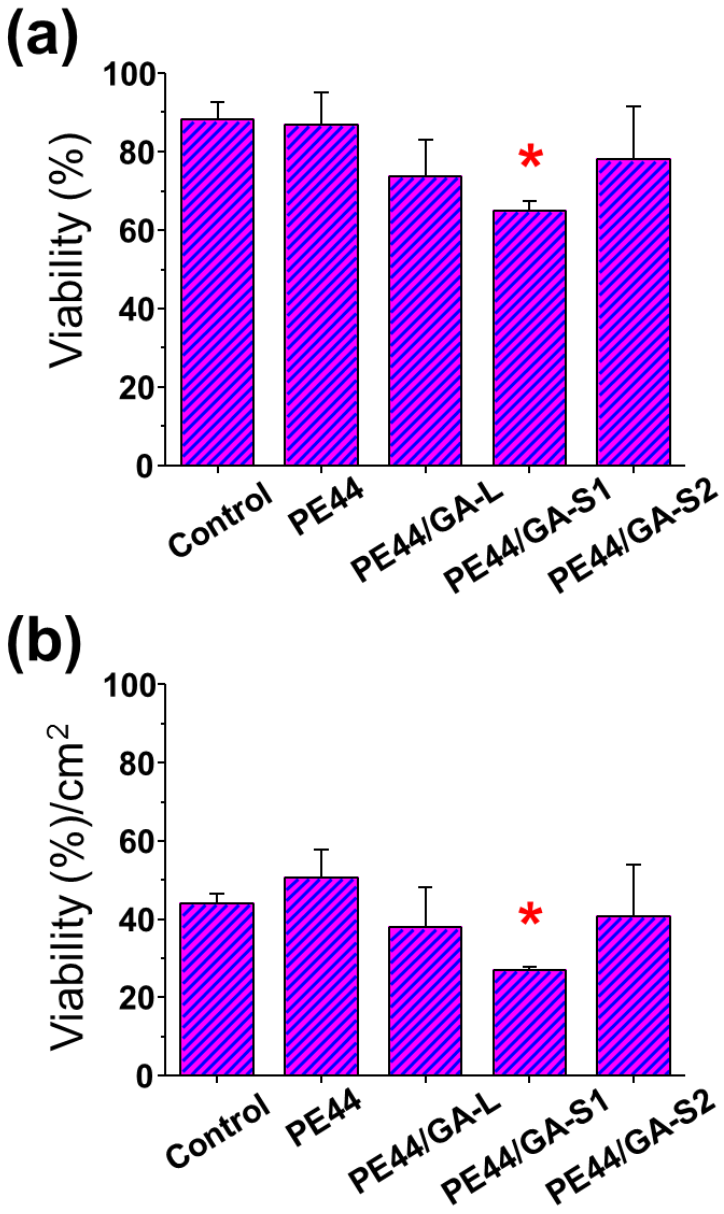

Figure 6.2.12 (a) Viability of MDCK cells in presence of TCPS (control), unloaded PE44, PE44/GA-S1, PE44/GA-S2 and PE44/GA-L samples. (b) Cellular adhesion onto TCPS (control) and fiber mats with unloaded or peptide-loaded fibers.

6.2.4 Conclusions

In this article we describe the successful preparation and properties of electrospun polyester fibers loaded with peptide antibiotics that were designed to enhance the stability of the bioactive conformation and to be resistant against proteolytic cleavage. We have proved that GA-S1 and GA-S2 cause important changes in the morphology, diameter, and properties (thermal stability and wettability) of PE44 fibers, whereas the characteristics of unloaded and GA-L loaded fibers are very similar. An important advantage of these peptide-loaded fibers as therapeutic platforms is that the polymeric matrix regulates the release of the antibiotic in hydrophilic environments similar to physiological media. The antimicrobial activity of PE44/GA-S1 and PE44/GA-S2 is comparable (Gram-negative) or higher (Gram-positive) than that of PE44/GA-L. Moreover, the antibiotic potency of both GA-S1 and GA-S2 is higher when loaded into polyester fibers than in solution, suggesting that the PE44 matrix enhances the stability of their bioactive conformation. Overall, these findings reflect that formulations such as biodegradable polymeric fibers loaded with engineered peptides are promising platforms for biomedical applications.

6.2.5 References

1. W.K. Wan, L. Yang, D.T. Padavan; *Nanomedicine*, vol. 2, pp. 483-509, 2007.
2. B.P. Timko, D.S. Kohane; *Clin. Ther.*, vol. 34, pp.S25–S35, 2012.
3. D.A. LaVan, T. McGuire, R. Langer; *Nat. Biotechnol.*, vol. 21, pp. 1184-1191, 2003.
4. S. Mura, J. Nicolas, P. Couvreur; *Nat. Mater.*, vol. 12, pp. 991-1003, 2013.
5. B.P. Timko, T. Dvir, D.S. Kohane; *Adv. Mater.*, vol. 22, pp. 4925-4943, 2010.
6. S.C. Balmert, S.R. Little; *Adv. Mater.*, vol. 24, pp. 3757-3778, 2012.
7. J. Gao, W. Li, Y.J. Guo, S.S. Feng; *Nanomedicine*, vol. 11, pp. 3261-3282, 2016.
8. S. Orawan; *Polym. Adv. Technol.*, vol. 27, pp. 1264-1273, 2016.
9. J. Natarjan, Q. Dasgupta, S.N. Shetty, K. Sarkar, G. Madras, K. Chatterjee; *ACS Appl. Mater. Interfaces*, vol. 8, pp. 25170-25184, 2016.
10. J. Pushpamalar, A.K. Veeramachineni, C. Owh, X.J. Loh; *ChemPlusChem*, vol. 81, pp. 504-514, 2016.
11. M.J. Cardoso, S.G. Caridade, R.R. Costa, J.F. Mano; *Biomacromol.*, vol. 17, pp. 1347-1357, 2016.
12. M. Winnacker, B. Rieger; *Polym. Chem.*, vol. 7, pp. 7039-7046, 2016.
13. I. Manavitehrani, A. Fathi, H. Badr, S. Daly, A.N. Shirazi, F. Deghani; *Polymers*, vol. 8, pp. 20-27, 2016.
14. N.D. Stebbins, J.J. Faig, W. Yu, R. Guliyev, K.E. Uhrich; *Biomater. Sci.*, vol. 3, pp. 1171-1187, 2015.
15. C. Du, J. Zhao, J. Fei, Y. Cui, J. Li; *Adv. Healthcare Mater.*, vol. 2, pp. 1246-1251, 2013.
16. L. Gao, Y. Cui, Q. He, Y. Yang, J. Fei, J. Li; *Chem. Eur. J.*, vol. 17, pp. 13170-13174, 2011.

17. H. Yan, Y.F. Hou, P.F. Niu, K. Zhang, T. Shoji, Y. Tsuboi, F.Y. Yao, L.M. Zhao, J.B. Chang; *J. Mater. Chem. B*, vol. 3, pp. 3677-3680, 2015.

18. N. Ashwanikumar, N.A. Kumar, S.A. Nair, G.S. V. Kumar; *Acta Biomater.*, vol. 10, pp. 4685-4694, 2014.

19. S. Maione, L.J. del Valle, M.M. Pérez-Madrigal, C. Cativiela, J. Puiggalí, C. Alemán; *RSC Adv.*, vol. 6, pp. 73045-73055, 2016.

20. M.M. Pérez-Madrigal, E. Llorens, L.J. del Valle, J. Puiggalí, E. Armelin, C. Alemán; *Express Polym. Lett.*, vol. 10, pp. 628-646, 2016.

21. M. Planellas, M.M. Pérez-Madrigal, L.J. del Valle, S. Kobauri, R. Katsarava, C. Alemán, J. Puiggalí; *Polym. Chem.*, vol. 6, pp. 925-937, 2015.

22. J.W. Liou, Y.J. Hung, C.H. Yang, Y.C. Chen; *PLOS One*, vol. 2015, 10, e0117065.

23. J.F. Yala, P. Thebault, A. Hequet, V. Humblot, C.M. Pradier, J.M. Berjeaud; *Appl. Microbiol. Biotechnol.*, vol. 89, pp. 623-634, 2011.

24. F. Wang, L.H. Qin, C.J. Pace, P. Wong, R. Malonis, J.M. Gao; *Chem.Bio.Chem.*, vol. 13, pp. 51-55, 2012.

25. J.M. David, T.A. Owens, S.P. Barwe, A.K. Rajasekaran; *Mol. Cancer Ther.*, vol. 12, pp. 2296-2307, 2013.

26. J.M. David, T.A. Owens, L.J. Inge, R.M. Bremmer, A.K. Rajasekaran; *Mol. Cancer Ther.*, vol. 13, pp. 788-799, 2014.

27. D. Wijesinghe, M.C. Arachchige, A. Lu, Y.K, Reshetnyak, O. A. Andreev; *Sci. Rep.*, vol. 3, pp. 3650-3658, 2013.

28. D.K. Rao, H.Y. Liu, S.V. Ambudkar, M. Mayer; *J. Biol. Chem.*, vol. 289, pp. 31397-31410, 2014.

29. H.N. Abdelhamid, M.S. Khan, H.F. Wu; *RSC Adv.*, vol. 4, pp. 50035-50046, 2014.

30. C. Dittrich, W. Meier; *Macromol. Biosci.*, vol. 10, pp. 1406-1415, 2010.

31. T.B. Schuster, D. de Bruyn Outboter, E. Bordignon, G. Jeschke, W. Meier; *Soft Matter*, vol. 6, pp. 5596-5604, 2010.

32. K. Wang, J. Ruan, H. Song, J. Zhang, Y. Wo, S. Guo, D. Cui; *Nanoscale Res. Lett.*, vol. 6, pp. 8, 2011.

33. E. Biron, J. Chatterjee, O. Ovadia, D. Langenegger, J. Brueggen, D. Hoyer, H.A. Schmid, R. Jelinek, C. Gilon, A. Hoffman, H. Kessler; *Angew. Chem., Int. Ed.*, vol. 47, pp. 2595-2599, 2008.

34. W.S. Horne, S.H. Gellman; *Acc. Chem. Res.*, vol. 41, pp. 1399-1408, 2008.

35. J.D. Sadowsky, J.K. Murray, Y. Tomita, S.H. Gellman; *ChemBioChem*, vol. 8, pp. 903-916, 2007.

36. C. Solanas, B.G. de la Torre, M. Fernández-Reyes, C. Santiverri, M. A. Jiménez, L. Rivas, A.I. Jiménez, D. Andreu, C. Cativiela; *J. Med. Chem.*, vol. 53, pp. 4119-4129, 2010.

37. G.F. Gause; *Nature*, vol. 154, pp. 703-70, 1944.

38. L.H. Kondejewski, S.W. Farmer, D.S. Wishart, R.E. Hancock, R.S. Hodges; *Int. J. Pept. Protein. Res.*, vol. 47, pp. 460-466, 1996.

39. E.J. Prenner, R.N. Lewis, R.N. McElhaney; *Biochim. Biophys. Acta*, vol. 1462, pp. 201–221, 1999.

40. C. Alemán; *J. Phys. Chem. B*; vol. 101, pp. 5046-5050, 1997.

41. C. Alemán, A.I. Jiménez, C. Cativiela, J.J. Pérez, J. Casanovas; *J. Phys. Chem. B*, vol. 106, pp. 11849-11858, 2002.

42. J. Casanovas, A.I. Jiménez, C. Cativiela, J.J. Pérez, C. Alemán; *J. Org. Chem.*, vol. 68, pp. 7088-7091, 2003.

43. A. Frenot, I.S. Chronakis; *Curr. Opin. Colloid Interface Sci.*, vol. 8, pp. 64-75, 2003.

44. D. Li, Y. Xia; *Adv. Mater.*, vol. 16, pp. 1151-1170, 2004.

45. K. Jayaraman, M. Kotaki, Y. Zhang, X. Mo, S. Ramakrishna; *J. Nanosci. Nanotechnol.*, vol. 4, pp. 52-65, 2004.

46. C. Solanas, B.G. de la Torre, M. Fernández-Reyes, C. Santiverri, M. A. Jiménez, L. Rivas, A.I. Jiménez, D. Andreu, C. Cativiela; *J. Med. Chem.*, vol. 53, pp. 4119–4129, 2010.

47. M.M. Pérez-Madrigal, E. Llorens, L.J.del Valle, J. Puiggalí, E. Armelin, C. Alemán; *Express Polym. Lett.*, vol. 10, pp. 628–646, 2016.

48. M. Planellas, M.M. Pérez-Madrigal, L.J. del Valle, S. Kobauri, R. Katsarava, C. Alemán, J. Puiggalí; *J. Polym. Chem.*, vol. 6, pp. 925–937, 2015.

49. http://dichroweb.cryst.bbk.ac.uk

50. L. Whitmore, B.A. Wallace; *Biopolymers*, vol. 89, pp. 392–400, 2008.

51. L. Whitmore, B.A. Wallace; *Nucleic Acids Res.*, vol. 32, pp. 668-673, 2004.

52. L. Whitmore, B.A. Wallace; *Biopolymers*, vol. 89, pp. 392-400, 2008.

53. L. Whitmore, B.A. Wallace; *Nucleic Acids Res.*, vol. 32, pp. 668-673, 2004.

54. http://dichroweb.cryst.bbk.ac.uk

55. Y. Chen, B.A. Wallace; *Biopolymers*, vol. 42, pp. 771-781, 1997.

56. E. Llorens, H. Ibañez, L.J. del Valle, J. Puiggalí; *Mater. Sci. Eng. C*, vol. 49, pp. 472-484, 2015.

57. H.Y. Wang, J.H. Ji, W. Zhang, Y.H. Zhang, J. Jiang, Z.W.Wu, S.H. Pu, P.K. Chu; *Acta Biomater.*, vol. 5, pp. 279-287, 2009.

58. J.F. Moulder, W.F. Stickle, P.E. Sobol, K.D. Bomben, Handbook of X-ray Photoelectron Spectroscopy, Perkin-Elmer Corp, *Eden Prairie, MN, USA*, 1992.

59. Z. Yang, S. Yuan, B. Liang, Y. Liu, C. Choong, S.O. Pehkonen; *Macromol. Biosci.*, vol. 14, pp. 1299-1311, 2014.

60. G.C. Smith; *J. Electron. Spectrosc. Relat. Phenom.*, vol. 148, pp. 21-28, 2015.

61. A. Marmur; *Soft Matter*, vol. 2, pp. 12-17, 2006.

62. E.H. Jeong, S.S. Im, J.H. Youk; *Polymer*, vol. 46, pp. 9538-9543, 2005.

63. L.J. del Valle, R. Camps, A. Díaz, L. Franco, A. Rodríguez-Galán, J. Puiggalí; *J. Polym. Res.*, vol. 18, pp. 1903-1917, 2011.

64. S. Murase, M. Aymat, A. Calvet, L.J. del Valle, J. Puiggalí; *Eur. Polym. J.*, vol. 71, pp. 196-209, 2015.

65. M. Nishio, J. Kohno, M. Sakurai, S.I. Suzuki, N. Okada, K. Kawano, S. Komatsubara; *J. Antibiot.*, vol. 53, pp. 724-727, 2000.

CHAPTER 7

General Conclusions

7.1 Part 1: Polythiophene-*g*-poly(ethylene glycol) graph copolymers as hybrid bioplatforms for tissue engineering

1. Comparison between PTh_3^*-*g*-PEG and PTh_5-*g*-PEG indicates that the optical and electrochemical properties of PTh-*g*-PEG graft copolymers improves with the increasing length of the conjugated segments, which depends on the number of consecutive unsubstituted Th units. However, the properties of linear PTh_3 are worse than those of the graft copolymers. This has been attributed to the porosity induced by the grafted PEG chains, which facilitates the transport of dopant ions during the Faradaic processes.

2. The ε_g of PTh-*g*-PEG ranges from 2.16 to 2.29 eV, depending of the length of the unsubstituted Th segments, the length of the PEG chains, and the dopant agent. The ε_g values obtained for PTh_5-*g*-PEG_n are slightly higher than those typically found for PTh_3 and 3-substituted PTh derivatives, evidencing that PEG chains cause a reduction in the conjugation length of the PTh backbone. In contrast, the ε_g of PTh_3^*-*g*-PEG is lower than that of PTh_3 (2.28 eV), reflecting that the combination of Th_3 units and macromonomers affects favorably to the elimination of undesirable α-β and/or β-β linkages during the polymerization process.

3. The hydrophilicity of PTh-*g*-PEG increases with the length of the PEG chains, which has been attributed to the independent organization of the PTh and PEG segments, and decreases with the length of the unsubstituted Th segments. Thus, in PTh-*g*-PEG copolymers with short segments of unsubstituted Th rings, as for example PTh_5-*g*-PEG_n, PEG chains are completely accessible to the solvent and this phenomenon is more pronounced for the highest *n*, while copolymers with large Th segments are dominated by the hydrophobicity of the Th ring.

4. PTh-*g*-PEG hybrids behave as electrochemically active matrices for cellular proliferation. This behavior is consequence of the synergy between the electrochemical properties of the PTh segments and the biocompatibility of the PEG fragments, as demonstrated by the increment of the current density obtained when films are coated with cells.

5. Cellular adhesion and proliferation on the surface of PTh-*g*-PEG copolymers have been found to increase with decreasing PEG / PTh ratio, while the biocompatibility of PTh_3 is very low because of its cytotoxic effects. However, the noxious cytotoxic effects of PTh_3 have been eliminated by incorporating a thin layer of collagen adsorbed onto the polymeric matrix, which acts as a stopper and enables cellular adhesion.

7.2 Part 2: Poly(3,4-ethylenedioxythiophene)-peptide conjugates based on chemical similarity

6. A previously proposed synthetic approach for the preparation of PEDOT-peptide conjugates has been modified to regulate the surface properties of the resulting materials. In this new strategy both the peptide and the monomer are incorporated to the generation medium during the second polymerization step, which induces the competition between the polymer growing and end-capping processes. The new methodology, which causes a more effective incorporation of the amino acid at the end of the polymer chains, affects the surface roughness, the wettability and the surface energy.

7. The new synthetic methodology does not affect the electro-biocompatibility of the resulting PEDOT-peptide conjugates. Viability assays indicate that the behavior as cellular matrix of the conjugates is similar, independently of the synthetic approach. On the other hand, the electrocompatibility of these two-component materials with living cells is more influenced by the cell line than by the synthetic approach used to prepare them.

8. The RG^ED peptide, which is an analogue of the adhesive RGD sequence, has been designed by chemical similarity with PEDOT and, subsequently, prepared through chemical synthesis. After this, PEDOT-RG^ED has been obtained by anodic polymerization, the EDOT side group of the GlE residue acting as a linker between the peptide and the polymer. Two strategies, the one originally proposed by Fabregat *et al.* and the

variation proposed in this Thesis, have been used to obtain hybrid materials with different surface properties.

9. Because the cell recognition abilities of the RGD motif remain in the $RG^{E}D$ sequence, cell attachment and spreading on PEDOT-$RG^{E}D$ have been significantly promoted with respect to PEDOT, independently of the synthetic strategy used for its preparation. However, comparison between the two PEDOT-$RG^{E}D$ conjugates prepared in this work indicates that the one obtained using the synthetic strategy proposed in this Thesis behaves much better as soft bioelectroactive support for cell attachment than the one prepared using the original methodology.

10. The electrochemical activity of the ECP is preserved in the PEDOT-$RG^{E}D$ conjugate because both the small size of the peptide and the utilization of an EDOT ring as linker between the ECP and the peptide, do not affect the transport of charge. Indeed, the electrochemical activity of the conjugates increases upon the adhesion of cell monolayers.

7.3 Part 3: Biodegradable Nanofibrous Scaffolds as Smart Delivery Vehicles for Amino Acids

11. Loading into edible non-nutritional PE44 NFs using electrospinning has been proposed as a reliable approach for the controlled delivery of AAs in humid environments. Because of their physical characteristics, loaded PE44/AA NFs could be incorporated into the diets of livestock and fish in farms for effective administration of essential and conditional AAs.

12. Electrospun PE44/AA NFs can be described as very stable biphasic systems made of AA crystals distributed into a polymeric matrix. The distribution of such crystals into PE44 NFs has been found to depend on the polarity of the AA.

13. Release assays in enzyme-free solutions with different polarities proved that loaded AAs are retained in aqueous environments, independently of the polarity of both the medium and the AA. In contrast, assays in lipase-containing solutions showed a very fast and complete

release. The enzyme preferentially attacks the PE44 regions, favoring the almost immediate release of the biomolecules.

7.4 Part 4: Loading and release of hydrophobic gramicidin in micro- and nanostructured polyester

14. Electrosprayed PE44 microspheres can be used to load GA-L, a highly hydrophobic pentadecapeptide that has been recently proposed as a potent therapeutic agent against different carcinomas. Unfortunately, this processing technique cannot be used to load the cyclic GA-S derivatives.

15. GA-L is mainly loaded at the surface of electrosprayed PE44 microparticles. This enhances the hydrophobicity of the microparticles while the thermal stability remains practically unaltered.

16. The release rate of GA-L from loaded PE44 microparticles increases with the hydrophobicity of the release medium. In spite of this, the delivery of this hydrophobic peptide in PBS is 70%.

17. Loading of GA-L into PE44 microspheres by electrospraying allows to preserve both the antibacterial activity of the peptide and the biocompatibility of the polymeric matrix.

18. Electrospun polyester fibers have been used to load GA-L, GA-S1 and GA-S2, even though the processing conditions used for the linear peptide were very different from those of the cyclic GA analogues. Indeed, GA-S1 and GA-S2 cause important changes in the morphology, diameter and properties (thermal stability and wettability) of PE44 fibers, whereas the characteristics of unloaded and GA-L loaded fibers are very similar.

19. Release assays using peptide-loaded PE44 fibers demonstrate that the polymeric matrix regulates the delivery of the antibiotic in hydrophilic environments similar to the physiological medium. The maximum peptide release, which stabilizes after around 5 days, reaches values of 97%±1%, 78%±2% and 62%±4% for GA-S1, GA-S2 and GA-L, respectively.

20. The antimicrobial activity of PE44/GA-S1 and PE44/GA-S2 is comparable (Gram-positive) or higher (Gram-negative) than that of PE44/GA-L. Moreover, the antibiotic potency of both GA-S1 and GA-S2 is higher when loaded into polyester fibers than in solution.